

## **Library Declaration and Deposit Agreement**

### **1. STUDENT DETAILS**

Andrew Furmanski

1155619

### **2. THESIS DEPOSIT**

2.1 I understand that under my registration at the University, I am required to deposit my thesis with the University in BOTH hard copy and in digital format. The digital version should normally be saved as a single pdf file.

2.2 The hard copy will be housed in the University Library. The digital version will be deposited in the University's Institutional Repository (WRAP). Unless otherwise indicated (see 2.3 below) this will be made openly accessible on the Internet and will be supplied to the British Library to be made available online via its Electronic Theses Online Service (EThOS) service. [At present, theses submitted for a Masters degree by Research (MA, MSc, LLM, MS or MMedSci) are not being deposited in WRAP and not being made available via EThOS. This may change in future.]

2.3 In exceptional circumstances, the Chair of the Board of Graduate Studies may grant permission for an embargo to be placed on public access to the hard copy thesis for a limited period. It is also possible to apply separately for an embargo on the digital version. (Further information is available in the Guide to Examinations for Higher Degrees by Research.)

2.4 (a) Hard Copy I hereby deposit a hard copy of my thesis in the University Library to be made publicly available to readers immediately.

I agree that my thesis may be photocopied.

(b) Digital Copy I hereby deposit a digital copy of my thesis to be held in WRAP and made available via EThOS.

My thesis can be made publicly available online.

### **3. GRANTING OF NON-EXCLUSIVE RIGHTS**

Whether I deposit my Work personally or through an assistant or other agent, I agree to the following: Rights granted to the University of Warwick and the British Library and the user of the thesis through this agreement are non-exclusive. I retain all rights in the thesis in its present version or future versions. I agree that the institutional repository administrators and the British Library or their agents may, without changing content, digitise and migrate the thesis to any medium or format for the purpose of future preservation and accessibility.

#### 4. DECLARATIONS

(a) I DECLARE THAT:

- I am the author and owner of the copyright in the thesis and/or I have the authority of the authors and owners of the copyright in the thesis to make this agreement. Reproduction of any part of this thesis for teaching or in academic or other forms of publication is subject to the normal limitations on the use of copyrighted materials and to the proper and full acknowledgement of its source.
- The digital version of the thesis I am supplying is the same version as the final, hardbound copy submitted in completion of my degree, once any minor corrections have been completed.
- I have exercised reasonable care to ensure that the thesis is original, and does not to the best of my knowledge break any UK law or other Intellectual Property Right, or contain any confidential material.
- I understand that, through the medium of the Internet, files will be available to automated agents, and may be searched and copied by, for example, text mining and plagiarism detection software.

(b) IF I HAVE AGREED (in Section 2 above) TO MAKE MY THESIS PUBLICLY AVAILABLE DIGITALLY, I ALSO DECLARE THAT:

- I grant the University of Warwick and the British Library a licence to make available on the Internet the thesis in digitised format through the Institutional Repository and through the British Library via the EThOS service.
- If my thesis does include any substantial subsidiary material owned by third-party copyright holders, I have sought and obtained permission to include it in any version of my thesis available in digital format and that this permission encompasses the rights that I have granted to the University of Warwick and to the British Library.

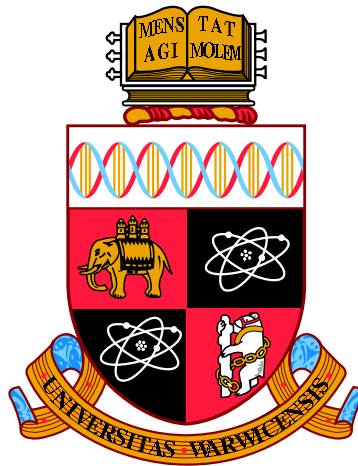
#### 5. LEGAL INFRINGEMENTS

I understand that neither the University of Warwick nor the British Library have any obligation to take legal action on behalf of myself, or other rights holders, in the event of infringement of intellectual property rights, breach of contract or of any other right, in the thesis.

---

*Please sign this agreement and return it to the Graduate School Office when you submit your thesis.*

Student's signature: .....Date: .....



**Charged-current Quasi-elastic-like neutrino  
interactions at the T2K experiment.**

by

**Andrew Furmanski**

**Thesis**

Submitted to the University of Warwick

for the degree of

**Doctor of Philosophy**

**Physics**

August 2015

THE UNIVERSITY OF  
**WARWICK**

# Contents

<b>List of Tables</b>	<b>v</b>
<b>List of Figures</b>	<b>vi</b>
<b>Acknowledgments</b>	<b>xi</b>
<b>Declarations</b>	<b>xiii</b>
<b>Abstract</b>	<b>xiv</b>
<b>Chapter 1 Introduction</b>	<b>1</b>
<b>Chapter 2 Neutrino Oscillations</b>	<b>3</b>
2.1 History of neutrinos . . . . .	3
2.2 Neutrino oscillations . . . . .	4
2.2.1 Matter effects . . . . .	7
2.3 CP-violation in the neutrino sector . . . . .	9
2.4 Summary of neutrino oscillation measurements . . . . .	10
2.4.1 Long baseline neutrino beam experiments . . . . .	10
2.4.2 Reactor neutrino experiments . . . . .	15
2.4.3 Anomalous results . . . . .	18
2.4.4 Near- and far-future experiments . . . . .	20
<b>Chapter 3 Neutrino interactions</b>	<b>25</b>
3.0.5 The weak interaction . . . . .	25
3.0.6 Terminology and conventions . . . . .	26
3.1 Neutrino-lepton scattering . . . . .	27
3.2 Neutrino-nucleon scattering . . . . .	29
3.3 Neutrino-nucleus scattering . . . . .	33
3.3.1 Nuclear effects . . . . .	34

3.3.2	Correlations and coherence . . . . .	35
3.4	Summary of cross section data . . . . .	37
3.4.1	Low energy processes . . . . .	38
3.4.2	Medium energy processes . . . . .	38
3.4.3	Very high energy processes . . . . .	43
3.5	Generators . . . . .	45
3.5.1	Current and past neutrino interaction generators . . . . .	46
3.5.2	Discussion of generators . . . . .	48
<b>Chapter 4 The T2K experiment</b>		<b>50</b>
4.1	Overview and motivation . . . . .	50
4.2	Neutrino beam . . . . .	50
4.2.1	Off-axis angle . . . . .	51
4.3	INGRID detector . . . . .	54
4.4	ND280 . . . . .	54
4.4.1	P0D . . . . .	55
4.4.2	Tracker . . . . .	57
4.4.3	ECals . . . . .	59
4.4.4	SMRD . . . . .	60
4.5	Super-Kamiokande . . . . .	62
4.6	NA61/SHINE . . . . .	63
4.7	Simulation . . . . .	64
4.7.1	beam . . . . .	64
4.7.2	Near detectors . . . . .	64
4.7.3	Super-K . . . . .	65
4.8	Current results and future physics sensitivity . . . . .	65
4.8.1	Latest results . . . . .	65
4.8.2	Future sensitivity . . . . .	67
<b>Chapter 5 The Spectral Function nuclear model in a neutrino inter-</b>		
<b>action simulation</b>		<b>70</b>
5.1	The NEUT interaction generator . . . . .	71
5.2	Nuclear models . . . . .	74
5.2.1	Relativistic Fermi Gas . . . . .	74
5.2.2	Local Fermi Gas . . . . .	74
5.2.3	Spectral Function . . . . .	75
5.2.4	Pauli blocking . . . . .	77
5.3	Spectral Function implementation in NEUT . . . . .	78

5.4	Efficiency improvements . . . . .	79
5.5	Validity over nuclei . . . . .	80
5.6	Verification . . . . .	81
5.7	Multi-nucleon ejection model . . . . .	83
5.8	Systematic uncertainties within the SF model . . . . .	85
5.8.1	Relative normalisation . . . . .	87
5.8.2	Mean-field peak width . . . . .	88
5.8.3	Pauli blocking . . . . .	89
5.8.4	Reweighting closure tests . . . . .	89
5.9	Determining the spectral function uncertainty scale . . . . .	91
5.9.1	Mean-field width and Pauli blocking . . . . .	92
5.9.2	Normalisation of the correlation term . . . . .	92
5.10	Summary . . . . .	93
<b>Chapter 6 Measuring the <math>CC0\pi</math> cross section</b>		<b>95</b>
6.1	Overview and motivation . . . . .	95
6.2	Implementation details . . . . .	96
6.3	Event selection . . . . .	97
6.3.1	$CC0\pi$ selection . . . . .	99
6.3.2	$CC1\pi$ and $CCother$ selections . . . . .	101
6.4	Cross section extraction . . . . .	102
6.4.1	Background subtraction . . . . .	103
6.4.2	Bayesian unfolding method . . . . .	104
6.4.3	Uncertainties . . . . .	105
6.4.4	Background estimation . . . . .	112
6.5	Binning choice . . . . .	116
6.6	Fake data studies . . . . .	119
6.6.1	Fake data sets used . . . . .	119
6.6.2	Reproducing MC truth . . . . .	120
6.6.3	Number of iterations . . . . .	120
6.6.4	“crazy” MC weighting . . . . .	129
6.7	Results . . . . .	131
6.7.1	Uncertainties . . . . .	131
6.7.2	Double differential cross section results . . . . .	133
6.7.3	Single differential cross section results . . . . .	137
6.7.4	Integrated cross section results . . . . .	139
6.8	Discussion . . . . .	140

<b>Chapter 7</b>	<b>Conclusions</b>	<b>143</b>
<b>Appendix A</b>	<b>SF appendices</b>	<b>145</b>
A.1	Derivation of cross-section formula Jacobian . . . . .	145
A.2	CCQE cross section calculation . . . . .	147
<b>Appendix B</b>	<b>CC0<math>\pi</math> appendices</b>	<b>149</b>
B.1	Alternative results plots . . . . .	149
B.2	Alternative prior tests . . . . .	149

# List of Tables

2.1	Current best knowledge of neutrino oscillation parameters . . . . .	24
4.1	Relative fractions of gases in the TPC detectors. . . . .	59
4.2	Table of differing details between ECal modules . . . . .	60
6.1	Data samples used in $CC0\pi$ measurement . . . . .	97
6.2	Composition of events in the $CC0\pi$ sample, by topology . . . . .	101
6.3	Composition of true $CC0\pi$ events in the $CC0\pi$ sample, by reaction. .	101
6.4	Summary of data comparisons in background selections. . . . .	113
6.5	Summary of error contributions for the full phase space. . . . .	131
6.6	Summary of error contributions for the restricted phase space. . . .	133
6.7	$\chi^2$ of agreement between three generator predictions and the double- differential data . . . . .	137

# List of Figures

2.1	Feynman diagrams demonstrating the concept of matter effects. . . .	8
2.2	Diagram showing potential neutrino mass hierarchies. . . . .	9
2.3	Asymmetry vs delta . . . . .	10
2.4	K2K disappearance results . . . . .	11
2.5	MINOS disappearance results . . . . .	12
2.6	T2K appearance 7.3 sigma result . . . . .	14
2.7	Atmospheric parameter constraints from several experiments . . . .	15
2.8	NOvA sensitivity to mass hierarchy . . . . .	16
2.9	Evidence for an additional reactor neutrino component from RENO	18
2.10	Allowed regions from the LSND and MiniBooNE sterile neutrino fits	20
2.11	Spectrum at an intermediate baseline reactor experiment designed to determine the mass hierarchy. . . . .	23
3.1	Generic neutrino scattering Feynman diagram . . . . .	27
3.2	Neutrino-lepton scattering Feynman diagram . . . . .	27
3.3	Differential cross section for neutrino-electron elastic scattering. . . .	28
3.4	Neutrino-nucleon elastic scattering Feynman diagrams. . . . .	29
3.5	Feynman diagram of resonant pion production. . . . .	32
3.6	NEUT prediction for different processes' cross sections as a function of energy. . . . .	34
3.7	Ratio of RPA-corrected to standard IA cross section . . . . .	37
3.8	Summary of inverse beta decay cross section measurements . . . . .	38
3.9	Summary of $\nu_\mu$ CCQE cross section measurements to date . . . . .	39
3.10	Summary of $\bar{\nu}_\mu$ CCQE cross section measurements to date . . . . .	40
3.11	Demonstration of resonant pion production data compared to predic- tions . . . . .	41
3.12	Comparison of high energy coherent interaction data and models. . .	42
3.13	Comparison of low energy coherent interaction data and models. . .	42

3.14	Existing measurements of the $(\nu_\mu + p \rightarrow \mu^- + p + \pi^+ + \pi^0)$ scattering cross section. . . . .	43
3.15	CC-inclusive data summary . . . . .	44
3.16	High energy CC-inclusive data . . . . .	44
4.1	Schematic of the target station and decay volume . . . . .	52
4.2	Neutrino energy as a function of pion energy for various off-axis angles. . . . .	53
4.3	Flux predictions for different off-axis angles . . . . .	53
4.4	ND280 schematic . . . . .	56
4.5	ND280 photograph with magnet open . . . . .	56
4.6	Schematic of POD detector active region . . . . .	57
4.7	Schematic of a TPC . . . . .	59
4.8	Photograph of an SMRD bar . . . . .	61
4.9	Schematic of Super-Kamiokande . . . . .	63
4.10	Electron neutrino events observed at SK during T2K runs 1-4 . . . . .	66
4.11	Muon neutrino events observed at SK during T2K runs 1-4 . . . . .	66
4.12	POT vs time . . . . .	67
4.13	Appearance probabilities as a function of distance . . . . .	69
4.14	T2K expected final precision for $\theta_{13}$ and $\delta_{CP}$ . . . . .	69
5.1	Pion scattering cross sections used to tune FSI routines in NEUT . . . . .	74
5.2	2D spectral function for oxygen . . . . .	76
5.3	1D Spectral Function for oxygen . . . . .	76
5.4	Example of electron scattering data compared to both SF and RFG models. . . . .	77
5.5	Comparison between NEUT predictions and NuWro predictions for the SF model. . . . .	81
5.6	Comparison between NEUT prediction and O. Benhars calculation for the SF model. . . . .	82
5.7	CCQE cross section as a function of energy predicted by NEUT and NuWro. . . . .	82
5.8	Ratio of different generators to NEUT SF cross section for $\nu_\mu$ . . . . .	83
5.9	Ratio of different generators to NEUT SF cross section for $\nu_e$ . . . . .	84
5.10	Oxygen spectral function separated by mean-field and correlation terms. . . . .	85
5.11	Nucleon momenta before FSI . . . . .	86
5.12	Nucleon momenta after FSI. . . . .	86
5.13	Widened SF momentum distribution. . . . .	89
5.14	Effect of SF mean-field width on muon kinematics. . . . .	90

5.15	Reweighting closure tests for varying the SF correlation normalisation.	91
5.16	Reweighting closure tests for varying the SF Pauli blocking. . . . .	92
5.17	A simple electron scattering simulation with different mean-field/correlated fractions. . . . .	94
6.1	Muon momentum and angle distributions for the CC0 $\pi$ selection, NEUT compared with GENIE. . . . .	100
6.2	Muon momentum and angle distributions for the CC0 $\pi$ selection, for only true CC0 $\pi$ interaction, separated by reaction. . . . .	100
6.3	Muon momentum and angle distributions for the CC1 $\pi$ selection. . .	102
6.4	Muon momentum and angle distributions for the CCothers selection.	102
6.5	CC1 $\pi$ selection data compared with MC prediction . . . . .	114
6.6	CCothers data compared with MC prediction . . . . .	115
6.7	Demonstration of the restricted phase space region. . . . .	117
6.8	Efficiency of selection in two dimensions. . . . .	118
6.9	Detector response matrix (full phase space). . . . .	118
6.10	Angular and momentum resolutions compared to the bin widths chosen.	119
6.11	Unfolded result compared to truth when unfolding MC with itself (full phase space). . . . .	121
6.12	Unfolded result compared to truth when unfolding MC with itself (restricted phase space). . . . .	121
6.13	Unfolded distributions for a NEUT fake data sample, compared to the truth prediction. . . . .	123
6.14	Mean statistical error against number of iterations for a NEUT fake data sample. . . . .	123
6.15	Mean and RMS biases against number of iterations for a NEUT fake data sample. . . . .	124
6.16	$\chi^2$ of change against number of iterations, for a NEUT fake data sample. . . . .	124
6.17	Mean statistical error against number of iterations for a GENIE fake data sample. . . . .	125
6.18	Mean and RMS biases against number of iterations for a GENIE fake data sample. . . . .	125
6.19	$\chi^2$ of change against number of iterations, for a GENIE fake data sample. . . . .	126
6.20	Mean statistical error against number of iterations for a SF fake data sample. . . . .	126

6.21	Mean and RMS biases against number of iterations for a SF fake data sample. . . . .	127
6.22	$\chi^2$ of change against number of iterations, for a SF fake data sample. . . . .	127
6.23	Momentum distributions of all CC1 $\pi$ and CCothers events, for NEUT and GENIE. . . . .	128
6.24	GENIE fake data unfolded results compared to the GENIE and NEUT predictions. . . . .	128
6.25	Weights applied as a function of true neutrino energy to generate a crazy fake data set. . . . .	130
6.26	Crazy fake data unfolded results compared to the crazy truth and NEUT predictions. . . . .	130
6.27	Fractional uncertainties over the full phase space for various sources. . . . .	132
6.28	“Lego plot” of results with full uncertainties, full phase space. . . . .	134
6.29	“Lego plot” of results with full uncertainties, restricted phase space. . . . .	134
6.30	Full phase space results sliced in $\cos\theta$ . . . . .	135
6.31	Restricted phase space results sliced in $\cos\theta$ . . . . .	136
6.32	Measured cross section as a function of muon momentum. . . . .	138
6.33	Measured cross section as a function of cosine of muon angle. . . . .	138
6.34	Measured cross section as a function of $Q_{QE}^2$ . . . . .	139
6.35	Total flux-integrated cross section. . . . .	140
6.36	Total flux-integrated cross section over restricted phase-space only. . . . .	141
B.1	Full phase-space results, compared to the NEUT nominal prediction. Inner error bars are statistical only. . . . .	150
B.2	Restricted phase-space results, compared to the NEUT nominal prediction. Inner error bars are statistical only. . . . .	151
B.3	Full phase-space results, presented as ratios to NEUT MC to inform comparisons with generators. Inner error bars are statistical only. . . . .	152
B.4	Restricted phase-space results, presented as ratios to NEUT MC to inform comparisons with generators. Inner error bars are statistical only. . . . .	153
B.5	Full phase-space results, presented as ratios to NEUT MC to inform comparisons with generators. Inner error bars are statistical only. . . . .	154
B.6	Restricted phase-space results, presented as ratios to NEUT MC to inform comparisons with generators. Inner error bars are statistical only. . . . .	155

B.7	(left) the nominal and two alternate priors, and (right) the ratios of all to the nominal prior. The full phase space is shown. . . . .	156
B.8	Real data alternative prior plots. Full phase space. . . . .	156
B.9	Real data alternative prior plots. Restricted phase space. . . . .	157

# Acknowledgments

Firstly I would like to thank my supervisors, Dr. Gary Barker and Dr. Steve Boyd for giving me the opportunity to pursue a career in particle physics. Having such friendly, approachable supervisors made asking for help a very easy process, and the combination of expert knowledge, a good sense of humour, and a slight disdain for bureaucracy really helped me get research done effectively and enjoyably.

The work in this thesis was largely carried out as a member of the T2K collaboration. This international collaboration has been contributed to by hundreds of scientists, engineers, and technicians over a period of many years, and much of the work I have done would have been impossible without the work of most of these people. Thanks must of course go to every member of the collaboration, but some special mentions should go to particular people who have made a significant impact on my work. Firstly, the Neutrino Interactions Working Group (NIWG) conveners, Prof. Kevin McFarland, Dr. Morgan Wascko, and Prof. Yoshinari Hayato, as well as Prof. Jan Sobczyk for their assistance and guidance in the work done in chapter 5. The cross section measurement in chapter 6 was performed under the ever watchful eye of Prof. Kendall Mahn who provided many words of advice and occasionally a well-needed boot up the expletive to get the work done in a timely manner. I would also like to mention the T2K spokespeople, Prof. Takashi Kobayashi and Prof. Chang Kee Jung. They have done a great job leading the collaboration over the past few years, particularly given the tough circumstances.

I was able to travel to Japan a number of times during my PhD, including one stay of 7 months. The friends I made in Tokai made my time there extremely enjoyable, so I would like to thank Dr. Sarah Foley, Dr. Jevon Keane-brennan,

Dr. Megan Friend, Dr. Matthew Lawe, Dr. Ben Smith, and Linda Cremonesi for their ability to avoid talking about work when out at dinner! A particular mention must go here to Dr. Megan Friend for her aggressive insistence that I start writing this document 18 months ago, it is largely because of this that I have been able to submit it for examination before the end of my funding period! In addition, I would like to thank Ayako Kikuchi, as well as the rest of the staff at the J-PARC users office and Masago international lodging for making my visits to Tokai so enjoyable and easy.

I was very fortunate to get on with everyone I shared an office with, so thanks to Dr. David Hadley, Dr. Martin Haigh, Dr. Dan Scully, Dr. Callum Lister, Dr. Nicola McConkey, Steve Dennis, and Eddy Larkin for providing well-needed distractions from time to time, as well as the less well-needed distractions... Particular thanks must go here to Dr. David Hadley for guiding me through the early stages of being a research student, and persuading me to use python in all that I do.

We now come to my non-physicist friends. There are far too many people in this category to name everyone, however a special thank you must go to Oliver Gazeley, who I have been sharing a house with for the last 7 and a half years. Simply putting up with me for that length of time is admirable, though perhaps the same could be said the other way round.

The final thanks must of course go to my family, in particular my wonderful mother. Although she may think she has not helped in any way, her love and support over the past 25 years have been incredible. From encouraging me to do whatever I want and helping me believe that I can do just that, to years of driving me around, helping me moving house, and countless smaller favours. I would not be writing this thesis at all if it wasn't for the start in life I was given.

# Declarations

The material presented in this document has not been published or submitted for examination at another institute. It represents my own work unless stated otherwise, complete with references.

Chapter 4 describes the T2K experiment, a large international collaboration to which several hundred people have contributed over many years, including myself. I spent a significant amount of time helping to develop improved variables and an improved algorithm for the particle identification in the electromagnetic calorimeters. This also included evaluating the systematic uncertainties associated with it.

Chapter 5 describes the implementation of a new nuclear model in a neutrino interaction event generator. NEUT is an interaction simulation written over a number of years, primarily by members of the Super-K collaboration. I am grateful for the assistance of Yoshinari Hayato for his assistance in the implementation in NEUT. The spectral function implementation draws heavily on that in another generator NuWro, and I am very grateful to the entire NuWro collaboration, in particular Jan Sobczyk, for their useful discussion. In addition, the work in chapter 5 on reweighting systematics was done within T2KReWeight, a reweighting package developed by a number of T2K collaborators.

The analysis presented in chapter 6 is my own work, though it uses a selection developed by other collaborators. In addition, the software framework used for the actual extraction of a cross section and evaluation of systematic uncertainties, xsTool, was developed primarily by Martin Heirholzer, with assistance from other users including myself.

# Abstract

T2K is a long-baseline neutrino oscillation experiment based in Japan. The experiment has already measured the appearance of  $\nu_e$  in a  $\nu_\mu$  beam, and is hoping to measure the appearance of  $\bar{\nu}_e$  in a  $\bar{\nu}_\mu$  beam, which would open the possibility of observing CP-violation in the lepton sector. The charged current quasi-elastic (CCQE) interaction ( $\nu_\mu + n \rightarrow \mu^- + p$ ) is of great importance to T2K as it is expected to make up over 80% of the interactions at the oscillation peak (600 MeV).

In recent years it has become clear that the most common model describing CCQE interactions on nuclei, the Relativistic Fermi Gas (RFG) model, is not able to describe low energy data on nuclear targets. An alternative model, the Spectral Function (SF) model, was implemented in the NEUT interaction generator. Relevant uncertainties in this model are identified and evaluated.

The charged current quasi-elastic-like cross section is then measured using the T2K near detector, ND280, as a function of muon momentum and angle. This data is then critically compared to the predictions from two implementations of the RFG model, and also to the newly implemented SF model. The total integrated cross section is found to be  $(4.06 \pm 0.757) \times 10^{-39} \text{ cm}^2 \text{ nucleon}^{-1}$ . This value is currently in agreement with all three predictions.

# Chapter 1

## Introduction

The Standard Model is widely hailed as the most precisely tested model ever. Measurements of the electroweak sector at LEP agree astoundingly well with predictions from theory, and the recent discovery of the Higgs boson at the LHC appears to have completed the picture.

Unfortunately the Standard Model has some very large, very obvious flaws. Firstly, it makes no statement about gravity despite it being one of the largest driving forces of the formation of galaxies, stars, and planets. In addition, measurements of the rotational velocities of galaxies have revealed that there is very likely more matter in the universe than we can see. The Standard Model does not make any predictions for what this “dark matter” could be made of. In fact, recent measurements of distant supernovae suggest that the expansion of the universe is accelerating, requiring some form of energy source - this “dark energy” is also not predicted anywhere in the Standard Model. The final large flaw is the models current inability to provide the drastic matter-antimatter asymmetry which is seen in the universe today.

The discovery of neutrino oscillations in the early 2000’s [1, 2], described in chapter 2 has shown one of the first glimpses of new physics beyond the Standard Model, as it demonstrates that neutrinos have mass (though it doesn’t tell us exactly what that mass is). This raises new and interesting questions such as what is the neutrinos mass, and why is it so small?

Neutrino oscillations allow the possibility of CP-violation in the lepton sector which is required by many new models which generate the matter-antimatter asymmetry in the universe. In addition, some proposals of additional “sterile” neutrinos can function as dark matter candidates. These sterile neutrinos, if they exist, may be indirectly discovered in oscillation experiments.

To answer these new questions and probe new physics further will require precise measurements of neutrinos including their masses, mixing parameters, and searches for sterile partners and other potential new phenomena. As will be discussed in chapter 3, studying neutrinos is only possible through observing their interactions with matter, and this is a matter of much difficulty and uncertainty. In the near future, our measurements of neutrino oscillations are set to become limited by our understanding of neutrino interactions with the nuclei in detectors.

The only way to improve our understanding of neutrino interactions is through a combination of developing new, more sophisticated theories and models, and collating as much data as possible to differentiate between them. The charged current quasi-elastic (CCQE) interaction is identified as being of large importance to several current and future oscillation experiments.

Chapter 4 therefore details the T2K experiment, a neutrino oscillation experiment in Japan. Chapter 5 describes the implementation of a new nuclear model for the description of CCQE interactions in a Monte Carlo simulation, and the T2K near detector is used in chapter 6 to perform a measurement of this interaction channel. This data is then compared to various theoretical predictions.

## Chapter 2

# Neutrino Oscillations

Neutrinos were added into the Standard Model as massless particles, which meant that they were defined entirely by their flavour eigenstates. We shall see in the following sections that this is no longer considered to be the case.

### 2.1 History of neutrinos

The neutrino was first hypothesised by Wolfgang Pauli in 1930 [3] to solve the problem of energy conservation in nuclear beta-decay. The particle proposed was required to have a very small mass and a very small interaction probability, making it almost impossible to detect. He called the particle the neutron, as the neutron as we know it today had not been discovered yet. The particle actually had some of the properties of the neutron, and was proposed as a nuclear constituent. Pauli was so unsure of his proposal that he wasn't willing to publish the idea.

Four years later Enrico Fermi proposed the same particle, called the neutrino (from the Italian for “little neutral one”), as part of his full theory of beta-decay. This neutrino, however, was not a nuclear constituent, but was created in the process of beta-decay and forms the basis of the theory of neutrinos today [3].

The neutrino was finally detected in 1956 [4] using inverse beta-decay to detect neutrinos from nuclear reactors. In 1962 the muon neutrino and electron neutrino were shown to be distinct particles [5], and finally in 2000 the existence of the tau neutrino was experimentally verified by the DONUT collaboration [6], having been theoretically assumed to exist since the discovery of the tau lepton.

It wasn't until the emergence of the solar neutrino problem in the 1970s and 1980s, that neutrinos became truly interesting in their own right. Theoretical calculations in the Standard Solar Model gave fairly precise predictions for the flux

of neutrinos coming from the sun, however when this was measured experimentally the number of neutrinos was found to be significantly less than predicted. The first experiment to observe this was the Brookhaven neutrino detector, run by Ray Davis in the Homestake mine [7]. The initial results suggested that the measured flux was roughly a third of the expected flux. The Brookhaven experiment ran for over 20 years, undergoing many improvements in that time to try to find the source of the discrepancy. Over all 108 runs, the conclusion remained the same – the solar neutrino flux was measured to be roughly one third of the prediction [8].

The Super-Kamiokande experiment, along with others, also measured the solar neutrino flux using a variety of methods, and concluded that there was an energy-dependent deficit in the electron neutrino flux from the sun [9]. It proved very difficult to provide a physically motivated non-standard solar model which agreed with this data, and people began to conclude that neutrinos must be changing flavour on their journey to the earth. This conclusion was motivated by an original idea by Pontecorvo [10].

Eventually, the SNO [1] experiment showed that in fact the solar neutrino flux measured by neutral current reactions was consistent with expectation, but the charged current measurements disagreed. This was interpreted to confirm that neutrinos were indeed changing to muon and tau flavour, which could not interact via the charged current channel at those energies due to the higher mass of the lepton which needs to be produced, but could still contribute to the neutral current signal.

## 2.2 Neutrino oscillations

In 1963 it was proposed that, in the quark sector, the states corresponding to weak interactions (their flavour state) are not the same as those corresponding to masses [11]. This is in stark contrast to the electromagnetic and strong interactions. This leads to the strange concept of mixing, which can lead to flavour oscillations, and potentially CP-violation.

In neutrinos, we define flavour states as a superposition of mass states, leading to the mixing equation:

$$\begin{pmatrix} \nu_e \\ \nu_\mu \\ \nu_\tau \end{pmatrix} = U_{PMNS} \begin{pmatrix} \nu_1 \\ \nu_2 \\ \nu_3 \end{pmatrix} \quad (2.1)$$

Assuming that there are only three neutrinos (an assumption strongly sup-

ported, for  $m_\nu < \frac{1}{2}m_Z$ , by measurements of the invisible Z width at LEP [12]), the matrix  $U_{PMNS}$  will be unitary. Applying this unitarity constraint allows us to parametrise the matrix in terms of three mixing angles ( $\theta_{12}, \theta_{23}, \theta_{13}$ ) and a CP-violating phase,  $\delta$ . Using the concise notation  $c_{\alpha\beta} = \cos \theta_{\alpha\beta}, s_{\alpha\beta} = \sin \theta_{\alpha\beta}$ , the mixing matrix is

$$U_{PMNS} = \begin{pmatrix} U_{e1} & U_{e2} & U_{e3} \\ U_{\mu1} & U_{\mu2} & U_{\mu3} \\ U_{\tau1} & U_{\tau2} & U_{\tau3} \end{pmatrix} \quad (2.2)$$

$$= \begin{pmatrix} 1 & 0 & 0 \\ 0 & c_{23} & s_{23} \\ 0 & -s_{23} & c_{23} \end{pmatrix} \begin{pmatrix} c_{13} & 0 & s_{13}e^{-i\delta} \\ 0 & 1 & 0 \\ -s_{13}e^{i\delta} & 0 & c_{13} \end{pmatrix} \begin{pmatrix} c_{12} & s_{12} & 0 \\ -s_{12} & c_{12} & 0 \\ 0 & 0 & 1 \end{pmatrix} \quad (2.3)$$

If neutrinos are Majorana particles (meaning they are their own antiparticles), then there are an extra two phases allowed ( $\alpha_1$  and  $\alpha_2$ ), leading to the parametrisation below:

$$U_{PMNS} = \begin{pmatrix} 1 & 0 & 0 \\ 0 & c_{23} & s_{23} \\ 0 & -s_{23} & c_{23} \end{pmatrix} \begin{pmatrix} c_{13} & 0 & s_{13}e^{-i\delta} \\ 0 & 1 & 0 \\ -s_{13}e^{i\delta} & 0 & c_{13} \end{pmatrix} \begin{pmatrix} c_{12} & s_{12} & 0 \\ -s_{12} & c_{12} & 0 \\ 0 & 0 & 1 \end{pmatrix} \begin{pmatrix} 1 & 0 & 0 \\ 0 & e^{i\alpha_1/2} & 0 \\ 0 & 0 & e^{i\alpha_2/2} \end{pmatrix} \quad (2.4)$$

The Majorana phases do not contribute to neutrino oscillations, and so will be ignored for the rest of this discussion. The Dirac CP-violating phase,  $\delta$ , does have a direct impact on neutrino oscillations and if found to be non-zero, would demonstrate leptonic CP-violation.

Neutrinos are created in a flavour eigenstate,  $\nu_\alpha$ , along with the corresponding lepton of flavour  $\alpha$ . This means they are formed in a superposition of mass eigenstates.

$$|\nu_\alpha\rangle = \sum_i U_{\alpha i} |\nu_i\rangle \quad (2.5)$$

These mass eigenstates propagate as plane waves, so that after a time,  $t$ , each mass state can be written (in natural units such that  $\hbar = c = 1$ ) as:

$$|\nu_i(t)\rangle = |\nu_i(0)\rangle e^{E_i \cdot t - \vec{p}_i \cdot \vec{x}} \quad (2.6)$$

In the ultra-relativistic limit, we can write:

$$t \approx L \quad (2.7)$$

$$E = \sqrt{p^2 + m^2} \approx p + \frac{m^2}{2p} \approx p + \frac{m^2}{2E} \quad (2.8)$$

$$|\nu_i(t)\rangle = |\nu_i(0)\rangle e^{-im_i^2 L/2E} \quad (2.9)$$

This means different mass states propagate with different phases, leading to interference. When the neutrino is detected some time later, the probability of it having a different flavour,  $\beta$ , is given by:

$$P(\alpha \rightarrow \beta) = |\langle \nu_\beta | \nu_\alpha(t) \rangle|^2 = \left| \sum_i U_{\alpha i}^* U_{\beta i} e^{-im_i^2 L/2E} \right|^2. \quad (2.10)$$

For the purposes of illustration, we shall briefly assume that the mixing is between just two neutrinos. Then there is only one mixing angle, and no complex phase. We also only have to consider two mass states. Then the situation simplifies to:

$$U = \begin{pmatrix} \cos \theta & \sin \theta \\ -\sin \theta & \cos \theta \end{pmatrix} \quad (2.11)$$

$$\begin{aligned} P(\alpha \rightarrow \beta) &= \left| \left( U_{\alpha 1} U_{\beta 1} e^{-im_1^2 L/2E} \right) + \left( U_{\alpha 2} U_{\beta 2} e^{-im_2^2 L/2E} \right) \right|^2 \\ &= \left| -\cos \theta \sin \theta e^{-im_1^2 L/2E} + \cos \theta \sin \theta e^{-im_2^2 L/2E} \right|^2 \\ &= 2 \cos^2 \theta \sin^2 \theta - \cos^2 \theta \sin^2 \theta e^{-i \frac{(m_1^2 - m_2^2)L}{2E}} + \cos^2 \theta \sin^2 \theta e^{i \frac{(m_1^2 - m_2^2)L}{2E}} \\ &= 2 \cos^2 \theta \sin^2 \theta \left( 1 - \frac{e^{i \frac{(m_1^2 - m_2^2)L}{2E}} + e^{-i \frac{(m_1^2 - m_2^2)L}{2E}}}{2} \right) \\ &= \frac{1}{2} \sin^2 2\theta \left( 1 - \cos \left( \frac{(m_1^2 - m_2^2)L}{2E} \right) \right) \\ &= \sin^2 2\theta \sin^2 \left( \frac{\Delta m^2 L}{4E} \right) \end{aligned} \quad (2.13)$$

where  $\Delta m^2 = m_1^2 - m_2^2$ .

This two-neutrino approximation is actually a good approximation in a large number of cases, as the mass splittings differ by several orders of magnitude ( $|\Delta m_{32}^2| \approx |\Delta m_{31}^2| \gg \gg |\Delta m_{21}^2|$ ), so the three-neutrino case can often be factorised. This is why

it is common to describe the “solar” and “atmospheric” regimes. In the general case, the vacuum oscillation probability for a neutrino of original flavour  $\alpha$  being detected as flavour  $\beta$  (where  $\alpha$  and  $\beta$  can be the same flavour) is given by:

$$P(\alpha \rightarrow \beta) = \delta_{\alpha\beta} - 4 \sum_{i>j} \text{Re}(U_{\alpha i}^* U_{\beta i} U_{\alpha j} U_{\beta j}^*) \sin^2(\Delta m_{ij}^2 L/4E) \quad (2.14)$$

$$+ 2 \sum_{i>j} \text{Im}(U_{\alpha i}^* U_{\beta i} U_{\alpha j} U_{\beta j}^*) \sin^2(\Delta m_{ij}^2 L/2E).$$

For illustration, we will consider the case where  $\alpha = \mu, \beta = e$ . In this case, and denoting  $\Delta m_{ij}^2 L/4E = \Phi_{ij}$ , equation 2.14 expands to [13]

$$P(\nu_\mu \rightarrow \nu_e) = 4c_{13}^2 s_{13}^2 s_{23}^2 \sin^2 \Phi_{31} \quad (2.15)$$

$$+ 8c_{13}^2 s_{12} s_{13} s_{23} (c_{12} c_{23} \cos \delta - s_{12} s_{13} s_{23}) \cos \Phi_{32} \sin \Phi_{31} \sin \Phi_{21}$$

$$- 8c_{13}^2 c_{12} c_{23} s_{12} s_{13} s_{23} \sin \delta \sin \Phi_{32} \sin \Phi_{31} \sin \Phi_{21}$$

$$+ 4s_{12}^2 c_{13}^2 (c_{12}^2 c_{23}^2 + s_{12}^2 s_{23}^2 s_{13}^2 - 2c_{12} c_{23} s_{12} s_{23} s_{13} \cos \delta) \sin^2 \Phi_{21}.$$

The terms involving  $\sin \delta$  are CP-violating. In this form, it can be seen that all three mixing angles are required to be non-zero for non-zero  $\delta$  to be observed, as all terms involving  $\delta$  are multiplied by  $(\sin_{12} \sin_{13} \sin_{23})$ . There is no particular relation between  $\delta$  and  $\theta_{13}$ , the fact they appear coupled in equation 2.2 is merely an artefact of the parametrisation and once the matrix is expanded out  $\delta$  is always accompanied by all three angles.

### 2.2.1 Matter effects

When neutrinos propagate through matter, coherent - meaning the outgoing neutrino is in the same state it was in before - interactions with the matter cause the neutrinos to feel a potential. This potential causes the effective mass of the neutrinos to change - in an analogous way to photons travelling through a medium where the potential is seen as a refractive index. The electron neutrino, however, can also undergo charged current interactions with electrons in matter (see figure 2.1), leading to it feeling a different potential to the other flavours. This difference leads to effective mass-splittings in matter that differ slightly from the vacuum mass-splittings [14], and this affects the oscillation probabilities (which depend on the mass-splittings).

Due to the way matter effects change the effective masses of neutrinos, they allow measurements of the signs of the mass splittings (vacuum oscillations only

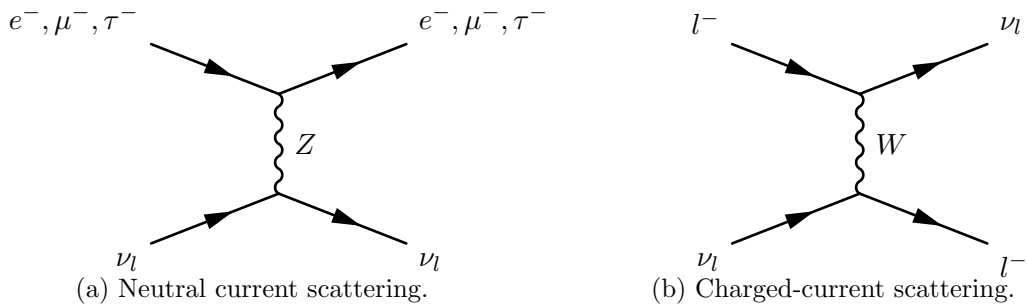


Figure 2.1: Feynman diagrams demonstrating the concept of matter effects ( $l = e, \mu, \tau$ ). The left-hand diagram occurs for all flavour combinations, but the right-hand diagram occurs only when the neutrino and lepton flavours are the same. As regular matter contains electrons, but not muons or taus the charged current process will only occur for electron neutrinos when passing through matter. An analogous diagram exists for electron anti-neutrinos, however for the matrix element for the anti-neutrino scattering has the opposite sign.

provide a measurement of the square of the mass splitting). Solar neutrinos travel through a large amount of very dense material in the sun, which affects their oscillation probability through this matter effect. In fact, due to the density of the sun and the energy of solar neutrinos, they actually encounter a resonance - the MSW resonance - where their oscillation probability becomes dramatically higher than their vacuum oscillation probability. As neutrinos propagate from the centre of the sun outwards, the electron density changes slowly (importantly, slowly enough for the change to be adiabatic). This adiabatic change allows a smooth transition between flavour states as the neutrinos pass through the resonance region, and this transition is known as the MSW effect [15].

By comparing solar neutrino oscillations, and reactor neutrino oscillations, which are dominated by the same mixing angle and mass-splitting, we can see clear evidence for matter effects in the sun [16]. From this evidence, we know that the mass of  $\nu_2$  is greater than that of  $\nu_1$  (as otherwise the solar oscillation probability would be larger than the vacuum oscillation probability, not smaller). Unfortunately we do not know whether  $\nu_3$  is heavier or lighter than the other two neutrinos. This leads to two possible hierarchies, known as “normal” and “inverted”. In the normal hierarchy,  $\nu_3$  is the heaviest, leading to the larger mass-splitting being between the heaviest and the second-heaviest neutrinos. This is analogous with the patterns of masses seen in the leptons and quarks. In the inverted hierarchy solution,  $\nu_1$  and  $\nu_2$  are almost degenerate. Figure 2.2 shows a graphical representation of the two hierarchy solutions.

Because the potentials felt by neutrinos and anti-neutrinos are the same

size, but differ in sign, terrestrial matter effects can lead to a neutrino-antineutrino asymmetry. This asymmetry can mimic CP-violating effects, so determining the true mass hierarchy is very important for searches of genuine CP-violation.

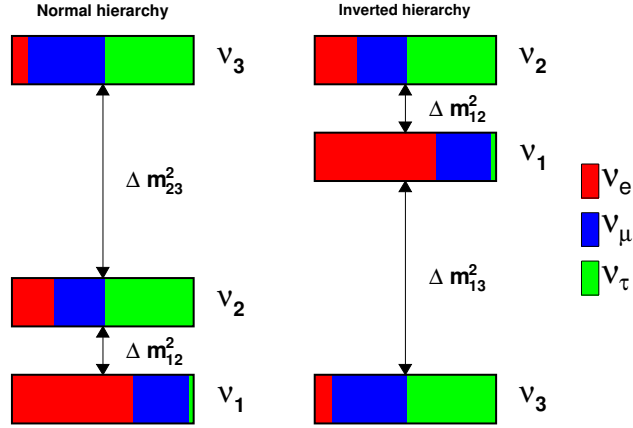


Figure 2.2: Graphical representation of the two mass hierarchy solutions. The different colours represent the flavour fraction of each mass state.

### 2.3 CP-violation in the neutrino sector

One of the particular reasons for great interest in neutrino oscillations is the potential for CP violation in the neutrino sector. It is well established that the quark sector exhibits CP violation, however the extent to which CP is violated is not enough to explain the matter-antimatter asymmetry observed in the universe when included in Baryogenesis models.

Leptogenetic models are a popular way of generating a matter-antimatter asymmetry in the early universe, and leptonic CP violation is a necessary prerequisite for these models. Leptonic CP violation would be clearly observable in the asymmetry between  $\nu_\mu \rightarrow \nu_e$  oscillations, and  $\bar{\nu}_\mu \rightarrow \bar{\nu}_e$  oscillations. Equation 2.14 gives the appearance probability for a neutrino flavour,  $\beta$ , in a beam of flavour  $\alpha$ . Noting that when considering oscillations of antineutrinos, the sign of the phase  $\delta_{CP}$  is reversed, then when we consider the asymmetry

$$\mathcal{A} = \frac{P(\nu_\mu \rightarrow \nu_e) - P(\bar{\nu}_\mu \rightarrow \bar{\nu}_e)}{P(\nu_\mu \rightarrow \nu_e) + P(\bar{\nu}_\mu \rightarrow \bar{\nu}_e)}, \quad (2.16)$$

the first two (real) terms from equation 2.14 will cancel in the subtraction as they are CP-even. If there is an imaginary component to the mixing matrix, however,

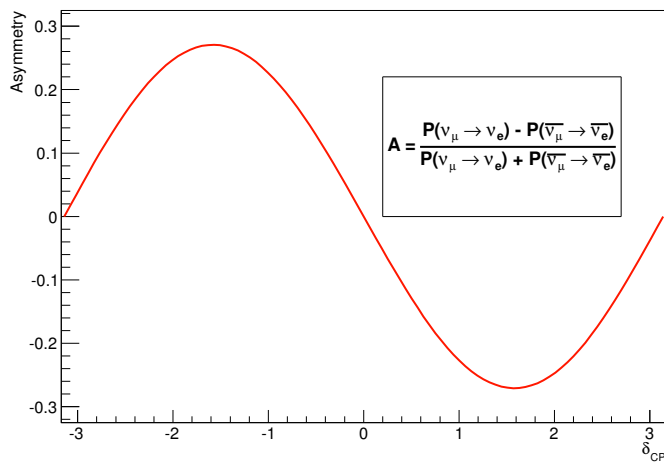


Figure 2.3: Asymmetry vs  $\delta_{CP}$  at the  $\nu_\mu \rightarrow \nu_e$  oscillation peak. Assuming  $\sin^2 2\theta_{13} = 0.1$ ,  $\theta_{23} = 45^\circ$ , and  $\sin^2 \theta_{12} = 0.31$ . Values for the mass splittings were taken from [17]. At the peak, the asymmetry can be over 25%.

then the CP-odd term will remain. Inserting our best measurements of the mixing parameters, reveals a possible asymmetry of over 25% for a neutrino oscillation experiment such as T2K. This asymmetry is shown as a function of  $\delta_{CP}$  in figure 2.3.

## 2.4 Summary of neutrino oscillation measurements

After the discovery of flavour oscillations in solar neutrinos, Super-Kamiokande also saw that the atmospheric neutrino flux varied as a function of zenith angle [2]. There have since been a multitude of experiments specifically designed to study both natural and artificial neutrino sources to measure oscillation parameters to an ever higher precision.

### 2.4.1 Long baseline neutrino beam experiments

Possibly the most controlled neutrino oscillation experiments, long baseline neutrino experiments use artificially created beams of neutrinos which are sent usually hundreds of kilometres or more to detectors. In this way it is possible to have relatively good control over the beam spectrum, and the baseline and energy can be carefully selected. The time-bunched structure of a neutrino beam also allows good control over cosmogenic and atmospheric backgrounds using precise timing.

The techniques used to create neutrino beams are still fairly crude. A muon

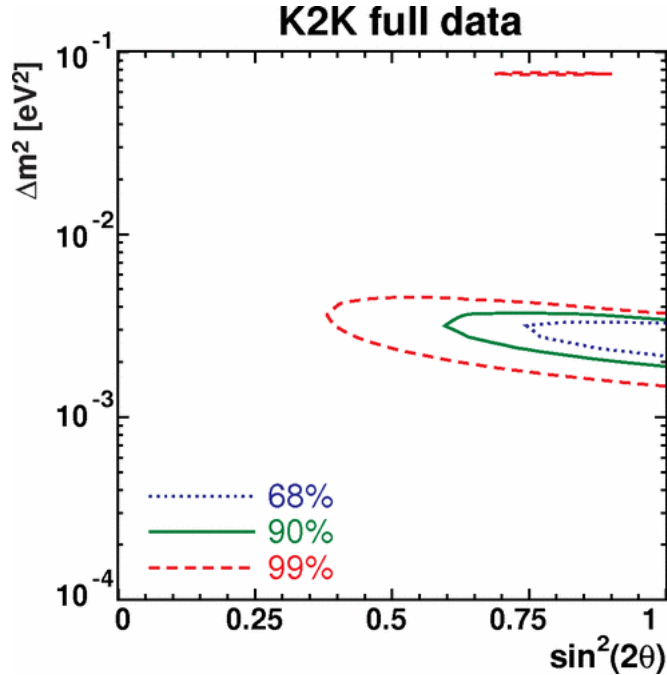


Figure 2.4: K2K disappearance results. Taken from [19].

neutrino beam can be generated with high purity. The T2K beam, for example, is over 93% pure around the peak [18]. The beam has contamination from mainly muon antineutrinos, but also an electron neutrino component and a small contamination from electron antineutrinos. An high-purity muon antineutrino beam can also be created, but due to the positive charge of the proton beam fewer negative pions are created leading to a lower flux and higher wrong-sign contamination. In fact, in the tail of the off-axis T2K antineutrino beam, above 5 GeV the wrong-sign flux is higher than the correct-sign flux.

#### 2.4.1.1 K2K

K2K was the first long baseline neutrino oscillation experiment. Based in Japan, it used a neutrino beam produced at KEK in Tsukuba, Japan, directed at Super-K. K2K had a baseline of 250km, and used near detectors to constrain the unoscillated  $\nu_\mu$  flux, observing a disappearance at the far detector. K2K witnessed a  $4.2\sigma$  significance observation of muon neutrino disappearance, and was able to place a constraint on the atmospheric oscillation parameters,  $|\Delta m_{23}^2|$  and  $\sin^2(2\theta_{23})$ . Their best fit point under a two-neutrino oscillation hypothesis, was  $\Delta m_{23}^2 = 2.8 \times 10^{-3} eV^2$  and  $\sin^2(2\theta_{23}) = 1.0$  [19]. The allowed contours in  $\Delta m^2 - \sin^2 2\theta$  space from the K2K data are shown in figure 2.4.

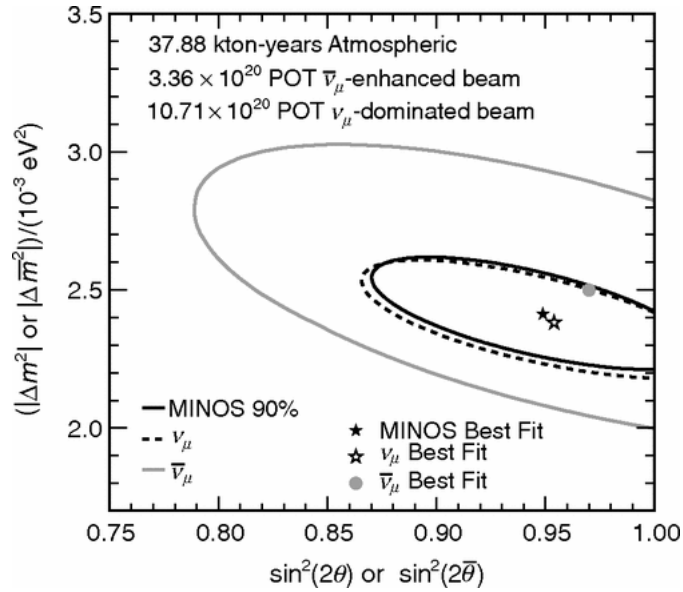


Figure 2.5: MINOS allowed regions from both beam polarities, and a combined fit which assumes the oscillation parameters are the same for both neutrinos and antineutrinos. Taken from [20].

#### 2.4.1.2 MINOS

MINOS, the Main Injector Neutrino Oscillation Search is a long baseline neutrino oscillation experiment running between the Main Injector accelerator at Fermilab, and a far detector in the Soudan mine in northern Minnesota. The experiment used detectors made out of alternating planes of magnetised steel and plastic scintillator, with a 27 ton near detector positioned 1 km from the target, and a 5 kton far detector at a baseline of 735 km. MINOS measured the atmospheric parameters,  $|\Delta m_{23}^2|$  and  $\sin^2(2\theta_{23})$ , through muon neutrino disappearance, as well as conducting a search for electron neutrino appearance, which would be an indication of non-zero  $\theta_{13}$ . The electron neutrino search saw a small excess over the background-only prediction, though this was within the experimental uncertainties.

MINOS was also able to reverse the polarity of their neutrino beam, and measure the same parameters with an antineutrino beam, by looking for a disappearance of  $\bar{\nu}_\mu$ . If a difference were measured between oscillation parameters for neutrinos and antineutrinos, this would imply observation of CPT-violation. Good agreement was found between the oscillation parameters measured in neutrino and antineutrino enhanced beams [20], as seen in figure 2.5.

### 2.4.1.3 T2K

T2K is the second long baseline neutrino experiment to utilise Super-K as a far detector, and the first neutrino experiment to use an off-axis beam. Based in Japan, it uses the main ring accelerator at J-PARC in Tokai, Ibaraki, to form a  $\nu_\mu$  beam, which is directed  $2.5^\circ$  off-axis at Super-K, which is 295 km away. The off-axis technique allows the experiment to tune the peak beam energy to the oscillation maximum, increasing statistics in the region of interest and eliminating high-energy backgrounds.

The primary goal was to search for electron neutrino appearance, and measure  $\theta_{13}$ , as well as improve the precision of measurements of the atmospheric parameters. In 2013 T2K reported the observation of 28 electron neutrino candidate events at Super-K, far in excess of the expected background of  $4.92 \pm 0.55$  [21]. This corresponds to a discovery of electron neutrino appearance at a significance of  $7.3\sigma$ , and a discovery of non-zero  $\theta_{13}$ . The allowed contours in  $\delta_{CP}$  and  $\theta_{13}$  from this result are shown in figure 2.6, compared with the value of  $\theta_{13}$  obtained by reactor experiments (see section 2.4.2).

T2K is described in much more detail in chapter 4. It has recently started collecting data with a reverse polarity beam, with preliminary results expected soon.

The atmospheric oscillation parameters have been measured by a number of complementary experiments. Figure 2.7 shows the most recent 1-sigma “atmospheric sector” contours from T2K, compared with several other experiments. The results show good agreement with each other, and put strong constraints on the values of  $|\Delta m_{23}^2|$  and  $\theta_{23}$ .

### 2.4.1.4 NO $\nu$ A

The NO $\nu$ A (NuMI off-axis  $\nu_e$  appearance) experiment is a long baseline experiment based in the USA. It uses the NuMI beam that was used for MINOS, running in a medium energy configuration, with the detectors placed 14 mrad (0.8 degrees) off-axis, making use of the same off axis technique as T2K. At 14 mrad off-axis, NO $\nu$ A has a peak beam energy of 2 GeV. With a baseline of 810 km, this leads to a value of L/E of 405 km/GeV at the flux peak (very similar to T2K’s 491 km/GeV). The 222 ton near detector is housed in a new tunnel adjacent to the previous NuMI tunnel in Fermilab, and the 14 kton far detector is based in a new site in Ash river, Minnesota. [23]

The two detectors are functionally identical, both using a hydrocarbon based liquid scintillator, contained in bars to allow tracking. NO $\nu$ A was built to measure

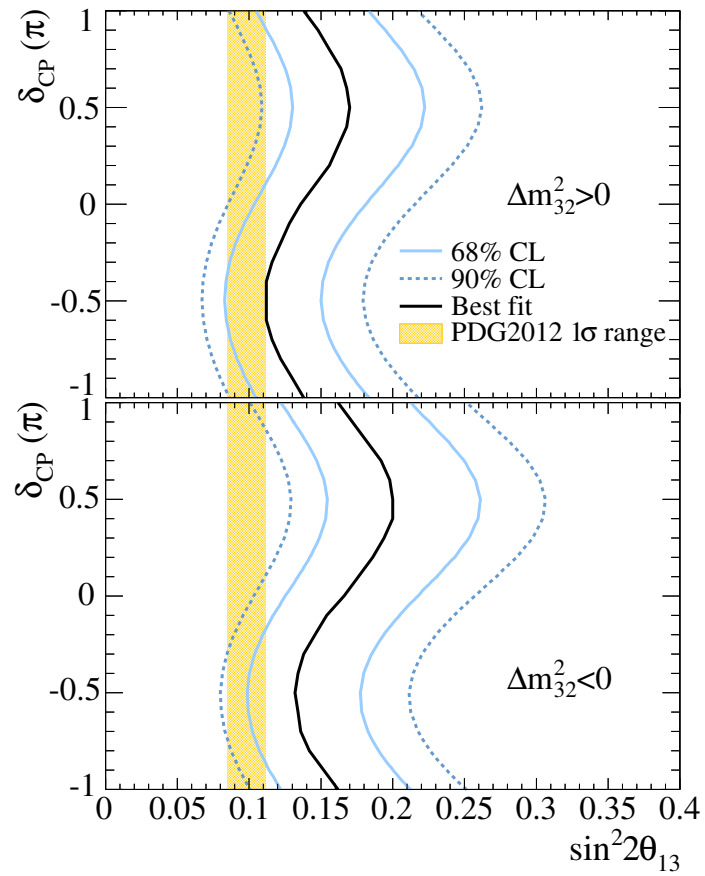


Figure 2.6: Allowed regions in  $\sin^2 2\theta_{13} - \delta_{CP}$  space assuming a normal mass hierarchy, from an analysis of electron neutrino appearance at the T2K experiment. Taken from [21].

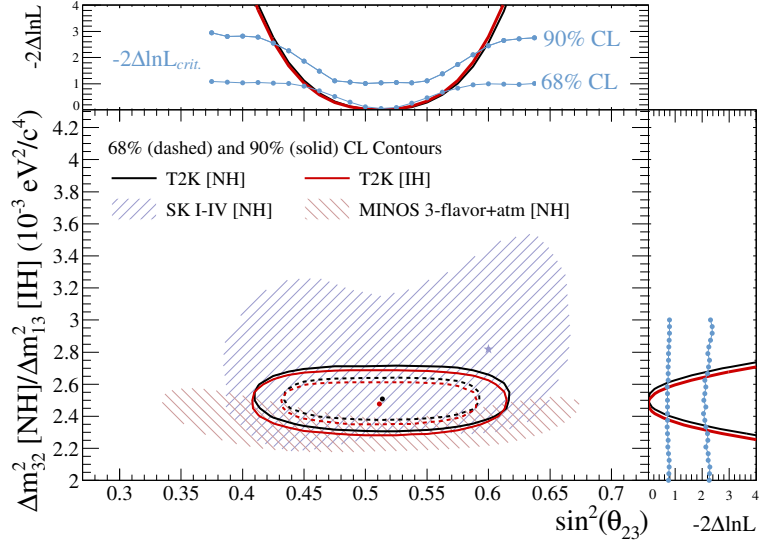


Figure 2.7: Most up-to-date constraints on the atmospheric oscillation parameters from SK, MINOS, and T2K. NH and IH refer to fits assuming the normal and inverted hierarchies respectively. [22]

$\theta_{13}$ , and to try and measure  $\delta_{CP}$ . It was also designed with a very long baseline of over 800 km to increase the size of matter effects and therefore have maximum sensitivity to the mass hierarchy. Figure 2.8 shows the fraction of  $\delta_{CP}$  space over which the mass hierarchy can be determined at a given sensitivity, after 3 years of neutrino running and 3 years of anti-neutrino running. In addition, by combining results with T2K,  $\text{NO}\nu\text{A}$  can be more sensitive to more of the  $\delta_{CP}$  parameter space (see discussion in chapter 4).

$\text{NO}\nu\text{A}$  has already taken physics data with a prototype detector, and the far detector is now fully constructed and taking data. Early results are expected soon, and the first run is intended to last approximately 6 years.

## 2.4.2 Reactor neutrino experiments

Nuclear reactors provide a pure, high intensity source of electron antineutrinos with energies of a few MeV. The first neutrinos ever detected were reactor neutrinos, and today they are still a valuable source. Neutrino fluxes from reactors can be accurately calculated, and comparisons of event rates with the reactor power over time allows calibration of backgrounds. Adding near detectors, as is done in neutrino beam experiments, allows a high degree of cancellation of any remaining flux uncertainties.

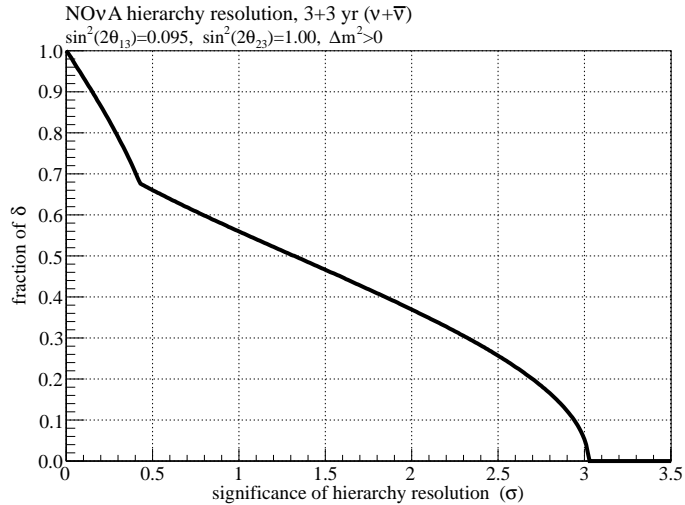


Figure 2.8: Given the parameters at the top of the figure (3 years of  $\nu$  running + 3 years of  $\bar{\nu}$  running,  $\sin^2 2\theta_{13} = 0.095$ ,  $\sin^2 2\theta_{23} = 1.00$ , normal hierarchy), this shows fraction of  $\delta_{CP}$  values over which the mass hierarchy can be determined at a given sensitivity by NO $\nu$ A . For example the mass hierarchy can be determined at  $2\sigma$  for roughly 37% of  $\delta_{CP}$  space. Taken from [24]

#### 2.4.2.1 KamLAND

The KamLAND (Kamioka Liquid scintillator Antineutrino Detector) experiment was based in the Kamioka mine, along with the Kamiokande and Super-Kamiokande experiments. Situated in Japan, it was surrounded by 55 nuclear reactors at typical baselines of around 200 km, producing a very large, well-known, neutrino flux. KamLAND consisted of 1 kton of liquid scintillator, surrounded by a water Cherenkov detector for vetoing external particles and absorbing entering neutrons and  $\gamma$  rays.

The intention of KamLAND was to confirm the existence of neutrino oscillations in the solar sector, and to constrain the possible solutions to the solar neutrino problem. With just 145 days of data taking, KamLAND successfully ruled out all solutions to the solar neutrino problem, except for the large mixing angle solution, which was strongly favoured [25]. In 2008, KamLAND released precise measurements of the solar mixing angle and mass splittings, which were combined with results from solar neutrino experiments to obtain  $\Delta m_{21}^2 = 7.59 \pm 0.21 \times 10^{-5} \text{eV}^2$  and  $\tan^2 \theta_{12} = 0.47^{+0.06}_{-0.05}$  [26].

#### 2.4.2.2 CHOOZ

The CHOOZ experiment was based in Chooz, France, and was designed to resolve one potential solution to the solar neutrino anomaly. At the time of construction,

it was not clear whether the solar neutrino anomaly was due to  $\nu_\mu \rightarrow \nu_e$  or  $\nu_\mu \rightarrow \nu_\tau$  oscillations. CHOOZ searched for a disappearance of  $\bar{\nu}_e$  at an L/E similar to that in the atmospheric neutrino measurements, which would be a strong indication that atmospheric neutrino oscillations were due to a  $\nu_\mu \rightarrow \nu_e$  transition. This possibility was ruled out by CHOOZ at high significance, and they set a limit for the mixing angle  $\theta_{13} < 0.1$  at 90% confidence [27].

CHOOZ was later “upgraded” to double Chooz, with the intention of reducing the limit of  $\theta_{13}$  further. Double Chooz was to run with a new detector in the old CHOOZ detector hall, and then add a near detector to cancel various systematics. Double Chooz reported indications of non-zero  $\theta_{13}$  in 2011 [28], and published a measurement of  $\sin^2 \theta_{13} = 0.102 \pm 0.028(\text{stat.}) \pm 0.033(\text{syst.})$  in 2014 [29]. In this most recent result, the background rate had been precisely measured using a period of data-taking where both reactors were shut down.

#### 2.4.2.3 RENO

The RENO (Reactor Experiment for Neutrino Oscillations) experiment is a short baseline reactor oscillation experiment based in South Korea. It detects antineutrinos from the 6 reactor cores in the Yonggwang nuclear power plant, and utilises a near detector at 290 m to constrain the flux expected at the far detector, which is located 1.4 km from the reactors (both average distances from all 6 reactors). In 2012, RENO published evidence at  $5\sigma$  for non-zero  $\theta_{13}$ , with a measurement of  $0.113 \pm 0.013(\text{stat}) \pm 0.019(\text{syst})$  from a rate-only analysis [30].

More recently, RENO have observed a new component in the prompt energy spectrum (roughly equal to the neutrino energy spectrum) at both the near- and far-detectors (see figure 2.9). Subtracting the expected neutrino flux spectrum for the best fit values of  $\theta_{13}$  and  $\delta m_{13}^2$ , a significant peak is seen at 5 MeV [31], which is currently unexplained.

#### 2.4.2.4 Daya Bay

Daya Bay is a short baseline reactor neutrino oscillation experiment situated at Daya Bay, in China. Similar to RENO, it consists of near- and far-detector halls around several reactor cores in two power plants. In 2012, just 2 weeks before RENO published evidence for non-zero  $\theta_{13}$ , the Daya Bay collaboration published data based on only 49 days of data taking, demonstrating  $\theta_{13} > 0$  at  $5\sigma$  significance [32]. The latest results from Daya Bay have measured  $\sin^2 2\theta_{13} = 0.09_{-0.009}^{+0.008}$ , and the results are in very good agreement with the results from RENO, Double Chooz,

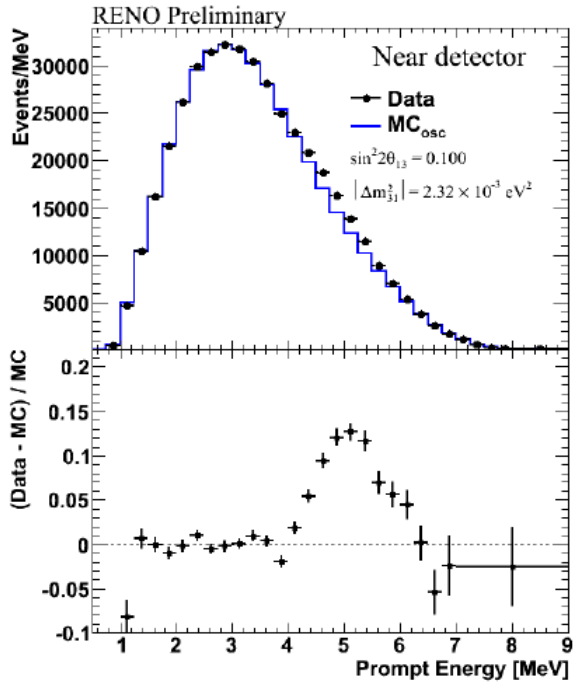


Figure 2.9: Evidence for an additional reactor neutrino component at 5MeV. Taken from [31]

MINOS, and T2K [33].

### 2.4.3 Anomalous results

Although the PMNS framework has been very successful in describing observations of neutrino oscillations, there remain some results which do not agree with the model predictions. It is possible that these results are due to incorrectly estimated fluxes, poor modelling of some background processes, or a misunderstood detector effect, but it is also possible that there is genuine physics. These results are limited in their significance, however it has not been categorically shown that they are not real effects so they remain in question.

#### 2.4.3.1 LSND

LSND (liquid scintillator neutrino detector) was an early oscillation search, based at the Los Alamos facility in the USA [34]. The detector was placed roughly 30m downstream of the neutrino source, which came from a combination of in-flight and stopped pions decaying (followed by the subsequent muon decay). This neutrino beam has a number of components due to the combination of at-rest and in-flight

decays, as well as the addition of the secondary muon decays all contributing, however most neutrinos had energies between a few tens of MeV and 200MeV. Using this setup, LSND was able to search for  $\nu_\mu \rightarrow \nu_e$  oscillations at a relatively high value of  $\Delta m^2$ .

In neutrino mode, LSND observed a total of 40  $\nu_e$  signal events, in excess of the  $21.9 \pm 2.1$  predicted background [35]. In anti-neutrino mode, an excess of  $87.9 \pm 23$  events was observed [36]. The interpretation of these excesses as neutrino oscillations lead to a mass splitting of the order of 1 eV, many orders of magnitude larger than the mass splittings which have been measured elsewhere. A large additional mass splitting, if confirmed, would suggest the existence of a neutrino which does not couple to the Z boson and is therefore considered “sterile”.

#### 2.4.3.2 MiniBooNE

Designed to look for oscillations at a similar L/E to the LSND anomaly, MiniBooNE (Mini Booster Neutrino Experiment) was a short-baseline experiment using neutrinos generated by the booster accelerator at Fermilab and a spherical mineral oil Cherenkov detector. The neutrino beam used has a peak energy around 0.6 GeV, with a baseline of 541m (giving it roughly the same L/E as LSND), and data was collected in both beam polarities. A search was conducted for an excess of  $\nu_e$  or  $\bar{\nu}_e$  events, and electron-like excesses were observed in both beam polarities at low reconstructed neutrino energies [37] ( $2.8\sigma$  in antineutrino mode, and  $3.4\sigma$  in neutrino mode).

The results of fitting an oscillation hypothesis with an additional sterile neutrino are shown in figure 2.10. There is clearly some overlap between the allowed regions from the MiniBooNE data and the LSND data. This overlap is more clear in the antineutrino data set, where an oscillation hypothesis provides a good fit to the MiniBooNE data.

#### 2.4.3.3 Reactor anomaly

Analysis of rates of reactor neutrino detection at a variety of detectors at varying baselines shows a deficit compared to prediction [38]. The significance of this deficit is fairly low, and it should be noted that the prediction of the total reactor neutrino production rates is highly model-dependent and subject to relatively large uncertainties. This deficit can be interpreted as evidence of a sterile neutrino, with a similar mass splitting to that used to explain the LSND and MiniBooNE anomalies. None of the anomalous results have a high level of significance, but nevertheless

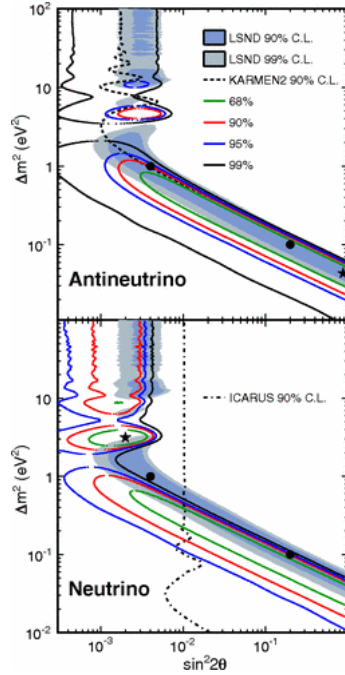


Figure 2.10: Allowed regions from the LSND and MiniBooNE sterile neutrino fits. The starred point shows the MiniBooNE best fit point in each case. The circles are example reference points for comparison. Taken from [37].

they do warrant more investigation.

#### 2.4.4 Near- and far-future experiments

Much has been learnt about neutrino oscillations in the last two decades, using a number of different techniques. The current generation of neutrino experiments are sure to improve our knowledge of these oscillations, however it is clear that there are some large missing pieces which require new technologies, and far higher statistics. A number of experiments have been proposed that should be able to determine the mass hierarchy, and observe CP-violation if it exists. Many of these require new technologies to be developed and tested, and as such are expected to take another two decades to complete their searches.

##### 2.4.4.1 Hyper-K

Hyper-Kamiokande (Hyper-K) is a proposed future experiment in Japan [39]. In essence, Hyper-K is an upgrade to the successful T2K long baseline neutrino oscillation experiment. The proposal is to construct a Mega-ton scale water Cherenkov detector close to the current Super-K site, upgrade the J-PARC neutrino beam

power to 1MW, and possibly build a new near-detector complex. The off-axis technique would continue to be used, providing very high-statistics measurements at the first oscillation maximum.

The benefits of this proposal are that much of the infrastructure is already in place, and Cherenkov detectors are a well-established, proven technology for this type of experiment. Unfortunately Hyper-K has many of the same limitations as Super-K, such as the inability to distinguish between electrons and photons, and a high threshold for reconstructing particles.

#### **2.4.4.2 DUNE**

DUNE (Deep Underground Neutrino Experiment), formerly LBNF, formerly LBNE, is a proposed neutrino oscillation experiment which would be based in the USA [40]. Unlike Hyper-K, and the currently running long baseline accelerator experiments, T2K and NO $\nu$ A, DUNE would utilise a wide-band neutrino beam, over an extremely long baseline (1300km), which would allow measurements of both the first and second oscillation maxima. As discussed in section 4.8.2.1, the CP-violating effects are much larger at the second maximum. Using a wide-band beam also gives DUNE access to shape information which allows careful testing of the three-neutrino paradigm.

DUNE is designed with a large-scale liquid argon time-projection-chamber (TPC) as the far detector. The technology required to build a liquid argon TPC of this size is not well understood, and due to the high granularity possible, reconstructing events in liquid argon is still a challenge. There are, however, many projects working on these aspects of the proposal, and ArgoNeuT [41] has already demonstrated liquid argon TPC technology in a neutrino beam. Other experiments are intended to continue this R&D, progressively using larger detectors, which can function as prototypes for the final DUNE far detector.

#### **2.4.4.3 MicroBooNE**

Positioned in the Booster neutrino beamline, MicroBooNE [42] is another progression in the BooNE series of experiments, studying the effects that were seen at LSND and MiniBooNE. As MicroBooNE is a liquid argon (LAr) TPC, it should have good power to discriminate between electron neutrino interactions and NC  $\pi^0$  production, which can look extremely similar in a Cherenkov detector such as the one used in MiniBooNE, and is often cited as a potential reason for the observed excesses in MiniBooNE. MicroBooNE is also able to be used as an R&D project for

a large liquid argon TPC detector in future, and can serve as a test-bed for various reconstruction algorithms. MicroBooNE has been successfully constructed and is due to start taking data in 2015.

#### 2.4.4.4 JUNO

JUNO (Jiangmen Underground Neutrino Observatory, previously known as Daya Bay II), is a proposed reactor neutrino oscillation experiment, which will sit at an intermediate baseline (approximately 50km) allowing it access to the mass hierarchy. [43] Due to the wide band of neutrino energies produced in a reactor, it is possible to cover many different values of  $E/L$ , and see a number of oscillation peaks. It should be possible to identify the hierarchy by looking for interference between the solar and atmospheric oscillations. The survival probability for a reactor neutrino can be written as

$$P_{ee} = 1 - \cos^4 \theta_{13} \sin^2 2\theta_{12} \sin^2 \Delta_{21} \quad (2.17)$$

$$- \sin^2 2\theta_{13} (\cos^2 \theta_{12} \sin^2 \Delta_{31} + \sin^2 \theta_{12} \sin^2 \Delta_{32}) \quad (2.18)$$

where  $\Delta_{ij} = \delta m_{ij}^2 \frac{E}{L}$  ( $\delta m_{ij}^2$  is the mass-squared splitting between states  $i$  and  $j$ ).

This leads, at these baselines, to oscillations dominated by the solar mass splitting, but with a secondary effect from the atmospheric mass splitting, as can be seen in figure 2.11. The frequency of these secondary oscillations depends on the mass hierarchy, due to the interference between the  $\Delta_{31}$  and  $\Delta_{32}$  terms, so a high-statistics measurement of many oscillation peaks can resolve which is the larger of the two terms.

#### 2.4.4.5 RENO-50

RENO-50 is another intermediate baseline reactor oscillation experiment, designed in a similar way to JUNO. The proposal is to continue to use the Yonggwang nuclear power plant used by RENO, but to extend the baseline up to 50km and use the same technique as JUNO to identify the hierarchy.

Both JUNO and RENO-50 have significant challenges in their energy reconstruction, as they need to resolve the small oscillations in figure 2.11. It is expected that the experiments require energy resolution better than  $3\%/\sqrt{E}$

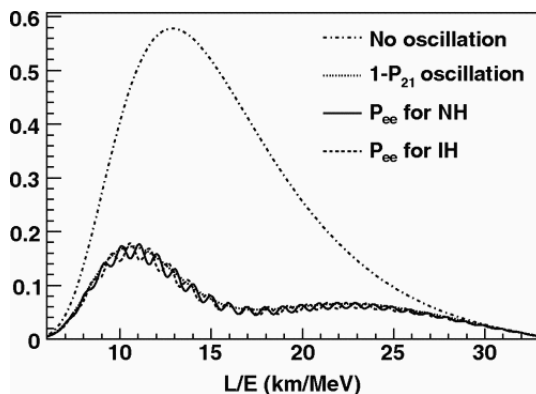


Figure 2.11: Expected spectrum at an intermediate baseline reactor experiment. The standard high mass-splitting regime (solar sector) oscillations can be seen, with additional faster oscillations due to the second mass-splitting (atmospheric sector). These smaller oscillations should allow determination of the mass hierarchy. [44]

#### 2.4.4.6 Current knowledge of oscillation parameters

It is clear from figure 2.7, that the atmospheric parameters (the “23” sector ) have been well measured by a number of experiments, which all agree well. The solar (“12” sector) parameters were extremely precisely measured by the Super-K, SNO, and KamLAND experiments, and recently, reactor experiments have placed extremely tight constraints on the mixing angle  $\theta_{13}$ , in agreement with data from long baseline accelerator experiments. Still unknown are the sign of the larger mass-splitting, and the CP-violating phase,  $\delta_{CP}$ . It is also not clear whether the mixing angle  $\theta_{23}$  is exactly  $45^\circ$ , and if not, which octant it is in. In addition, there have been some hints of additional sterile neutrinos, though nothing conclusive. These questions are likely to dominate neutrino physics for the next several decades.

Table 2.1 summarises the most up-to-date measurements of all of the neutrino oscillation parameters.

Parameter	Value with uncertainty
$\sin^2 \theta_{23}$	$0.437^{+0.033}_{-0.023}$ ( $0.455^{+0.039}_{-0.031}$ )
$\sin^2 \theta_{12}$	$0.308 \pm 0.017$
$\sin^2 \theta_{13}$	$0.0234^{+0.0020}_{-0.0019}$ ( $0.0240^{+0.0019}_{-0.0022}$ )
$\Delta m_{12}^2$	$7.54^{+0.26}_{-0.22} \times 10^{-5} \text{eV}^2$
$ \Delta m_{23}^2 $	$2.43 \pm 0.06$ ( $2.38 \pm 0.06$ ) $\times 10^{-3} \text{eV}^2$
$\delta_{CP}$	unknown

Table 2.1: Current best knowledge of neutrino oscillation parameters. Values all taken from [17]. Values in brackets assume the inverted hierarchy solution.

## Chapter 3

# Neutrino interactions

Neutrinos, being electrically neutral and colourless, are only able to interact via the weak interaction. This makes them a unique probe of the Standard Model, however it also makes them very difficult to detect and measure. In order to determine the properties of a neutrino, one must observe the products of an interaction, and thus in order to make measurements of neutrino oscillation parameters, we must understand these different interactions.

### 3.0.5 The weak interaction

Before proceeding to discuss neutrino interactions in detail, it is useful to discuss briefly the weak interaction in general terms. Fermi's original theory for nuclear  $\beta$ -decay was that of a 4-particle point interaction, with the particle fields,  $\Phi$ , and the empirically measured Fermi constant,  $G_F$ , the matrix element is given by

$$M_{fi} = G_F g_{\mu\nu} [\bar{\Phi}_e \gamma^\mu \Phi_{\bar{\nu}_e}] [\bar{\Phi}_p \gamma^\nu \Phi_n], \quad (3.1)$$

which clearly has no dependence on the 4-momentum transfer,  $q^2$ , due to the lack of a propagator. This interaction is not capable of violating parity. In 1957, however, it was discovered, by studying the  $\beta$ -decays of cobalt nuclei, that the weak interaction was able to violate parity [45]. In this experiment, the cobalt nuclei spins were aligned with a magnetic field, and then the decay electron distribution was measured. It was found that electrons were emitted preferentially anti-parallel to the magnetic field, and as magnetic fields are parity-even, this decay therefore violates parity.

It turns out the weak interaction behaves as a linear combination of vector and axial-vector interactions. Each of these does not violate parity, but the vector interaction is parity-even and the axial-vector interaction is parity-odd. This means that both contributions individually conserve parity, but their sum or difference

does not.

Experimentally it has been determined that the weak interaction has the structure  $V - A$ , which leads to the W and Z boson currents taking the forms [46]

$$J_W^\mu = \bar{u} \frac{-ig_W}{2\sqrt{2}} (\gamma^\mu - \gamma^\mu \gamma^5) u \quad (3.2)$$

$$J_Z^\mu = \bar{u} \frac{-ig_Z}{2} (g_V \gamma^\mu - g_A \gamma^\mu \gamma^5) u \quad (3.3)$$

where  $g_V$  and  $g_A$  depend on the particular neutrino or lepton involved.

To calculate matrix elements we then need to include the propagator which, for a particle with mass  $M$ , takes the form

$$-i \frac{g_{\mu\nu} - \frac{q_\mu q_\nu}{M^2}}{q^2 - M^2} \quad (3.4)$$

At low energies ( $q^2 \ll M^2$ ) this approximates to

$$i \frac{g_{\mu\nu}}{M^2} \quad (3.5)$$

This in turn, allows us to relate the Fermi constant,  $G_F$  to the intrinsic strength of the interaction,  $g_W$ :

$$G_F = \frac{\sqrt{2}g_W^2}{8M^2} \quad (3.6)$$

which shows why the weak interaction is so weak - at low energies, where the available range of  $q^2$  is small, the relatively large mass of the W and Z bosons reduces the apparent coupling constant considerably.

### 3.0.6 Terminology and conventions

A generic neutrino interaction with a target is displayed in figure 3.1. It will also be helpful to define the following variables for discussion later.

- 4-momentum of projectile,  $k^\mu$
- 4-momentum of target,  $p^\mu$
- Energy transfer to the nucleus,  $\omega = k^0 - k'^0$
- momentum transfer to the nucleus,  $\vec{q} = \vec{k} - \vec{k}'$
- four-momentum transfer to the nucleus,  $q^2 = \omega^2 - |\vec{q}|^2$

- $Q^2 = -q^2$
- 4-momentum of outgoing hadronic system,  $p'^\mu$
- outgoing hadronic invariant mass,  $W = \sqrt{p' \cdot p'}$

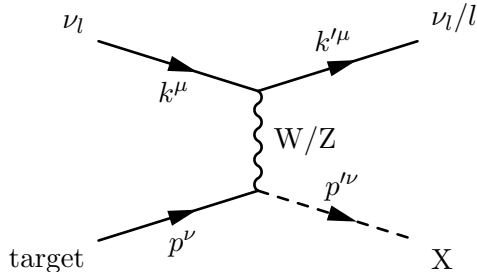


Figure 3.1: Generic scattering of a neutrino and a fermion.

### 3.1 Neutrino-lepton scattering

In the discussion of neutrino interactions, we will begin with the simplest interaction type, that is the elastic scattering of a neutrino and a lepton. In this case, we can evaluate exactly the matrix elements for the leading order tree-level diagram. For simplicity we will consider the interaction ( $\nu_\mu + e^- \rightarrow \nu_\mu + e^-$ ), such that only the neutral current process contributes.

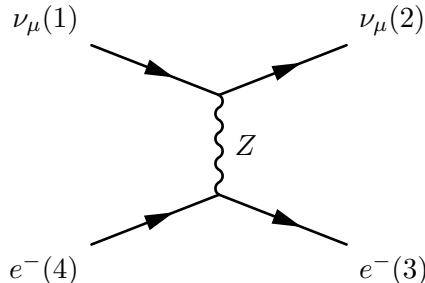


Figure 3.2: Neutral current scattering of a muon neutrino and an electron.

Denoting the Dirac spinors for each particle  $u$ , the matrix element for this process can be written (assuming the  $Z$  mass is large compared to the energy) as

$$\mathcal{M} = [\bar{u}_2(g_V^\nu - g_A^\nu \gamma^5)u_1] \frac{g_Z^2}{4M_Z^2} [\bar{u}_3(g_V^e - g_A^e \gamma^5)u_4], \quad (3.7)$$

which can be used to derive to the spin-averaged differential cross section [47]

$$\frac{d\sigma}{dy} = \frac{m_e G_F^2 E_\nu}{2\pi} \left( (g_V + g_A)^2 + (g_V - g_A)^2 (1 - y)^2 - (g_V^2 - g_A^2) \frac{m_e y}{E_\nu} \right) \quad (3.8)$$

where we have used the Lorentz-invariant Bjorken variable,  $y = (q \cdot p)/(k \cdot p)$ , as the differential variable. The last term in equation 3.8 can be safely neglected at energies above 100 MeV or so due to the small electron mass.

One feature of neutrino-electron scattering is that the final-state particles are very forward-going in general. Figure 3.3 shows the differential cross section in neutrino scattering angle,  $\theta$ , for a 1 GeV neutrino scattering from a stationary electron. The distribution is highly peaked in the forward ( $< 15^\circ$ ) direction, and by kinematic arguments, the distribution of electron scattering angle will be similarly forward-peaked. This cross section is precisely predicted by the Standard Model, and the forward peaked nature allows accurate neutrino direction reconstruction, which makes the interaction a very good probe of a neutrino source. Unfortunately the cross section is very low - at  $E_\nu = 1\text{GeV}$  the total cross section is only  $1.25 \times 10^{-41} \text{ cm}^2$ , which is several orders of magnitude less than the cross sections available when nucleons are used as the target. This is because the higher target mass increases the centre-of-mass energy considerably. As a free electron target is impractical (electrons will always be bound in atoms in a detector), the dominant processes for most experiments involve interactions on atomic nuclei simply due to the much higher cross sections. As we will see, these processes are not as well predicted by the Standard Model and bring additional complexity to the problems faced.

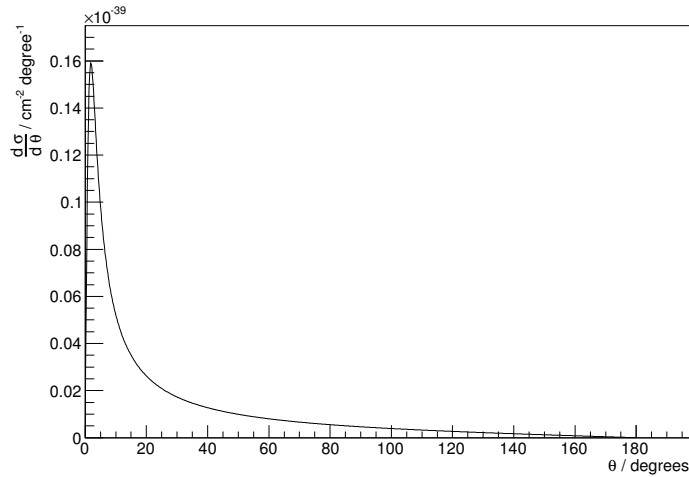


Figure 3.3: Differential cross section for  $\nu_\mu + e^- \rightarrow \nu_\mu + e^-$  elastic scattering, as a function of neutrino scattering angle.

## 3.2 Neutrino-nucleon scattering

As with leptons, the exact cross sections could be deduced for neutrino interactions with free quarks, however due to colour confinement free quarks are never seen. Instead quarks are found in bound states, the most common of these being the proton and neutron. This colour confinement adds considerable complexity to the process, and cannot currently be predicted from first principles so approximations must be made. As nucleons are extended objects with internal structure, their response to a probe depends largely on the wavelength of that probe. In the case of neutrino interactions, the probe is either a Z- or a W- boson and the wavelength depends on the 4-momentum transfer from the leptonic system.

### 3.2.0.1 Elastic and quasi-elastic scattering

At low momentum transfer, elastic scattering is the dominant interaction between neutrinos and nucleons. It is also possible for this elastic scattering to proceed via a charged current interaction, leading to the production of a charged lepton, and a change of isospin for the struck nucleon (see figure 3.4). Due to the change in lepton mass, this is known as a charged current quasi-elastic (CCQE) interaction. The formalism used to describe these interactions was first laid out in the Llewellyn-Smith model [48].

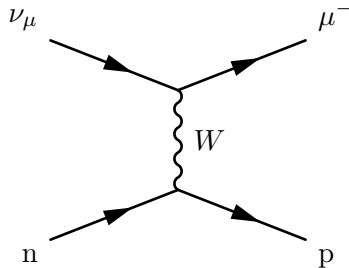


Figure 3.4: Feynman diagram demonstrating charged current neutrino-nucleon quasi-elastic scattering

Due to nucleon being an extended object, it is possible to describe it as if it were a fundamental fermion, but replacing the vertex factor with a function which describes the data. Starting from completely general arguments, appendix A.2 details the derivation of the cross section formula, the final result of which is

$$\frac{d\sigma(\nu n \rightarrow l^+ p)}{dQ^2} = \frac{M^2 G_F^2 \cos^2 \theta_c}{8\pi E_\nu^2} \left[ A(Q^2) \pm B(Q^2) \frac{(s-u)}{M^2} + C(Q^2) \frac{(s-u)^2}{M^4} \right]. \quad (3.9)$$

where  $M$  is the “isoscalar” nucleon mass,  $\theta_c$  is the Cabibbo mixing angle,  $s$  and  $u$  are the Lorentz-invariant Mandelstam variables  $s = (p+k)^2$  and  $u = (k-p')^2$ . With the lepton mass,  $m$ , the “isoscalar nucleon” mass,  $M$ , and the difference between the anomalous magnetic moment of the proton and neutron,  $\xi$ , the terms A, B, and C, are functions of only  $Q^2$  and are given by

$$A(Q^2) = \frac{m^2 + Q^2}{4M^2} \left[ \left(4 + \frac{Q^2}{M^2}\right) |F_A|^2 - \left(4 - \frac{Q^2}{M^2}\right) |F_1|^2 + \frac{Q^2}{M^2} \xi |F_2|^2 \left(1 - \frac{Q^2}{4M^2}\right) \right. \\ \left. + \frac{4Q^2 \Re(F_1^* \xi F_2)}{M^2} - \frac{Q^2}{M^2} \left(4 + \frac{Q^2}{M^2}\right) |F_{3A}|^2 \right. \\ \left. - \frac{m^2}{M^2} (|F_1 + \xi F_2|^2 + |F_A + 2F_P|^2 - \left(4 + \frac{Q^2}{M^2}\right) (|F_{3V}|^2 + |F_P|^2)) \right] \quad (3.10)$$

$$B(Q^2) = \frac{Q^2}{M^2} \Re(F_A^* (F_1 + \xi F_2)) \\ - \frac{m^2}{M^2} \Re \left[ \left(F_1 - \frac{Q^2}{4M^2} \xi F_2\right)^* F_{3V} - \left(F_A - \frac{Q^2 F_P}{2M^2}\right)^* F_{3A} \right] \quad (3.11)$$

$$C(Q^2) = \frac{1}{4} \left( |F_A|^2 + |F_1|^2 + \frac{Q^2}{M^2} \left| \frac{\xi F_2}{2} \right|^2 + \frac{Q^2}{M^2} |F_{3A}|^2 \right) \quad (3.12)$$

where we have introduced six “form factors”,  $F_X$  (where  $X=1, 2, A, P, 3^A, 3^V$ ), which are functions of  $Q^2$ . These form factors can be considered as the Fourier transforms of spatial charge distributions.

$F_1$  and  $F_2$  are the Dirac and Pauli electromagnetic vector form factors, the vector form factors of the first class currents. They are related to the Sachs electric and magnetic nucleon form factors,  $G_E$  and  $G_M$  by:

$$F_1(Q^2) = \left(1 + \frac{Q^2}{4M^2}\right)^{-1} \left[ G_E(Q^2) + \frac{Q^2}{4M^2} G_M(Q^2) \right] \quad (3.13)$$

$$\xi F_2(Q^2) = \left(1 + \frac{Q^2}{4M^2}\right)^{-1} \left[ G_M(Q^2) + G_E(Q^2) \right] \quad (3.14)$$

When examining the same elastic scattering process, but with electrons as the probe rather than neutrinos, the same formalism may be adopted. In this case, the only form factors allowed to be non-zero are the vector form factors, and the ability to measure the incoming and outgoing electron to high precision has allowed extensive measurements of these form factors. The Sachs vector form factors have been found to follow an approximately dipole shape as a function of  $Q^2$  (see equations 3.15 and 3.16), though more recent fits show that the form factors

diverge from a dipole, especially at high  $Q^2$  [49].

$$G_E(Q^2) \simeq \frac{1}{(1 + Q^2/M_V^2)} \quad (3.15)$$

$$G_M(Q^2) \simeq \frac{1 + \xi}{(1 + Q^2/M_V^2)} \quad (3.16)$$

where the parameter  $M_V$  can be fitted to data, and is approximately 840 MeV.

The form factors  $F_{3V}$  and  $F_{3A}$  are G-parity violating second class currents. T-invariance demands that all form factors are real and charge symmetry demands that  $F_{3V}$  and  $F_{3A}$  are imaginary, which leads to the second class currents being constrained to be identically zero <sup>1</sup>. This implies conservation of G-parity.

$F_A$  and  $F_P$  are the axial form factors of the first class currents.  $F_P$  is often referred to as the pseudo-scalar form factor. From the Goldberger-Treiman relation [51], it can be shown that:

$$F_P(Q^2) = \frac{2M^2 F_A(Q^2)}{m_\pi^2 + Q^2}, \quad (3.17)$$

where  $M$  is the nucleon mass and  $m_\pi$  is the pion mass. This leaves us with only one unknown form factor,  $F_A$ . It is common to make the assumption that this will also follow a dipole form:

$$F_A(Q^2) = \frac{F_A(0)}{(1 + Q^2/M_A^2)^2} \quad (3.18)$$

$$F_A(0) = 1.23.$$

The value of  $F_A$  at  $Q^2 = 0$  has been determined through  $\beta$ -decay leaving one free parameter,  $M_A$ , which can only be determined through neutrino scattering.

Under the interpretation of a form factor as the Fourier transform of a charge distribution, the axial mass would be interpreted as the ‘‘axial radius’’ of a nucleon. The axial mass would therefore be expected to be of order 1 GeV, and fits to hydrogen and deuterium data generally find that is in fact the case. In fact, theoretically the axial mass is simply a convenient fitting parameter. The charge distribution seen by a probe depends on the wavelength of that probe and, as mentioned previously, recent fits to large amounts of data have shown that the quasi-elastic vector form

---

<sup>1</sup>The second class currents,  $F_{3V}$  and  $F_{3A}$ , if they exist, could have a small effect on the cross section, in particular they are always coupled to the lepton mass, so they could lead to a  $\nu_\mu/\nu_e$  cross section difference [50].

factors deviate from a dipole shape, suggesting the dipole shape doesn't hold any fundamental physical significance.

### 3.2.0.2 Resonance production

Once the centre-of-mass energy of a neutrino-nucleon collision exceeds the mass of a delta baryon, it is possible to excite a resonance. This usually leads to the production of a real pion, and can be accessed through both charged- and neutral current interactions. Figure 3.5 shows an example of how this interaction proceeds.

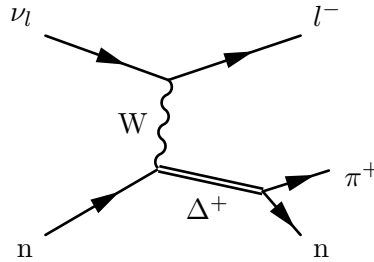


Figure 3.5: Feynman diagram of resonant pion production. A nucleon is excited into a delta resonance, which rapidly decays into a nucleon and a pion.

Resonant production of a pion can occur through any channel that conserves charge, allowing a wide range of final states, with positive, negative, and neutral pion production possible by any neutrino flavour. For example positive pions can be produced in the following ways:

$$\begin{aligned} \nu + p &\rightarrow \nu + n + \pi^+ \\ \nu + p &\rightarrow l^- + p + \pi^+ \\ \nu + n &\rightarrow l^- + n + \pi^+ \\ \bar{\nu} + p &\rightarrow \bar{\nu} + n + \pi^+ \end{aligned}$$

As the neutrino energy increases, further resonances become available, and different final states become available. These can include the production of kaons, photons, or multiple particles.

Calculations of the resonant single pion production cross section were first performed by Rein and Sehgal [52] in 1980, which considered the first 18 resonances, up to masses of 2 GeV, and also included the interference between them.

Resonant pion production on nuclei can be treated in a similar way to elastic interactions, using form factors to be able to treat the extended nucleus as a point particle. For resonance production, the form factors are different, and differ-

ent constraints apply, however a common parametrisation assumes that they have a dipole shape similar to the elastic form factors. After fitting the vector form factors using electron scattering data, the axial parts remain, usually leaving two free parameters, known as  $C_5^A$ , and  $m_A$  to be fitted to data (the equivalent to  $C_5^A$  for the elastic form factors is determined in beta-decay). The resonance axial mass,  $m_A$  is often considered separate to the CCQE axial mass, and known as  $m_A^{RES}$  or  $m_A^{\Delta}$ . Theoretically there is some reason to assume this axial mass is equal to the QE axial mass, however to get good agreement with data it is often necessary to treat them separately. In addition, when we come to discuss interactions with nuclei, it will become apparent that these parameters are often used as effective parameters to cover data/theory differences that are assumed to come from poorly-understood or unknown effects.

### 3.2.0.3 Inelastic scattering

As the neutrino energy increases further, and the wavelength of the probe decreases accordingly, the probe is able to resolve the individual quarks in a proton or neutron. This is the region of inelastic scattering, equivalent to the process discovered in electron scattering in the 1960s.

The tree level diagram is a simple elastic scatter off a quark, however due to colour confinement the free quark is not seen, instead hadronisation occurs, and a hadronic jet is produced. In this case there is a transition from final states with multiple pion production to states where the original nucleon breaks up entirely. The neutrino is able to scatter off not only the three valence quarks, but also the sea quarks, meaning at higher energies it is possible to produce more exotic, higher mass mesons. Above neutrino energies of about 10-20 GeV DIS is by far the dominant interaction process.

## 3.3 Neutrino-nucleus scattering

There are many reasons for using heavy nuclear targets. As event rates scale roughly linearly with target mass, a simple way of increasing statistics is to use a more dense target material. In addition, the only way of obtaining free, or nearly-free nucleon targets is to build a liquid hydrogen or liquid deuterium detector, which has obvious safety risks. Materials are often chosen based on cost and ease of fabrication, which has led to many modern detectors being built from materials such as iron, lead, water, and various hydrocarbons. Liquid argon is also used, and is being seriously considered for future long-baseline neutrino oscillation experiments, due

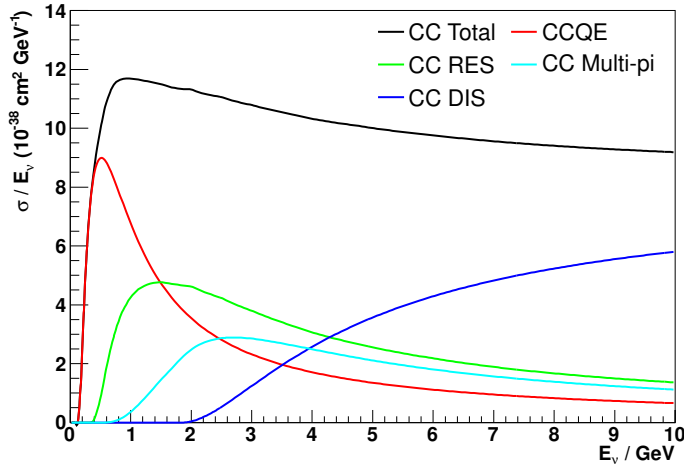


Figure 3.6: The prediction from NEUT 5.1.4.2 for different processes' cross sections as a function of energy.

to the ability to achieve high event rates, and utilise the charge-transport properties to construct large liquid time-projection-chambers. Unfortunately using complex nuclei introduces a number of effects which serve to complicate the situation yet further, when compared with free nucleons.

The NEUT [53] generator prediction for the cross sections on carbon for the dominant processes is shown as a function of energy in figure 3.6. There are only a few regions where any one process is dominant, meaning most experiments with beam energies between 0.5 GeV and 10 GeV have to understand several processes in their detector.

### 3.3.1 Nuclear effects

Often the best way to think about interactions with a heavy nucleus is to consider interactions with the individual nucleons inside, however the nucleons are bound, and moving around, inside the nucleus. The distribution of energies and momenta found inside the nucleus is actually very poorly known, leading to uncertainties when considering low-energy interactions. Historically a Fermi gas model has been used, as the results can be analytically calculated (this formalism was first laid out in [54], and was extensively deployed in generators), however other models exist, and they will be discussed in more detail in chapter 5. At this point it is not clear which, if any, of these models is correct.

Another complication when considering interactions with nucleons in a nuclear medium is what happens to the final state. Any hadrons produced in the

initial interaction will be travelling through a dense nuclear medium, and can easily undergo strong interactions. These are known as final-state interactions (FSI) and can not only cause particles to scatter and change their momentum, but also can change the multiplicity and type of particles visible outside the nucleus. Particles can be absorbed by the nucleus, new particles can be created in hadronic collisions, and pions can exchange charge with the nucleus (for example the interaction  $\pi^+ + n \rightarrow \pi^0 + p$ ). These effects are most problematic at lower energies, where the nucleus does not break up, and the outgoing particles are of low enough energy that they have a high chance of interacting in the nuclear medium. At higher neutrino energies, and higher  $Q^2$ , reactions are dominated by deep inelastic scattering (DIS), where the nucleus breaks up and most outgoing particles have high momenta. Fortunately leptons can travel through nuclear matter largely unimpeded, except for radiative effects which can affect the cross section [55]. Several techniques have been developed to predict the effects of FSI, and implemented in Monte Carlo event generators, usually based on propagating a cascade of outgoing particles through the nucleus (see discussion in section 5.1). It is not widely believed that this cascade model is a complete description of FSI. It is, however it is a useful way of modelling the effects, and can be tuned to agree with data.

Another similar effect to FSI is the phenomenon of Pauli blocking. Pauli blocking arises because protons and neutrons are fermions, so when an interaction changes their momentum it can only change it to a state which is not already filled. This limits the phase space available to particles and serves to suppress the cross section, particularly at low values of  $Q^2$ , when outgoing nucleons would have low momenta. Again, the exact details of how Pauli blocking applies to nucleons in a nucleus is not understood well, and can depend on the nuclear model used.

These effects can cause significant difficulties for oscillation experiments. For example, a CCQE interaction can in principle be used to determine the neutrino energy through 2-body kinematics, however, identifying a  $\mu + p$  final state in a detector is not sufficient to say definitively that the interaction was a CCQE interaction. In addition, the Fermi motion and binding energy in the initial state leads to smearing and potential biases even when muons from correctly identified CCQE events are used to reconstruct the neutrino energy.

### 3.3.2 Correlations and coherence

In addition to the interaction modes listed above, there are other interactions that can only occur on nuclear targets. The first of these interaction modes is the coherent production of mesons, where the final state nucleus is in exactly the same state as

it was before the interaction. This occurs when the neutrino-nucleus amplitudes sum coherently, leading to the cross sections scaling with the square of the nuclear mass, rather than linearly. Theoretical descriptions of coherent interactions have been successful at describing data at high neutrino energies, however the standard approaches are not valid below about 1 – 2 GeV. Data is scarce at energies below this, but indications are that the cross section is much lower than models currently predict (see section 3.4.2.3).

The second interaction type that can only occur when multiple nucleons are present is an interaction with a correlated pair of nucleons in the nucleus. There is growing experimental evidence for interactions which lead to the production of pairs of nucleons [56, 57], and there are also several models that predict these interactions. The models can largely be separated into one-body current models, and two-body current models, though there is some ambiguity. One-body current models predicting multi-nucleon ejection predict the existence of high momentum nucleons in the nucleus, which are in a two-particle correlated state, analogous to a quasi-deuteron. An interaction with one of these particles will then lead to the correlated partner also being ejected from the nucleus (except for, of course, FSI effects which may re-absorb either nucleon). The two-body current models predict interactions mediated by mesons being exchanged between nucleons (and are therefore often referred to as meson-exchange currents, or MEC, though also known as 2p2h or npnh for the multi-particle multi-hole final state). These interaction modes are seen as separate to the “standard” reaction modes, and could enhance cross sections on nuclear targets. For this reason they are often used to explain the high value of  $M_A$  reported in fits of CCQE data recently (particularly the MiniBooNE results). Examples of this type of model are those developed by Nieves et al. [58], and Martini et al. [59, 60]. Phenomenological models also exist to describe the discrepancies that npnh models were intended to address, such as the transverse enhancement model based on superscaling [61].

Most theories for low energy interactions with nuclei (particularly for elastic and resonant events) use the impulse approximation. In this approximation, the interaction occurs over a short enough time period to be considered to be an interaction with one single nucleon. Unfortunately, as the energy transfer changes so does the wavelength of the probe, and once this wavelength is larger than the size of a nucleon, the surrounding nucleons will have an effect on the response. The in-medium polarisation effect affects the W boson self-energy, and can be calculated in the many body formalism using random phase approximation (RPA). RPA computes the propagation of a p-h pair through the nuclear medium, and thus takes

into account long-range correlations. A calculation of this effect has been performed by Nieves et al. [62].

An alternative way of thinking about this effect is to consider that the interaction is with a quasi-particle, which contains contributions from many real particles. The contributions must be summed coherently and, as the probe gets larger, the relative phases become less correlated leading to a suppression of the cross section. Figure 3.7 shows the RPA correction as a function of  $Q^2$ . A suppression is seen at low  $Q^2$ , with an enhancement at medium values of  $Q^2$ , while at high  $Q^2$  the RPA correction does very little.

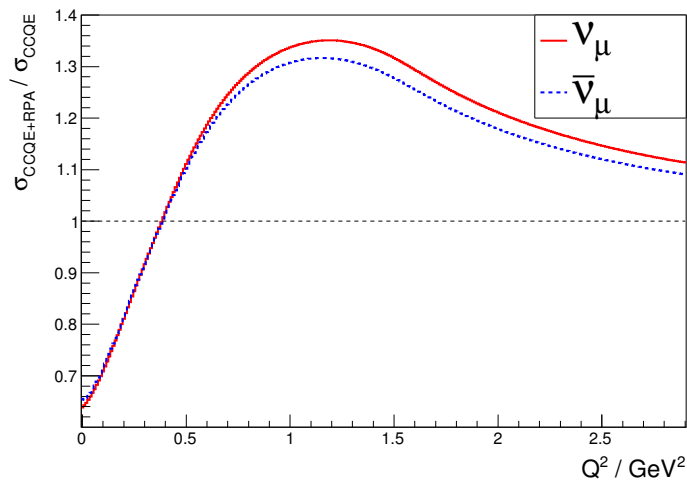


Figure 3.7: Ratio of RPA-corrected to standard IA cross section, for CCQE interactions on carbon, assuming a local Fermi gas model. It can be seen there are slight differences in the effect between neutrinos and antineutrinos. Plot made using the T2K implementation of the Nieves RPA calculation [62].

### 3.4 Summary of cross section data

It is important at this point to consider the data that exists of measurements of neutrino cross sections. As they are most relevant, we will focus here on interactions with nucleons and nuclei. As we will see, the data is generally sparse with large uncertainties. Where there is precise data, there tend to be fairly large tensions between different data sets and theoretical predictions. For more extensive reviews, see [17, 47]

### 3.4.1 Low energy processes

At low energies, below the threshold for creation of a lepton, the dominant neutrino interaction process is inverse beta decay. This process is relatively well understood and there is reasonable agreement between the available data and theoretical predictions. For an example, see figure 3.8

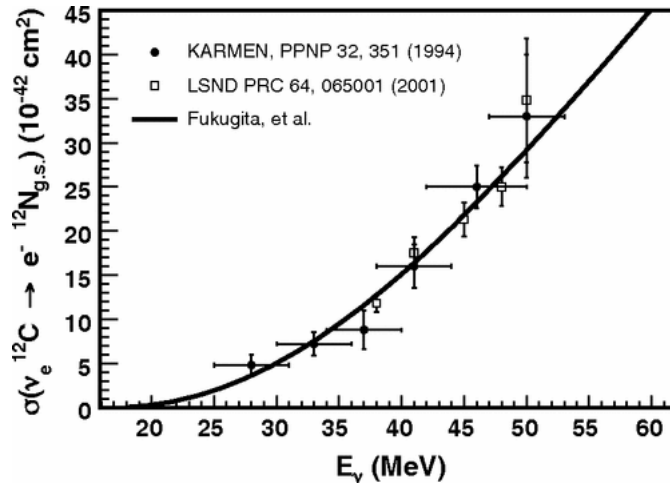


Figure 3.8: Cross section as a function of energy for the inclusive process  $^{12}\text{C}(\nu_e, e^-)^{12}\text{N}$ . There is reasonable agreement between the data and the theoretical prediction. Taken from [47].

### 3.4.2 Medium energy processes

At higher energies, more processes become available, and nuclei are no longer left in their ground state. In the region of 100 MeV – 20 GeV, many processes contribute to the total cross section.

#### 3.4.2.1 Quasi-elastic

The lowest threshold process is quasi-elastic scattering, and a large amount of data was collected with hydrogen and deuterium targets between the 1970s and 1990s. This allowed a very precise determination of the parameter  $M_A = 1.026 \pm 0.021$  GeV, which is in reasonably good agreement with the value obtained from pion electroproduction ( $1.069 \pm 0.016$  GeV) [63].

More recently, high-statistics data has been collected on nuclear targets such as carbon and oxygen, and fits to this data have resulted in much larger values of  $M_A$  [64].

Figure 3.9 shows existing measurements of the  $\nu_\mu$  QE scattering cross section on a variety of targets, as a function of neutrino energy. Care must be taken when interpreting the data on heavier targets, as the theoretical prediction shown is for a free nucleon. It is clear, however, that the data tend to have a large spread with large uncertainties. Of note here is the MiniBooNE data, which shows a clear enhancement with respect to the prediction. This enhancement of QE-like cross sections on a nuclear target is one of the driving forces behind the development models such as MEC (see section 3.3.2).

Figure 3.10 shows the existing measurements of the same process for  $\bar{\nu}_\mu$ . In this case it is clear that the data cover a narrower energy range, and provide a worse constraint than in the neutrino case.

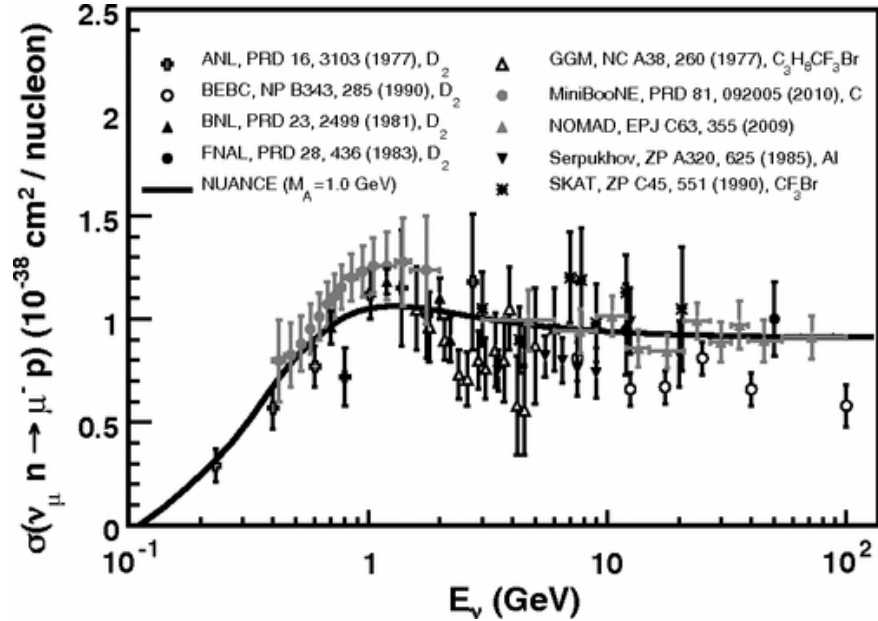


Figure 3.9: Summary of  $\nu_\mu$  CCQE cross section measurements to date, as a function of neutrino energy on various targets. The free nucleon prediction assuming  $M_A = 1.0$  GeV is also shown. Taken from [47].

There is additionally some data available for some NC elastic scattering, though usually provided as a ratio to CC quasi-elastic, and integrated over the experiments neutrino energy spectrum. These data generally have very large uncertainties.

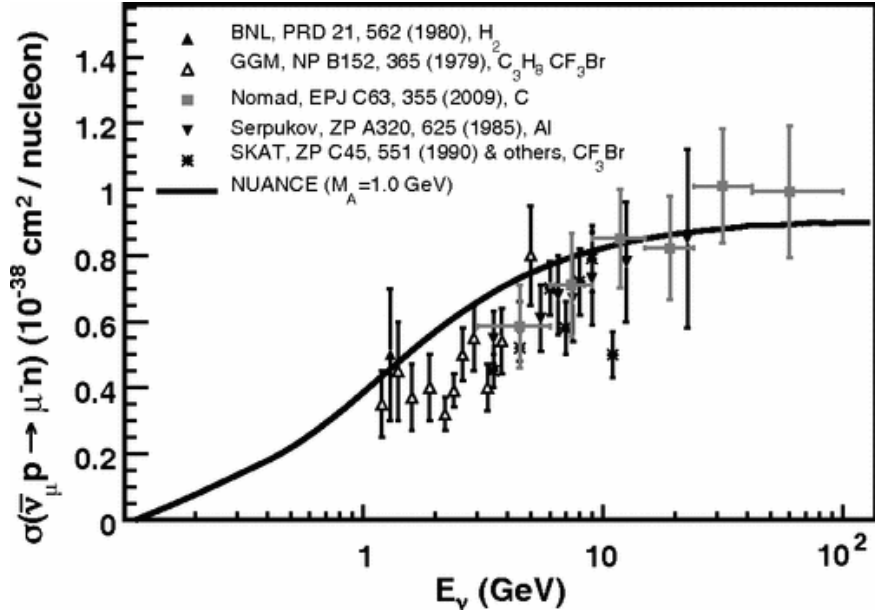


Figure 3.10: Summary of  $\bar{\nu}_\mu$  CCQE cross section measurements to date, as a function of neutrino energy on various targets. The free nucleon prediction assuming  $M_A = 1.0$  GeV is also shown. Taken from [47].

### 3.4.2.2 Resonant pion production

The resonant pion production channel has a number of distinctly different final states which can all be measured independently. The first of these, the charged current channels, have reasonable data coverage. The data have large uncertainties, and again it is important to stress that data on heavier targets than hydrogen or deuterium should be interpreted with care as poorly understood nuclear effects could be present. The data for an example channel ( $\nu_\mu + p \rightarrow \mu^- + p + \pi^+$ ) are shown in figure 3.11.

### 3.4.2.3 Coherent pion production

Coherent pion production has been observed in both the neutral and charged current channels, on a variety of targets. Detailed comparisons have to make assumptions of the way the cross section varies with nuclear mass, however at high energies models based on the partially-conserved axial current (PCAC) hypothesis are expected to be valid and cross sections are expected to scale approximately as  $A^{1/3}$  [65]. Figure 3.12 shows the data available for  $\nu_\mu$  and  $\bar{\nu}_\mu$  CC coherent pion production for energies above 5 GeV, compared to the predictions from two generators. It is clear that though both generators predict drastically different shapes, both are completely

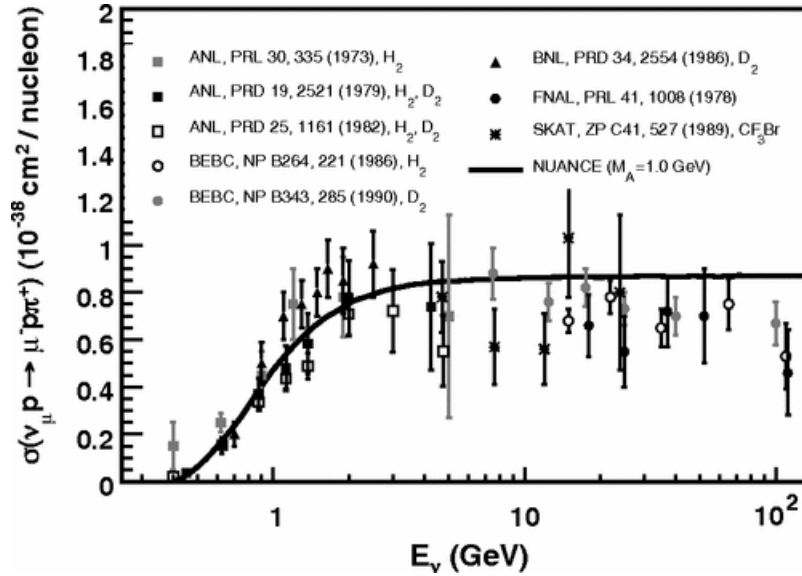


Figure 3.11: Summary of measurements of the resonance process  $\nu_\mu + p \rightarrow \mu^- + p + \pi^+$ . The prediction assumes  $M_A = 1.1$  GeV. Taken from [47].

compatible with the data due to the large uncertainties.

Below 2 GeV, it is understood that the standard PCAC approach to coherent pion production will fail. This is because the PCAC-derived relationship between the neutrino-nucleus cross section and pion-nucleus cross section is strictly only valid at  $Q^2 = 0$ . At high energies the muon and pion are very forward going and this is approximately true, however at lower energies the transverse momentum fraction becomes much larger and the approximation of  $Q^2 = 0$  becomes very poor.

In addition, due to the difficulties that arise in low energy interactions on heavy targets, and the fact that the coherent cross section is small, identifying coherent interactions has proved difficult below 2 GeV. In this region the available models have drastically different predictions for the cross section, and currently the best measurements provide only upper limits on the total cross section. These limits are shown in figure 3.13, along with the predictions from GENIE and NEUT. It is clear that more data in this energy range is desperately needed.

#### 3.4.2.4 Inelastic scattering and multiple pion production

In the region between resonant pion production and deep inelastic scattering, higher mass resonances contribute to final states containing multiple pions. These final states are inherently more difficult to identify so there is not much data available. Those data that are available are generally on deuterium targets, for example the

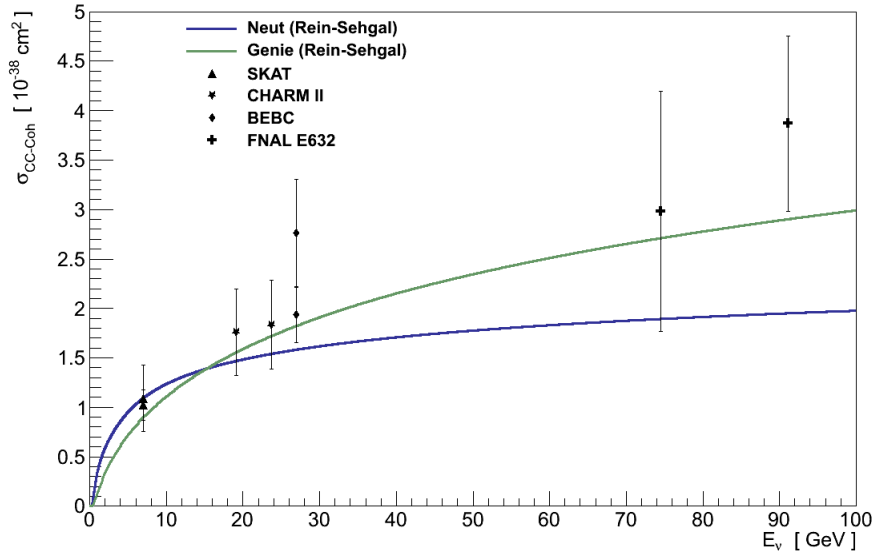


Figure 3.12: A comparison of coherent scattering cross section models and measurements above 5 GeV. Taken from [66].

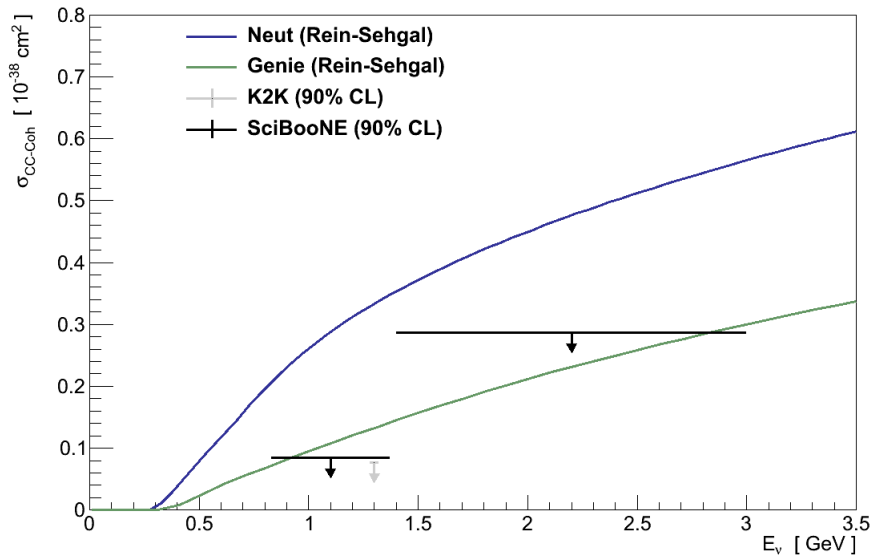


Figure 3.13: A comparison of coherent scattering cross section models and measurements below 3 GeV. Taken from [66].

data in figure 3.14. In addition, the CHORUS experiment measured various multiplicity distributions in an emulsion target [67]. On heavier targets, final state

interactions play a much larger role and it is known that there are large uncertainties surrounding these interactions.

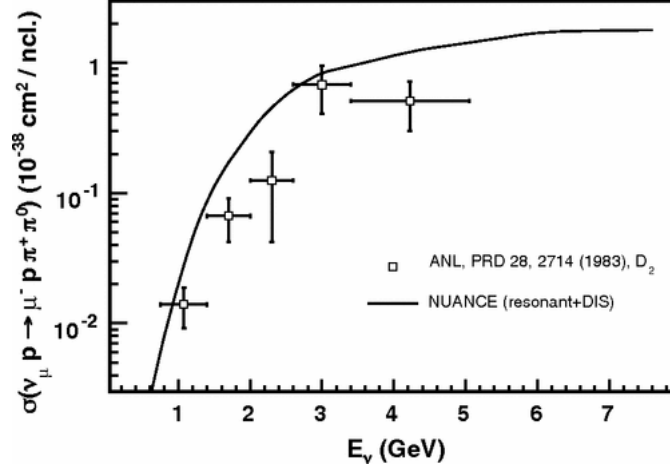


Figure 3.14: A comparison of the existing measurements of the  $(\nu_\mu + p \rightarrow \mu^- + p + \pi^+ + \pi^0)$  scattering cross section, with the theoretical prediction from a generator. Taken from [47].

### 3.4.2.5 Medium energy inclusive processes

The CC-inclusive channel represents the sum of all channels available at this energy. This channel is very clean to isolate experimentally as the signal is simply the presence of a muon. Unfortunately it is less useful for constraining theoretical predictions, as there are many processes contributing. Nevertheless, the data even here provides very little actual constraint on the CC-inclusive cross sections, as can be seen in figure 3.15 where it is clear that the overall cross section normalisation could be scaled up or down by 20% and remain consistent with the available data.

### 3.4.3 Very high energy processes

In the region 20 GeV - 500 GeV, neutrino scattering of nucleons and nuclei is dominated by DIS. Theoretically this cross section is reasonably easy to calculate, as the interaction can be viewed as an interaction between fundamental fermions (neutrino and quark). In addition, the nuclear effects that were problematic at lower energies are now insignificant compared to the energy transferred from the neutrino.

Figure 3.16 shows charged current inclusive cross section measurements for  $\nu_\mu$  and  $\bar{\nu}_\mu$ , from 20 GeV up to 350 GeV. In this region, the amount of data and its power to constrain the cross section is remarkable when compared with lower energy data.

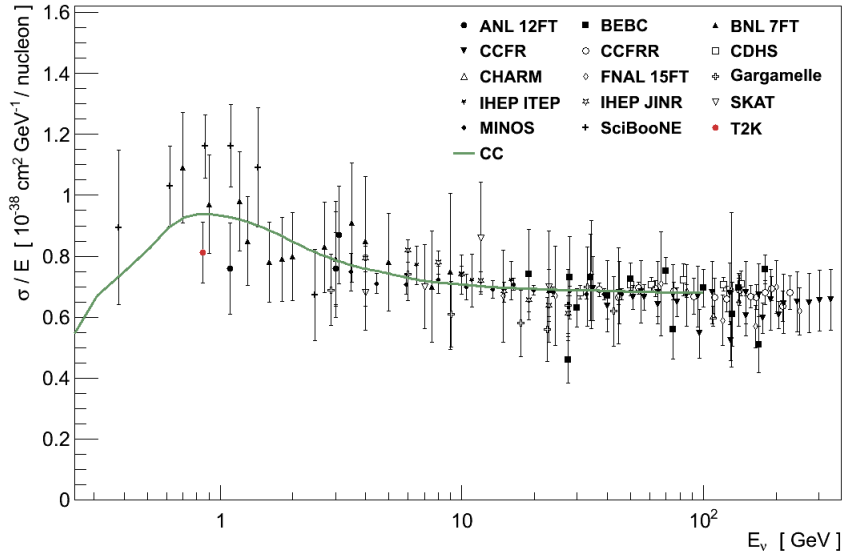


Figure 3.15: Data on  $\nu_\mu$  CC-inclusive scattering cross section divided by energy, compared to the prediction from GENIE. Taken from [66]

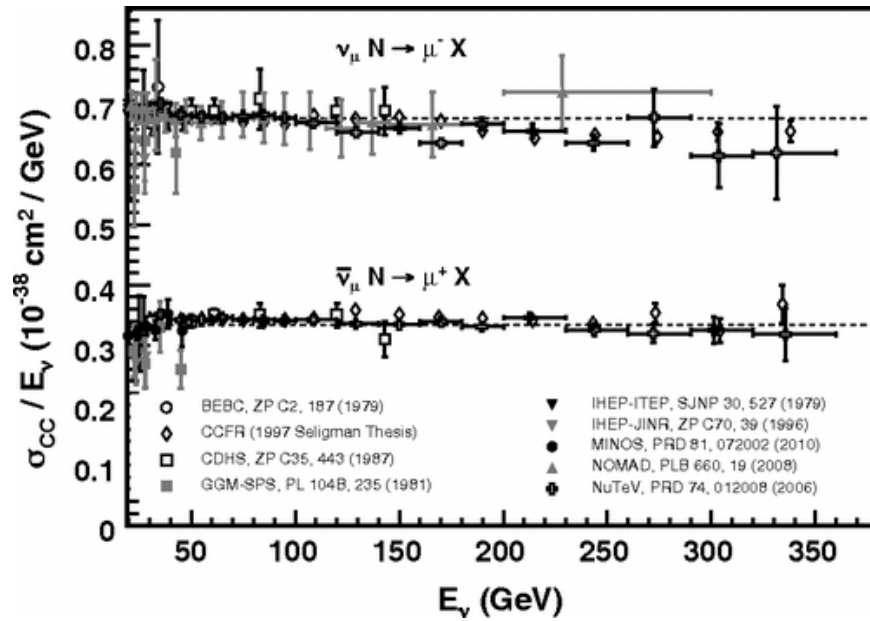


Figure 3.16: Data on  $\nu_\mu$  and  $\bar{\nu}_\mu$  CC-inclusive scattering cross section divided by energy, at high energies, such that the dominant process is deep inelastic scattering. Taken from [47].

Despite the good agreement found with data, there remain effects in the DIS regime which are poorly understood. For example, an effect known as the EMC

effect (named after the experiment that first saw it in charged lepton scattering [68]) suggests that quarks in heavy nuclei behave differently to those in free nucleons - a naive prediction assuming quarks reside in quasi-free nucleons cannot explain the data seen. This leads to different structure functions needing to be used for heavy nuclei and free nucleons.

### 3.5 Generators

To perform oscillation analyses, experiments use Monte Carlo simulations to make predictions. This will involve a simulation of the interactions in the detector which usually requires a dedicated interaction simulation followed by a detector simulation (which tends to be GEANT4-based). In the past, experiments usually wrote and maintained their own interaction generator specific to their energy range and target, however in recent years there has been development of a number of more generic generators. All oscillation experiments rely on interaction generators to perform oscillation measurements, so the measurement can have some dependence on the model used (though there are ways to mitigate this using a near detector). Cross section measurements usually use generators to predict their backgrounds and as such can have dependence on the generator and should be treated with some care. It is also common to see cross section measurements compared with the prediction from various generators, so it is important to understand how the different generators differ before interpreting these comparisons.

Most generators are based around the same philosophy of factorising the generation into several steps (with the notable exception of GiBUU, which is very different in design to most generators, as it is designed as a nuclear simulation rather than a neutrino simulation). Usually the total cross section as a function of energy for each mode is computed before the event generation and stored in tables or splines – though occasionally it can be done on-the-fly. Knowledge of the total cross section for each mode allows the selection of a neutrino in any interaction mode consistent with the flux and cross section. An event can then be generated for the interaction mode selected, where the momentum and direction of every outgoing particle is specified. Often this event generation step is factorised again to reduce the dimensionality of the problem – though care must be taken to evenly sample the full phase space. After the simulation of an interaction, the outgoing particles are propagated through the nuclear medium where they are allowed to interact to simulate FSI.

### **3.5.1 Current and past neutrino interaction generators**

#### **3.5.1.1 NUANCE**

NUANCE [69] was a FORTRAN based interaction generator, which was used in the K2K and MiniBooNE experiments (MiniBooNE made a number of modifications to the original code, and maintained their own private version). Although it was written to be applicable over a range of experiments, and was used successfully, NUANCE is no longer maintained, and has fallen out of use.

#### **3.5.1.2 NEUT**

Possibly the oldest interaction generator, NEUT [53] was originally written for the Kamiokande nucleon decay experiment. NEUT was adopted by Super-Kamiokande, and has been continuously updated and extended for use by K2K and then also T2K. More recently the T2K collaboration have made significant updates to the models available, particularly for CCQE and CCQE-like models and also added a reweighting library for the study of systematic uncertainties. NEUT is, unfortunately, not publicly available, which restricts its usefulness for the community in general. Many results in this thesis are produced using NEUT, and the work in chapter 5 revolves around adding a new nuclear model to NEUT, so it will be discussed in more detail there.

#### **3.5.1.3 NEUGEN**

NEUGEN [70] was written for the Soudan 2 experiment [71], where it was used originally to predict neutrino backgrounds in a proton-decay search. NEUGEN was then adapted for use by the MINOS experiment, and extended to higher energies and additional neutrino flavours and interaction types.

#### **3.5.1.4 GENIE**

GENIE [72] was originally a C++ version of NEUGEN, though the code has since been extensively developed. GENIE has been developed with the intention of being a truly general interaction generator, and is therefore structured in an experiment-agnostic manner. The code is structured in a very modular manner, such that it is simple to add new models, and replace models. GENIE has been used in a large number of experiments to date, including being used in the T2K experiment alongside NEUT, where it is mainly used for cross-checks and fake data studies. This

is possible because of the generic way in which it is written, allowing new fluxes and detector geometries to be used very easily.

GENIE has a similar set of interactions and models as NEUT and other generators, but with some notable differences which are summarised below.

- **Nuclear model**

GENIE uses the relativistic Fermi gas model as default for all interaction types, however it uses the model as described by Bodek and Ritchie, in which a high-momentum tail is included to account for nucleon-nucleon correlations such as those predicted by the spectral function model (see chapter 5). The nuclear de-excitation photons are also simulated, but currently only in limited cases.

- **Axial mass**

the default axial mass in GENIE is 0.99 GeV. This is in agreement with the value found in hydrogen and deuterium experiments, and somewhat different to the value used in NEUT (1.21 GeV), which was tuned to agree with the data found by K2K.

- **Resonant pion production**

GENIE employs the Rein Sehgal model for resonant pion production, with some differences to the description in the original paper. The resonance parameters are updated according to more recent data, however interference between resonances is neglected.

- **Coherent pion production**

The Rein Sehgal model for coherent pion production is adopted, however it uses an updated version of the PCAC formula which includes lepton mass terms. In addition, the pion-nucleus scattering data used is more recent than the original Rein Sehgal paper, so the GENIE results are not expected to agree with the original authors' results.

- **Other interactions simulated**

GENIE simulates a number of other interactions which many generators neglect. These include charm production, both in quasi-elastic and inelastic modes. In addition, the inverse muon decay (IMD) and neutrino-electron scattering interactions are considered. These have low cross sections compared to the interactions simulated with nuclei, however they are potentially separable in a high-statistics neutrino experiment and as they have known cross sections they could be very useful.

### 3.5.1.5 NuWro

NuWro [73] [74] is a modern C++ based neutrino generator, developed by a theory group, which has largely been used as a test bed for new models. NuWro has not been used as the main generator in any experiments, though it has been used by T2K to generate small samples with new models, to check for biases, and can be used to calculate cross sections to compare to data, assuming various combinations of models.

### 3.5.1.6 GiBUU

Although it is not a “true” neutrino interaction generator, GiBUU is usually included in a discussion of generators. GiBUU is a semiclassical nuclear physics simulation, which treats the initial- and final-state interactions in the nucleus in a unified and self-consistent manner, and has been extended to include descriptions of neutrino-nucleus interactions. GiBUU takes much longer to compute than the other generators, because of the way it is constructed to analytically solve transport equations. For this reason it cannot realistically be used by experiments, however results from GiBUU can nonetheless be very useful when considering comparisons to data, and inclusion of new models.

### 3.5.1.7 Related code

At high energies, DIS becomes the dominant interaction process. Routines to deal with hadronisation are usually taken from PYTHIA [75], though generators are usually required to use ad-hoc methods in the region between resonance modes, and DIS, often referred to as the shallow-inelastic scattering (SIS) region, and often use modifications to obtain a better description of the available data. The exact way this is done varies from generator to generator.

## 3.5.2 Discussion of generators

One must be careful when comparing models to data using neutrino generators. Generators are only useful to experimentalists if they are efficient, and they often try to incorporate models which are only valid in certain energy ranges. These, as well as other considerations, lead to compromises being made and ad hoc methods being introduced to transition between models that have different validity regions.

It is also difficult to make comparisons between different generators, as there are so many different elements to a generator, and many ways in which each one can differ subtly (and sometimes less subtly). This leads to it being impossible

to assess the differences between generators, even when looking at the same model. Figure 3.13 demonstrates this quite well, as NEUT and GENIE have nominally both implemented the “Rein Sehgal” model for coherent pion production, but they have slight differences in the approximations used; for example they use different data for pion-nucleon cross section. The result is that the cross section predictions for the “same” model differ at low energies by more than a factor of two.

There is therefore good reason to only use one generator in all experiments, which should make these comparisons clearer, however experiments often want generators tuned to agree well with their energy range and target. It is not clear what the path forward will be, but GENIE may well become a standard, as it is already being used by almost all experiments.

## Chapter 4

# The T2K experiment

### 4.1 Overview and motivation

T2K (Tokai-to-Kamioka) is a long-baseline neutrino oscillation experiment [76]. Based in Japan, the  $\nu_\mu$  beam is created at the Japan Proton Accelerator Research Complex (J-PARC) in Tokai, Ibaraki, on the Pacific coast. The near detector complex is also based within J-PARC, after which the neutrino beam travels 295 km to Super-Kamiokande.

T2K began data taking in 2010, with the primary goal of reducing the limit on the (at the time) unknown mixing parameter  $\theta_{13}$ . It is also capable of making precision measurements of the atmospheric oscillation parameters,  $\theta_{23}$  and  $\Delta m_{23}^2$ , through a disappearance of muon neutrinos. With the discovery in 2012 of a relatively large value of  $\theta_{13}$  by Daya Bay [32] and RENO [77], confirmed by T2K [78], it may also be possible for T2K to have sensitivity to the value of  $\delta_{CP}$ , the CP-violating phase.

T2K is the first experiment to utilise the innovative off-axis placement of both near and far detectors, which provides a much narrower spectrum, tuned to peak at the energy corresponding to the far detector oscillation maximum. This also reduces the high energy component of the neutrino beam which can lead to large backgrounds at Super-Kamiokande from neutral pion production.

### 4.2 Neutrino beam

J-PARC is a multi-purpose research facility in Tokai, Japan. The accelerator system begins with a  $H^-$  LINAC, after which the ions are converted to protons by charge-stripping foils. The protons are then accelerated in the RCS (Rapid Cycling

Synchrotron), after which most are sent to the Materials and Life Sciences Facility (MLF). About 5% of the protons from the RCS are passed into the MR (main ring), which is shared between the Hadron hall and the neutrino beamline facility.

The neutrino beamline is divided into two sections, primary and secondary. In the primary neutrino beamline, the protons are fast extracted (meaning every bunch is extracted in its entirety within one turn) at 30 GeV by a set of kicker magnets and bent inside the main ring to point towards the T2K detectors.

At the end of the primary beamline is a titanium alloy beam window, after which the proton bunches enter the secondary beamline where they are collimated by a graphite baffle, before they impinge on a 91.4 cm long graphite target, which is housed inside a magnetic focusing horn. There are two more magnetic horns downstream of the target, which are used to focus the desired charged mesons (positive for neutrino beam, negative for an anti-neutrino beam) into the decay volume, and reject the wrong-sign mesons. The horns were designed to operate at a current of 320 kA, however they have been operated at 250 kA for most of the run periods so far.

After focusing, the mesons travel into a 96 m long decay volume, which is filled with helium gas at atmospheric pressure. The mesons produce neutrinos in this volume through decays to lepton/neutrino pairs. At the end of the decay volume, a beam dump absorbs most of the energy of remaining particles, and a muon monitor (MUMON) provides data with which the beam simulation can be tuned. Figure 4.1 shows a schematic representation of the target station and decay volume.

Most of the mesons focused into the decay volume are the desired-sign pions, however there is contamination from wrong-sign pions, and kaons of both signs. Kaons contribute mainly to the high-energy tail of the neutrino beam, and wrong sign pions lead to an anti-neutrino component to the beam. There is electron neutrino contamination from kaon decays, as well as muons from pion and kaon decay further decaying to produce both a muon neutrino and an electron neutrino.

Because of the way in which the neutrino beam is created, it is common to describe the size of data samples with the number of protons-on-target (POT).

#### 4.2.1 Off-axis angle

T2K was the first long-baseline neutrino experiment to utilise an “off-axis” beam, meaning that the main detectors are placed not along the central beam direction, but rather  $2.5^\circ$  away from the axis. This method results in a far more mono-energetic beam than found along the beam axis. Equation 4.1 gives the energy of a neutrino from a pion decay to a muon and neutrino pair, as a function of neutrino

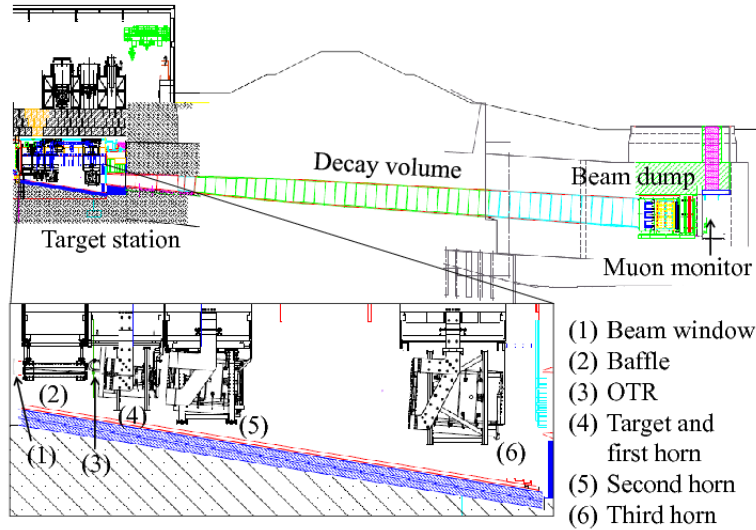


Figure 4.1: Schematic of the target station and decay volume. The inset image shows a more detailed view of the target station, including the horn arrangement. Figure taken from [79].

angle and pion energy. Plotting this as a function of pion energy (see figure 4.2) for various angles demonstrates that a wide-band pion spectrum can lead to a narrow-band neutrino spectrum when detectors are moved off-axis. The flux predictions at various off-axis angles are shown in figure 4.3, showing that it is possible to tune the flux peak to match the muon neutrino disappearance probability by simply changing the angle.

$$E_\nu = \frac{m_\pi^2 - m_\mu^2}{2(E_\pi - p_\pi \cos \theta)} \quad (4.1)$$

The advantages of this peaked spectrum are two-fold for T2K. Firstly, although the total beam flux at both the near and far detectors is reduced, the flux at the oscillation maximum is actually increased, adding statistics in the most important region. Secondly, the high-energy region of the flux is significantly reduced in size. Neutrinos at these energies contribute little to the oscillation signal, but can contribute to backgrounds in the oscillation region, so removing them from the beam leads to reduced systematic uncertainties.

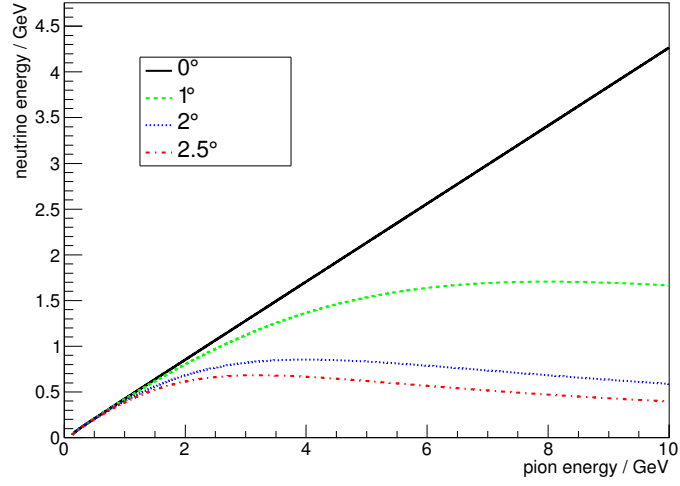


Figure 4.2: Neutrino energy as a function of pion energy for various off-axis angles.

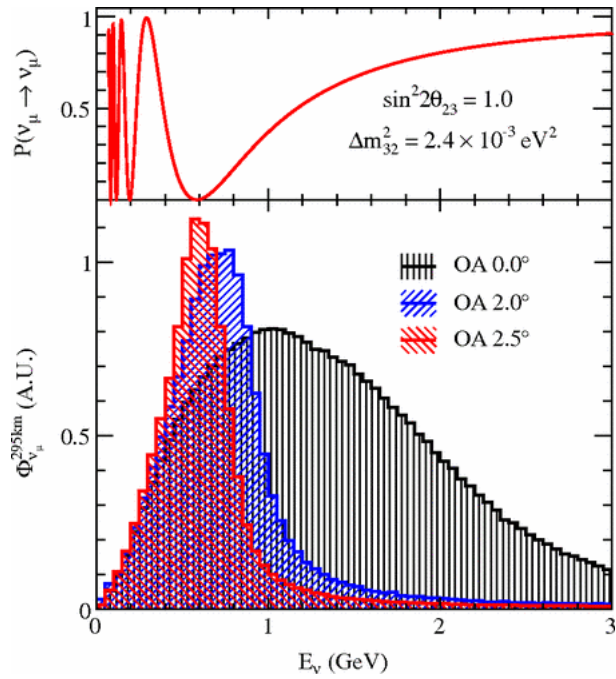


Figure 4.3: Predicted flux for different off-axis angles, and the muon neutrino survival probability at 295 km [18].

### 4.3 INGRID detector

The INGRID (Interactive Neutrino GRID) detector is based at the near-detector complex, and sits on the beam axis. It was designed primarily to measure the beam direction to high precision. To know the neutrino energy spectrum at the ND280 and at Super-K, it is required to know the off-axis angle to a precision better than 1 mrad, so the main goal of INGRID is to be able to measure the beam angle to this precision.

As the off-axis angle can have a large effect on where the beam flux peaks, the direction needs to be tracked as a function of time, so INGRID has a large target mass in order to achieve an event rate high enough to monitor the beam direction on a day-to-day basis.

INGRID consists of a set of identical modules arranged in a cross, with 7 modules forming a vertical column and another 7 modules forming a horizontal row. Two more modules are placed on a diagonal, to test for any asymmetries in azimuthal angle.

The INGRID modules are made up of alternating layers of iron and plastic scintillator bars for tracking. The plastic scintillator layers consist of a plane of horizontal bars and a plane of vertical bars, with each plane containing 24 bars. The dimensions of the scintillator bars are 5 cm  $\times$  1 cm  $\times$  1.2 m, and the iron layers are 6.5cm thick. There are also veto planes on the external faces, and the faces in between adjacent modules to track external particles, and particles that cross several modules.

An additional module, called the proton module, is added at the centre of the INGRID cross, between the vertical and horizontal module groups. The thick iron plates in the main INGRID module makes identifying protons impossible, as they very rarely have enough momentum to traverse more than one layer. The proton module has only scintillator, allowing protons to travel further, and in addition the central region is more finely grained, allowing finer tracking of particles. This additional module helps to separate CCQE events from other CC events as the outgoing protons can be tracked in the finely grained scintillator. A more complete description of the INGRID detector can be found in [80].

### 4.4 ND280

It is common for the design of a neutrino oscillation experiment to incorporate identical (or as close as feasible) near- and far-detectors. This allows effective cancellation

of some systematic uncertainties in an oscillation analysis. For T2K, it was decided to use very different detector designs. ND280, the off-axis near detector, has been designed to be able to make detailed measurements of the flux, and cross-sections for different processes important to T2K. ND280 sits at the same off-axis angle as Super-Kamiokande.

At the upstream end of ND280 is a detector optimised for the detection of neutral pions, known as the P0D (pi-zero detector), downstream of this is a tracking region, comprised of alternating scintillator target modules, and gas TPC (time-projection chamber) modules. Surrounding the P0D and tracker regions are ECals (electromagnetic calorimeters) which can be used for complementary particle identification, and to force the conversion of photons. Finally, the entire detector is enclosed in a 0.2 T magnet, refurbished after its use in the UA1 and NOMAD experiments. This magnet is instrumented with scintillating bars to track muons leaving the detector.

A schematic of the arrangement of detectors inside the magnet is shown in figure 4.4, and a photograph of the assembled detector is shown in figure 4.5.

It is worth defining the ND280 coordinate system here. The  $z$ -axis is approximately parallel to the beam direction, though it is aligned along the centre of the tracker (whereas the beam direction points slightly downwards). Positive  $z$  is more downstream, further from the target. Then the  $x$ -axis is horizontal and the  $y$ -axis is vertical, both roughly perpendicular to the neutrino beam direction. This coordinate system is right handed, with positive  $y$  upwards. This means the magnetic field lines lie along the  $x$ -axis, such that particles curve in the  $y - z$  plane (negative particles curve downwards and positive particles curve upwards, assuming they were originally propagating in the  $z$ -direction).

#### 4.4.1 P0D

The  $\pi^0$  detector, or P0D, was designed to measure the production of neutral pions, which are known to be a major background to an electron neutrino appearance signal at the far detector, but have very large cross-section uncertainties at T2K energies. The P0D uses plastic scintillator bars, read out through optical fibres to multi-pixel photon counters (MPPC) at each end. In contrast to the other scintillator-based detectors in ND280, the P0D is based around triangular bars, which are stacked to form flat layers. These layers are then arranged in  $x - y$  pairs, alternating with water bags, which can be drained, such that data can be taken in “water-in” and “water-out” modes (also known as water and air configurations), to extract event rates on water.

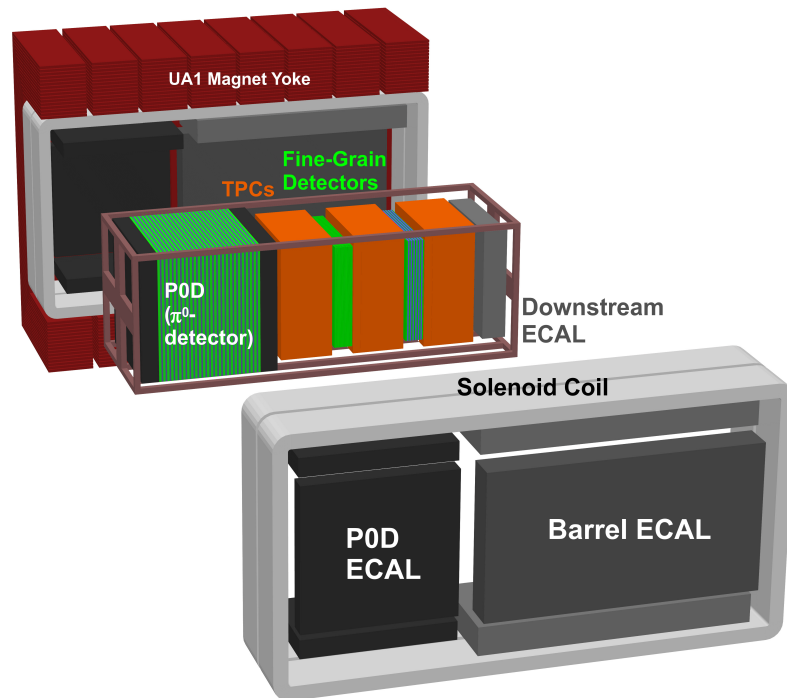


Figure 4.4: Exploded schematic showing the arrangement of subdetectors inside ND280. Taken from [81].



Figure 4.5: Photograph of the ND280 detector before closing the magnet. Several ECAL modules were missing at this point. Taken from [79].

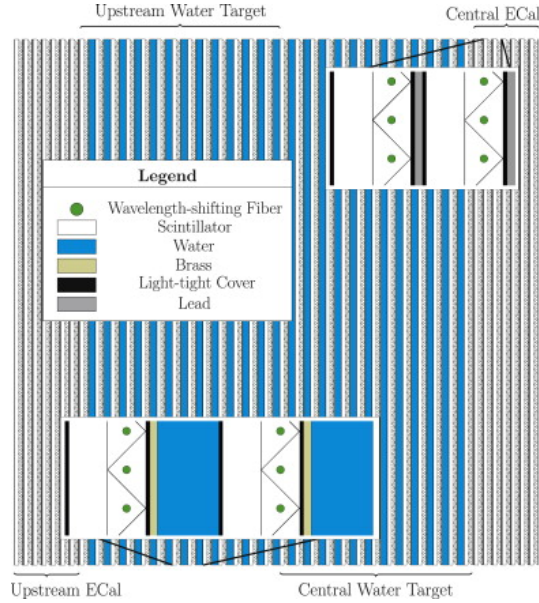


Figure 4.6: Schematic of the active region of the P0D. The triangular bars and alternating water/scintillator layers are clearly seen. Taken from [76].

Between each pair of scintillator layers, and the next water layer, there is a thin sheet of brass to help increase the rate of photon conversion. The most upstream and most downstream eight layers have no water bags between them, but instead have thin lead layers to catch unconverted photons. These sections are known as the upstream ECal and central ECal, though they are considered part of the P0D subdetector, rather than part of the ECal subdetector. Figure 4.6 shows a schematic of the active region of the P0D.

As will be mentioned later, the P0D is surrounded by simple ECal modules, which are designed to be able to detect high-angle particles, and distinguish muons from photons in the angular region where the P0D is less effective due to the bar geometry. For a complete description of the P0D, see [82].

#### 4.4.2 Tracker

The section immediately downstream from the P0D is known as the tracker, and is made up of the two Fine Grained Detectors (FGDs) sandwiched between the three TPCs. The tracker region was designed primarily to measure charged particles from both  $\nu_\mu$  and  $\nu_e$  charged current interactions (predominantly CCQE) to constrain the flux and cross-sections. The design comes from compromising event rate for fine tracking. The FGDs provide a suitable large target mass whilst the TPCs can provide precise momentum measurements from curvature, and PID from  $dE/dx$

measurements.

#### 4.4.2.1 FGDs

ND280 contains two FGD modules. Both FGD modules use plastic scintillator bars, read out with wavelength shifting fibres to an MPPC on one end (the other end is mirrored to maximise light yield). FGD1 is constructed from entirely plastic scintillator bars, whereas FGD2 contains alternating layers of active plastic scintillator and passive water target.

FGD1 consists of 30 layers, each containing 192 scintillator bars. Each layer contains bars oriented perpendicular to the layers either side of it, in either the  $x$  or  $y$  direction. In FGD2, there are only 14 layers, and these are grouped into 7  $x - y$  pairs, separated by water target. The scintillator bars all have a  $9.6 \text{ mm} \times 9.6 \text{ mm}$  cross section, and are 186 cm long.

The overall dimensions of the two FGDs is identical, which is intended to allow for a subtraction of the rate on plastic leading to a measurement of the pure water interaction rate, although it is sometimes possible to make these measurements using FGD2 alone. For a full description of the FGDs, refer to [83].

#### 4.4.2.2 TPCs

The three TPCs form a “sandwich” with the two FGDs, to provide precise tracking, momentum measurements and charge identification from the magnetic field, and PID from  $dE/dx$  (energy loss) measurements. All three TPCs are constructed identically, and filled with mostly argon gas, with roughly 5% mixture of other gases. Table 4.1 lists the relative amounts of different gases in the TPCs. This mixture was selected as it achieved a high drift velocity, and low diffusion [84]. An electric field is formed in the  $x$ -direction (the same direction as the magnetic field) between a central cathode and the Micromegas read-out pads. 3D reconstruction is possible in the TPCs using the information from the time of hits giving the co-ordinate in the drift direction.

A schematic showing the TPC design is shown in figure 4.7, and a full description of the TPCs is given in [84]. The spatial resolution of a TPC track is better than 1 mm except for at very short drift distances ( $<100 \text{ mm}$ ) where the spatial resolution gets as high as 1.2 mm. This allows the momentum resolution to be kept better than  $0.1 p_{\perp} / (\text{GeV}/c)$ .

Compound	fraction
$^{40}\text{Ar}$	95%
$\text{CF}_4$	3%
$\text{iC}_4\text{H}_{10}$	2%
$\text{O}_2$	<10ppm
$\text{H}_2\text{O}$	<100ppm
$\text{CO}_2$	<100ppm

Table 4.1: Relative fractions of gases in the TPC detectors.

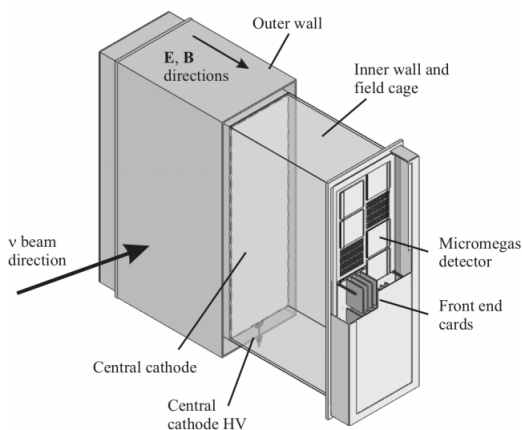


Figure 4.7: Schematic showing the design of the three TPCs. Taken from [85].

### 4.4.3 ECals

13 ECal modules surround the P0D and tracker region. There are three distinct sections to the ECal – the tracker region is wrapped by the barrel ECal (6 modules), with the downstream ECal (1 module) placed at the most downstream end, and the P0D ECal (6 modules) which surrounds the P0D. All the modules are attached to the inside of the magnet, except for the downstream ECal which is held within the basket with the P0D, FGDs and TPCs. The ECals are all constructed from alternating layers of plastic scintillator bars and lead. The scintillator bars are all 4 cm wide, and 1 cm thick, but there is variation in the bar length, lead thickness, and other variables depending on the bars location. This is due to the detector geometry requiring differences in the module shape and size. Table 4.2 contains the details of the scintillator bar sizes and lead thicknesses for the different ECal modules. In the tracker ECals and downstream ECal, the scintillator bars alternate direction, allowing 3D tracking of particles, however in the P0D ECal the bars are all oriented in the same direction to simplify construction. In testbeam measurements

Module	View	Layers	Bars/Layer	Bar Length/m	read out	Lead/mm
Downstream	XZ	17	50	2.00	double	1.7
	YZ	17	50	2.00	double	1.7
Barrel top	ZY	16	96	1.52	single	1.7
	XY	15	38	3.84	double	1.7
Barrel side	ZX	16	96	2.28	single	1.7
	YX	15	57	3.84	double	1.7
Barrel bottom	ZY	16	96	1.52	single	1.7
	XY	15	38	3.84	double	1.7
P0D top	XY	6	38	2.34	single	4.0
P0D side	XY	6	69	2.34	single	4.0
P0D bottom	XY	6	38	2.34	single	4.0

Table 4.2: Table of differing details between ECal modules

the energy resolution was found to be roughly 10% at 1GeV, which is slightly larger than the predicted resolution from monte carlo simulations [86]. For a complete description of the ECal modules, see [86].

#### 4.4.4 SMRD

The ND280 magnet return yoke was instrumented with plastic scintillator modules. These are collectively known as the SMRD (side muon range detector).

The SMRD is used for the ND280 cosmic trigger, as well as being useful to use as a veto for particles coming from neutrino interactions in the magnet. It may also be used to measure the momentum of muons originating in the basket, by measuring their range.

Each module is constructed from either four 167 mm wide bars (horizontal), or five 175 mm wide bars (vertical), all of the bars being 875 mm long and 7 mm thick. Modules are then placed in the gaps in the iron return yokes, a total of 192 horizontal and 248 vertical modules were installed. Most areas of the magnet was instrumented with three layers of modules, although the three downstream-most yoke segments contain 4, 6, and 6 layers on the sides, as there is a higher rate of particles crossing these layers from the tracker, and these particles are generally at a higher energy.

The scintillator bars each have a curved groove in the surface, into which a wavelength shifting fibre is placed. This fibre is read out with MPPCs at both ends to collect as much of the light as possible.

A photograph of one SMRD bar is shown in figure 4.8, and a more complete description of the SMRD design and operation is given in [87].

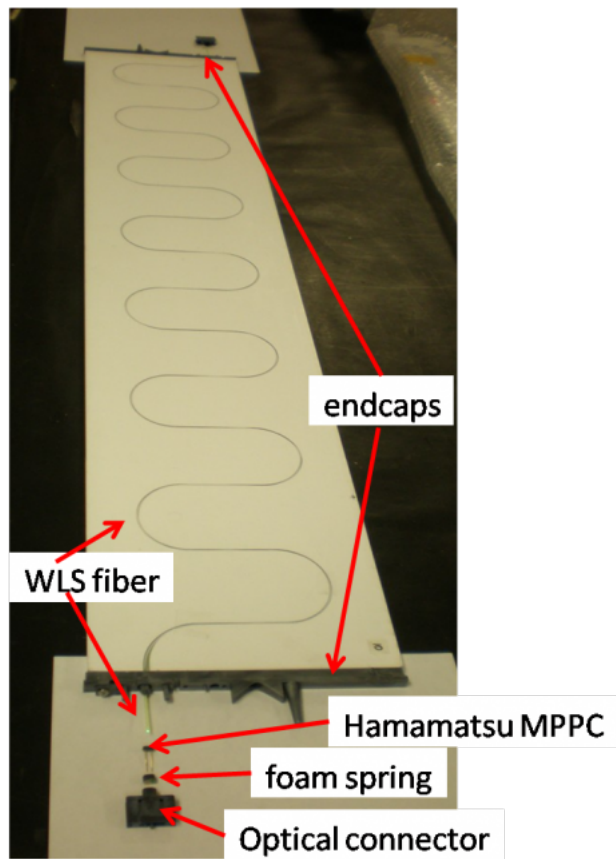


Figure 4.8: Photograph of an SMRD bar, showing the curved groove containing the wavelength-shifting fibre. Taken from [79].

## 4.5 Super-Kamiokande

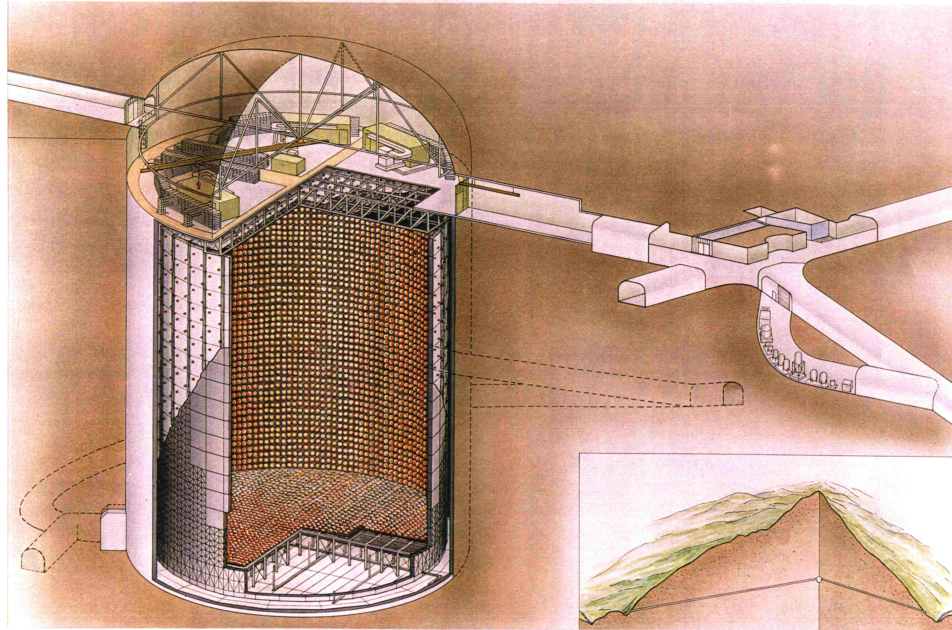
Super-K, originally an upgrade for Kamioka-NDE (Kamioka nucleon decay experiment), is perhaps the most famous detector in neutrino physics. Having made significant contributions to the establishment of the phenomenon of neutrino oscillations in the late 1990s and early 2000s, through measurements of both atmospheric and solar neutrinos, it has already been utilised as the far detector for the K2K [19] experiment, and is now being used again as the far detector for T2K.

Super-K is 295 km from the beam target, in the Kamioka mine in the Japan Alps, and lies  $2.5^\circ$  off the beam axis, the same angle as ND280. It consists of a large cylindrical tank of highly pure water, 39 m in diameter, and 41 m tall. This is separated into an inner and outer detector by a steel wall, 2 m from the edge of the detector. The outer detector is present to act as a veto for particles entering the detector from the rock outside.

Both regions of the detector are instrumented with vacuum photomultiplier tubes (PMT), the inner detector has 40% coverage from 11129 large (50 cm diameter) PMTs, and the outer detector has 1885 smaller (20 cm diameter) PMTs, giving it significantly less coverage than the inner detector. Figure 4.9 shows a schematic of the detector layout inside the mine.

Super-K derives its ability to detect particles from the Cherenkov radiation given off by particles travelling faster than the speed of light in water. This radiation is detected as rings of light by the photomultiplier tubes. The inner edge of the ring corresponds to where the particle's momentum fell below Cherenkov threshold, such that an exiting particle will show up as a completely filled in circle.

Particle ID can be performed by noting that electrons will shower, however muons, due to their larger mass, will travel largely in straight lines, with minimal interactions with the water and no bremsstrahlung. Because of this difference, muons lead to very sharp Cherenkov rings, whereas those from electrons have a more “fuzzy” appearance. Unfortunately, Super-K has some obvious limitations. Firstly, there is no magnetic field, so charge identification cannot be done, and therefore it is not possible to tell whether an interaction came from a neutrino or an anti-neutrino. Also, showers from photons look identical to showers from electrons, which is why NC  $\pi^0$  interactions can form an important background to  $\nu_e$  appearance measurements.



SUPERKAMIOKANDE (c) Kamioka Observatory, ICRR(Institute for Cosmic Ray Research), The University of Tokyo  
 INSTITUTE FOR COSMIC RAY RESEARCH UNIVERSITY OF TOKYO NIKKEN SEKKI

Figure 4.9: Schematic of Super-Kamiokande and its location inside the Mozumi mine. Taken from [88].

### 4.6 NA61/SHINE

The NA61 experiment (also known as SHINE) is a hadron production experiment based at the CERN SPS. One major goal of NA61 is to reduce the uncertainties in the T2K flux prediction, so a proton beam of the same energy as T2K (30 GeV) is extracted from the SPS and is directed at a carbon graphite target. Data is taken on two targets - a thin (2 cm) target intended to measure only the primary proton interactions, and a replica of the T2K target which is much thicker which therefore involves secondary and tertiary interactions of the produced particles.

Currently only the thin target data from 2007 [89, 90] is fully analysed and incorporated into the T2K flux simulation. This data includes over  $6 \times 10^5$  events. NA61 utilises two particle identification techniques – the first is  $dE/dx$  measurements in tracking TPCs immediately downstream of the target, and the second is time of flight (ToF) measurements using scintillator panels. The combination of these two PID methods allows good separation of the different particles produced between momenta of 0.2 GeV and 19 GeV. NA61 utilises magnets around the TPCs to accurately measure the momentum of each particle produced.

The pion momentum and angle spectra cover 90% of the phase space that

contributes to neutrino flux at SK, and the uncertainties are dominated by systematics. The kaon spectra, however, due to the lower production rate and difficulty in high-momentum identification, only cover 60% of the phase space required and the uncertainties are dominated by statistics.

In future it is expected that more recent high-statistics data sets will become available from both the thin target and replica target data. These newer data sets are also expected to expand the analysed phase space and consider additional rarer particle types such as  $K^-$ . This will have a large impact on the total flux uncertainty, which is currently dominated by these hadronic interaction uncertainties. An improved flux normalisation uncertainty is very important for neutrino cross section measurements (though not as crucial for an oscillation analysis where many flux uncertainties cancel).

## 4.7 Simulation

### 4.7.1 beam

The primary beam simulation is based on FLUKA, though the simulated events are reweighted to agree with data from NA61/SHINE (see section 4.6). The particles that exit the target are propagated and decayed by GEANT3, which propagates all resulting particles through the geometry of the horns, decay volume, and monitors. This simulation is used to predict the flux at the near detectors, the far detector, and also in the material upstream of the ND280 pit, the products of which can reach ND280 and be an additional source of background. This package is known collectively as JNUBEAM.

### 4.7.2 Near detectors

Both INGRID and ND280 take the incoming neutrinos from JNUBEAM, and pass them to either NEUT or GENIE (see section 3.5.1 for a discussion of interaction generators) to simulate neutrino interactions in the detector. After the initial interaction and nuclear final state interactions, GEANT4 is used to propagate particles through the detector geometries. A custom package, ELECSIM, then simulates the detector response to particles. For the scintillator-based detectors, this means simulating light in the scintillator bars and wavelength shifting (WLS) fibres, and the collection of this light by the MPPCs. For the TPCs, ELECSIM is responsible for simulating electrons drifting in the electric field. ELECSIM also simulates the response of the electronics that read out from each detector.

### 4.7.3 Super-K

Super-Kamiokande begins its simulation in a very similar way to the near detectors, using NEUT to simulate interactions based on neutrinos from the JNUBEAM simulation. After these interactions, a custom package, SKDETSIM, is used to propagate final-state particles, and simulate the response of the PMTs and electronics to the Cherenkov light given off.

## 4.8 Current results and future physics sensitivity

### 4.8.1 Latest results

After summer 2013, a total of 28 electron neutrino candidates had been seen at the far detector, compared to a predicted background of  $4.92 \pm 0.55$ . This corresponds to a  $7.8\sigma$  significance of electron neutrino appearance, the first observation of neutrino flavour appearance at over  $5\sigma$  significance. 120 candidate muon neutrino events were observed, compared with a no-oscillation prediction of 445, clear evidence for oscillations. This used  $6.57 \times 10^{20}$  POT of data.

Figures 4.10 and 4.11 show the event distributions as a function of neutrino energy for these two samples. The oscillation parameters derived from these data samples were discussed in section 2.4.1.3

During late 2013 and early 2014, maintenance was performed on the J-PARC accelerator systems, as well as the ND280 detector complex. T2K then began taking data again, this time with the focusing horns using the opposite polarity. Between April 2014 and December 2014, T2K collected  $1.796 \times 10^{20}$  POT in antineutrino-enhanced beam mode. This initial data will be used to compare neutrino disappearance rates with antineutrino disappearance rates.

Figure 4.12 shows the integrated POT and beam power as a function of time during all T2K run periods. The antineutrino-enhanced mode is shown in purple.

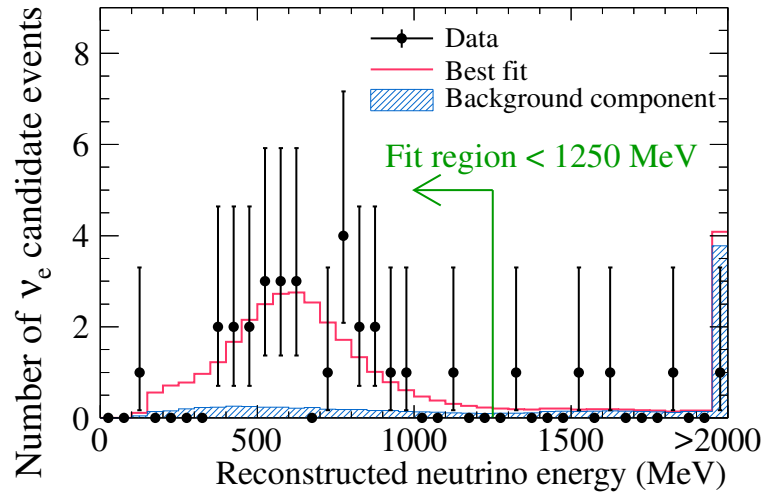


Figure 4.10: Electron neutrino event rate as a function of reconstructed neutrino energy, compared to the background-only prediction and the best-fit line assuming oscillations. Plot taken from [21].

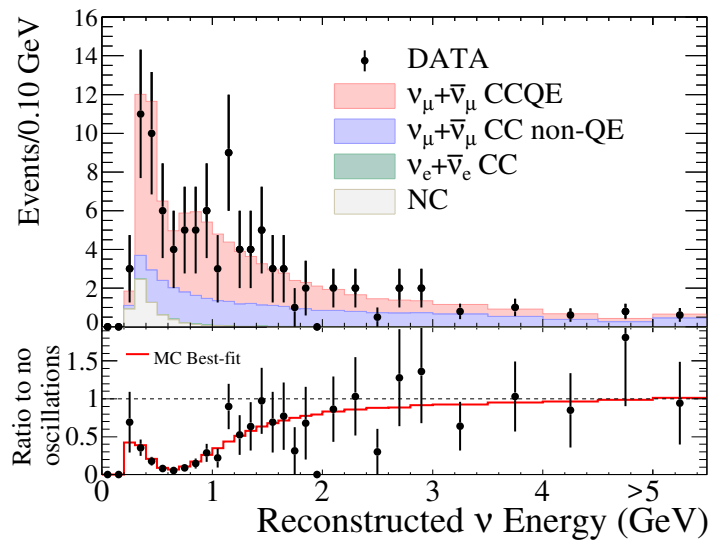


Figure 4.11: (top) Muon neutrino event rate as a function of reconstructed neutrino energy, compared to the best oscillation fit prediction, and (bottom) the ratio of this data to the no-oscillations prediction. Plot taken from [22].

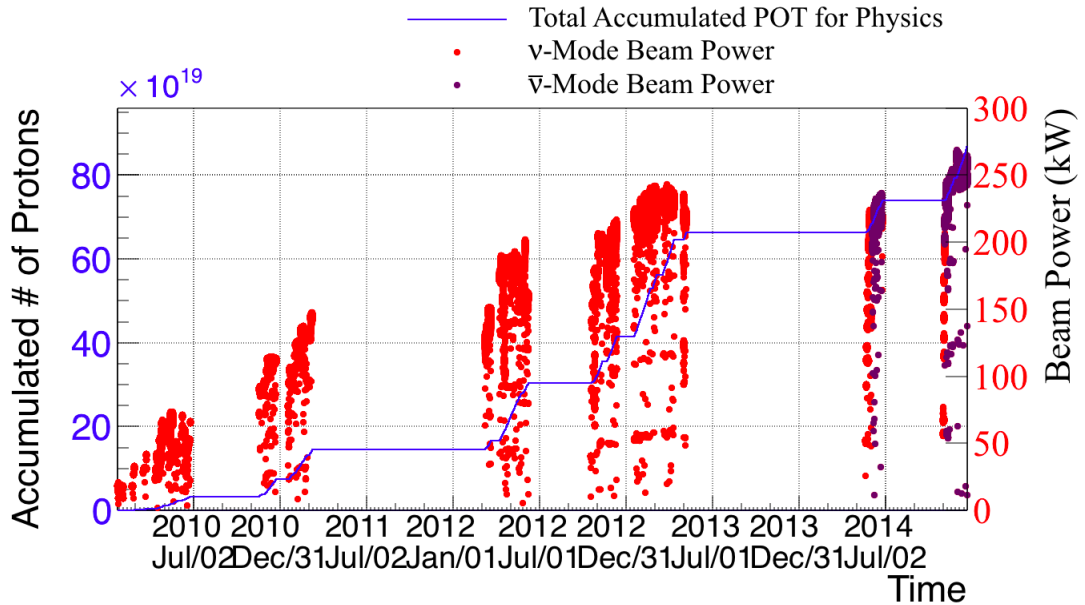


Figure 4.12: (blue line) Integrated POT against time for all T2K run periods, (red points) beam power when operating in neutrino mode, and (purple points) beam power when operating in antineutrino mode.

## 4.8.2 Future sensitivity

After the discovery of a surprisingly large value of  $\theta_{13}$ , internal studies were performed to see what sensitivity T2K can have to other parameters, such as the CP-violating phase, and mass hierarchy [91]. These studies considered different run plans, with different exposures of neutrinos and anti-neutrinos. They also considered what sensitivity might be achieved if the results from T2K were combined with those from NO $\nu$ A [23].

### 4.8.2.1 CP-violation

Using the value of  $\theta_{13}$  obtained by Daya Bay [33], it is possible to calculate the asymmetry:

$$A_{CP} = \frac{P(\nu_{\mu} \rightarrow \nu_e) - P(\bar{\nu}_{\mu} \rightarrow \bar{\nu}_e)}{P(\nu_{\mu} \rightarrow \nu_e) + P(\bar{\nu}_{\mu} \rightarrow \bar{\nu}_e)} \quad (4.2)$$

This asymmetry can be used to determine the value of  $\delta_{CP}$ , and can be as large as 25%. Unfortunately, antineutrinos come from negative meson decays, and the majority of mesons produced by a proton beam colliding with a graphite target are positive, due to the positive charge of the proton beam. This leads to a

lower flux of antineutrinos, and also a much higher wrong-sign background. Coupled with the 2 – 3 times lower interaction cross-sections experienced by antineutrinos, antineutrino data has to be taken for roughly 4 times as long to achieve the same statistical uncertainty, and is likely to have larger systematic errors.

The other way to measure  $\delta_{CP}$  is to utilise the second oscillation maximum. Figure 4.13 shows the  $\nu_\mu \rightarrow \nu_e$  oscillation probability as a function of distance for several values of  $\delta_{CP}$ , showing how much larger the effect of  $\delta_{CP}$  is at the second oscillation maximum. Unfortunately this would involve building a second detector at roughly 900km, which is not considered feasible (though originally a site in South Korea was considered for this purpose). The studies therefore focused on ways to combine neutrino and antineutrino data at Super-K for best sensitivity.

Figure 4.14 shows the expected 90% sensitivity contours for  $3.9 \times 10^{21}$  POT (half the total T2K expected data set) of neutrino mode running, the same for anti-neutrino mode running, and the contours that can be obtained by combining them to the full T2K expected data set. As the contours mirror each other, combining them leads to a large amount of phase space being disfavoured, and in this case, where true  $\delta_{CP} = -90^\circ$  roughly 50% of  $\delta_{CP}$  values are ruled out at over 90% confidence level. Adding a constraint from reactor measurements of anti-electron neutrino disappearance (figure 4.14c), can put an even more stringent constraint on the values of  $\theta_{13}$  and  $\delta_{CP}$ .

#### 4.8.2.2 Mass hierarchy

The matter effect (described in section 2.2.1) causes a neutrino-antineutrino asymmetry which can mimic that from genuinely CP-violating effects. This makes the job of determining either  $\delta_{CP}$  or the mass hierarchy difficult for a single experiment at a fixed baseline. However, because NO $\nu$ A is designed with a higher energy and longer baseline to T2K, combining the results may allow the effects to be disentangled (due to the size of the matter effect increasing roughly linearly with energy and baseline).

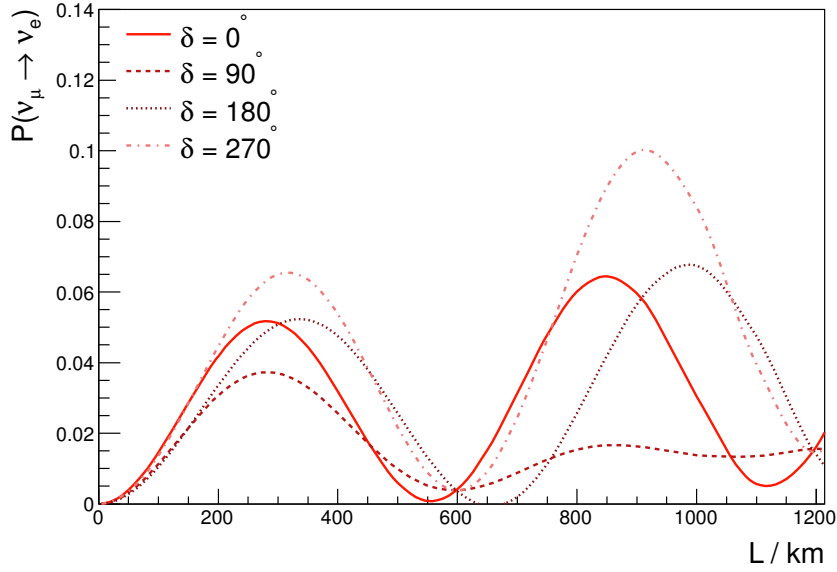
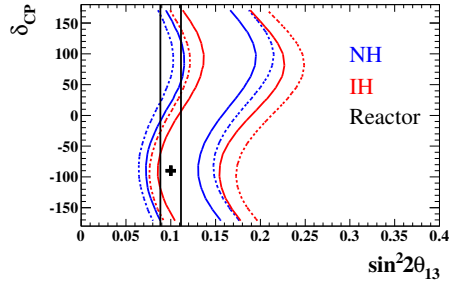
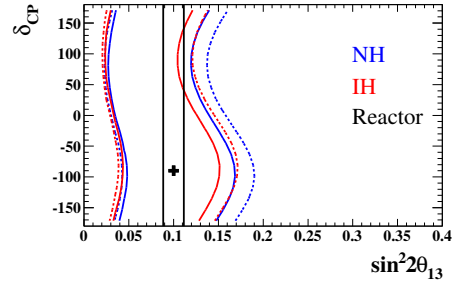


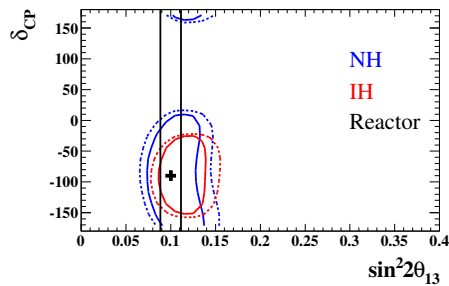
Figure 4.13:  $\nu_\mu \rightarrow \nu_e$  oscillation probabilities for a 600MeV neutrino beam, for several different values of  $\delta_{CP}$ , assuming  $\sin^2 2\theta_{13} = 0.1$ .



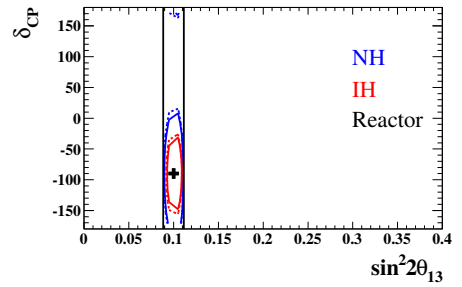
(a) 50%  $\nu$ -mode running only.



(b) 50%  $\bar{\nu}$ -mode running only.



(c) 50%  $\nu$ -mode, 50%  $\bar{\nu}$ -mode running.



(d) 50%  $\nu$ , 50%  $\bar{\nu}$  running, including a realistic future reactor constraint.

Figure 4.14: T2K expected final precision for  $\theta_{13}$  and  $\delta_{CP}$ , also when a reactor constraint is included. [92]

## Chapter 5

# The Spectral Function nuclear model in a neutrino interaction simulation

The dominant reaction mechanism at T2K beam energies is the quasi-elastic interaction. One reason for using the CCQE interaction as a signal at Super-K is that the two-body kinematics mean reconstructing the neutrino energy from just the muon kinematics should be simple and reliable. Assuming a stationary target neutron bound in a fixed potential, the neutrino energy can be reconstructed as

$$E_{\nu, QE} = \frac{M_p^2 - (M_n - E_b)^2 - m_\mu^2 + 2E_\mu(M_n - E_b)}{2(M_n - E_b - E_\mu + p_\mu \cos \theta_\mu)} \quad (5.1)$$

where  $M_p$  and  $M_n$  are the proton and neutron masses,  $m_\mu$  is the muon mass, and  $E_b$  is the nuclear binding energy. The only variables remaining are the muon kinematics  $p_\mu$  and  $\theta_\mu$ .

When dealing with nuclear matter, such as the carbon in ND280 or oxygen in Super-K, Fermi motion inside the nucleus leads to a smearing of the reconstructed energy. In an oscillation measurement, this smearing leads to events migrating into, and out of, the oscillation dip, changing the size and shape of the dip. Because of this it can affect measurements of the mixing parameters, so for precision measurements it is critical to understand this effect. Previously experiments all used a Relativistic Fermi Gas (RFG) model due to its simplicity, however there is strong evidence from electron scattering data that a better representation can be achieved using what is referred to as a ‘‘Spectral Function’’ (SF) model.

This chapter outlines the main differences between these models, describes

the implementation of the SF model in NEUT, and discusses the areas of both models where systematic uncertainties can arise.

## 5.1 The NEUT interaction generator

The NEUT interaction generator was originally written for the Kamiokande nucleon decay experiment, to predict the neutrino background to proton decay searches. It was adopted by the Super-K experiment, and in the years since has undergone progressive upgrades and extensions for use in the K2K and now also T2K long baseline neutrino oscillation experiments. NEUT is predominantly written in FORTRAN, though the systematics reweighting library and ND280 interfaces were written more recently in C++. NEUT is described in more detail in reference [53], however a summary of the important points is given here.

NEUT considers many different interactions, and has multiple options for many of them. The most important in the 100 MeV - few GeV energy range are listed below.

- **Quasi elastic scattering**

The standard Llewellyn-Smith formalism, as described in chapter 3, is adopted for CCQE events. For events on bound nucleons the nucleon is selected from the Fermi sea, the neutrino is boosted into that nucleons rest frame, and a  $Q^2$  value is selected based on the differential cross section. The particles are then boosted back into the lab frame, and Pauli blocking is applied. For neutral current elastic scattering the same formalism is adopted, however the total cross sections are estimated by assuming that the ratio to the charged current interactions is constant, using the following relations

$$\sigma(\nu_l p \rightarrow \nu_l p) = 0.153 \times \sigma(\nu_l n \rightarrow l^- p) \quad (5.2)$$

$$\sigma(\bar{\nu}_l p \rightarrow \bar{\nu}_l p) = 0.218 \times \sigma(\bar{\nu}_l p \rightarrow l^+ n) \quad (5.3)$$

$$\sigma(\nu_l n \rightarrow \nu_l n) = 1.5 \times \sigma(\nu_l p \rightarrow \nu_l p) \quad (5.4)$$

$$\sigma(\bar{\nu}_l n \rightarrow \bar{\nu}_l n) = 1.5 \times \sigma(\bar{\nu}_l p \rightarrow \bar{\nu}_l p) \quad (5.5)$$

Originally the RFG model was used, however this chapter details the addition of the SF model (for which the event generation algorithm was altered for efficiency reasons). Within the SF model, the neutral current scattering total cross sections are explicitly calculated rather than using constant ratio approximations.

- **Resonant pion production**

Pion production through a delta resonance is modelled with the Rein Sehgal model [52]. The NEUT implementation contains updates with respect to the original paper to include the effects of Pauli blocking and Fermi motion and, more recently, alternative form factors have been added as an option.

The same resonance model by Rein and Sehgal also predicts the production of kaons, photons, and eta mesons. These are considered to be separate interaction modes to resonant pion production, though the Rein Sehgal model is used for all resonant production of mesons.

In addition, 20% of delta resonances decay without producing a pion - a process known as pion-less delta decay.

- **Deep inelastic scattering**

For DIS, the total cross section is given [47] by the integral of

$$\frac{d^2\sigma}{dxdy} = \frac{G_F^2 M_N E_\nu}{\pi} \left[ (1 - y + \frac{1}{2}y^2 + C_1)F_2(x, q^2) \pm y(1 - \frac{1}{2}y + C_2)(xF_3(x, q^2)) \right], \quad (5.6)$$

with

$$C_1 = \frac{yM_l^2}{4M_N E_\nu x} - \frac{xyM_N}{2E_\nu} - \frac{M_l^2}{4E_\nu^2} - \frac{M_l^2}{2M_N E_\nu x} \quad (5.7)$$

$$C_2 = -\frac{M_q^2}{4M_N E_\nu x}, \quad (5.8)$$

where  $x$  and  $y$  are the normal Bjorken variables, and  $M_N$  and  $M_l$  are the nucleon and lepton mass. The nucleon structure functions,  $F_2$  and  $F_3$ , are taken from GRV94 [93]. To generate actual events, two regimes are considered. At high energies, the PYTHIA/JetSet [75] external libraries (which were written to simulate high-energy collider events) are used, however for hadronic invariant masses  $W < 2$  GeV/c PYTHIA does not describe the available data so NEUT has its own routines. These routines use KNO scaling [94] to determine the value of  $W$ , and the pion multiplicity is selected according to a fit to bubble chamber data.

The neutral current cross sections are approximated using functions fitted to data on the NC/CC cross section for DIS. These functions can be found in

[53].

- **Coherent pion production**

The model used for coherent pion production is the Rein Sehgal model [65] (a separate model to the resonance production model from the same authors), which is based on the hypothesis of partially conserved axial current (PCAC). This model relates the neutrino-nucleus cross section to the pion-nucleus cross section. There are also terms to account for absorption of the pion in the nucleus. This relies on data for the pion-nucleus cross section and pion, for which fits were given in the original Rein Sehgal paper. Though newer data is now available it is not included in the NEUT model.

- **Meson exchange currents**

None of the versions of NEUT used in this thesis contain an MEC model. However, for completeness it should be mentioned that in parallel to the work done here, the Nieves meson exchange current model [58] was implemented in NEUT. This model considers two-body currents, for charged current interactions leading to the ejection of two nucleons.

- **Final state interactions**

As NEUT can generate events on nuclei, the hadronic particles are transported through the nuclear medium, simulating FSI. The model that is used is known as a cascade model, which relies on stepping the particles through the nucleus and allowing them to interact according to the mean free path for each interaction type. This relies heavily on data from pion-nucleus and proton-nucleus scattering experiments to predict the probabilities for various interaction types. Figure 5.1 shows the NEUT inputs and the data it is tuned to, for various pion interaction cross sections. For pions the interactions considered are inelastic scattering, charge exchange (for example  $\pi^+ + n \rightarrow \pi^0 + p$ ), and absorption. For nucleons the interactions considered are elastic scattering, and production of either one or two delta resonances.

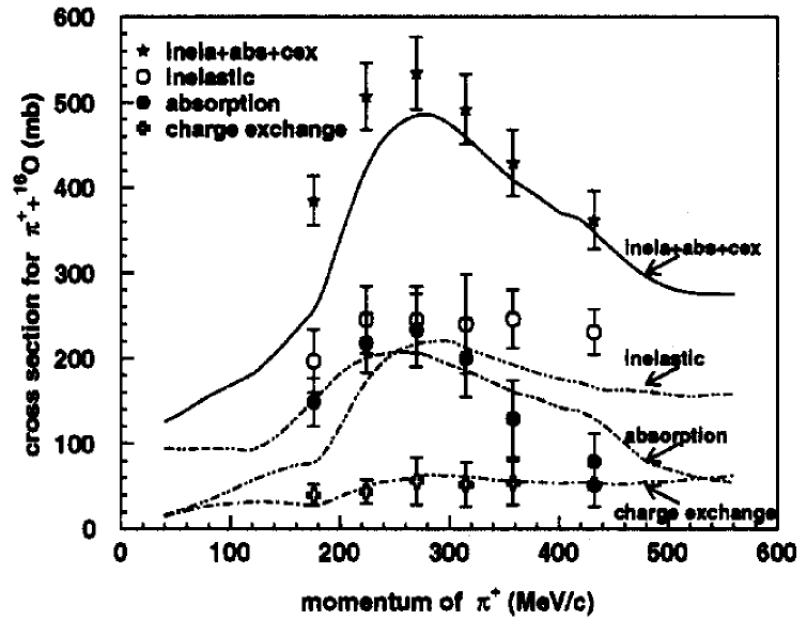


Figure 5.1: Pion-oxygen cross sections for various processes, compared to the predictions which are used as an input to the NEUT FSI model. Plot taken from [53].

## 5.2 Nuclear models

### 5.2.1 Relativistic Fermi Gas

The RFG model is a simple model which is commonly applied to Fermionic physical systems. The assumption is that all particles are in a potential, and form plane-wave states, leading to all states being filled up to a Fermi-level, above which no states are filled. The Fermi-gas model has a flat distribution of states in momentum space (see figure 5.3), and a constant binding energy.

In neutrino-nucleus interactions, the RFG model allows for numerical integration over nucleon states, and as such makes analytical theoretical calculations possible. This model has been used in neutrino interaction generators for many years due to its simplicity.

### 5.2.2 Local Fermi Gas

The RFG could be described as a global Fermi gas model, meaning that the Fermi momentum and binding energy are considered a constant of the nucleus, and the momentum distribution is not location-dependent. In a Local Fermi Gas (LFG)

model, the same Fermi gas idea is applied, but variations in nuclear density are taken into account. This means the Fermi momentum depends on the location in the nucleus, leading to a smoothed momentum spectrum. The LFG model is not currently implemented in either of the generators used by T2K (NEUT and GENIE), however it has been implemented in NuWro. It will not be discussed further here.

### 5.2.3 Spectral Function

The discontinuity at the Fermi momentum in the RFG model is unlikely to be a realistic description of nature, so a more physically motivated model would be preferable. “Spectral function” is a generic term for a function that describes the momentum and energy distributions of initial nucleons in a nucleus (the RFG can be described by a spectral function very easily, as it is a simple step-function - see figure 5.3). Spectral functions have been calculated analytically for light nuclei ( $A \leq 4$ ) [95, 96, 97, 98], and for infinite nuclear matter [99, 100]. For medium-size nuclei, such as carbon and oxygen, various approximations need to be made, but spectral functions can still be built by combining information from electron scattering data with the theoretical calculations from uniform nuclear matter of different densities. The spectral functions used in NEUT were provided by O. Benhar [101].

The Spectral Function is made up of two different terms: a mean-field term for single particles, and a term from correlated pairs of nucleons. The correlation term leads to a very long tail in both momentum and binding energy, and accounts for roughly 20% of the total Spectral Function. These initial-state correlations lead to the ejection of a second nucleon (see section 5.7), however the interaction is only with one nucleon, and the kinematics are pure one-particle CCQE.

As the data used to tune the Spectral Functions are from  $e^- + p$  final states, the Spectral Functions describe the proton initial state. We approximate the neutron Spectral Function to be the same, and uncertainties discussed in section 5.8 are expected to cover any potential differences between them.

Figure 5.2 shows the oxygen Spectral Function, in which the nuclear shell model energy levels can be clearly seen along the energy axis (labelled as “removal energy”, also referred to as binding energy). These shell orbitals are part of the mean field term. The correlation term extends out to very high momenta and removal energies. Figure 5.3 shows the oxygen Spectral Function projected onto the momentum axis, with the equivalent distribution shown for the RFG model. The correlation term can be clearly seen extending out to very high momenta.

Figure 5.4 demonstrates how the Spectral Function better reproduces the QE peak in electron scattering, while also helping to fill in the “dip” region between the

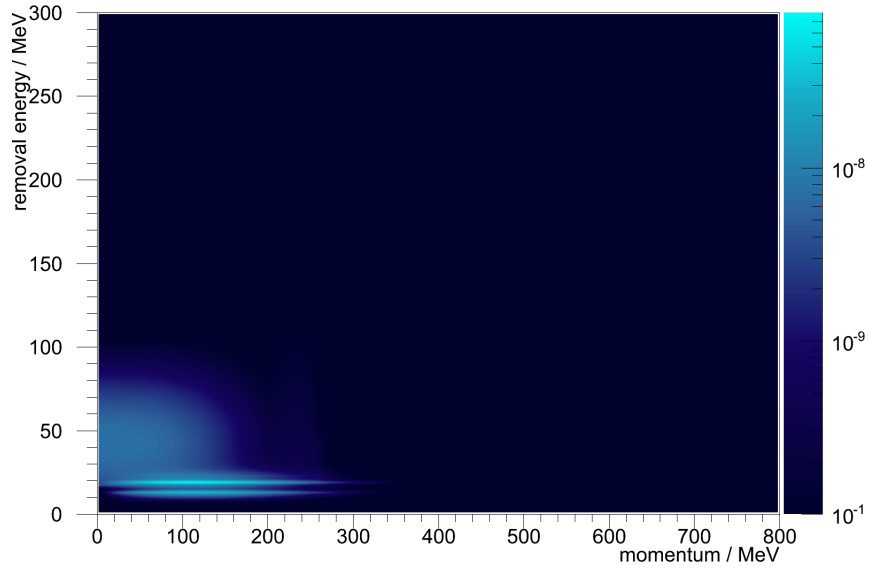


Figure 5.2: Benhars 2D Spectral Function for oxygen. The shell model orbitals are clearly seen as lobes along the removal energy axis.

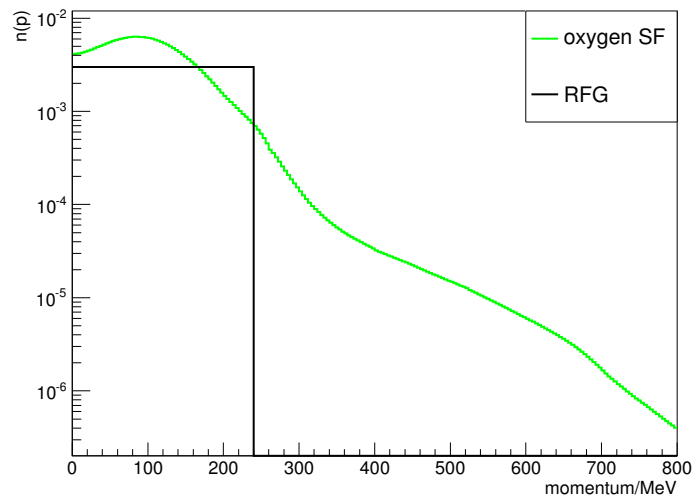


Figure 5.3: Spectral Function for oxygen projected onto the momentum axis. The black line corresponds to RFG with a Fermi momentum of 220 MeV, green is the spectral function calculated by Benhar [101].

QE peak and the  $\Delta$ -resonance. This dip is filled in primarily from the highly bound nucleons in the correlation term of the Spectral Function, with contributions from resonant pion production, as well as other non-resonant, and DIS backgrounds.

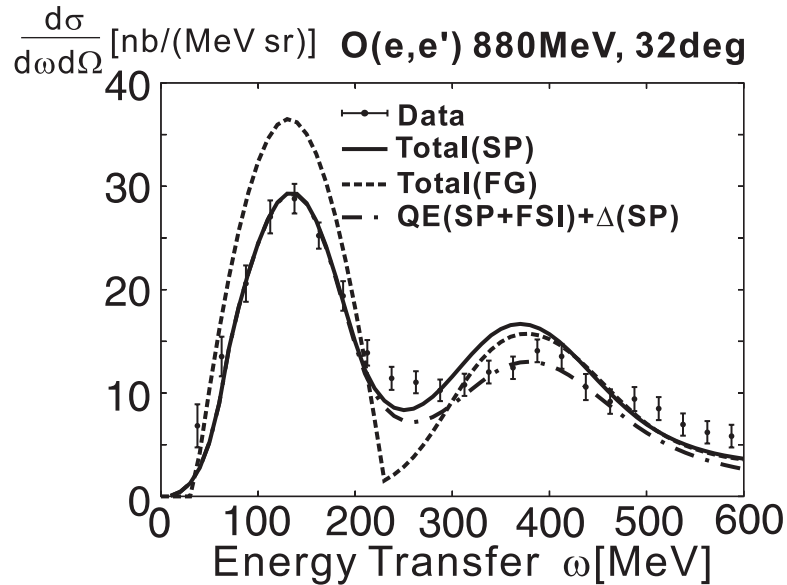


Figure 5.4: Example of electron scattering data on oxygen compared to both SF and RFG models [102]. “SP” in the legend corresponds to what this thesis refers to as “SF” and “FG” is a global relativistic Fermi gas (RFG) model.

#### 5.2.4 Pauli blocking

In both the RFG and LFG model, all states up to the Fermi level are filled, so particles can’t be ejected in momentum states lower than this level. This naturally leads to a phenomenon known as Pauli blocking which reduces the cross section by reducing the available phase space for the outgoing nucleon. This threshold momentum is commonly referred to as the Fermi momentum, or  $p_F$ .

In the SF model, Pauli blocking is still expected to occur, but it does not arise from the model as naturally. It is therefore common to use approximations when implementing these models in calculations or simulations. Often these approximations are as crude as applying a hard cut off at the value of the Fermi momentum that would be used if using the RFG model. More sophisticated options include applying Pauli blocking to a nucleon according to the probability that the state is filled, which is taken from the spectral function distribution itself. The differences to the total cross section and muon kinematics are minimal, so when the SF model was incorporated into NEUT a hard cut off approximation was used. The value of this cut off will be known as the Fermi momentum and denoted  $p_{SF}$  to distinguish it from that used in the RFG model.

### 5.3 Spectral Function implementation in NEUT

The implementation of the SF model inside NEUT was initially based on the implementation of the same model in NuWro [73, 74]. When implementing the model in a Monte Carlo-based generator, several issues must be taken into account. Firstly, the implementation has to be efficient and fast for it to be useful. In addition most details were kept as flexible as possible so it is fairly simple to adjust the model, for example if improved spectral function calculations become available.

Throughout this chapter we will use the same notation defined in chapter 3, particularly the variables defined in figure 3.1. Some additional variables will need to be defined. For convenience, the important kinematic variables used are listed here:

- neutrino:  $k^\mu = (E_\nu, \vec{k})$
- muon:  $k'^\mu = (E', \vec{k}')$
- final state nucleon:  $p'^\mu = (E_{\mathbf{p}'}, \vec{p}')$
- four-momentum transfer:  $q^\mu = k^\mu - k'^\mu$
- $E_{\mathbf{p}}$  is the energy that a free nucleon with momentum  $\vec{p}$  would have
- $\tilde{E}$  is the removal energy, defined in the following way:

$$\tilde{E} = M + \omega - E_{\mathbf{p}'} \quad (5.9)$$

where  $\omega$  is the energy component of  $k^\mu$ , and  $M$  is the mass of the struck nucleon. This definition assumes an infinitely heavy recoil nucleus. It can be thought of as the energy required to raise the nucleon out of the nuclear potential, and give it the same total energy as a stationary free nucleon.

The equation for the total cross section can be written completely generally as

$$\sigma = \int d^3p \int d\tilde{E} \int d^3k' \delta(\omega - M - \tilde{E} - E_{\mathbf{p}'}) L_{\mu\nu} H^{\mu\nu} \frac{G_F^2 \cos^2 \theta_C}{8\pi^2 E_\nu E' E_{\mathbf{p}'} E_{\mathbf{p}}} P(\tilde{E}, \vec{p}), \quad (5.10)$$

where  $G_F$  is the Fermi constant, and  $\theta_C$  is the Cabbibo mixing angle.  $L_{\mu\nu} H^{\mu\nu}$  is the contraction of the leptonic and hadronic tensors - the calculation of this is given

in A.2.  $P(\tilde{E}, \vec{p})$  is the spectral function. It has a probabilistic interpretation, and is normalised such that

$$\int d\tilde{E} \int d^3p P(\tilde{E}, \vec{p}) = N_{nucleons}. \quad (5.11)$$

In general, for a given neutrino, equation 5.10 can be integrated numerically by sampling the  $(\tilde{E}, \vec{p}, \vec{k}')$  space evenly and calculating the integrand (applying the required energy-momentum conservation), then taking the average of all the values obtained. Additionally, events can be generated by the same process, but using the selection/rejection method to pick events based on the weight calculated from the integrand of equation 5.10. This event generation requires knowledge of the maximum possible differential cross section, which it is possible to estimate when calculating the total cross section, as the entire phase space should be scanned. It is very unlikely we randomly selected the actual peak cross section at any point in the phase space scan, so our estimate will tend to be slightly too low. For this reason a ‘‘safety factor’’ can be included in this estimation, at the cost of some efficiency.

## 5.4 Efficiency improvements

At low energies in particular, the usual accept/reject method can become quite inefficient, as a large fraction of the calculated weights are rejected. A significant efficiency improvement can be achieved by generating events in the neutrino-nucleon centre-of-mass frame, as it becomes trivial to conserve energy and momentum. This was shown to be a big improvement when used in NuWro [73, 74].

With this change, the cross section formula becomes

$$\sigma = \int d^3p \int d\tilde{E} \int d^3k'_{CM} J_{CM} \delta(\omega - M - \tilde{E} - E_{\mathbf{p}'}) L_{\mu\nu} H^{\mu\nu} \frac{G_F^2 \cos^2 \theta_C}{8\pi^2 E_\nu E' E_{\mathbf{p}'} E_{\mathbf{p}}} P(\tilde{E}, \vec{p}), \quad (5.12)$$

where  $J_{CM}$  is the Jacobian to convert the lepton momentum integral from the lab frame to the centre-of-mass frame. The derivation of  $J_{CM}$  is given in A.1.

The algorithm actually implemented in NEUT then takes the following steps:

1. Select a neutrino based on pre-calculated tables of  $\sigma(E_\nu)$
2. Select a nucleon according to  $P(\tilde{E}, \vec{p})$ , using the rejection method
3. Calculate the centre-of-mass energy. This must be larger than the sum of the lepton and final hadron mass, the event is rejected otherwise.

4. Boost into the neutrino-nucleon centre-of-mass frame
5. Create the outgoing lepton and nucleon in a random direction
6. Boost final state particles back into lab frame
7. Apply Pauli blocking (if  $p' < pF_{SF}$ , reject the event)
8. Calculate  $q$  and  $\tilde{q} = (\tilde{\omega}, \vec{q})$ , where  $\tilde{\omega} = E_{p'} - E_p$
9. calculate weight from cross section formula (where  $L_{\mu\nu}H^{\mu\nu}$  is calculated using the reduced energy transfer,  $\tilde{\omega}$ )
10. Use rejection method again to decide whether event occurs or not based on this weight. If not, begin again from step 2.

## 5.5 Validity over nuclei

It is well known that the part of the spectral function from correlations has almost no dependence on the mass of the nucleus (in fact, the correlated part is calculated assuming infinite nuclear matter), however the mean-field part is expected to vary with both  $A$  and  $Z$ .

Published results were only available for  $^{12}\text{C}$ ,  $^{16}\text{O}$ , and  $^{56}\text{Fe}$ . As a first assumption, the neutron spectral functions were assumed to be the same as the proton spectral functions, though in the case of iron the normalisation is scaled. It was also assumed that other isotopes could be treated with the same same spectral functions, again scaled for the different number of nucleons. Given the size of the difference between the oxygen and carbon spectral functions, it is expected the dependence on the number of neutrons - and the difference between the proton and neutron spectral functions - is small enough that these approximations are valid, and uncertainties discussed later would be expected to cover any differences.

For other nuclei, NEUT falls back to the RFG model, as there is no known simple way to evaluate the spectral function for an arbitrary nucleus. It may be possible in future to approximate other targets by extrapolating from nearby elements for which there is a calculation, using methods like those discussed in [103]. Most other elements are not present in significant quantities, except for lead, which is a significantly larger nucleus than those for which calculations exist.

## 5.6 Verification

For verification of the code, comparisons were made with predictions from both the NuWro generator [73, 74] (in which the SF model was already implemented) and also theoretical calculations from O. Benhar [104]. A selection of the comparisons with NuWro is shown in figure 5.5. A selection of the comparisons with plots from O. Benhar is shown in figure 5.6.

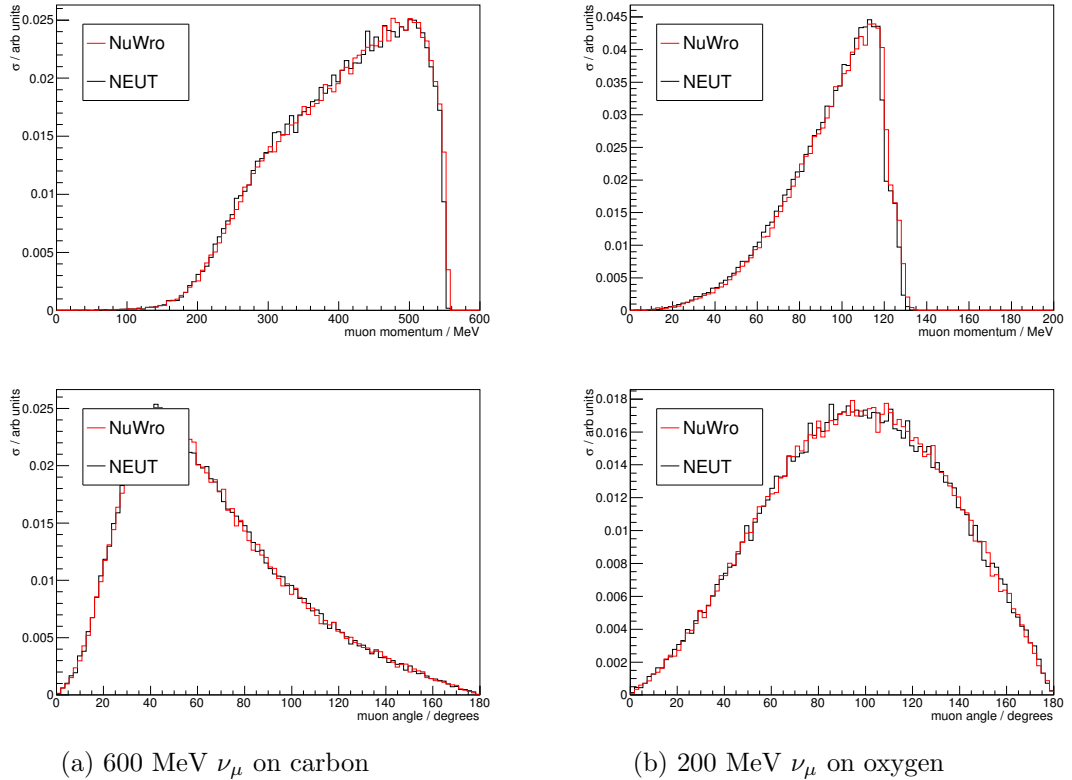
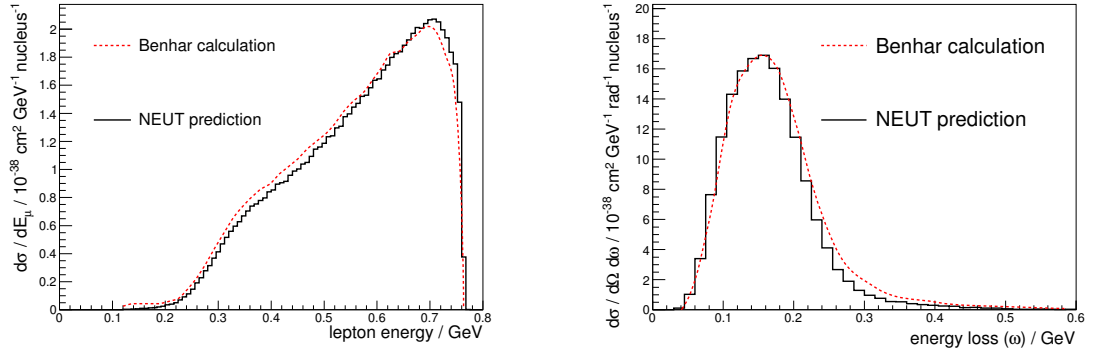


Figure 5.5: Momentum and angle distributions of outgoing leptons for NEUT and NuWro CCQE interactions for various initial states. Plots are normalised to unit area for a shape comparison.

The total cross section in NuWro is evaluated at run-time, so this was calculated at several fixed energies. In NEUT, total cross section tables are pre-computed, and provided in tables, which require interpolation.

Figure 5.7 shows a comparison of the CCQE cross section as a function of energy between NEUT and NuWro for  $\nu_\mu$  interactions on carbon nuclei, with the NEUT RFG cross section included too.

Figures 5.8 and 5.9 show ratios of the NuWro SF and NEUT RFG cross sections to NEUT SF, as a function of energy. NuWro uses analytical fits to the SF



(a) Cross section differential in outgoing lepton energy for an 800 MeV  $\nu_\mu$  beam on an  $^{16}\text{O}$  target. Benhar prediction taken from published plot in [104]. Conversion from image could lead to small differences.

(b) Cross section differential in energy loss for a 1 GeV  $\nu_e$  beam on an  $^{16}\text{O}$  target, at  $30^\circ$ . NEUT events are taken from a  $4^\circ$  window centred on  $30^\circ$ . Benhar prediction taken from published plot in [104].

Figure 5.6

momentum distribution, whereas NEUT simply interpolates between points on the tables provided, so some differences can be seen, particularly near the threshold for interactions.

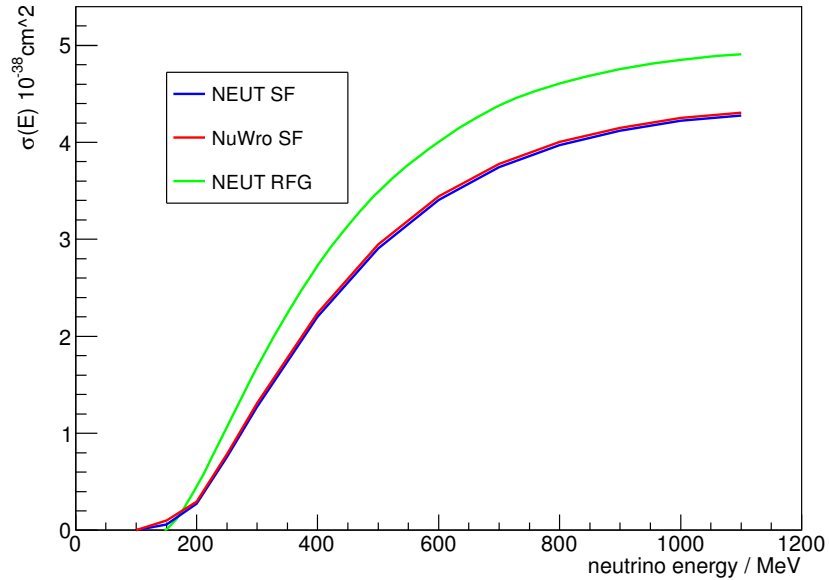


Figure 5.7: CCQE cross section as a function of energy for  $\nu_\mu$  CCQE interactions on carbon-12, for NEUT SF, NuWro SF, and NEUT RFG.

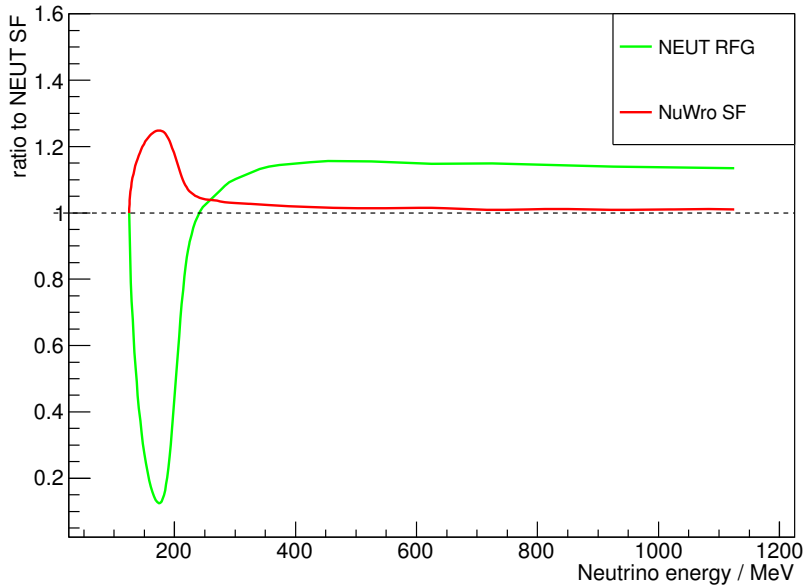


Figure 5.8: Ratio of different generators to NEUT SF cross section for  $\nu_\mu$  CCQE interactions on carbon, as a function of energy. Large differences can be seen near the threshold, but beyond 200 MeV, NEUT and NuWro agree very well. The SF model consistently predicts a lower total cross section than the RFG model.

## 5.7 Multi-nucleon ejection model

As discussed in section 5.2.3, the spectral function contains two terms. The correlation term is comes from correlated pairs of nucleons which are excited out of the Fermi sea, and can have very large momenta. To remain bound in the nucleus, these high momentum nucleons must have large binding energies.

As the spectral function is used to describe CCQE interactions, the neutrino still only interacts with one of the nucleons (unlike in meson exchange current models which are interactions with pairs of nucleons). The “second” nucleon, a spectator in this interaction, will be in an excited state. The correlation between the two nucleons was keeping the spectator nucleon in the nucleus, but after the first has been knocked out, this correlation no longer exists and the spectator nucleon is also ejected from the nucleus.

To get an estimate for the kinematics of this second nucleon, a brief argument can be made in terms of momentum conservation. As the initial nucleons in the correlated tail tend to have high momenta, to retain a nucleus which is stationary overall, the momentum of the second nucleon must be roughly opposite to the first.

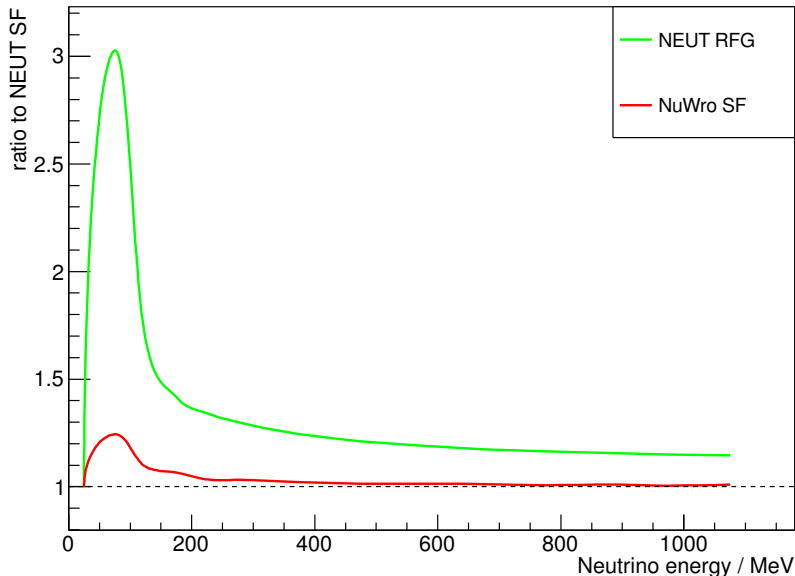


Figure 5.9: Ratio of different generators to NEUT SF cross section for  $\nu_e$  CCQE interactions on carbon, as a function of energy. NEUT and NuWro agree very well, and the threshold effects seen in  $\nu_\mu$  interactions is not present. The SF model consistently predicts a lower total cross section than the RFG model.

As a first approximation, this is taken to be exactly equal and opposite (some smearing would be expected, though it is not clear how much. The effects of FSI are expected to smear the outgoing particle kinematics such that it is unlikely that this approximation makes a significant difference).

A method to determine which events to add an extra nucleon to is required. In order to do this it must be evaluated, for a given event, whether the initial nucleon was in the correlated tail or not. Fortunately the mean-field and correlated parts of the spectral function occupy largely different regions in  $(p, \tilde{E})$  space.

As can be seen in Figure 5.10, above about 300 MeV in momentum, the spectral function is almost entirely from the correlation term, and outside of this region, the correlation term makes up a very small part of the total spectral function. In a similar manner, above about 100 MeV in binding energy the function consists almost entirely of correlation term.

The separation was made by approximating the mean-field part to be everything with  $p < 300$  MeV and  $\tilde{E} < 100$  MeV. Everything outside of this region is assumed to be from the correlation term, and would have an additional nucleon outgoing.

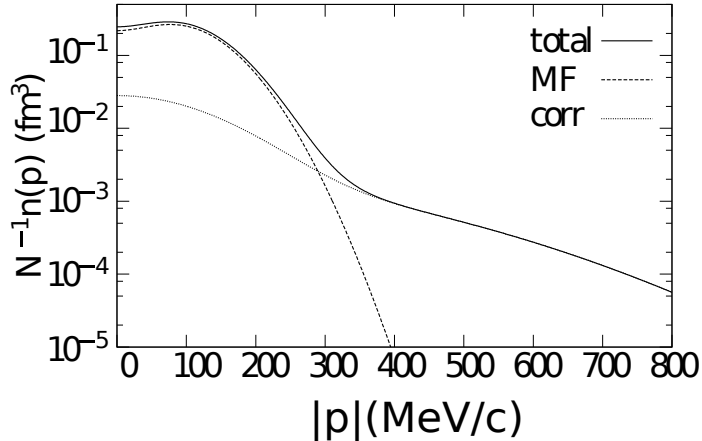


Figure 5.10: Momentum distributions of nucleons in oxygen. The mean-field and correlation terms are shown separately, the solid curve represents their sum.  $N$  is the number of nucleons, and the y-axis is scaled by  $N^{-1}$  so that the total integral is unity. Taken from [105].

As an example of what this model predicts for hadron kinematics, a small sample of CCQE events were generated on carbon using a 600 MeV  $\nu_\mu$  beam. Figure 5.11 shows the pre-FSI spectrum of these nucleon pairs, split either into high/low momentum, or struck/spectator nucleon. Figure 5.12 shows the post-FSI spectrum for the leading (highest momentum) proton, and also all escaping protons.

## 5.8 Systematic uncertainties within the SF model

All T2K analyses have to estimate the effects of systematic uncertainties, many of which are common between analyses. Because of this, T2K have developed a general-purpose reweighting package, T2KReWeight, which calculates weights for events and can be used to predict the effect of changing a parameter in Monte Carlo. This means that one nominal MC can be used to give the predictions for any parameter set, without having to generate MC with several different parameter sets. If the SF model is to be used, associated uncertainties need to be identified, and reweighting methods for these need to be added to T2KReWeight.

Previously the difference between the RFG and SF predictions was used as an uncertainty on the nuclear model. There were also uncertainties applied to the parameters of the Fermi gas model, namely the Fermi momentum and binding energy can be varied. The approach of using the difference between two nuclear models as a systematic caused difficulties when considering fits to T2K near detector data to propagate to the far detector. Crucially many fitting routines require smooth

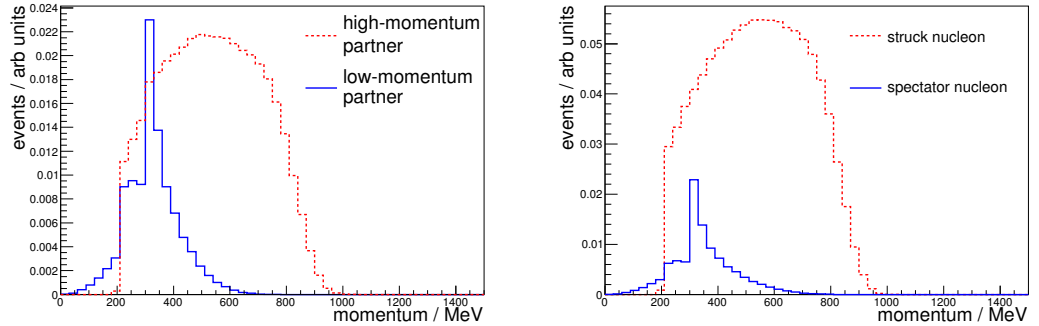


Figure 5.11: Nucleon momenta before final-state interactions. In the high/low separation, only nucleons from the correlated tail are plotted, however for the struck/spectator separation all struck nucleons are included (however the spectators have to come from the correlated tail). The sharp cut-offs seen at 300 MeV are due to the imperfect separation of the mean-field and correlated terms using kinematics, and those at 200 MeV are due to Pauli blocking.

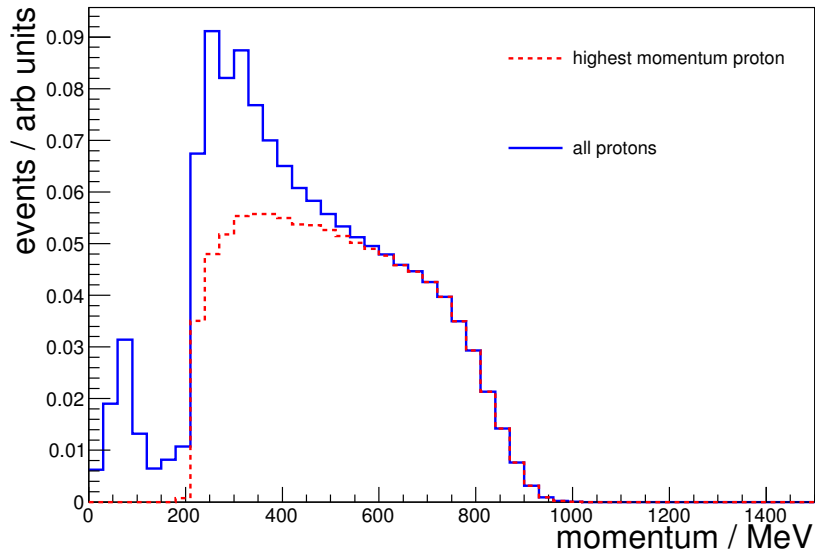


Figure 5.12: Nucleon momenta after the effects of FSI. Shown are the leading (highest momentum) proton, and also the spectrum obtained when considering all ejected protons. The sharp change at 200 MeV is due to Pauli blocking.

differentials, so interpolation between the RFG and SF predictions was allowed. This led to fits being allowed to fit halfway between the RFG and SF predictions, which was considered poorly physically motivated and difficult to interpret. In addition, there were occasionally problems with the parameter being bounded. To improve

on this situation, appropriate uncertainties in the SF model should be identified and evaluated.

Consideration of O. Benhar’s paper [101] lead to the selection of three physics-motivated parameters which could be changed to alter the cross section within the SF model. In this section we will discuss the three parameters, determine the effect of each on the cross section, and determine how much each could be varied without ruining the agreement with electron scattering data. The three parameters are:

1. The relative normalisation of the mean-field and correlation terms in  $P(\tilde{E}, p)$
2. The width of the mean-field momentum peak
3. The value of the Fermi momentum used for Pauli blocking

Reducing the size of the correlation term should make the cross section appear closer to the prediction from Fermi gas-based models, which do not have a high-momentum correlated tail. This also reduces the fraction of events which have additional ejected nucleons. Varying the width of the mean-field peak and varying the Pauli blocking parameter are analogous to varying the Fermi momentum in the RFG model except, in the SF model the two effects can be varied independently whereas in the RFG model Pauli blocking and the width of the initial momentum spectrum are intrinsically linked.

All of these parameters can be varied within the confines of the model while maintaining reasonable agreement with electron scattering data (agreement with a QE peak is kept to within 10%). The mean-field width and the relative normalisation between the two terms are determined largely by electron scattering fits, which have uncertainties. Applying uncertainties to the Pauli blocking parameter,  $pF_{SF}$ , seems reasonable as the implementation of Pauli blocking as a hard cut off does not arise naturally from the model so is expected to be only an approximation.

### 5.8.1 Relative normalisation

As shown in Equation 5.12, the cross section for each event is proportional to  $P(p, \tilde{E})$ . Therefore given a new spectral function,  $P'(p, \tilde{E})$ , the ratio  $P'(p, \tilde{E})/P(p, \tilde{E})$  defines the weight required to reweight events generated with the original spectral function, to be equivalent to events generated with the new spectral function. This does assume that this effect is decoupled from Pauli blocking, and therefore won’t affect the distribution of outgoing nucleons. This is an approximation, but it is shown in Section 5.8.4 that it works fairly well. It should be noted that the spectral

functions must both be normalised such that

$$\int d^3p d\tilde{E} P(p, \tilde{E}) = \int d^3p d\tilde{E} P'(p, \tilde{E}) = N_{Nucleons}. \quad (5.13)$$

As discussed in section 5.7, the correlation tail is largely confined to high momenta and binding energies, and the mean-field term is largely confined to lower momenta and binding energies. This means that although we only have access to the sum of the two terms, we can get an approximation to each term individually using the separation described previously. In this way we assume that the mean-field part is everything satisfying  $p < 300$  MeV and  $\tilde{E} < 100$  MeV. Everything outside of this region is assumed to be from the correlation term.

Using this separation will introduce discontinuities in the spectral function once the relative normalisations change, however this is not expected to cause discontinuities in the cross section for any observable.

### 5.8.2 Mean-field peak width

To estimate the effect of widening the mean-field peak, the two terms were first separated using the same method as for the rescaling of the correlation term. Then the mean-field part was multiplied by an arbitrary function, which was found to result in a wider mean-field peak. The function used was a constant plus a Gaussian of width 50 MeV slightly offset from the mean-field peak.

$$1 + 0.9 \times \exp \left[ \frac{1}{2} \left( \frac{p - 250 \text{ MeV}}{50 \text{ MeV}} \right)^2 \right] \quad (5.14)$$

The mean-field part was then renormalised before adding the correlation term back on. This retains both the total normalisation, and the relative normalisation of the correlation term, though is likely to introduce discontinuities where the two terms join (which are mediated slightly by using interpolation when finding values of  $P(p, \tilde{E})$ ). Figure 5.13 shows the spectral function momentum distribution before and after this change.

Events can be reweighted using the ratio  $P'(p, \tilde{E})/P(p, \tilde{E})$  as before, where  $P'(p, \tilde{E})$  is the modified spectral function. For the widened SF shown in figure 5.13 almost no effect is seen on the distributions of outgoing particles, as shown in Figure 5.14. There is a very small effect found on the double-differential cross section for a mono-energetic neutrino beam. The mean-field width could potentially be left as a free parameter and fitted to data, however this short study shows that reasonably drastic changes have a negligible effect on the cross section, so this is unlikely to

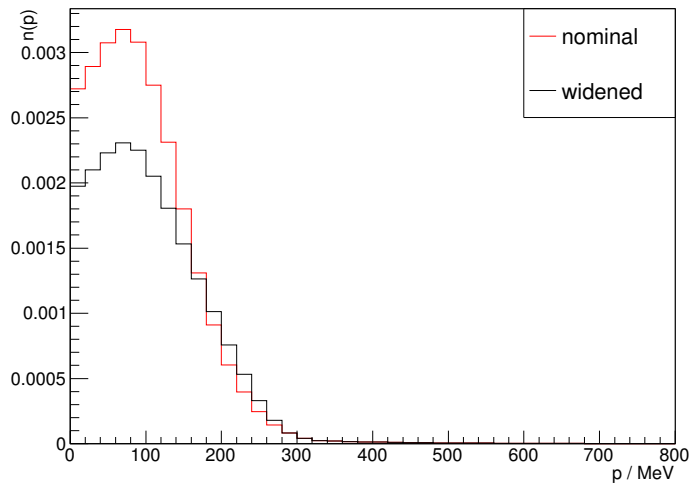


Figure 5.13: The nominal carbon spectral function momentum distribution, and that obtained after widening the mean-field peak.

have significant predictive power. In addition the method chosen here used ad-hoc methods as there is no actual free parameter available to change the mean-field peak width - to perform a rigorous fit a better treatment would need to be found.

### 5.8.3 Pauli blocking

The implementation of Pauli blocking as a hard cut off for outgoing nucleons, makes it simple to implement a reweighting scheme by removing events with momenta below a given new Fermi momentum. Unfortunately it is not possible to reweight events into existence, so the Fermi momentum can only be increased in a reweighting scheme such as this.

Because under this scheme events are always given a weight of either 0 or 1, the cross section as a function of Fermi momentum has discontinuities. As some fitting frameworks cannot deal with these discontinuities, an additional option was added which applied weights linearly from 0 to 1 over a space of 10 MeV either side of the Fermi momentum selected. This means even a very small change in Fermi momentum is almost guaranteed to lead to a change in some event weights.

### 5.8.4 Reweighting closure tests

Once the reweighting functions were added to T2KReWeight, it was necessary to test that the reweighting procedure gave the same answer as generating a fresh MC with the new parameters. For each systematic MC samples were generated with various

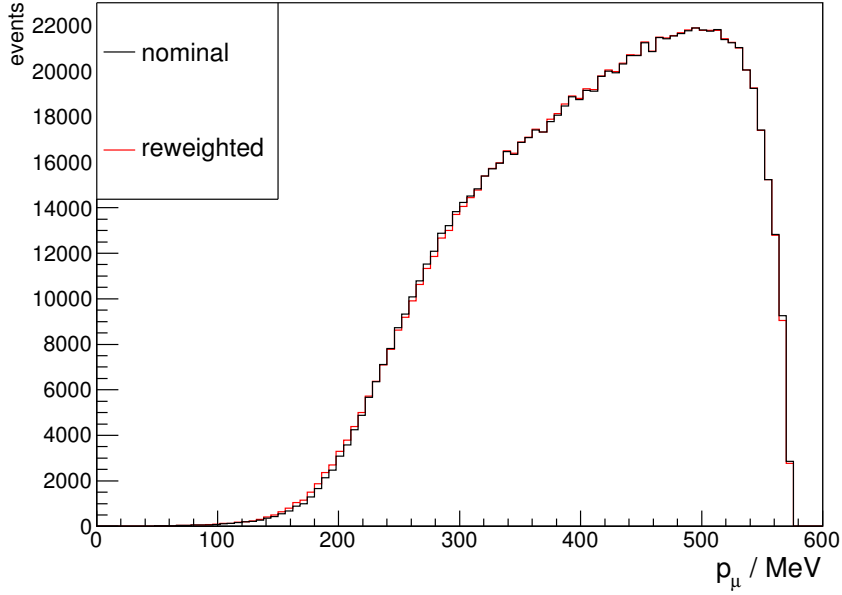


Figure 5.14: Muon momentum distribution, for a 600 MeV  $\nu_\mu$  beam on carbon-12, for the nominal SF and the modified (wider mean-field) SF. Almost no difference can be seen. No effect was seen on the muon angle or proton kinematics for these events either.

parameters, with  $10^6$  events in each sample. One of these samples is referred to as the reference MC. For each sample histograms of either muon momentum or angle were filled with the events, and scaled to the correct total cross section calculated for that parameter value. For every test, the simulation was of a 600 MeV muon neutrino beam incident on a carbon-12 target. The reference MC sample was then reweighted to the same parameter value and filled into an equivalent histogram. For each pair of generated and reweighted histograms, the fractional difference was then calculated for each bin,  $i$ , as

$$d_i = \frac{gen_i - rew_i}{gen_i} \quad (5.15)$$

where  $gen_i$  and  $rew_i$  are the number of events in each bin,  $i$ , for the generated and reweighted samples.

To test the reweighting of the correlation normalisation, seven MC samples were generated, with the correlation normalisation set to 0, 0.1, 0.25, 0.5, 0.75, 1, 1.5, and 2 (where 1 corresponds to the nominal model, 0 corresponds to completely removing the term, and 2 corresponds to doubling the size of it). In the case of the

Pauli blocking systematic, a reference MC was generated with a Fermi momentum of 0, and five other samples were generated with Fermi momenta of 189, 199, 209, 219, and 229 MeV.

Figure 5.15 shows the fractional differences as a function of momentum for the six correlation normalisation MC samples. Figure 5.16 shows the fractional differences as a function of momentum for the five Pauli blocking MC samples.

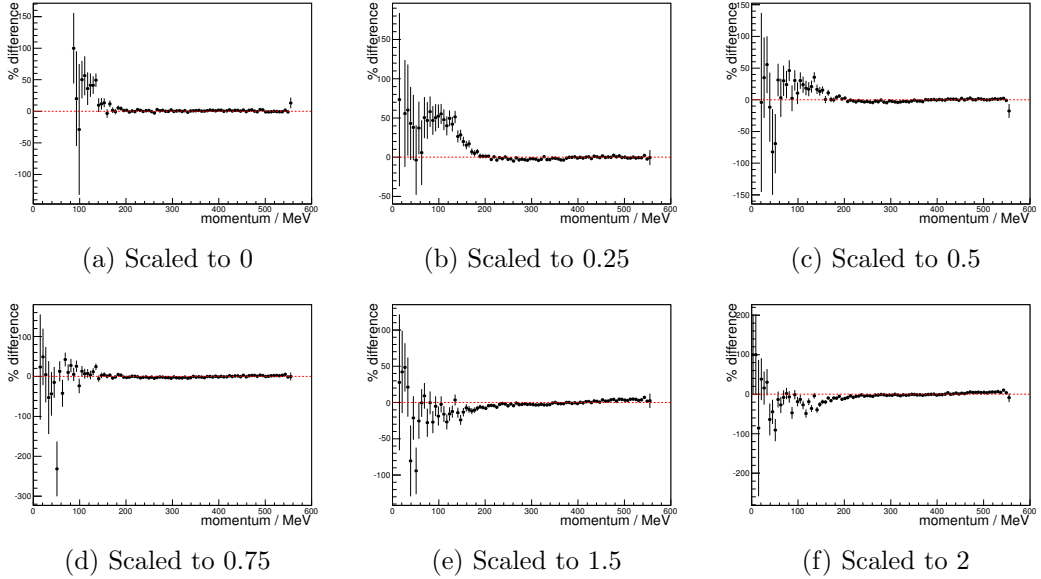


Figure 5.15: Fractional differences between generated and reweighted Monte Carlo data sets from varying correlation normalisation. The red dotted line indicates zero. Differences can be seen in the low momentum region, however this is where there are low statistics, so reweighting is less likely to work correctly.

## 5.9 Determining the spectral function uncertainty scale

Section 5.8 identified three parameters within the SF model which are potentially free to float, and can vary the size and shape of the total cross section. It is not immediately clear how much these parameters should be free to float, so here we discuss the origin and effect of the parameters in the context of determining a prior uncertainty on them. In the future, it would be hoped that this model could be implemented in a complete electron scattering simulation, and rigorously compared to data to determine these uncertainties. As that is not possible, currently conservative estimates based on fairly naive assumptions are used.

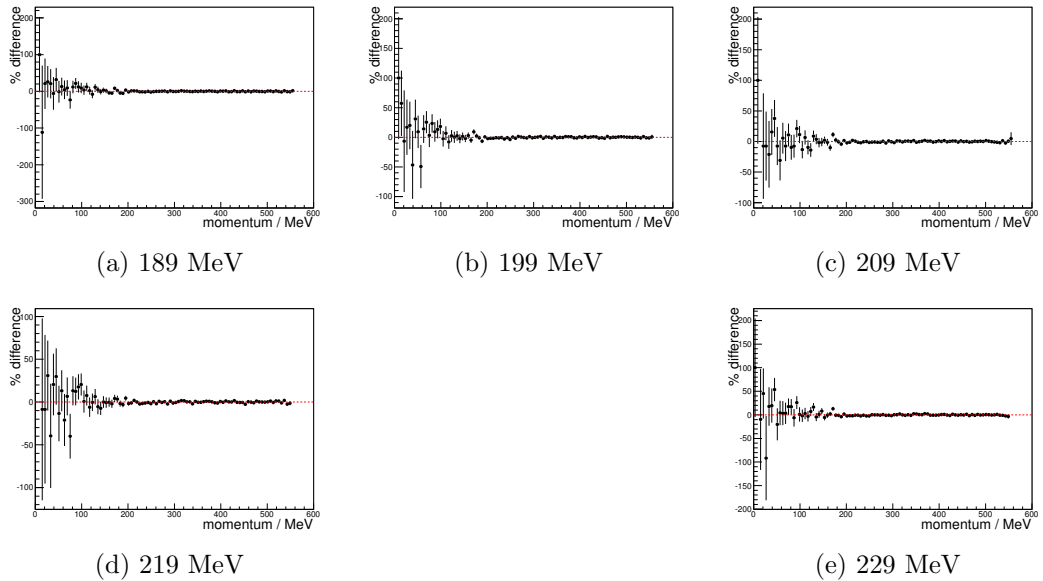


Figure 5.16: Fractional differences between generated and reweighted Monte Carlo data sets from varying Pauli blocking. The red dotted line indicates zero.

### 5.9.1 Mean-field width and Pauli blocking

The Pauli blocking parameter and the mean-field width, seen as a pair, are addressing the same fundamental physics as the Fermi momentum in the RFG model. Because of this, it is relatively safe to assume that the uncertainty on these two parameters is equivalent to the uncertainty on the RFG Fermi momentum. Previously, the T2K oscillation analyses have used an uncertainty of 25 MeV [106], which was taken from fits to electron scattering data [107]. For this reason the nominal uncertainty on both parameters will be assumed to be 25 MeV, and the parameters are treated as uncorrelated. As the mean-field width has very little effect on the cross section, treating the parameters as correlated or uncorrelated makes minimal difference.

### 5.9.2 Normalisation of the correlation term

In the absence of a full simulation, a simple calculation can be made of the electron scattering cross section using the SF model. This naive calculation is missing various important effects, such as FSI and radiative corrections, but the calculation can still be used as an order of magnitude estimate of the effect of varying the normalisation of the correlation term.

In the electron scattering data compared to, inclusive measurements are made

at specific beam energies and scattering angles, and plotted as a function of energy loss. At relevant energies (around 1 GeV), these plots contain the following features: A peak at low energy transfer from quasi-elastic scattering, a peak at higher energy transfer from resonant pion production, and a dip between them. An example of this type of plot is shown in figure 5.4. The correlation term in the spectral function serves to help “fill in” the dip region compared with the RFG models, so ideally we would use this region to estimate the nominal size of this term, and its uncertainty. Unfortunately, this region contains contributions from many effects, such as the low end of the resonant peak, and several sources of non-resonant background, and it is also the region where effects such as MEC (meson-exchange currents) and other proposed multi-nucleon models would contribute. For these reasons, it was decided to use the height of the quasi-elastic peak to estimate our uncertainty on the relative normalisation. When increasing the size of the correlation term, the mean-field term must be reduced to compensate, so the height of the quasi-elastic peak is also reduced. This effect makes the QE peak height useful for estimating the uncertainty due to the correlation normalisation.

By studying plots in [104] by eye, we can estimate that the largest differences at the quasi-elastic peak between data and the SF model prediction is about 10%. This is in agreement with a statement by the authors to the same effect, so the model is assumed to have a 10% uncertainty on this peak.

Figure 5.17 shows the nominal prediction from the naive electron scattering simulation, with the same line scaled up and down by 10%. At the peak, to achieve the same 10% height difference, the SF term is required to have a 100% normalisation change (i.e. removing the term altogether, or doubling its relative size). This, unfortunately, is a very large uncertainty, and in one direction a physical limit is reached within  $1\sigma$ .

For this estimation, the maximum deviation from the data was used as a  $1\sigma$  uncertainty in order to remain conservative. This uncertainty would be expected to go down when a complete analysis can be done in an internally consistent fit over all the data, with a more realistic full simulation.

## 5.10 Summary

The spectral function nuclear model has been implemented in the NEUT interaction generator for charged current quasi elastic scattering, and neutral current elastic scattering. This implementation has been compared to theoretical calculations and other generators for validation.

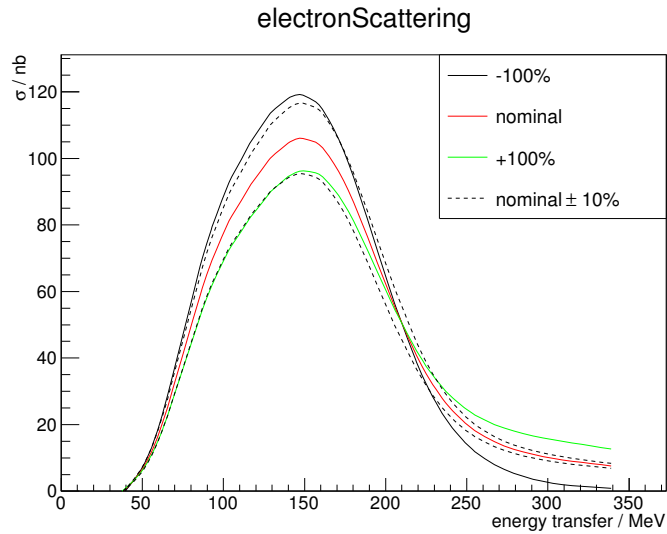


Figure 5.17: The results from a naive electron scattering simulation. The nominal cross section has been scaled by  $\pm 10\%$  for comparison. It is found that applying a 100% error to the normalisation of the correlation term give roughly the same 10% difference in the height of the quasi-elastic peak.

The SF model shows better agreement with electron scattering data than the RFG model, however the agreement is not perfect. For this reason three parameters were identified which could be tuned to improve agreement with data, and to provide realistic uncertainties on the model. The T2K neutrino interactions working group recently studied how well this model, with the additional inclusion of MEC events, could fit several data sets [108]. Four CCQE data sets were used, MiniBooNE muon neutrino and muon antineutrino, and MINERvA muon neutrino and muon antineutrino. It was found that, although the model parameters could be adjusted to fit individual data sets well, it was not possible to simultaneously describe all of the available data sets.

Nevertheless it is worth comparing this model to more model-independent data, as the T2K groups fits mentioned here found that every model tested showed considerable tension when confronted with multiple data sets.

## Chapter 6

# Measuring the $CC0\pi$ cross section

### 6.1 Overview and motivation

As previously discussed, the charged current quasi-elastic (CCQE) cross-section is of utmost importance to T2K. The two-body kinematics involved in a pure CCQE event allows a simple reconstruction of the neutrino energy using only the final state lepton kinematics. Unfortunately the neutrino energy resolution is limited (and potentially biased) by smearing from nuclear effects such as Fermi motion and binding energy. This is an unavoidable consequence of using nuclear targets such as water and plastic.

As discussed in chapter 3, recent measurements of CCQE interactions on heavy nuclear targets don't agree well with predictions based on data from hydrogen and deuterium targets and simple nuclear models. Alternative models exist to account for these discrepancies, and currently it is not apparent which best describe reality.

One of the largest complications that arises when studying interactions on nuclear targets, is final state interactions (FSI). These interactions can lead to events mimicking CCQE, for example the production of a single pion followed by its absorption. In addition, true CCQE events can lead to the production of a pion, leading to a misclassification by an experimenter. With this in mind, it is clear that it is in general not possible to determine which events are “true” CCQE. In fact it is becoming apparent that our factorisation of events into an initial neutrino interaction followed by final-state interactions may not be sufficient to describe nature, and as such a CCQE cross section is not even a well defined concept.

For these reasons, no attempt will be made here to measure the CCQE cross section as defined by an interaction generator. Instead, the definition of signal events is taken from which particles *leave* the nucleus, an unambiguous statement.

The CCQE interaction is categorised by the presence of a muon and a proton, however the protons are often very low momentum and cannot be seen in ND280 (if they even escape the nucleus). In addition, as discussed in chapter 3, other categories of event known as multinucleon interactions might look like CCQE but have two or more outgoing protons. Therefore we will define our CCQE-like signal as  $CC0\pi$ , meaning there is one muon, and no pions, though there can be any number of protons or neutrons. Other topologies that will be discussed are  $CC1\pi$  (one muon, one positive pion, any number of nucleons) and  $CCother$  (all other CC interactions).

Cross sections are often calculated as a function of energy, or as a function of Lorentz invariant variables such as  $Q^2$ . Unfortunately it is not possible to measure the neutrino energy directly and it is known that reconstructing the neutrino energy could be biased by multinucleon interactions and other effects, as discussed previously. In the same manner, any fundamental variable which needs to be reconstructed will rely on a model to convert from measurable quantities. As we are making a measurement in a model-independent manner, we cannot use this type of variable - we are therefore forced to measure the cross section in terms of final-state variables which are measurable. Because of this, we will measure the differential cross section in muon momentum and angle. We can also project this 2D distribution onto various 1D axes, and integrate the distribution to give the total cross section.

In all of these results, no attempt is made to predict the neutrino flux contributing to each bin as this would rely heavily on models. Instead, the distributions are normalised by the total integrated neutrino flux, to give “flux-integrated” cross sections. This concept is defined more rigorously in section 6.4.

The chosen interaction target is FGD1, as it is fully active, and has a high enough target mass to achieve a high interaction rate whilst having a low enough density to track most particles produced. TPC2 can then be used to achieve an accurate momentum measurement and particle identification of the particles that escape the FGD.

## 6.2 Implementation details

The data, and also the MC simulation used, was processed by the ND280 computing group using official software. This was from a processing batch known as “production

5F”, which used version v10r11p23 of the ND280 software.

T2K runs 2 – 4 are used, a total of  $5.73 \times 10^{20}$  protons on target (POT). This data was collected between September 2010 and May 2013. Run 1 is not used because there were significant changes between run 1 and run 2 (including the beam properties, and the number of ECals installed in ND280), and run 1 would not contribute a significant amount of additional data. A full breakdown of the POT collected in each period is listed in table 6.1. In this table, “water” and “air” refer to whether the P0D water bags were filled or not.

Run	MC POT / $10^{21}$	data POT / $10^{20}$
Run 2 water	0.428	0.428
Run 2 air	0.355	0.355
Run 3b air	0.214	0.215
Run 3c air	1.348	1.348
Run 4 water	1.939	1.6248
Run 4 air	1.448	1.7624
Total	5.73	5.73

Table 6.1: POT used in this analysis. “water” and “air” refer to whether the P0D water bags were filled or not.

After processing, the analysis-level files are “flattened” using a very inclusive selection to reduce the size of the data. These flat tree files can then be analysed using high level analysis packages.

For this analysis, the event selection was inherited from the oscillation analysis. This event selection is defined in a package called HIGHLAND (HIGH Level Analysis at the Near Detector), which also applies various corrections, flux tuning, and can apply systematic variations.

### 6.3 Event selection

The event selections used in this analysis were inherited from the ND280  $\nu_\mu$  group, who developed the samples for the near detector fit which is used in the oscillation analyses. These cuts are described extensively in references [109, 110]. These samples are designed to select particular topologies, rather than the interaction modes. Firstly, a  $\nu_\mu$  charged current selection is defined using the following cuts:

#### 1. Data quality cut

The beam and ND280 groups report on a spill-by-spill basis whether all beam monitors, horns, and sub-detectors were functioning correctly at the time the

data was collected. For the spill to be included in the analysis all systems must have passed this quality test.

## 2. **Bunching**

The beam spill is separated into its individual bunches, defined by time relative to trigger. The times of bunch centre relative to trigger vary between runs in data, and are different again for MC. Any data more than 60 ns from the centre of a bunch is discarded, assumed to be due to backgrounds. The width of a bunch is approximately 15 ns.

## 3. **TPC multiplicity >0**

There must be a track in TPC2, as this will be used to measure the momentum and particle type.

## 4. **TPC track quality and FGD fiducial volume**

There must be at least one TPC track with more than 18 nodes, as with fewer than this the momentum measurement and PID hypothesis becomes far less reliable. In addition at least one of these tracks must have an FGD component and start within the FGD fiducial volume.

## 5. **Definition of the muon candidate**

The highest momentum good quality negative track is selected as the muon candidate. Then the TPC is used to identify the particle type based on  $dE/dx$  measurements. Given the particle's momentum, the expected energy loss can be calculated and compared to the measured value to construct likelihoods of various particle hypotheses. These likelihoods are cut on to select a high-purity muon sample.

## 6. **Backwards going track veto, and upstream veto**

This cut is designed to remove poorly reconstructed events which have entered the FGD1 fiducial volume from the upstream detectors. Firstly, any track reconstructed as backwards-going is removed, as it was found most backwards reconstructed negative tracks were in fact forward-going positive tracks. In addition, if there are any tracks starting more than 150 mm upstream of the muon candidate the event is rejected on the basis there is probably a track entering the detector from upstream.

## 7. **Broken track cut**

This cut is designed to remove events which pass all the way through the FGD from upstream, and are reconstructed as two separate tracks, one of

which starts inside the FGD. If the muon candidate's start position is more than 425 mm away from the FGD1 upstream edge and there is an FGD-only track which starts outside the FGD fiducial volume, the track is assumed to be an external track which the reconstruction split into two pieces, and the event is rejected.

The charged current selection is then subdivided into three further samples defined by the number of pions identified in the final state (0 pions, 1 positive pion, other). A search is therefore performed to explicitly look for:

- Charged pion tracks in TPC
- Electrons or positrons in TPC
- Iso-FGD pion tracks (tracks from pions contained in the FGD)
- FGD Michel electrons

The first two of these use the TPC PID to assign a particle hypothesis to every TPC track identified. The Iso-FGD pion tracks are identified using FGD PID, which works in a similar way to the TPC PID by comparing the measured and expected size of energy deposits along the track. Again, particle hypotheses are assigned to each FGD-only track. FGD Michel electrons are searched for in the time after the beam bunch window. A time-delayed FGD1 cluster with more than 200 photo-electrons is assumed to be a Michel electron and tagged as coming from a positive pion.

For this analysis the  $CC0\pi$  sample, that is the sample with no identified pions or electron-like tracks, is defined as the signal sample. The  $CC1\pi$  sample is intended to be predominantly resonant events. It is selected by requiring exactly one positively charged pion track, whether identified in the TPC or the FGD, or exactly one Michel electron, but no electron-like tracks in the TPC. All other CC-inclusive events are placed in the  $CCother$  sample, which is dominated by inelastic scattering and  $\pi^0$  production events.

### 6.3.1 $CC0\pi$ selection

Figure 6.1 shows the momentum and angle distributions for the selected muon in data and NEUT MC, with MC separated by true topology type and a GENIE prediction overlaid for comparison. Figure 6.2 shows only the true  $CC0\pi$  component of the sample, separated by reaction type.

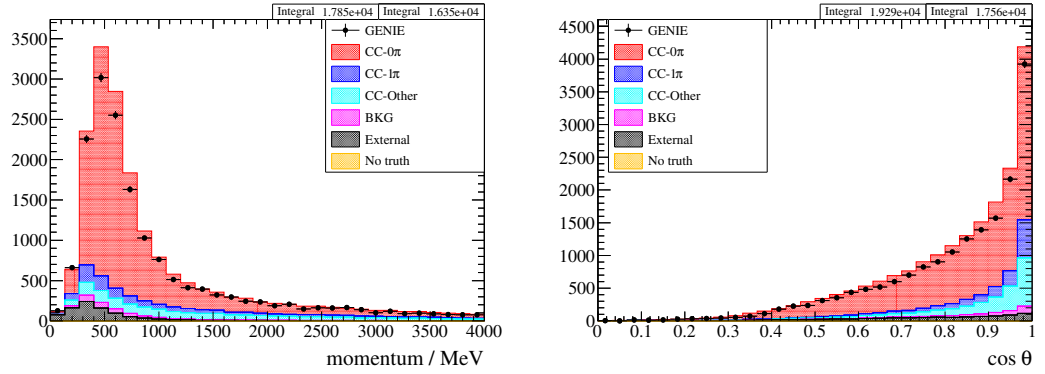


Figure 6.1: Momentum and angle distributions for the selected muon candidate in the  $CC0\pi$  selection, with NEUT MC separated by event topology. Bullets represent GENIE MC with statistical errors for comparison, normalised to the same POT.

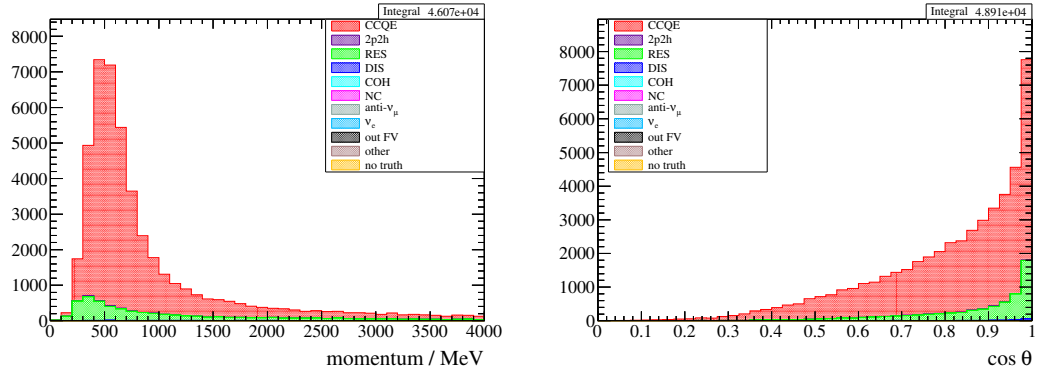


Figure 6.2: Momentum and angle distributions for the selected muon candidate in the  $CC0\pi$  selection, for only true  $CC0\pi$  interactions, with NEUT MC separated by reaction type. There is no 2p2h mode in the MC used, so this category is empty by definition.

Table 6.2 shows the composition of the  $CC0\pi$  sample according to the NEUT simulation. The sample is roughly 72% pure, and 94% of the selected muon candidates are true muons. 97% of  $CC0\pi$  events in the CC-inclusive sample are retained in the  $CC0\pi$  sample, with the remaining 3% being split roughly evenly between the  $CC1\pi$  and  $CCother$  samples. Table 6.3 shows the composition of only the true  $CC0\pi$  events in the selection, according to reaction code and selected particle type. From this it is clear why the selection is sometimes referred to as CCQE-like, being over 85% CCQE.

Topology	Fraction
CC0 $\pi$	72.2%
CC1 $\pi$	8.6%
CCother	11.7%
External and BKG	7.5%

Table 6.2: Composition of events in the CC0 $\pi$  sample by topology according to the NEUT MC. 50% of the CCothers contamination comes from events with neutral pions, which are easily missed if the photons escape to the ECals.

Reaction	Fraction
CCQE	86.6%
RES	12.7%
DIS	0.5%
OTHER	0.2%

Table 6.3: Composition of true CC0 $\pi$  events in the CC0 $\pi$  sample, according to reaction type.

### 6.3.2 CC1 $\pi$ and CCothers selections

In addition to the CC0 $\pi$  sample, the remainder of the CC-inclusive selection is separated further into CC1 $\pi$  and CCothers samples. The CC1 $\pi$  sample contains events with exactly one signature of a positive pion (either a positive pion-like track in the TPC or FGD, or a Michel electron), and no signs of other pions, either charged or neutral. The CCothers sample contains all events which were not actively selected by the CC0 $\pi$  or CC1 $\pi$  selections. These samples both have a very low contamination from CC0 $\pi$  events.

Figures 6.3 and 6.4 show the distributions of the muon candidate from these samples, separated by true topology, with the same selection on a GENIE sample for comparison.

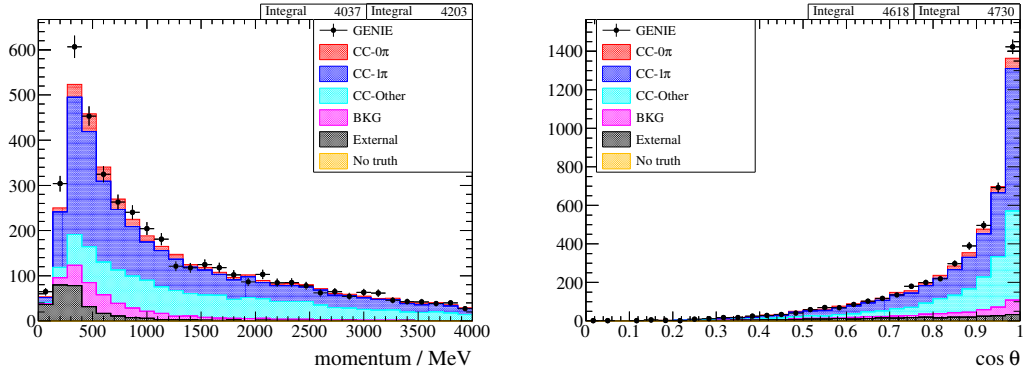


Figure 6.3: Momentum and angle distributions for the selected muon candidate in the CC1 $\pi$  selection, with NEUT MC separated by event topology. Bullets represent GENIE MC with statistical errors for comparison, normalised to the same POT.

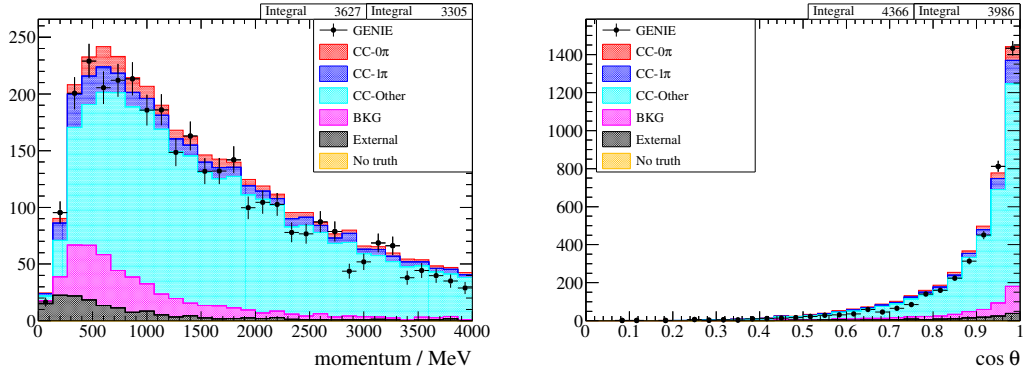


Figure 6.4: Momentum and angle distributions for the selected muon candidate in the CCothers selection, with NEUT MC separated by event topology. Bullets represent GENIE MC with statistical errors for comparison, normalised to the same POT.

## 6.4 Cross section extraction

The flux-integrated cross section in each bin,  $i$ , is calculated as

$$\left\langle \frac{d\sigma_i}{dp_\mu d\cos\theta_\mu} \right\rangle_\Phi = \frac{N_i^{unfolding}}{\Phi N_{targ} \Delta_i \epsilon_i} \quad (6.1)$$

where  $N_i^{unfolding}$  is the estimated number of true events in bin  $i$ ,  $\Phi$  is the integrated flux,  $\epsilon_i$  is the efficiency of selecting signal events in bin  $i$ ,  $\Delta_i$  is the width (area in the case of 2 dimensions) of bin  $i$ , and  $N_{targ}$  is the number of targets in the fiducial volume. The result will be presented as a per nucleon cross section.

The quantity  $N_i^{unfolding}$  is extracted from the data using a Bayesian unfolding

method (see section 6.4.2), and includes the subtraction of a background extracted directly from MC (see section 6.4.1) as well as bin-migration from detector effects. The only effect that uncertainties on  $\Phi$  and  $N_{targ}$  have on the total cross section is an overall normalisation uncertainty.

This cross section definition is chosen because it is one of the most model-independent ways of presenting a cross section. No attempt is made to predict the neutrino energy spectrum contributing to each muon bin, so the main effect an incorrectly predicted flux would have is an overall normalisation error.

### 6.4.1 Background subtraction

The number of background events in each bin is predicted by MC. The main backgrounds in the CC0 $\pi$  sample are CC1 $\pi$  and CCOther (at about 10% each), largely due to failed reconstruction of pions. Currently no attempt is made to constrain these backgrounds directly using ND280 data, the prediction is instead taken directly from simulation. Future improvements to this analysis should focus on placing a constraint on these backgrounds to reduce the total uncertainty.

The T2K neutrino interactions working group studied various external data sets and fitted various parameters in the NEUT MC to these data sets. In some cases ad-hoc additional parameters were included to achieve good agreement. The central values and uncertainties obtained for the various parameters in these fits is reported, and known as the “BANFF prefit” prediction. The nominal NEUT MC is reweighted to this prediction for use as the nominal MC prediction.

Because there is no data constraint, a comparison is performed between the NEUT simulation and data for these backgrounds in a control sample, to show that such a constraint is not needed. This is done in section 6.4.4. Uncertainties on this background can come from flux, cross section, and detector systematics, which are dealt with in section 6.4.3.

There is also potential background from interactions in the sand and pit walls upstream of the ND280 detector (known as “sand muons”). A dedicated simulation of these interactions is produced by the computing group, and these events are processed using the same analysis software as the standard MC and data. The contamination from these particles is found to be very small (below 0.5% of the event sample).

The uncertainties on sand muon rates were studied by the ND280  $\nu_\mu$  group [110]. These uncertainties are included and propagated to the final result, however due to the low contamination this is not expected to be a large uncertainty.

### 6.4.2 Bayesian unfolding method

To estimate the true spectrum from the reconstructed spectrum, the Bayesian unfolding method is used [111]. The object of this is to account for detector inefficiencies and misreconstruction to “unsmear” the reconstructed spectrum to the original true spectrum.

From Monte Carlo simulation, it is simple to calculate a “smearing matrix”,

$$R_{ij} = P(r_i|t_j) \quad (6.2)$$

which gives the probability of an event in true bin  $j$ , being reconstructed in reconstructed bin  $i$ . This matrix encodes both migration between bins, as well as the detector (and selection) efficiency in each bin. In fact, the efficiency for a true bin,  $j$ , is given by

$$\epsilon_j = \sum_{\alpha}^{\text{reco bins}} P(r_{\alpha}|t_j) \quad (6.3)$$

Using MC again, we can get prior estimates of  $P(t_j)$  and  $P(r_i)$  for each  $i$  and  $j$ . These are the “probabilities” of finding an event in a given bin (essentially normalised event distributions - see equations 6.4 and 6.5).

$$P(t_j) = \frac{N_{t_j}}{\sum_{\alpha}^{\text{true bins}} N_{t_{\alpha}}} \quad (6.4)$$

$$\begin{aligned} P(r_i) &= \sum_{\alpha}^{\text{true bins}} P(r_i|t_{\alpha})P(t_{\alpha}) \\ &= \frac{N_{r_i}}{\sum_{\alpha}^{\text{true bins}} N_{t_{\alpha}}} \end{aligned} \quad (6.5)$$

This allows us to use Bayes’ theorem to provide us with our “unsmearing matrix”

$$P(t_j|r_i) = \frac{P(r_i|t_j)P(t_j)}{P(r_i)} \quad (6.6)$$

Applying this to the reconstructed data distribution returns the first estimate of the true distribution,

$$N_{t_j}^{\text{unfolded}} = \frac{1}{\epsilon_j} \sum_i P(t_j|r_i)(N_{r_i} - B_{r_i}), \quad (6.7)$$

where  $N_{r_i}$  is the number of events reconstructed in bin  $i$ ,  $B_{r_i}$  is the number of

predicted background events in reconstructed bin  $i$ , and  $\epsilon_j$  is the efficiency in true bin  $j$ . It would also be possible to use a purity correction to give the number of signal events in each bin, instead of a background subtraction.

The newly estimated true spectrum can then be inserted into equation 6.4 to determine a more realistic estimate of  $P(t_j)$  as it is driven by data. We can then follow the rest of the calculation to get an updated unsmearing matrix, and a second estimate for  $N_{t_j}$ . It is thus possible to continue to iterate this procedure, allowing the data to train the unfolding. The algorithm described here is available as a software package, RooUnfold [112], which was integrated into the analysis software.

From equation 6.7, one can see that each true bin in the final result can contain contributions from several reconstructed bins, leading to potentially large correlations between bins in the final result. There is also no requirement that there are the same number of true and reconstructed bins, in fact the distributions are allowed to cover different regions of phase-space.

Unfortunately there are problems with Bayesian unfolding, particularly when iterating too many times. The main issues are that statistical errors become amplified, and distributions begin to pick up large fluctuations. The first problem can be seen to be due to each iteration taking information from the data, leading to larger statistical uncertainty. The second is due to statistical fluctuations in the data (and in the MC) becoming amplified each iteration, essentially because the algorithm starts to “train” on these fluctuations, as if they were genuine differences from physics. Because of these problems a small number of iterations is preferred, and a study into the number of iterations to be used is discussed in section 6.6.3.

There are mechanisms designed to deal with the problems in Bayesian unfolding. Examples include smoothing the distribution between iterations (as we assume the physical distributions are smooth) to overcome the problem of amplified statistical fluctuations. Other algorithms attempt to use Fourier methods to cut out high-frequency modes which tend to come from statistical fluctuations. Unfortunately in both of these cases it is not obvious how to apply them to a 2D distribution, so it was decided to not use any of these alternatives.

### 6.4.3 Uncertainties

All uncertainties are propagated using pseudo-experiments to build a covariance matrix. For each source of uncertainty,  $s$ ,  $N$  pseudo experiments are performed and the results propagated through the unfolding procedure, giving a new differential cross section each time,  $\sigma^{(s_n)}$ . With the nominal cross section in bin  $i$  being given

by  $\sigma_i^{(nom)}$ , the covariance matrix is calculated as:

$$V_{ij}^{(s)} = \frac{1}{N} \sum_{s_n=1}^N \left( \sigma_i^{(s_n)} - \sigma_i^{(nom)} \right) \left( \sigma_j^{(s_n)} - \sigma_j^{(nom)} \right) \quad (6.8)$$

For some of the fake data studies, shape-only uncertainties are considered. In this case, the cross section distribution for each pseudo-experiment is scaled to have the same integral as the nominal distribution before constructing the shape-only covariance matrix. In this case, the shape-only covariance matrix can be defined as:

$$V_{ij}^{shape(s)} = \frac{1}{N} \sum_{s_n=1}^N \left( \frac{\sigma_{total}^{(nom)}}{\sigma_{total}^{(s_n)}} \sigma_i^{(s_n)} - \sigma_i^{(nom)} \right) \left( \frac{\sigma_{total}^{(nom)}}{\sigma_{total}^{(s_n)}} \sigma_j^{(s_n)} - \sigma_j^{(nom)} \right) \quad (6.9)$$

where, given the bin widths,  $\Delta_i$ , the total cross section is

$$\sigma_{total}^{(x)} = \sum_{i=1}^{N_{bins}} \Delta_i \sigma_i^{(x)} \quad (6.10)$$

In section 6.7, each source of uncertainty is evaluated for the analysis. Here we simply list the different categories of uncertainty that can contribute, and what tools are used to estimate their impact.

#### 6.4.3.1 Statistical uncertainties

RooUnfold has the ability to calculate uncertainties due to the data statistics, and modifications were available to account for limited MC statistics too, however in low statistics bins the assumptions can lead to an underestimate, and the memory usage does not scale well with the number of bins used. For these reasons it was decided to use pseudo-experiments to propagate statistical uncertainties too.

For both data and MC statistics, the contents of each histogram that is an input to the unfolding are varied around the nominal value, according to a Gaussian with mean  $N$ , and width  $\sqrt{N}$ , where  $N$  is the number of events in a given bin. This Gaussian is truncated at 0, to avoid unphysical negative event populations being input to RooUnfold. A Gaussian is used as an approximation to a Poisson distribution, as the discrete nature of the Poisson distribution was seen to cause problems when passing through RooUnfold. For data and MC separately, 2000 pseudo-experiments are performed. For the MC statistical uncertainty the input histograms include the background prediction, signal prior, and detector response matrix.

### 6.4.3.2 Detector uncertainties

There are a large number of potential detector effects that could affect this analysis. The ND280  $\nu_\mu$  group have determined the detector uncertainties that affect these selections, and estimated the size of their effects [110]. The detector systematics that have a non-negligible effect on the analysis are:

- **FGDMass**

There is some small uncertainty on the number of target nuclei in FGD1, due to the engineering tolerances involved in its production. Previous studies show that the uncertainty on the total target mass is 0.67% [113].

- **BField**

The momentum measurements in this analysis come from curvature in a magnetic field, so it is important to know what the magnetic field is. Unfortunately due to the finite size of the magnet, there is some variation in magnetic field strength across the detector. The uncertainty in the size of these distortions is incorporated into this systematic.

- **MomRes**

There are two ways in which the momentum measurements in ND280 have uncertainty - firstly there is an uncertainty on the absolute size of the momentum, and secondly there is an uncertainty on the resolution of each measurement. The momentum resolution is found to differ between data and MC, so a systematic uncertainty is applied to account for this. This systematic smears the momenta of reconstructed tracks in MC so that the widths agree between data and MC. The uncertainty varies slightly as a function of momentum but is roughly 5 – 10%. This systematic can have a large effect on the shape of the final cross section due to varying the amount of smearing between different momentum bins.

- **MomScale**

The absolute scale of the momentum measurements depends on our knowledge of the magnetic field strength. This is separate to the magnetic field distortions described earlier. From measurements with a hall probe, extrapolated to expectation with the full magnetic field, the uncertainty on the absolute momentum scale is set at 0.5%. This is cross-checked with comparisons of momentum measurements in the TPC and the range of the same particles in the more dense detectors such as the FGD. This systematic will mainly

affect the shape of the final cross section in a similar way to the momentum resolution systematic.

- **ChargeConf**

One of the crucial selection cuts is the identification of a negative particle as the muon candidate. This charge determination comes from measuring the curvature of the track in the magnetic field. Unfortunately for high-momentum tracks, or those with a small momentum component perpendicular to the field, the curvature can be quite small. For these tracks, there is some uncertainty on how often the incorrect charge will be assigned. At momenta between 500 MeV and 3 GeV roughly  $(1 \pm 0.2)\%$  of tracks are assigned the wrong charge. The charge identification and its uncertainty both increase at high momenta (above 5 GeV) due to tracks becoming straighter, and low momenta (below 100 MeV) due to reconstruction difficulties.

- **FGDTrackEff**

This systematic concerns only FGD-only tracks, and the efficiency of correctly reconstructing them. As this analysis contains cuts on FGD-only tracks it is important to accurately predict how efficiently they are reconstructed. The main effect of this systematic is the efficiency of rejecting background events. The FGD tracking efficiency are found to have an uncertainty of 5 – 10%, being lowest at high momenta, and highest at low momenta.

- **TPCPID**

The TPC PID depends on measurements of the energy loss along the track. After TPC calibration, some differences are still seen between data and MC, so uncertainties are applied to the MC to cover the differences. These uncertainties include both shifts and smearings of the TPC PID “pull” variables, and depend on the particle type and momentum. The largest uncertainties applied are of the order 5%, although for muons the uncertainties tend to be less than 1%.

- **MichelEleEff**

The efficiency of reconstructing decay electrons in the FGD is important for identifying, and rejecting, backgrounds with low-momentum pions. In general, good data/MC agreement is found for this efficiency, however there is still an absolute uncertainty of roughly 1% on the efficiency. This leads to a fractional uncertainty of approximately 2% for the rate at which Michel electron events are tagged as such.

- **SIPion**

Pions produced in neutrino interactions can undergo hadronic secondary interactions (SI) in the detector some distance from the production point. These interactions are modelled in the detector simulation, however significant differences have been observed between GEANT4 and external measurements (which themselves have uncertainties of 20% or more). Several different reaction mechanisms are available to a pion interacting with a nucleus, such as absorption, elastic scatter, and charge exchange. All of these significantly affect our ability to reconstruct and identify pion tracks in ND280, and therefore the rate at which we reject background events. To estimate the effect of this weights are given to all tracks based on the probabilities of various different interactions occurring (including no interaction) under different cross section assumptions.

- **OOFV**

Selected particles which originated from interactions outside the FGD fiducial volume are known as “external” (EXT) or “out-of-fiducial-volume” (OOFV) events. This includes everything from simple reconstruction failures, to neutral particles which originate in the magnet or barrel ECal and interact in the FGD, generating charged tracks in the FGD. These events are separated into a number of categories and uncertainties assigned to the rates of them individually. Most of these event categories have reconstruction-related uncertainties applied to them, which are individually studied for each failure mode. Much of the OOFV background comes from complex interactions in the magnet or ECals, which contain heavy elements such as iron and lead where we know neutrino interaction cross sections are poorly known. Additional normalisation uncertainties are therefore assigned to the cross sections for these events and included as part of this systematic. These OOFV events tend to have large uncertainties applied, ranging up to over 150% for some categories.

### 6.4.3.3 Flux uncertainties

The uncertainty on the neutrino flux is encoded in a covariance matrix, evaluated by the T2K beam group. This uncertainty is predominantly from uncertainties in hadron production at the target, which is constrained by measurements at NA61/SHINE (see section 4.6). The predominant uncertainty on the flux is the overall normalisation of the muon neutrino flux, an uncertainty of approximately 11%. This affects the normalisation of the cross section measurement. In addition, some

shape effects will be seen, due to the flux uncertainties affecting the background prediction, but also the flux shape potentially affecting the efficiency of signal event selection.

Ninety-nine throws are made from the flux covariance matrix to reweight the events in the analysis forming 99 pseudo-experiments with which to calculate a final covariance matrix.

#### 6.4.3.4 Model uncertainties

There are a number of ways in which poor understanding of neutrino interactions could affect this measurement. The analysis is designed to be independent of the model for the signal interaction, though this could have a small effect on the efficiency. The models we use for the background, however, are very important as there is no direct data constraint.

The BANFF “pfit” discussed in section 6.4.1 provides central values for the model parameters in the simulation used, as well as the uncertainties on them and their correlations. This information is provided in the form of a covariance matrix, and 99 throws were made from this to form 99 pseudo-experiments. T2KReWeight was used to calculate weights for all events based on these throws.

The parametrisation of the cross section model uses the following parameters

- **MaQE**

The axial mass in quasi-elastic interactions. This affects the CCQE normalisation, as well as its shape as a function of  $Q^2$ . It is not expected to be a large cause of uncertainty as it mainly affects signal interactions.

- **CCQE energy-dependent normalisation**

Additional CCQE normalisation uncertainties cover differences in data across different energy regimes. There are three normalisation parameters covering the regions  $E_\nu < 1.5$  GeV,  $1.5$  GeV  $< E_\nu < 3.5$  GeV, and  $E_\nu > 3.5$  GeV.

- **PF**

The Fermi momentum used in the RFG model of the nucleus. This has a small effect on the cross section normalisation and shape for CCQE events, however this is not expected to be a dominant uncertainty.

- **SF**

A “spectral function” uncertainty is considered, given the poor agreement the RFG model shows with electron scattering data. The uncertainty is taken to be the difference in cross section between the SF and RFG model, evaluated

as a function of neutrino energy, and muon momentum and angle. This only affects CCQE events.

- **MaRES**

The axial mass in resonant interactions. Because this is an effective parameter it is treated as a separate parameter to the quasi-elastic axial mass. This is expected to affect the CC1 $\pi$  component of the background significantly.

- **CC1pi energy-dependent normalisation**

Additional CC1pi normalisation uncertainties are included. These are separated into  $E_\nu < 2.5$  GeV and  $E_\nu > 2.5$  GeV. These are expected to affect the CC1pi background considerably and contribute significantly to the total uncertainty.

- **CC Coherent**

There is very little data on coherent pion production at T2K energies. The data that exists below 2 GeV simply places upper limits on the cross section (see section 3.4.2.3). The NEUT coherent prediction is drastically larger than this, so a 100% uncertainty is placed on the normalisation of coherent events. This is not expected to be a significant source of uncertainty as there are very few coherent events selected.

- **NC1 $\pi^0$**

As there is very little data on the neutral current production of neutral pions at T2K energies, the uncertainty regarding this is encoded in a simple normalisation uncertainty. This is not expected to be an important uncertainty as very few NC events are selected.

- **CC Other**

Multi-pion and inelastic scattering uncertainties are also encoded in a simple normalisation uncertainty, as there is minimal data to constrain them and they are not a dominant process at T2K energies. Nonetheless this is expected to affect the CCothers background in this analysis and therefore can be an important uncertainty.

- **NC other**

All other NC modes are given a normalisation uncertainty. This is not expected to be a dominant systematic as NC interactions are efficiently rejected.

- **W-shape**

The W-shape parameter is an empirical parameter which affects the pion mo-

momentum spectrum from resonant interactions. The nominal NEUT model with FSI included shows very poor agreement with data when this pion momentum spectrum is considered. This parameter doesn't have a large effect on the muon kinematics or total cross section so it is not expected to be a dominant uncertainty.

#### 6.4.3.5 FSI uncertainties

Final state interactions (FSI) occur within the nucleus after a neutrino interaction has taken place. These could be considered with model uncertainties, but the treatment is slightly different so the discussion here is separate.

Direct reweighting of events to reflect FSI parameter changes is difficult to implement, and therefore was not available in T2KReWeight, the reweighting framework used for cross section uncertainties. An alternative to direct reweighting is to create response functions - encoding the response of the cross section to parameter changes as a function of some variable. Unfortunately due to the highly correlated nature of the parameters involved in FSI, varying one parameter causes the variations of others (probability has to be conserved) and therefore it is not possible to encode variations in a simple response function. For this reason FSI uncertainties are approximated using 16 different parameter sets defined in such a way that they cover the full uncertainty range. These 16 parameter sets are used to define the response of the cross sections, and calculate event weights to simulate 16 pseudo-experiments. This method was developed for previous T2K oscillation analyses, and simply re-used here.

The FSI parameters are assumed to have no correlation with the cross section model parameters.

#### 6.4.4 Background estimation

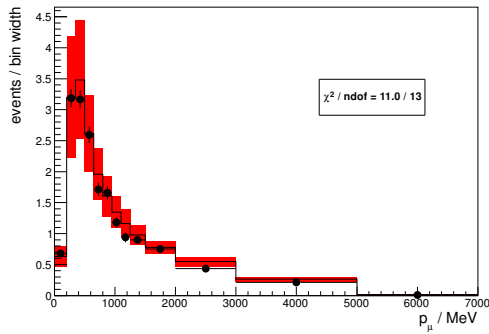
It is important to be confident that the estimation of the non-CC0 $\pi$  contamination in our signal sample is well modelled. To perform this check, we utilised special selections that separated the CC1 $\pi$  and CCOther components (which are the largest background components), described in section 6.3.2.

Within the xsTool framework it is possible to use the xsEngineNoop class to produce MC predictions with error envelopes. This was done for many variables for both the CC1 $\pi$  and CCOther samples, and the results were compared with data. In each case, the MC statistics, cross section, and FSI uncertainties were evaluated, and the  $\chi^2$  between the data and MC is calculated using the full covariance matrix

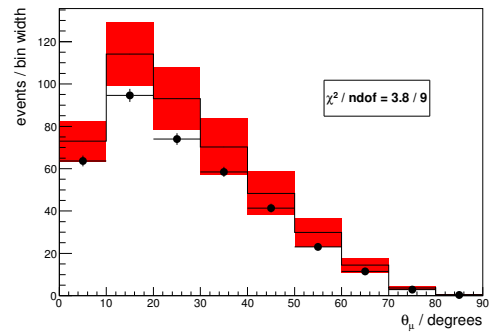
Selection	Variable	$\chi^2/\text{ndof}$
CC1 $\pi$	muon momentum	12.2 / 13
	muon angle	3.8 / 9
	$\pi^+$ momentum	27.7 / 13
	$\pi^+$ angle	9.0 / 8
CCother	muon momentum	17.4 / 13
	muon angle	11.6 / 9
	$\pi^+$ momentum	27.5 / 13
	$\pi^+$ angle	4.0 / 8
	$\pi^-$ momentum	12.0 / 13
	$\pi^-$ angle	13.3 / 8

Table 6.4: Summary of variables and selections considered for background model comparisons to data, and the values of found for each comparison.

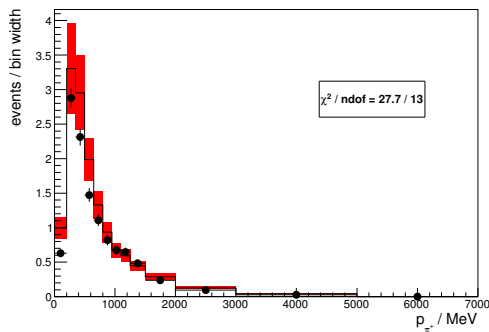
(to account for correlations between bins). In all cases the MC prediction shown is the BANFF prefit weighted NEUT MC. It is quite clear that over many kinematic variables the agreement is very good (see figures 6.5 and 6.6), suggesting that the cross section and FSI model uncertainties cover any differences between the data and the model. The  $\chi^2$  values obtained show that in general the uncertainty is a good representation of the level of agreement. Table 6.4 summarises the selections, variables, and  $\chi^2$  values found.



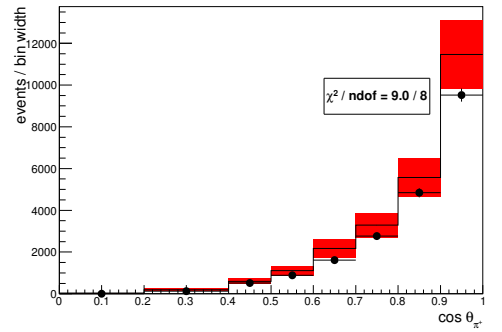
(a) Muon momentum



(b) Muon angle

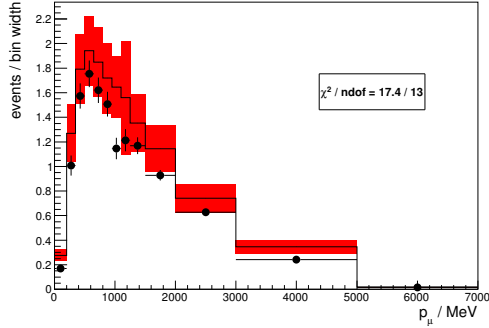


(c) Leading positive pion momentum

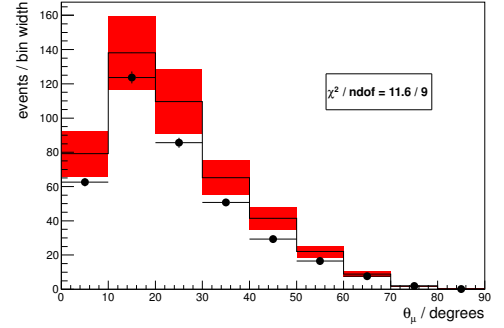


(d) Leading positive pion angle cosine

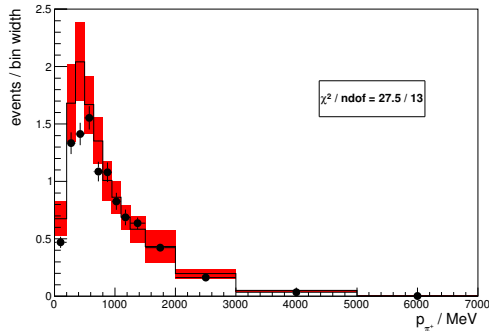
Figure 6.5:  $CC1\pi$  selection data compared to Monte Carlo for several variables. The red error band indicates the MC uncertainties due to cross section and FSI modelling, as well as the MC statistics. The black error bars indicate the data statistical uncertainty.



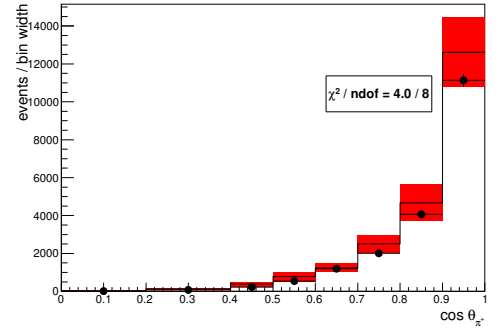
(a) Muon momentum



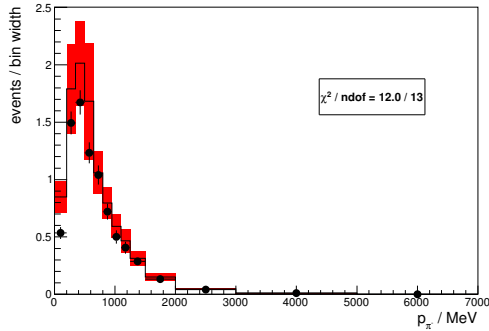
(b) Muon angle



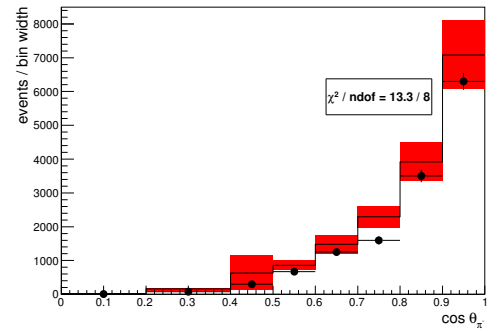
(c) Leading positive pion momentum



(d) Leading positive pion angle cosine



(e) Leading negative pion momentum



(f) Leading negative pion angle cosine

Figure 6.6: CCoher selection data compared to Monte Carlo for several variables. The red error band indicates the MC uncertainties due to cross section and FSI modelling, as well as the MC statistics. The black error bars indicate the data statistical uncertainty.

## 6.5 Binning choice

Binnings were optimised to ensure that shape errors were not dominated by statistical uncertainties. In 2 dimensions this is difficult to maintain everywhere, so in those cases the low cross section regions were neglected in favour of the high cross section peak.

Two binning regimes are considered for the 2D result. The first covers the full phase space available to true particles, and the second is restricted to regions of phase space where the ND280 selection efficiency is greater than about 30% (i.e. momentum above 200 MeV, and  $\cos\theta$  above 0.6). This “restricted phase-space” binning does still contain bins on the edge of the available phase-space, for example at a high angle and high momentum, where very few signal events are expected, and importantly no signal events are simulated. The efficiency in this region is not well defined, however the framework used does not allow binning schemes to be non-rectangular, so these bins are masked by hand, for both true and reconstructed events.

Figure 6.7 shows a graphical representation of the restricted phase space region. The restricted phase space is expected to contain roughly 55% of the total number of events in the full phase space, but 85% of the total selected events. Figure 6.8 shows the selection efficiency in 2D, with the restricted phase space indicated. It is clear that most of the phase space being cut out has zero or undefined efficiency, and all bins in the restricted phase space have efficiencies above 30%. It should be noted that the binning in momentum extends up to 30 GeV, however in most plots this bin will be cut off at 7 GeV for readability.

For convenience, a 1D representation of the full 2D phase space will frequently be used. In these cases, the axis will be simply labelled “bin number”. This bin number corresponds to looping through momentum bins for each angular bin in turn, with the angular bins ordered in increasing  $\cos\theta$ . i.e. the lowest 3 momentum bins of the first angular bin are bins 1, 2, and 3, and the second angular bin starts at bin number 12 (for the restricted phase space).

The response matrix for the final binning is shown in figure 6.9 (for the full phase space – the reconstructed phase space response matrix is very similar). The bin width is of a similar order of magnitude to the resolution, however the resolution function has a narrow peak with long tails so an unfolding procedure is expected to be necessary to account for the migration between bins. In fact, the angular resolution is very good, it is the momentum resolution which is most limiting. Figure 6.10 shows the how the angular and momentum resolutions vary

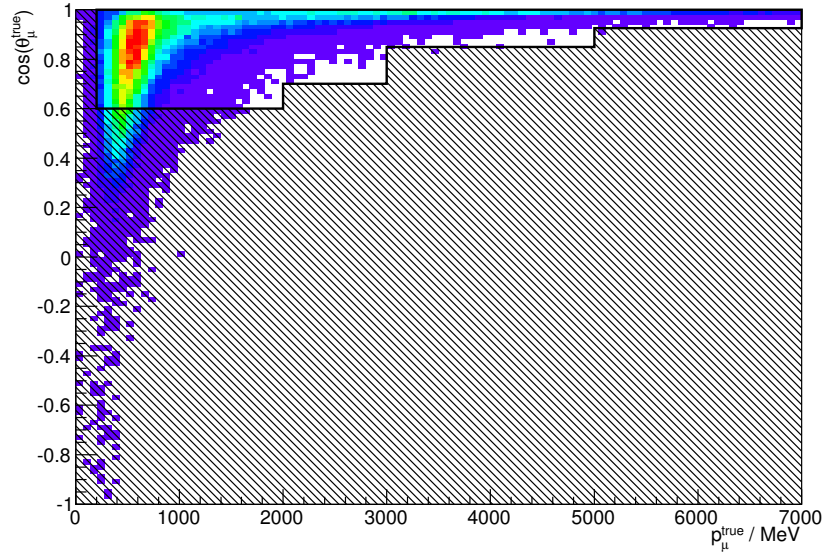


Figure 6.7: Demonstration of the region considered for the restricted phase space. The 2D histogram shows all selected events, and the non-shaded region is the restricted phase space region.

across the phase space, compared to the bin widths across that phase space. The resolutions shown in this figure are the Gaussian resolutions, estimated by fitting Gaussians to the distribution of (true - reco) in each bin. This resolution is slightly misleading as the distribution is non-Gaussian and has quite long tails, leading to additional migration.

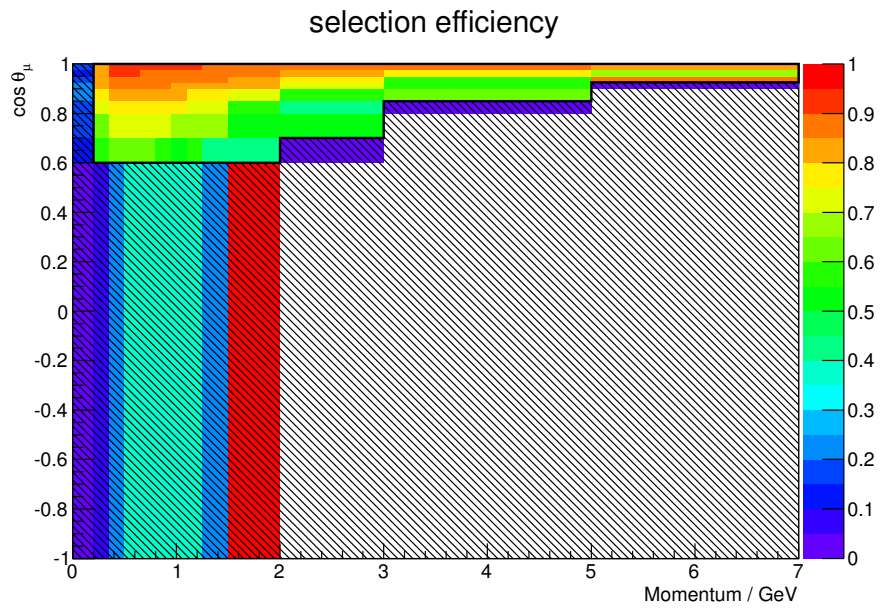


Figure 6.8: Demonstration of the region considered for the restricted phase space. The 2D histogram shows the selection efficiency, and the non-shaded region is the restricted phase space region. Bins near the edge of the phase space have low statistics and the efficiency will have a large uncertainty.

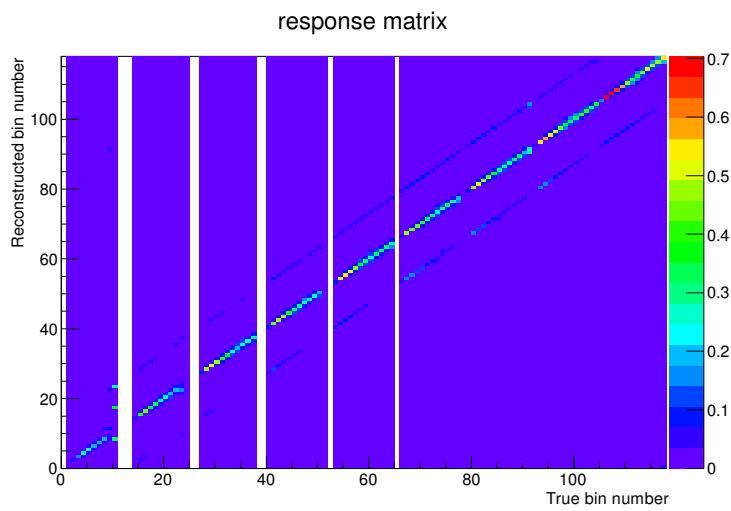


Figure 6.9: Response matrix for the full phase space

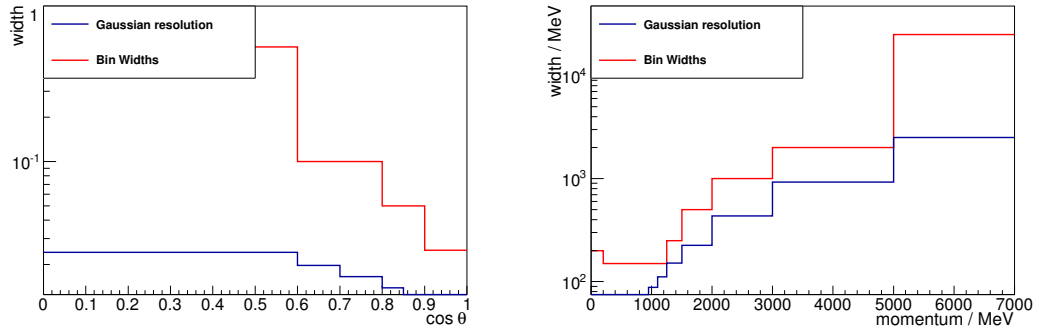


Figure 6.10: (left) Angular resolution and (right) momentum resolution, as a function of the respective variable. The relevant bin widths are also shown for comparison. Note that the resolution is generally smaller than the bin width.

## 6.6 Fake data studies

This analysis was performed blind to the data in the signal selection, though the real data was looked at in the  $CC1\pi$  and  $CCother$  samples to ensure adequate coverage by the background uncertainties. Fake data sets were used to study the effects of various aspects of the unfolding procedure.

### 6.6.1 Fake data sets used

For all of these tests, the nominal NEUT MC sample is used to generate the prior for unfolding, however the fake data sample is changed each time. The fake data sets used were:

- **NEUT training MC**

The first fake data set considered is a replica of the sample used to generate the priors. This data set is intended only for very simple tests of internal consistency.

- **Statistically independent NEUT MC**

A second NEUT sample was generated, using a statistically independent set of events. The simulated POT was the same as the real data POT.

- **GENIE MC**

A data-sized sample of GENIE MC was generated, this was taken from the official ND280 5F production. This production used the official GENIE release v2.6.4.

- **NEUT MC with spectral function nuclear model**

The computing group ran a special production using the spectral function nuclear model for CCQE events, as described in chapter 5. This was a “basket” production, meaning that events were only generated in the basket, not the surrounding ECal and magnet region. For this reason the external backgrounds are not correctly simulated and a similar basket production was used for the training. The training basket MC does not have as much simulated POT as the full MC, so the fake data POT is boosted to try to account for this, however it should be noted that tests with this sample are more statistically limited.

- **“crazy” weighted NEUT MC**

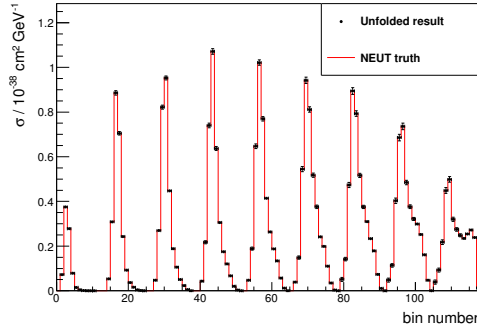
This is the same set of events as the “statistically independent” NEUT sample, however the events are reweighted as a function of neutrino energy to give the sample a very different shape and normalisation, as well as potentially varying the efficiency for any events where the efficiency varies with neutrino energy.

### 6.6.2 Reproducing MC truth

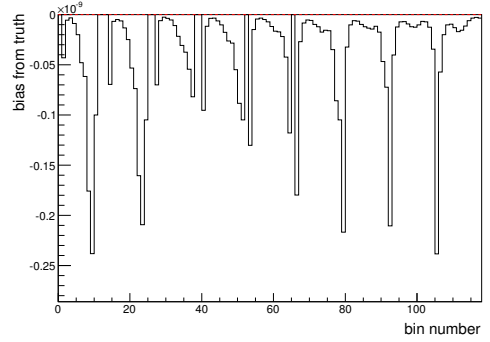
For a simple check of the software, the nominal MC (scaled to data POT) is unfolded with itself using one iteration. The expectation is to see a perfect match of the unfolded fake data to the MC prediction. Figure 6.11a shows the true prediction from the MC, and the unfolded distribution with statistical uncertainties. It can be clearly seen that the unfolded result matches the prediction well. Figure 6.11b shows the fractional bias as a function of bin number, where the fractional bias is defined as the fractional difference between the unfolded result and the true prediction from the MC. The biases can be seen to be very small (order  $10^{-10}$ ), suggesting that the unfolding routines work correctly within numerical precision of the order  $10^{-10}$ . Figure 6.12 shows the same for the restricted phase space analysis. Again, the biases are very small.

### 6.6.3 Number of iterations

As discussed in section 6.4.2, the Bayesian unfolding technique as described by D’Agostini [111] can be performed iteratively, but problems can be seen when too many iterations are performed. In this section we will consider what happens to the results as the number of iterations is varied. It is possible to consider “zero” iterations, in which we assume that there is no migration between bins, and simply apply an efficiency correction in each bin. This is not considered sensible in the

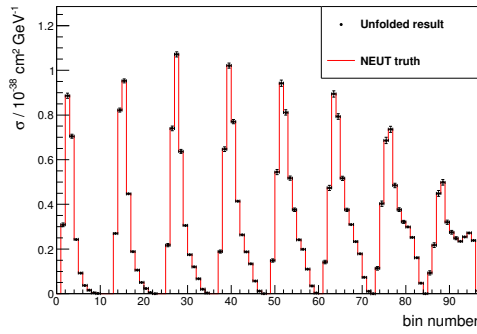


(a) The result when unfolding the nominal MC with itself.

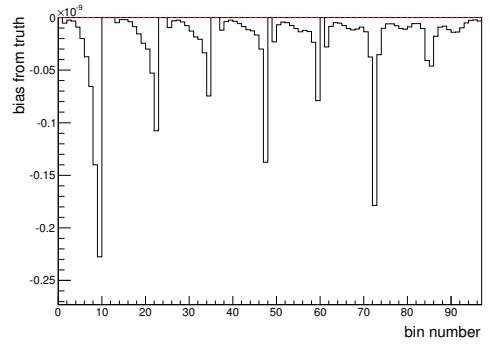


(b) Biases when unfolding MC with itself.

Figure 6.11: The unfolded result compared to truth, and biases from truth, for the case where the training MC is used as the fake data set. The full phase space is used.



(a) The result when unfolding the nominal MC with itself.



(b) Biases when unfolding MC with itself.

Figure 6.12: The unfolded result compared to truth, and biases from truth, for the case where the training MC is used as the fake data set. The restricted phase space is used.

full phase space analysis, as there are regions where we rely almost entirely on the unfolding to predict the number of events.

The metrics that will be considered are:

- fractional bias from expected true result
- statistical uncertainty
- convergence

As there are many bins, we shall consider the mean and spread of these quantities

over all bins, and we shall restrict our considerations to bins where the predicted cross section is more than 10% of the maximum, as the bins that do not fulfil this condition tend to be very low cross section bins with large statistical fluctuations, and do not provide much information. Cutting out these bins gives us a “truncated” mean and RMS for the bias and statistical uncertainty, over the remaining bins. The truncated mean bias will hereafter be referred to as  $\mu'_b$ , the truncated RMS bias will be referred to as  $\sigma'_b$ , and the truncated mean statistical uncertainty will be referred to as  $\mu'_s$ . The convergence is determined by the  $\chi^2$  of change between iterations, defined as

$$\chi_N^2 = \sum_i^{\text{all bins}} \frac{(x_N^i - x_{N-1}^i)^2}{(\sigma_N^i)^2} \quad (6.11)$$

where  $x_N^i$  is the cross section result in bin  $i$ , after  $N$  iterations, and  $\sigma_N^i$  is the statistical uncertainty on the result in bin  $i$ , after  $N$  iterations. For the case of zero iterations, iteration  $N - 1$  is taken to be the true result, simply for something to compare to. If the results from iteration  $N+1$  agree with those from iteration  $N$ , within statistical uncertainty, then there is no need to perform iteration  $N + 1$ . This  $\chi^2$  of change takes all non-zero bins into account, including the low cross section bins which are omitted for the bias and uncertainty considerations, however the bin contents must be non-zero in both iteration  $N$  and  $N - 1$ . This should not be viewed as a true  $\chi^2$  test, as the two results have the same input data, but a useful number that demonstrates whether the result has converged or if the unfolding is still being trained by the data.

### 6.6.3.1 NEUT fake data

The first test is the case where the fake data is a statistically independent NEUT sample. In this case we expect the prior to be very close to the “measured” true distribution. Figure 6.13 shows the distributions for the full- and restricted-phase space after one iteration, compared to the true distributions as predicted by the training sample, and the fake data sample (which can vary within statistics).

$\mu'_s$  is shown as a function of iteration in figure 6.14. It can be seen that the uncertainty is smallest for the case of 1 iteration being performed, after which the uncertainties increase. In addition, figure 6.15 shows the mean and RMS of the bin-by-bin biases from truth ( $\mu'_b$  and  $\sigma'_b$ ), and it can be seen that the mean bias is smallest for 1 iteration, and the spread of the biases is also smaller, indicating that this is the point where most bins are closest to the truth prediction. Finally, figure 6.16 shows the  $\chi^2$  per degree of freedom for the change between each iteration, which

falls below 1 for iteration 2 suggesting iterations 1 and 2 are in agreement and there is no need to perform the additional iteration.

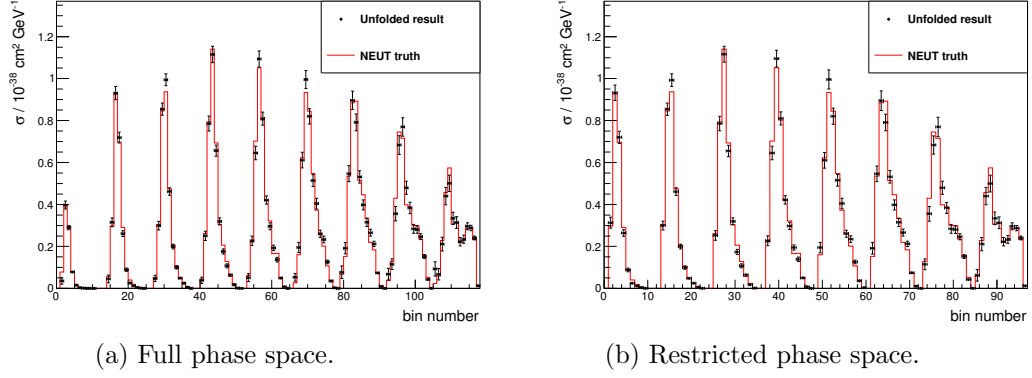


Figure 6.13: Unfolded distributions compared to the true predictions, after 1 iteration, for a statistically independent NEUT fake data sample.

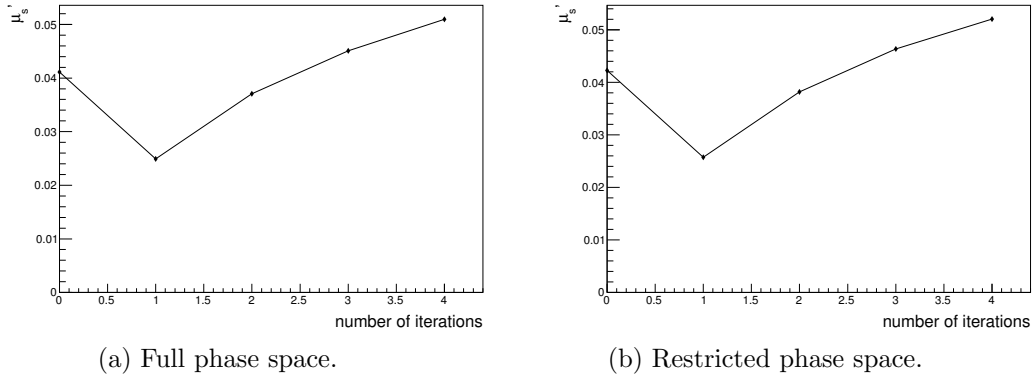


Figure 6.14: Mean statistical uncertainty,  $\mu'_s$ , as a function of number of iterations, for a statistically independent NEUT fake data sample. Left is the full phase space, right is the restricted phase space.

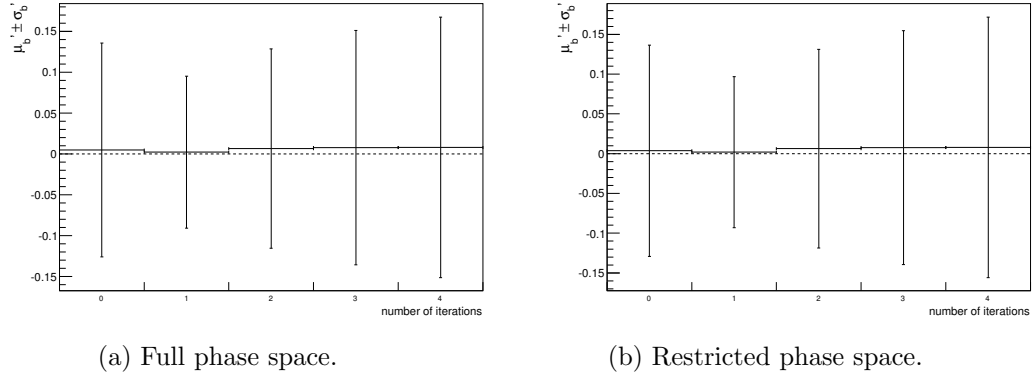


Figure 6.15: Mean and RMS bias,  $\mu'_b \pm \sigma'_b$ , as a function of number of iterations, for a statistically independent NEUT fake data sample. Left is the full phase space, right is the restricted phase space.

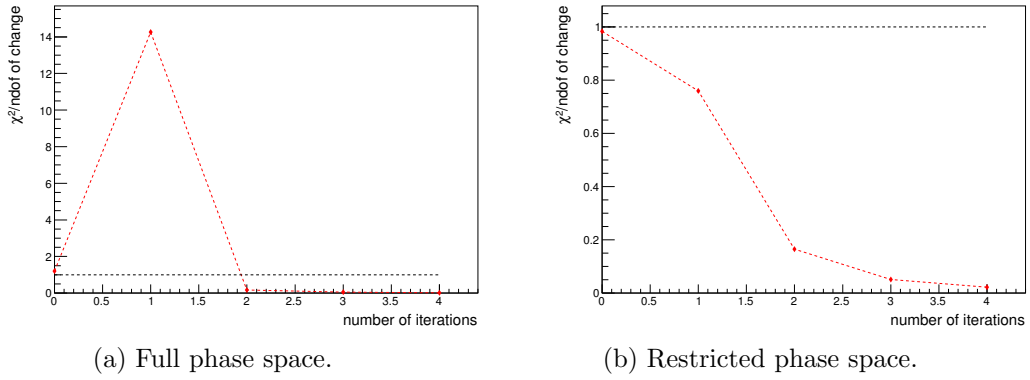


Figure 6.16:  $\chi^2$  of change, as a function of number of iterations, for a statistically independent NEUT fake data sample. Left is the full phase space, right is the restricted phase space.

Of course, we expect to be able to unfold a model with itself in one iteration, and it is well known that the uncertainties increase as the number of iterations increases. A better test is to use different models for the training prior and the fake data, to see if more iterations are required in this case.

### 6.6.3.2 Fake data with different models

Two more tests were performed, using the GENIE and SF fake data samples. Figures 6.17, 6.18, and 6.19 show the same set of plots for the GENIE fake data sample, and 6.20, 6.21, and 6.22 show the same plots for the SF fake data sample. In each case the conclusion is the same - using one iteration of unfolding achieves the smallest

statistical uncertainties and the smallest biases, on average across all bins, and is enough to converge on a stable solution, so there is no need to perform an extra iteration.

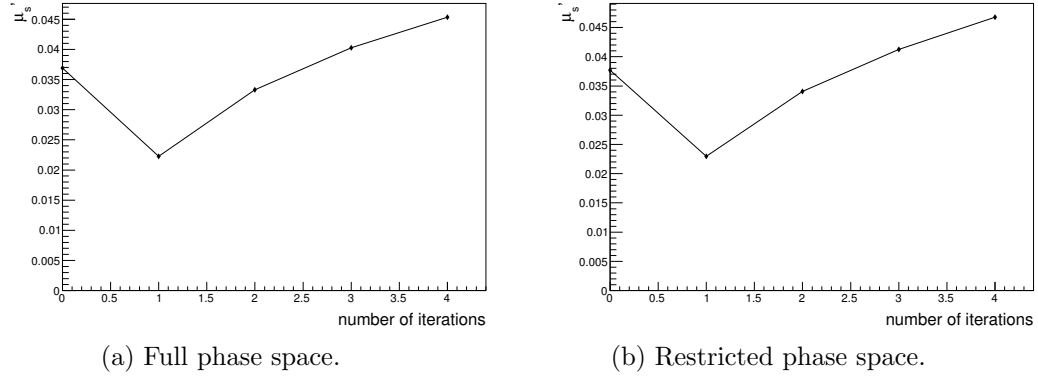


Figure 6.17: Mean statistical uncertainty,  $\mu'_s$ , as a function of number of iterations, for a GENIE fake data sample. Left is the full phase space, right is the restricted phase space.

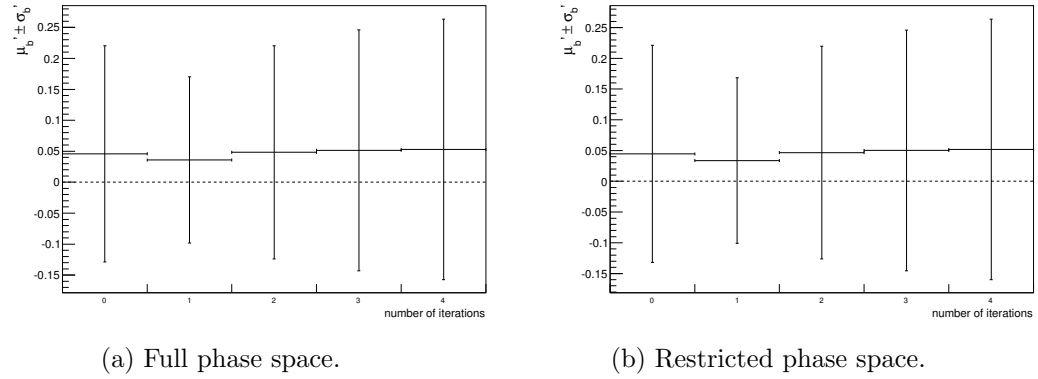
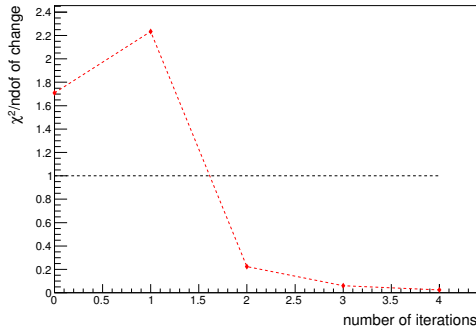
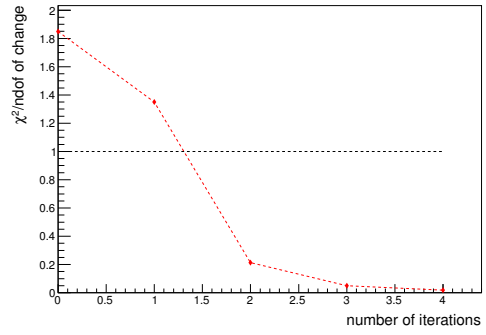


Figure 6.18: Mean and RMS bias,  $\mu'_b \pm \sigma'_b$ , as a function of number of iterations, for a GENIE fake data sample. Left is the full phase space, right is the restricted phase space.

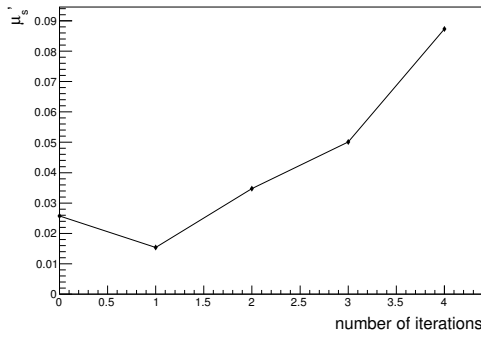


(a) Full phase space.

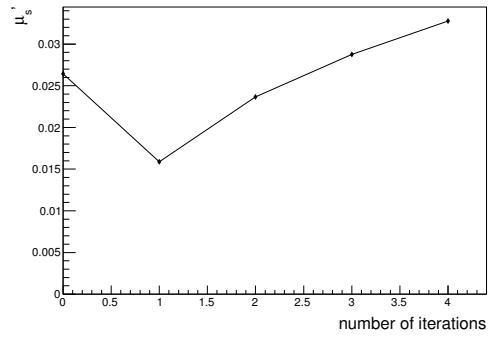


(b) Restricted phase space.

Figure 6.19:  $\chi^2$  of change, as a function of number of iterations, for a GENIE fake data sample. Left is the full phase space, right is the restricted phase space.



(a) Full phase space.



(b) Restricted phase space.

Figure 6.20: Mean statistical uncertainty,  $\mu'_s$ , as a function of number of iterations, for a SF fake data sample. Left is the full phase space, right is the restricted phase space.

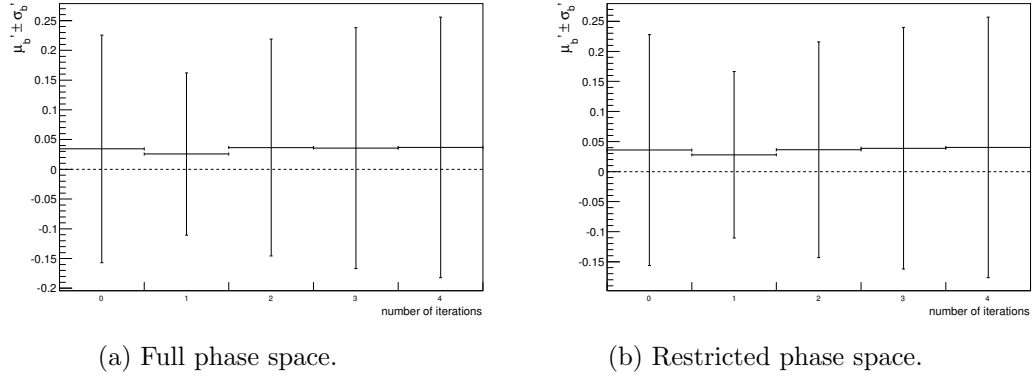


Figure 6.21: Mean and RMS bias,  $\mu'_b \pm \sigma'_b$ , as a function of number of iterations, for a SF fake data sample. Left is the full phase space, right is the restricted phase space.

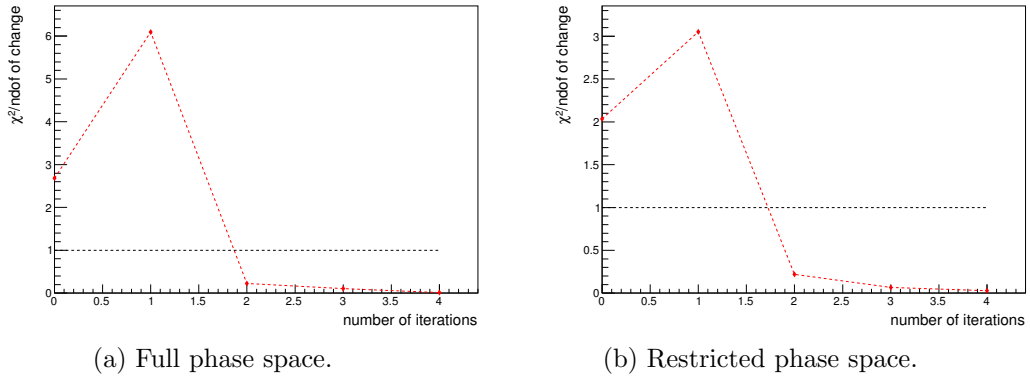
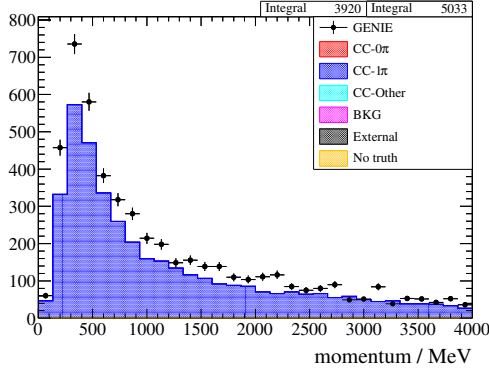
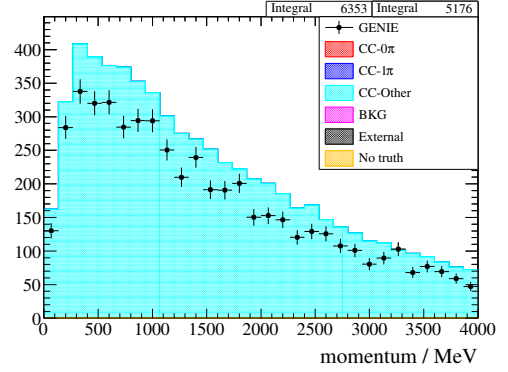


Figure 6.22:  $\chi^2$  of change, as a function of number of iterations, for a SF fake data sample. Left is the full phase space, right is the restricted phase space.

The GENIE fake data sample sees a reasonably large mean bias of almost 5%. This is not unexpected, as the background models used in GENIE are different to those in NEUT (see figure 6.23). Figure 6.24 shows the GENIE unfolded result compared to the NEUT and GENIE truth predictions, with the inclusion of only statistical and cross section uncertainties (inner error bars are statistical only). It can be clearly seen that the unfolded GENIE result agrees with the GENIE truth prediction within the given uncertainty, which is expected to be the dominant source of uncertainty between the two.

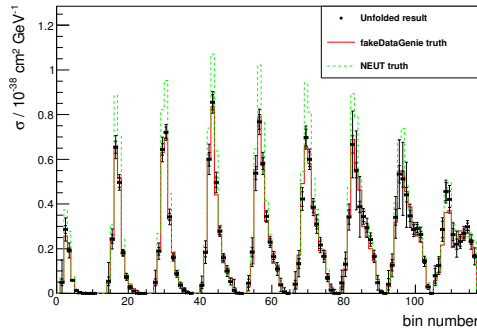


(a) CC1 $\pi$  events

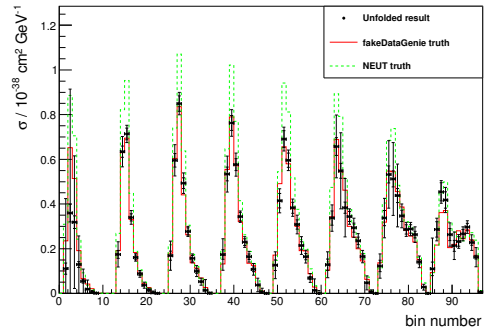


(b) CCothers events

Figure 6.23: Momentum distributions of all CC1 $\pi$  and CCothers events, for NEUT and GENIE, normalised by POT. The bullets represent GENIE MC, the filled histograms represent NEUT. Clear differences are visible in shape and normalisation.



(a) Full phase space.



(b) Restricted phase space.

Figure 6.24: GENIE fake data unfolded results compared to the GENIE (red, solid) and NEUT (green, dashed) truth predictions. Inner error bars are statistical only, and outer error bars are statistical and cross section uncertainties. Only a few bins are more than one standard deviation away from the GENIE truth prediction, showing that the uncertainties cover the difference between NEUT and GENIE background predictions.

#### 6.6.4 “crazy” MC weighting

As a final test of the unfolding algorithm, a fake data set was used which comprised the nominal NEUT fake data set, with an additional reweighting applied to all true  $CC0\pi$  events. In this reweighting, CCQE events were given a weight 0.9, and resonant events were given a weight 1.2. In addition all charged current events were weighted as a function of neutrino energy. Energies above 2 GeV were given a weight of 1. Between 1.5 GeV and 2 GeV, the weight changes linearly from 1.5 to 1. Between 0.5 GeV and 1.5 GeV, the weight changes linearly from 0.5 to 1.5. Below 0.5, the weight changes linearly from 1 to 0.5. Figure 6.25 shows the weight used as a function of neutrino energy, as this is an easier method of representing it.

Note, this weighting as a function of neutrino energy does not affect the flux, but affects the energy dependence of the cross section for signal events.

Figure 6.26 shows the unfolded result with statistical errors only, for the crazy data set, as well as the truth prediction for that crazy data set. From this test it is clear that the unfolding algorithm is able to deal with drastic differences between the data and the prior used for training, as the unfolded data is in good agreement with the expected truth, and not with the prior (shown in green). This is the case even though the prior and fake data differ in normalisation by up to a factor of 2, but also in shape. We expect that our real data has a more similar shape to the prior than this crazy model as the nominal model and parameters have shown reasonable agreement with real data in other fits (and indeed the T2K oscillation analysis), so there is good reason to expect that the unfolding algorithm with one iteration will not bias our data measurement considerably.

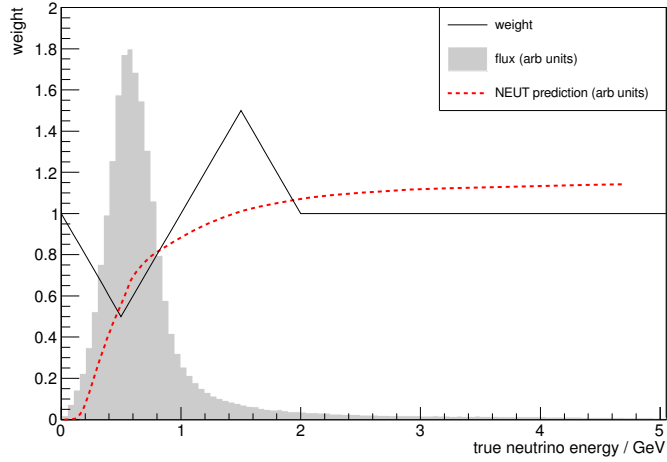


Figure 6.25: Weights applied as a function of true neutrino energy, for the crazy data set. Also shown for reference are the neutrino flux, and the NEUT cross section prediction (both in arbitrary units).

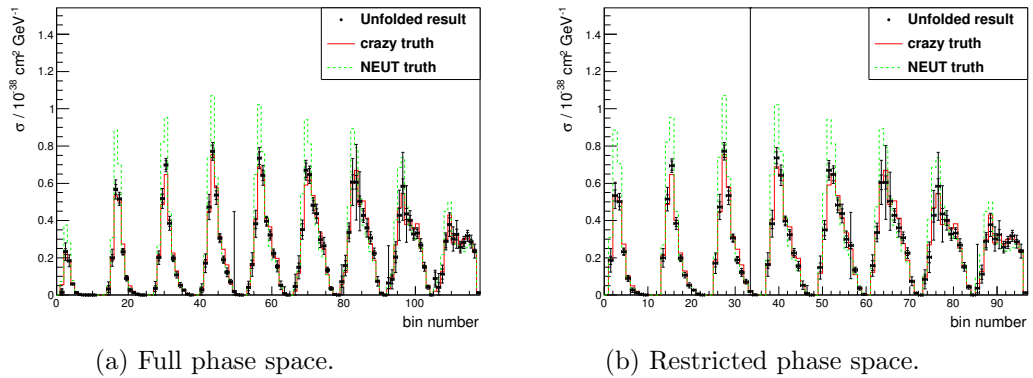


Figure 6.26: Crazy MC unfolded results as a function of bin number, the left shows the full phase-space, and the right shows the restricted phase-space. Inner error bars are data statistics only, outer error bars include the cross section model uncertainty.

## 6.7 Results

In this section, the final uncertainties and results on real T2K data are discussed.

### 6.7.1 Uncertainties

Figure 6.27 shows the size of the fractional uncertainties in all bins, in the full phase-space analysis. In general, the flux normalisation uncertainty is dominant around the peak, though towards the edges of the phase space the other sources of uncertainty increase in size, and can become dominant in these regions.

Table 6.5 shows the effect of different sources of uncertainty on the integrated cross section value for the full phase space, and table 6.6 shows the effect of the same sources on the restricted phase space analysis.

Source	Effect
FGDMass	0.78 %
BField	0.35 %
ChargeConf	3.11 %
FGDPID	0.12 %
FGDTrackEff	1.34 %
MomRes	0.69 %
MomScale	0.60 %
OOFV	3.02 %
PileUp	0.11 %
SandMuons	0.12 %
SIPion	2.03 %
TPCClusterEff	negligible
TPCFGDMatchEff	negligible
TPCPID	0.71 %
TPCTrackEff	0.13 %
MichelEleEff	0.70 %
detector total	4.93 %
data statistics	2.13 %
MC statistics	0.70 %
Cross section	6.52 %
Flux	16.12 %
FSI	3.96 %
total	18.64 %

Table 6.5: Effect of different sources of uncertainty on total cross section value for the full phase space.

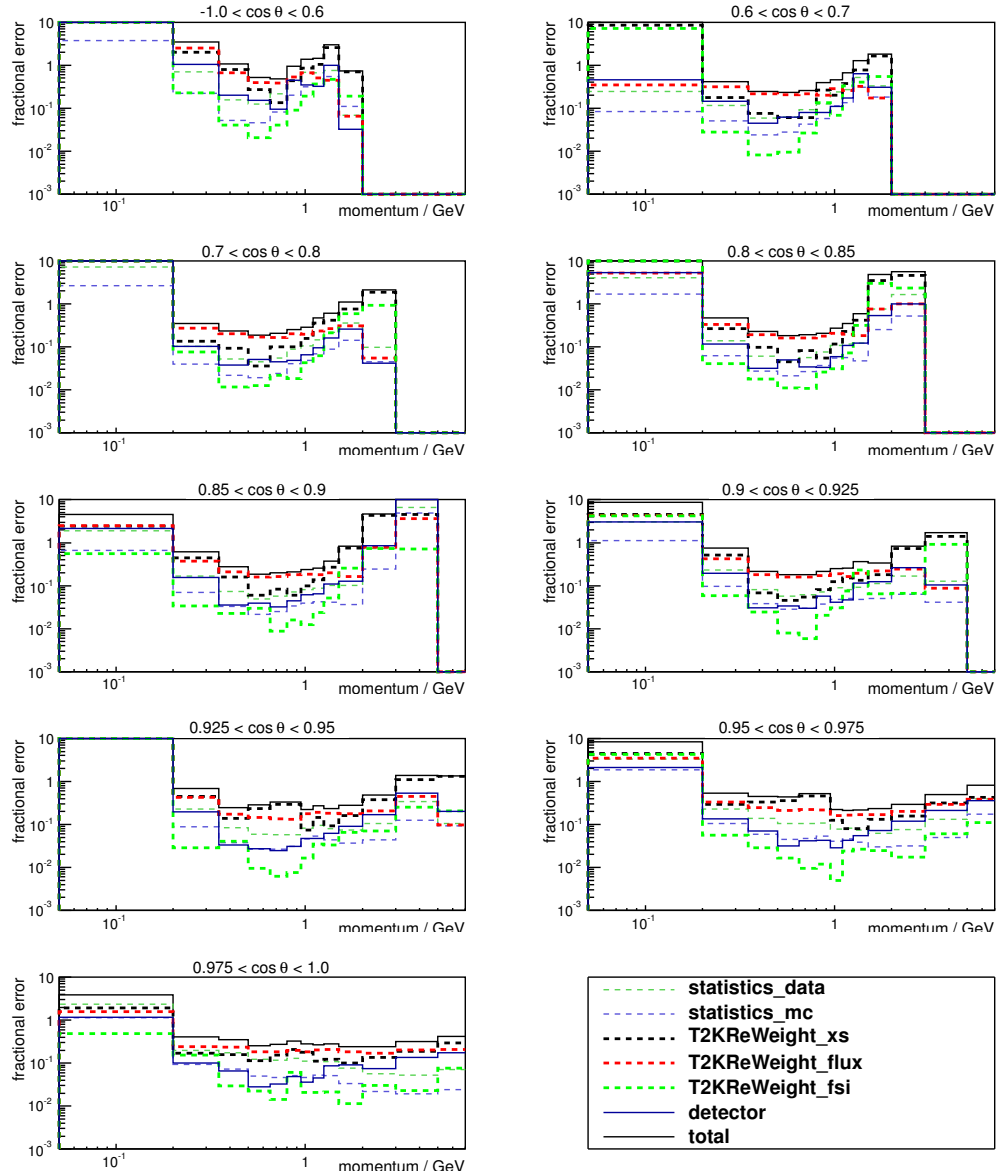


Figure 6.27: Fractional uncertainties in the full phase space analysis, divided by bins in  $\cos \theta$ . At the edges of phase space, many uncertainties become greater than 100%, however in the important regions the uncertainties are usually dominated by a 10-15% flux uncertainty.

Source	Effect
FGDMass	0.82 %
BField	negligible
ChargeConf	2.54 %
FGDPID	negligible
FGDTrackEff	1.83 %
MomRes	0.56 %
MomScale	negligible
OOFV	0.73 %
PileUp	0.11 %
SandMuons	negligible
SIPion	3.28 %
TPCClusterEff	negligible
TPCFGDMatchEff	negligible
TPCPID	1.14 %
TPCTrackEff	0.19 %
MichelEleEff	0.96 %
detector total	4.63 %
data statistics	1.31 %
MC statistics	0.47 %
Cross section	5.57 %
Flux	15.82 %
FSI	1.51 %
total	17.52 %

Table 6.6: Effect of different sources of uncertainty on total cross section value for the restricted phase space.

### 6.7.2 Double differential cross section results

Figure 6.28 shows a “lego plot” representation of the results with the uncertainty in each bin. Figure 6.29 shows the same style plot for the restricted phase space analysis.

A more clear, though less concise way of presenting the data is to draw slices in a variable. Figures 6.30, and 6.31 show the final result with full uncertainties, for the full phase-space and restricted phase-space analyses respectively. In this case the “sliced” variable is  $\cos\theta$ , however appendix B.1 contains slices in momentum, as well as plots where the momentum axis is shown without the log scale.

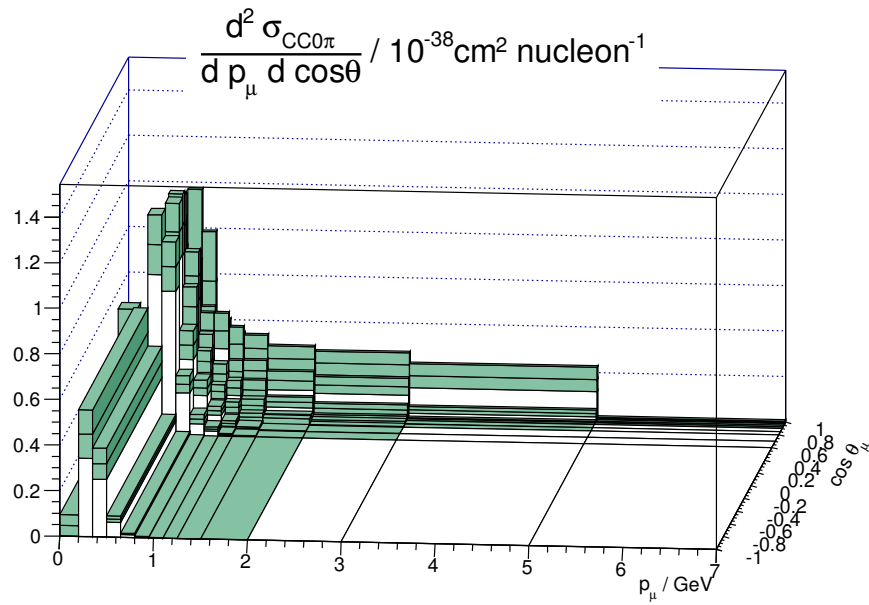


Figure 6.28: “Lego plot” of results with full uncertainties, full phase space.

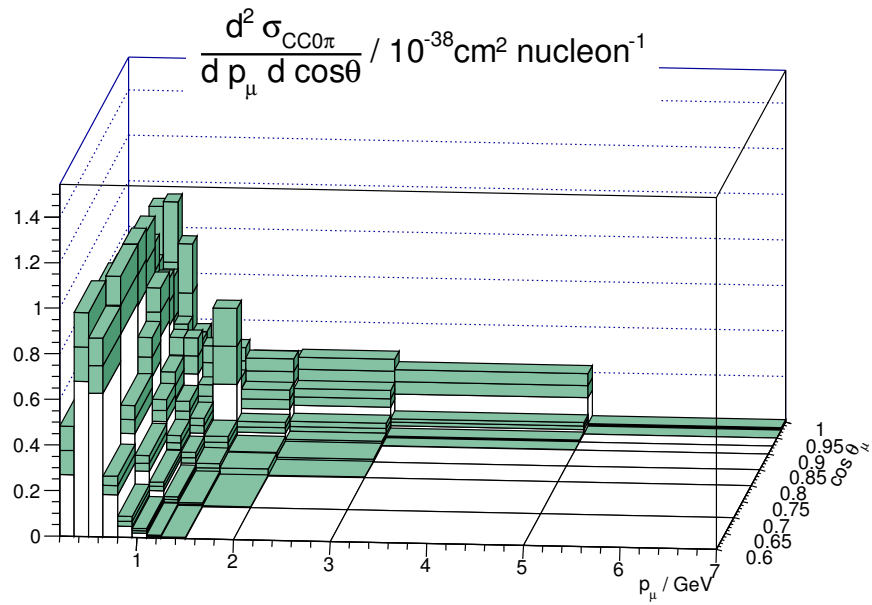


Figure 6.29: “Lego plot” of results with full uncertainties, restricted phase space.

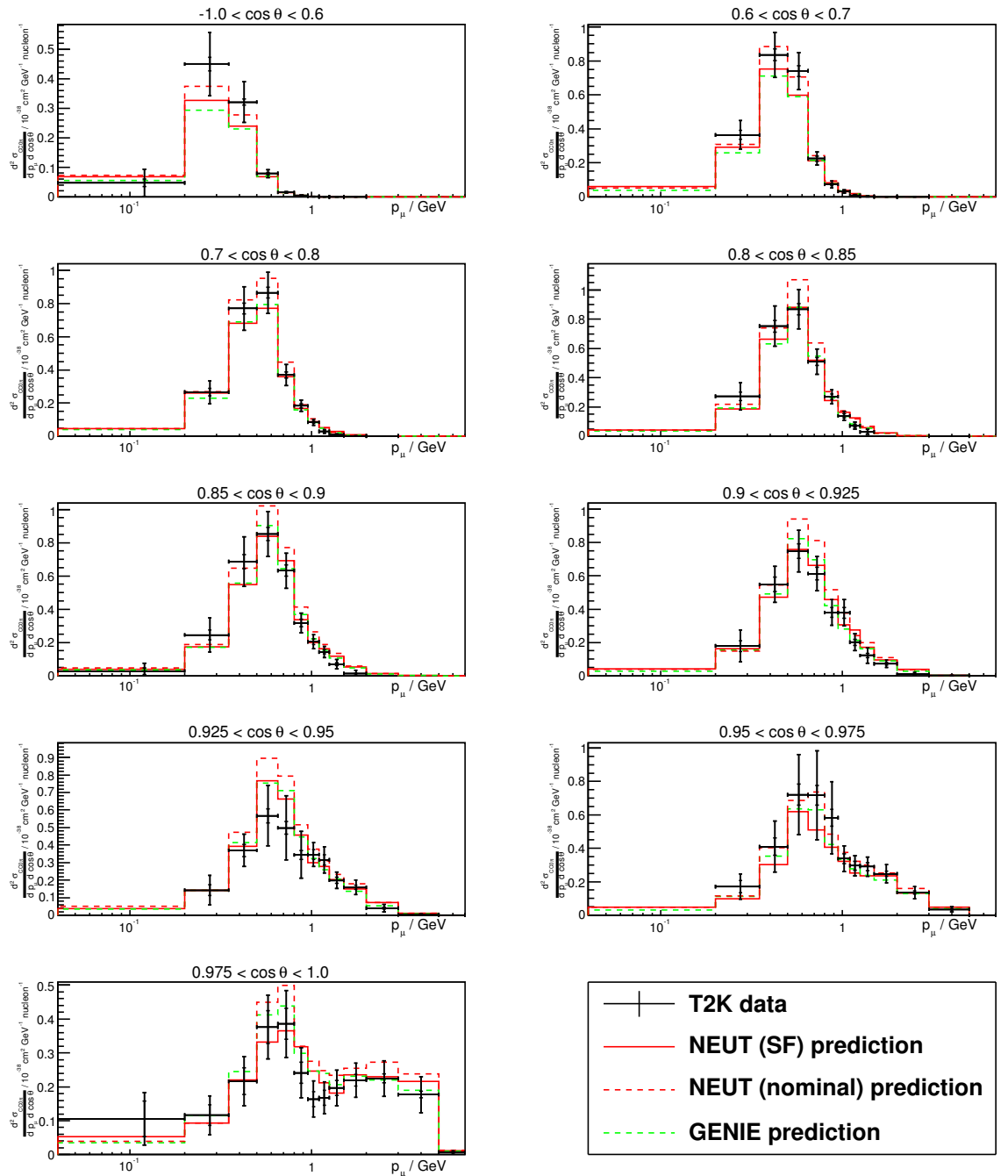


Figure 6.30: Full phase-space results, compared to the NEUT nominal prediction, GENIE nominal prediction, and also the SF model prediction. Inner error bars are statistical only.

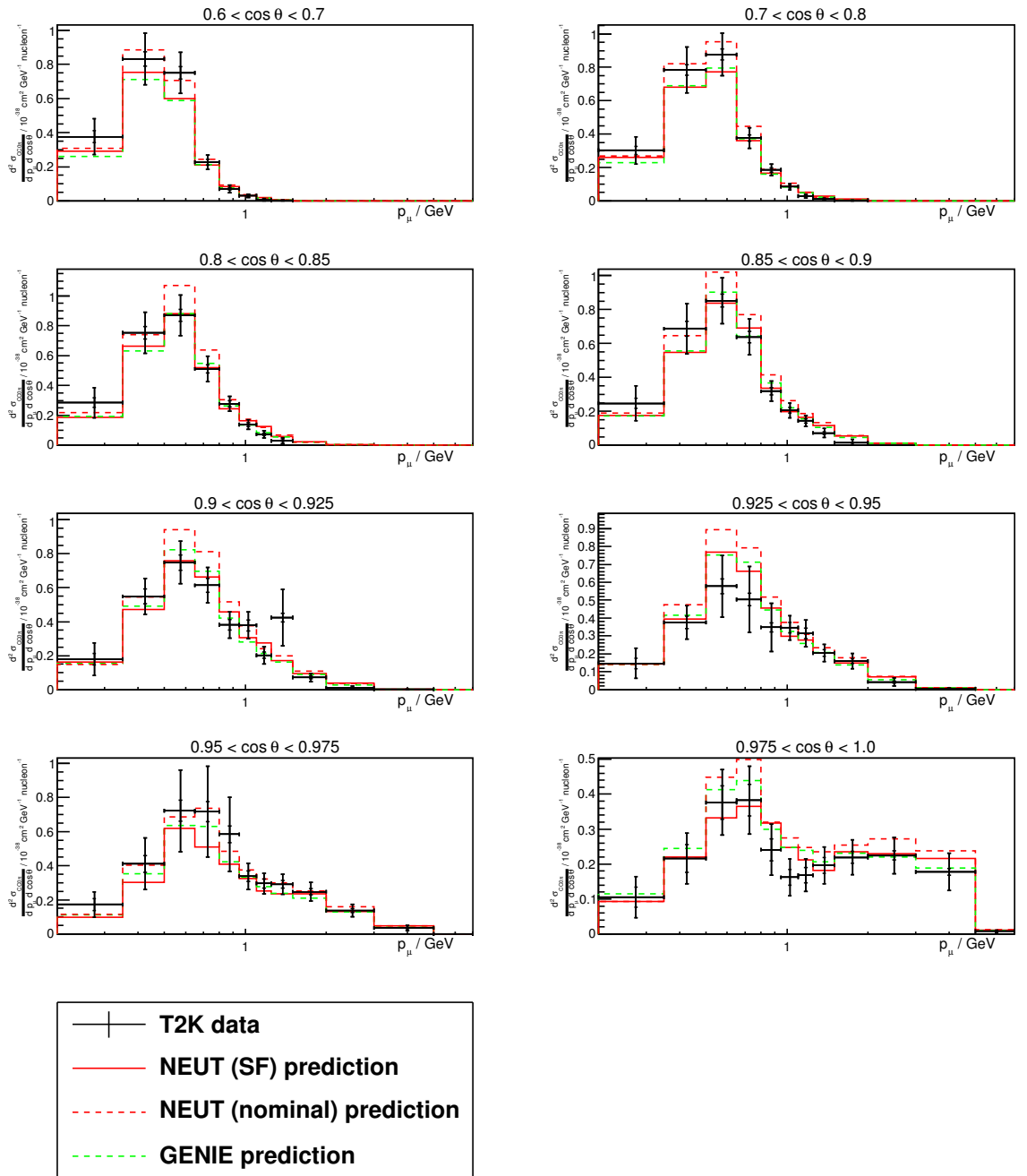


Figure 6.31: Restricted phase-space results, compared to the NEUT nominal prediction, GENIE nominal prediction, and also the SF model prediction. Inner error bars are statistical only.

As the error bars are correlated, a  $\chi^2$  value is calculated to show the level of agreement with each of the generator predictions. These values are summarised in table 6.7. All give relatively poor agreement, with GENIE giving the best agreement to the data with the SF model giving the worst of agreement.

Generator	$\chi^2/\text{ndof}$
NEUT	135.6 / 83
GENIE	130.1 / 83
SF	186.8 / 83

Table 6.7:  $\chi^2$  of agreement between three generator predictions and the double-differential data. The restricted phase space is used as the full-phase space results have larger uncertainties and more model-dependence.

### 6.7.3 Single differential cross section results

It may be easier to interpret the results physically if they are projected onto one axis. Instead of “projecting” the 2D results, the data is simply unfolded directly through the muon momentum, muon angle, or the variable  $Q_{QE}^2$  (which is calculated directly from the muon momentum and angle, as defined in equation 6.12).

$$Q_{QE}^2 = m_\mu^2 - 2E_\nu E_\mu + 2E_{\nu, QE} p_\mu \cos \theta_\mu \quad (6.12)$$

$$E_{\nu, QE} = \frac{M_p^2 - (M_n - E_b)^2 - m_\mu^2 + 2E_\mu(M_n - E_b)}{2(M_n - E_b - E_\mu + p_\mu \cos \theta_\mu)} \quad (6.13)$$

$M_p$  = proton mass

$M_n$  = neutron mass

$E_b$  = binding energy = 27 MeV

When performing bias studies with fake data sets, it was clear that there was a large model dependence introduced by considering the full phase space. This is because the efficiency has large variations over the full phase space. As the efficiency is relatively flat over the restricted phase space, there was no model dependence observed when only considering events from this region. For this reason, the 1D results are presented for the restricted phase space only.

Figure 6.32 shows the unfolded result on real data for the muon momentum, figure 6.33 shows the unfolded result on real data for the cosine of the muon angle, and figure 6.34 shows the unfolded result on real data for  $Q_{QE}^2$ .

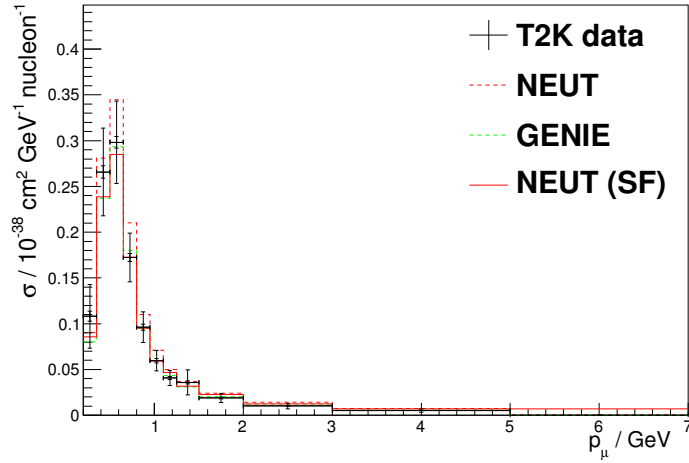


Figure 6.32: Results unfolded through muon momentum over the restricted phase-space, compared to the NEUT nominal prediction, GENIE nominal prediction, and also the SF model prediction. Inner error bars are statistical only.

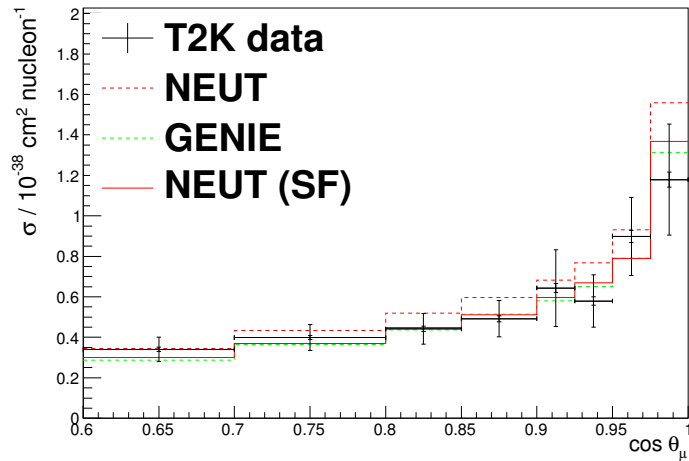


Figure 6.33: Results unfolded through muon angle over the restricted phase-space, compared to the NEUT nominal prediction, GENIE nominal prediction, and also the SF model prediction. Inner error bars are statistical only.

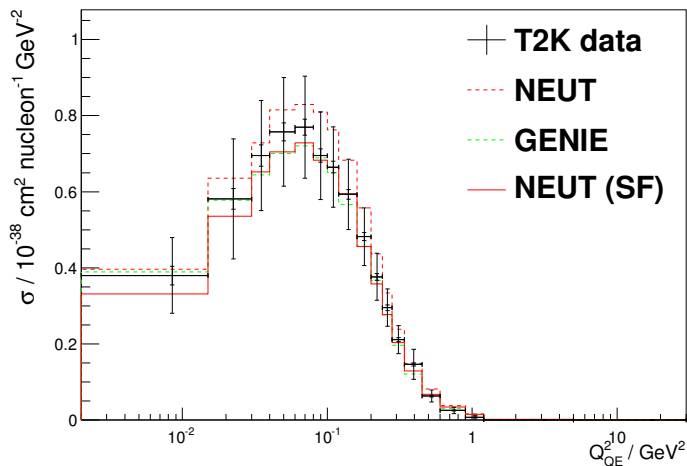


Figure 6.34: Results unfolded through  $Q_{QE}^2$  over the restricted phase-space, compared to the NEUT nominal prediction, GENIE nominal prediction, and also the SF model prediction. Inner error bars are statistical only.

#### 6.7.4 Integrated cross section results

For the full phase-space analysis, it is simple to integrate over all bins to obtain a total cross section. Each bin has a “width”,  $\Delta_i$ , which is the product of the width in each dimension. Then the total cross section is given by

$$\sigma_{total} = \sum_{i=1}^{N_{bins}} \Delta_i \sigma_i \quad (6.14)$$

and the uncertainty on that cross section, given a covariance matrix,  $V_{ij}$ , is given by

$$\sigma_\sigma = \sqrt{\sum_{i=1}^{N_{bins}} \sum_{j=1}^{N_{bins}} (V_{ij} \Delta_i)} \quad (6.15)$$

This value, and error, can be presented as a total flux-integrated cross section. The result over the full phase space is shown in figure 6.35. The data point is centred on the x-axis, at the mean value of the  $\nu_\mu$  flux, and the error bars in that direction are placed such that they contain 90% of the flux. For reference, the NEUT prediction for the  $CC0\pi$  cross section as a function of energy, as well as the flux-integrated value, are shown, as well as the flux. It should be noted that the NEUT predictions are taken from MC, and the NEUT prediction as a function of energy has been

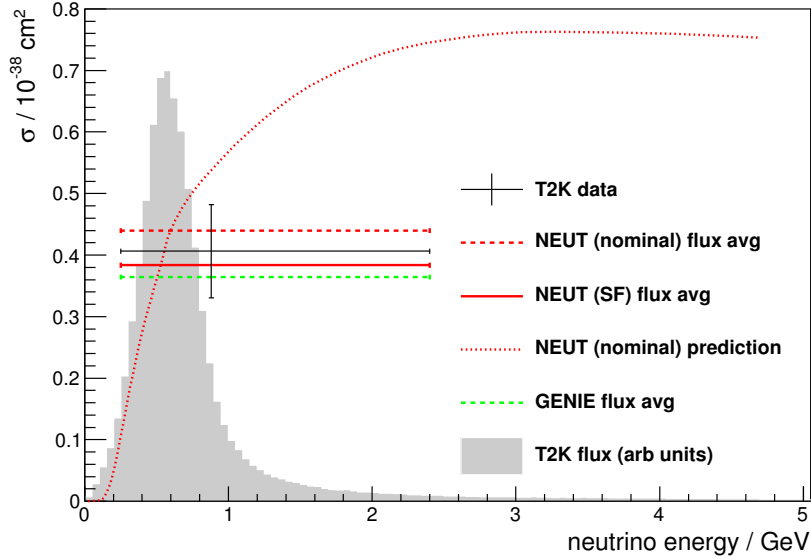


Figure 6.35: Total flux-integrated cross section.

calculated in bins, with a smooth line drawn through the centres of the bins. There is therefore some non-negligible statistical uncertainty on this line.

It is possible to define a total cross section for the restricted phase space analysis too - but in this case we only integrate over the phase space we are restricted to. This can be compared directly to generator predictions relatively simply, and has a smaller total uncertainty (which may help distinguish between models) due to the ability to ignore low cross section, and low purity, bins. This plot is shown in figure 6.36.

## 6.8 Discussion

For the full phase space result, we find a total cross section of  $\langle\sigma\rangle_\phi = (4.06 \pm 0.757)10^{-39} \text{ cm}^2 \text{ nucleon}^{-1}$ . This is in agreement with both the NEUT nominal and GENIE nominal predictions of  $\langle\sigma\rangle_\phi = 4.39 \times 10^{-39} \text{ cm}^2 \text{ nucleon}^{-1}$  and  $\langle\sigma\rangle_\phi = 3.33 \times 10^{-39} \text{ cm}^2 \text{ nucleon}^{-1}$  respectively.

When integrating over only the restricted phase space, we find a total cross section of  $\langle\sigma\rangle_\phi^{RPS} = (2.02 \pm 0.354)10^{-39} \text{ cm}^2 \text{ nucleon}^{-1}$ . This is also in agreement with the generator predictions from NEUT ( $2.52 \times 10^{-39} \text{ cm}^2 \text{ nucleon}^{-1}$ ) and GENIE ( $1.81 \times 10^{-39} \text{ cm}^2 \text{ nucleon}^{-1}$ ).

The differential results show good agreement with the SF model and the

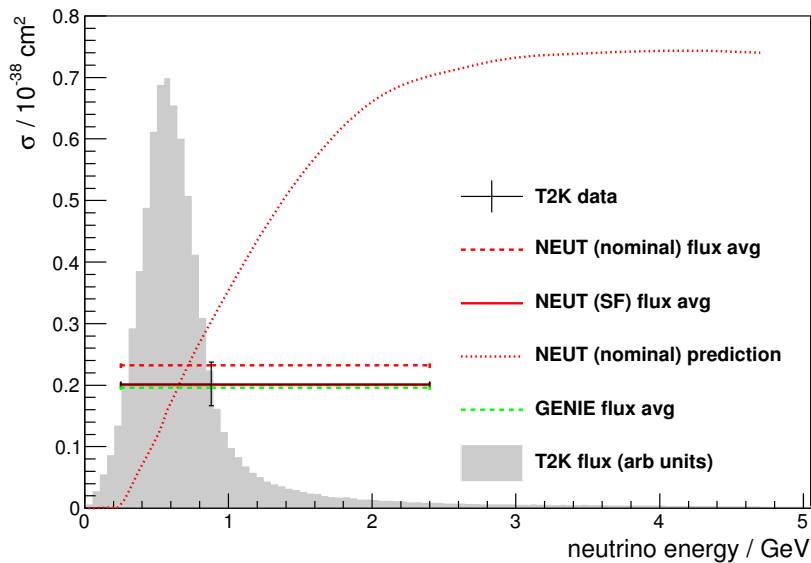


Figure 6.36: Total flux-integrated cross section over restricted phase-space only.

GENIE nominal model. In some regions of 2D phase space the data show large suppression with respect to the NEUT model. There appears to be some small enhancement at high angles, however this region is limited due to the forward nature of the selection. The most forward-going bin shows a dip in the momentum distribution around 1 GeV – this dip is predicted to be higher in momentum and not as deep by all three models.

In this particular region the muon momentum is well approximated by the neutrino energy, and as this is in the transition from the flux peak to the high energy tail this could be due to an incorrectly modelled flux.

The dominant uncertainty for this result is the flux normalisation, which contributes both to the normalisation of the final result and the number of background events that are subtracted. There are two ways to address this uncertainty – firstly simply reducing the flux normalisation is possible by using new data from NA61/SHINE which has reduced uncertainties and increased phase space coverage. Finding a good way to constrain the number of CC1pi and CCothers background events would improve the secondary flux uncertainty, and also improve the uncertainty due to cross section model uncertainties – the second largest uncertainty source.

These results have been shown to be highly independent of the signal model used, however there is a dependence on the background model used. This depen-

dence has been shown to be covered by the systematic uncertainties applied to this background model.

Understanding this channel is critical for the reduction of uncertainties on oscillation parameters and the observation of CP-violating effects in the neutrino sector. Taken with other modern data on CCQE-like interactions on nuclear targets at low energies, this data is expected to be able to inform models and theories and lead to greatly improved understanding of this interaction channel.

Future effort should be focused on identifying protons in these event samples and comparing their multiplicity and kinematics to those predicted from models. This should open up the possibility of identifying the presence of correlated nucleons in the nucleus.

## Chapter 7

# Conclusions

This thesis presents two analyses related to charged current quasi elastic neutrino scattering off medium sized nuclear targets. In chapter 5 the implementation of the spectral function nuclear model in the NEUT interaction generator was described. This model is more sophisticated than the previous relativistic Fermi gas model, and includes effects such as short-range nucleon-nucleon correlations which lead to 2-particle knock out. The model was selected due to its improved agreement with electron scattering data when compared with the RFG model. Relevant uncertainties on the model were identified and included in the T2K error reweighting package.

In chapter 6 the T2K near detector, ND280, was used to perform a model-independent measurement of the CCQE-like cross section, as a function of reconstructed kinematic variables. The total cross section was found to be  $(4.06 \pm 0.757) \times 10^{-39} \text{ cm}^2 \text{ nucleon}^{-1}$  which is in agreement with both GENIE ( $3.33 \times 10^{-39} \text{ cm}^2 \text{ nucleon}^{-1}$ ) and NEUT with a RFG model ( $4.39 \times 10^{-39} \text{ cm}^2 \text{ nucleon}^{-1}$ ). It is also in very good agreement with the SF model prediction of  $3.83 \times 10^{-39} \text{ cm}^2 \text{ nucleon}^{-1}$ . The differential results show better agreement with GENIE than NEUT. The 2 dimensional distributions also agree very well with the SF model prediction. When considering 1-dimensional distributions such as muon momentum or angle, or reconstructed  $Q_{QE}^2$  the phase space considered is restricted to the regions of high efficiency to retain the model-independent nature of the result. In this case it is again found that the agreement is best with GENIE, though agreement is also very good with the SF model.

Future experiments such as Hyper-K and DUNE are being designed often assuming a total uncertainty of under 5% (reference [114] assumes ‘a prediction of the far detector unoscillated flux with a precision of  $\leq 2\%$ ’). Achieving this is seen as critical for the successful determination of the neutrino mass hierarchy and

observation of leptonic CP-violation.

The results shown here have a total uncertainty of almost 20%. If the flux normalisation uncertainty is neglected, as this uncertainty largely cancels in an oscillation experiment with a near detector, the remaining uncertainties still total approximately 10%.

In future, this analysis can easily be improved by increasing the available phase space to higher angles and backwards-going tracks, and reducing the flux uncertainties (new NA61/SHINE data is now available which reduces the uncertainty on the integrated flux from 11% to 8%). In the restricted phase space, where the data coverage is best, the second largest uncertainty sources are from the background modelling (6%) and pion secondary interactions in the detector (3%). Both of these uncertainties can only be reduced by measuring the processes carefully, either in situ or in a separate experiment. It would not be unreasonable to expect that these uncertainties may be reduced to 3-4% and 1-2% respectively, however even with these ambitious projections the uncertainty on the  $CC0\pi$  cross section remains above 5%.

Processes such as MEC have been proposed by theorists to address differences seen between data and predictions. These models are still in their infancy, and there is currently no conclusive evidence for the existence of these processes (though there are hints from the MINERvA [57] and ArgoNeuT [56] data). Searches for these processes, for example in a high-pressure TPC detector, could have a large impact in constraining the current uncertainties on the  $CCQE$ -like cross section.

It is clear, therefore, that achieving a total uncertainty of 5% in an oscillation experiment in 10 years time is going to be a major challenge requiring concentrated efforts, both experimental and theoretical, to constrain neutrino cross sections. Dedicated neutrino cross section experiments are almost certainly required to bridge the gap in understanding required to meet these targets.

# Appendix A

## SF appendices

### A.1 Derivation of cross-section formula Jacobian

To change the cross-section integration from the lab frame to the centre of momentum frame, we need to include the Jacobian.  $\frac{d^3k}{d^3k_{com}}$  [115]

Define:

$$x = \frac{G_F^2 \cos^2 \theta_C}{8\pi^2 E_{\mathbf{k}}}, \quad y = E_{\mathbf{k}} + M - E, \quad z = \frac{L_{\mu\nu} H^{\mu\nu}}{E_{\mathbf{p}} E_{\mathbf{k}'} E_{\mathbf{p}'}}. \quad (\text{A.1})$$

Now, the cross-section is given by:

$$\sigma = x \int dE d^3p P(\mathbf{p}, \tilde{E}) \int d^3k' \delta(E_{\mathbf{k}'} + E_{\mathbf{p}'} - y) z \quad (\text{A.2})$$

From solving the delta function in Equation A.2, and using  $\mathbf{k} + \mathbf{p} = \mathbf{k}' + \mathbf{p}'$ , the velocity of the centre of mass frame is found to be:

$$\mathbf{v} = \frac{\mathbf{p}' + \mathbf{k}'}{E_{\mathbf{k}'} + E_{\mathbf{p}'}} = \frac{\mathbf{p} + \mathbf{k}}{y}. \quad (\text{A.3})$$

Denoting CMS frame quantities using the suffix 'com', we can use the fact that  $\mathbf{p}_{com} + \mathbf{k}_{com} = 0$  to write the delta function as:

$$\delta(E_{\mathbf{k}'} + E_{\mathbf{p}'} - y) = \delta(\gamma(E_{\mathbf{p}'_{com}} + E_{\mathbf{k}'_{com}}) - y) \quad (\text{A.4})$$

$$= \delta(\gamma(\sqrt{M^2 + \mathbf{k}'_{com}{}^2} + \sqrt{m^2 + \mathbf{k}'_{com}{}^2}) - y) \quad (\text{A.5})$$

$$|\mathbf{k}'_{com}| = \sqrt{\frac{(s + m^2 - M^2)^2}{4s} - m^2}, \quad \text{where } s = \left(\frac{y}{\gamma}\right)^2 \quad (\text{A.6})$$

Then we can use

$$\int \delta(f(x))g(x)d^3x = \oint \frac{g(x)}{\nabla f(x)}dS \quad (\text{A.7})$$

and we calculate

$$|\nabla_{\mathbf{k}'}(E_{\mathbf{k}'} + E_{\mathbf{p}'} - y)| = \left| \frac{\mathbf{k}'}{E_{\mathbf{k}'}} - \frac{\mathbf{p}'}{E_{\mathbf{p}'}} \right| = |\mathbf{v}_{\mathbf{k}'} - \mathbf{v}_{\mathbf{p}'}| \quad (\text{A.8})$$

$$dS = \sqrt{\sin^2 \theta_{com} + \gamma \cos^2 \theta_{com}} dS_{com} \quad (\text{A.9})$$

$$= \sqrt{\sin^2 \theta_{com} + \gamma \cos^2 \theta_{com}} |\mathbf{k}'_{com}|^2 d\phi_{com} d \cos \theta_{com} \quad (\text{A.10})$$

Putting these together, we get the following Equation for the cross-section, now in the centre-of-mass variables

$$\sigma = \frac{G_F^2 \cos^2 \theta_C}{8\pi^2 E_{\mathbf{k}}} \int dE d^3p P(\mathbf{p}, \tilde{E}) \int \frac{L_{\mu\nu} H^{\mu\nu}}{E_{\mathbf{p}} E_{\mathbf{k}'} E_{\mathbf{p}'}} \quad (\text{A.11})$$

$$\frac{\sqrt{\sin^2 \theta_{com} + \gamma \cos^2 \theta_{com}}}{|\mathbf{v}_{\mathbf{k}'} - \mathbf{v}_{\mathbf{p}'}|} |\mathbf{k}'_{com}|^2 d\phi_{com} d \cos \theta_{com} \quad (\text{A.12})$$

## A.2 CCQE cross section calculation

In completely general terms, though neglecting the differences between incoming and outgoing nucleon masses, the nucleon weak current matrix element can be written as [48]:

$$\langle p(p') | J_\mu^+ | n(p) \rangle = \cos \theta_c \bar{u}(p') \Gamma_\mu u(p) \quad (\text{A.13})$$

$$\begin{aligned} \Gamma_\mu &= \gamma^\mu (F_1 - \gamma^5 F_A) + \frac{i}{2M} \sigma^{\mu\nu} q_\nu (F_2 - \gamma^5 F_{A^3}) \\ &+ \frac{1}{M} q^\mu (F_{V^3} - \gamma^5 F_P) \end{aligned} \quad (\text{A.14})$$

where we can see the V-A structure of the weak interaction in each term. Then, noting the relationship

$$q^\mu = p'^\mu - p^\mu, \quad (\text{A.15})$$

and following through trace algebra, which will not be written out in full here, we find the hadronic tensor can be written as

$$\begin{aligned} H^{\mu\nu} &= -g^{\mu\nu} M^2 H_1 + p^\mu p^\nu H_2 + \frac{i}{2} \epsilon^{\mu\nu\kappa\lambda} p_\kappa q_\lambda H_3 \\ &- q^\mu q^\nu H_4 + \frac{1}{2} (p^\mu q^\nu + q^\mu p^\nu) H_5 \end{aligned} \quad (\text{A.16})$$

where

$$\begin{aligned} H_1 &= F_A^2 (1 + \tau) + \tau (F_1 + F_2)^2 \\ H_2 &= F_A^2 + F_1^2 + \tau (F_2^2 + 4F_{3A}) \\ H_3 &= 2F_A (F_1 + F_2) \\ H_4 &= \frac{1}{4} (F_2^2 - \tau (F_2 - 2F_{3V})^2) + \tau (F_P + F_{3A})^2 \\ &- F_{3V}^2 - \frac{1}{2} F_1 (2F_{3V} - F_2) - 2F_A (F_P + F_{3A}) \\ H_5 &= H_2 + 2F_{3V} (F_1 - \tau F_2) - F_{3A} (F_A - 2\tau F_P). \\ \tau &= \frac{Q^2}{4M^2} \end{aligned} \quad (\text{A.17})$$

The leptonic tensor is:

$$L_{\mu\nu} = 2(k_\mu k'_\nu + k'_\mu k_\nu - k \cdot k' g_{\mu\nu} - i \epsilon_{\mu\nu\rho\sigma} k^\rho k'^\sigma) \quad (\text{A.18})$$

where  $\epsilon$  is the antisymmetric tensor, and  $\epsilon_{\nu\mu\rho\sigma} \epsilon^{\nu\mu\kappa\lambda} = \delta_\rho^\kappa \delta_\sigma^\lambda - \delta_\rho^\lambda \delta_\sigma^\kappa$ .  $q^\mu = (\omega, \vec{q})$  should be replaced by  $\tilde{q}^\mu = (\tilde{\omega}, \vec{q})$  to take into account the initial nucleon being off-

shell.

Contracting  $L_{\mu\nu}H^{\mu\nu}$  leads to the following expression:

$$\begin{aligned}
L_{\mu\nu}H^{\mu\nu} = & -2k \cdot k' M^2 H_1 \\
& + (2k \cdot p k' \cdot p - k \cdot k' p \cdot p) H_2 \\
& + (k \cdot \tilde{q} k' \cdot p - k \cdot p k' \cdot \tilde{q}) H_3 \\
& + (k \cdot k' \tilde{q} \cdot \tilde{q} - 2k \cdot \tilde{q} k' \cdot \tilde{q}) H_4 \\
& + (k \cdot p k' \cdot \tilde{q} + k' \cdot p k \cdot \tilde{q} - k \cdot k' p \cdot \tilde{q}) H_5
\end{aligned}$$

the third term of which, has the opposite sign when the incoming particle is an antineutrino. Rearranging the formula in terms of  $(s - u)$  gives us the equation

$$\begin{aligned}
L_{\mu\nu}H^{\mu\nu} = & (s - u)^2 H_2 - (s - u)(2q^2 H_3 + 2m^2 H_5) \\
& + (q^2 - m^2)[2H_1 + (4M^2 - q^2)H_2 - m^2 H_4] \tag{A.19}
\end{aligned}$$

$$= A(Q^2) + B(Q^2) \frac{(s - u)}{M^2} + C(Q^2) \frac{(s - u)^2}{M^4} \tag{A.20}$$

# Appendix B

## CC0 $\pi$ appendices

### B.1 Alternative results plots

Figures B.1 and B.2 show the final results in momentum slices, rather than cosine theta slices for the full, and restricted phase spaces.

Figures B.3 and B.4 show the generator comparisons presented in  $\cos \theta$  slices as ratios to the nominal NEUT MC, for the full- and restricted phase spaces. Figures B.5 and B.6 show the generator comparisons presented in muon momentum slices as ratios to the nominal NEUT MC, for the full- and restricted phase spaces.

### B.2 Alternative prior tests

Figures B.8 and B.9 show the unfolded result for the T2K data in the full- and restricted phase space respectively, for the nominal and two alternate priors. These priors are shown in figure B.7 This shows that the result is not biased by our choice of prior. Similar tests were performed for the 1D differential result, and for the restricted phase space results the conclusion is the same.

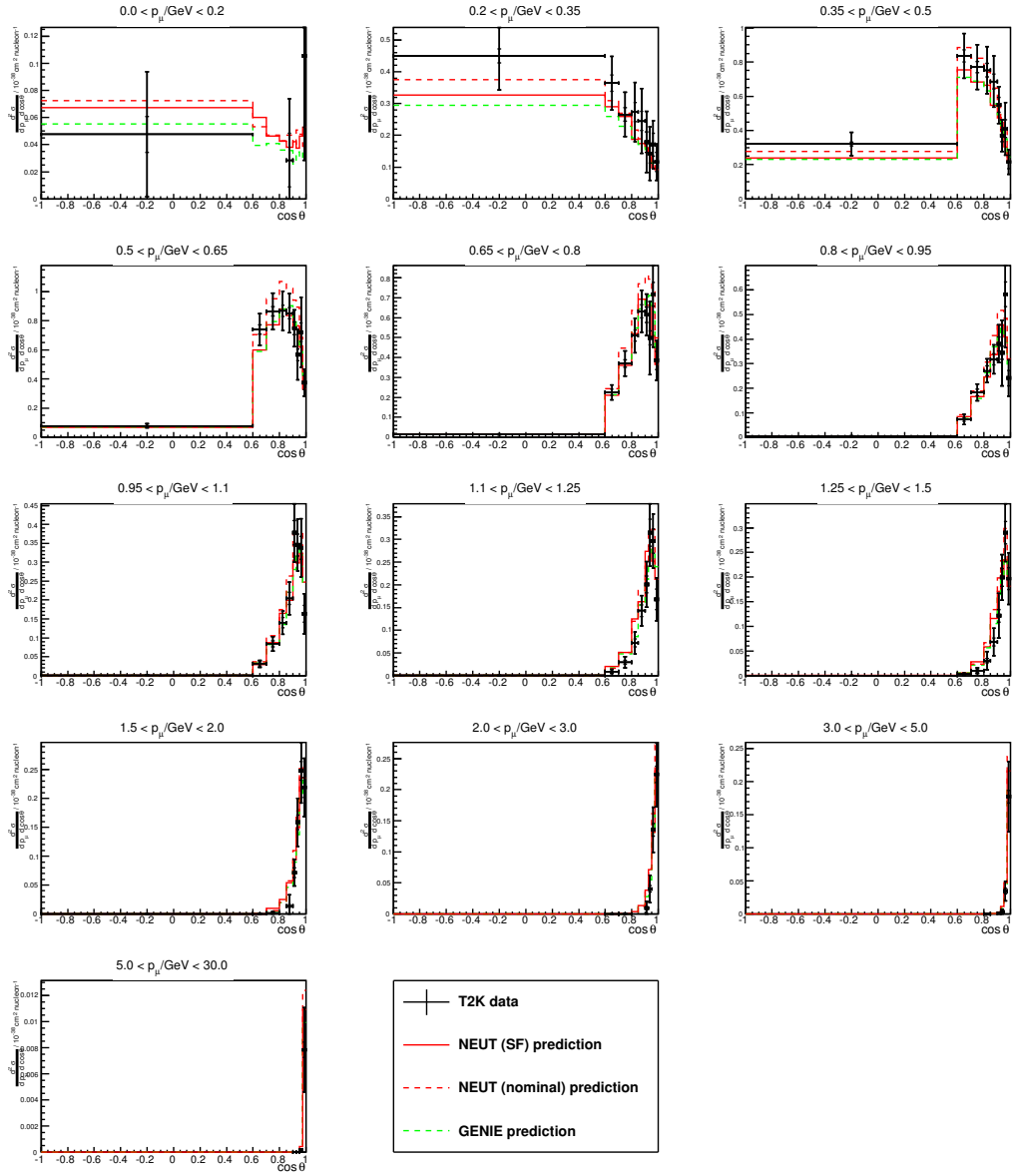


Figure B.1: Full phase-space results, compared to the NEUT nominal prediction. Inner error bars are statistical only.

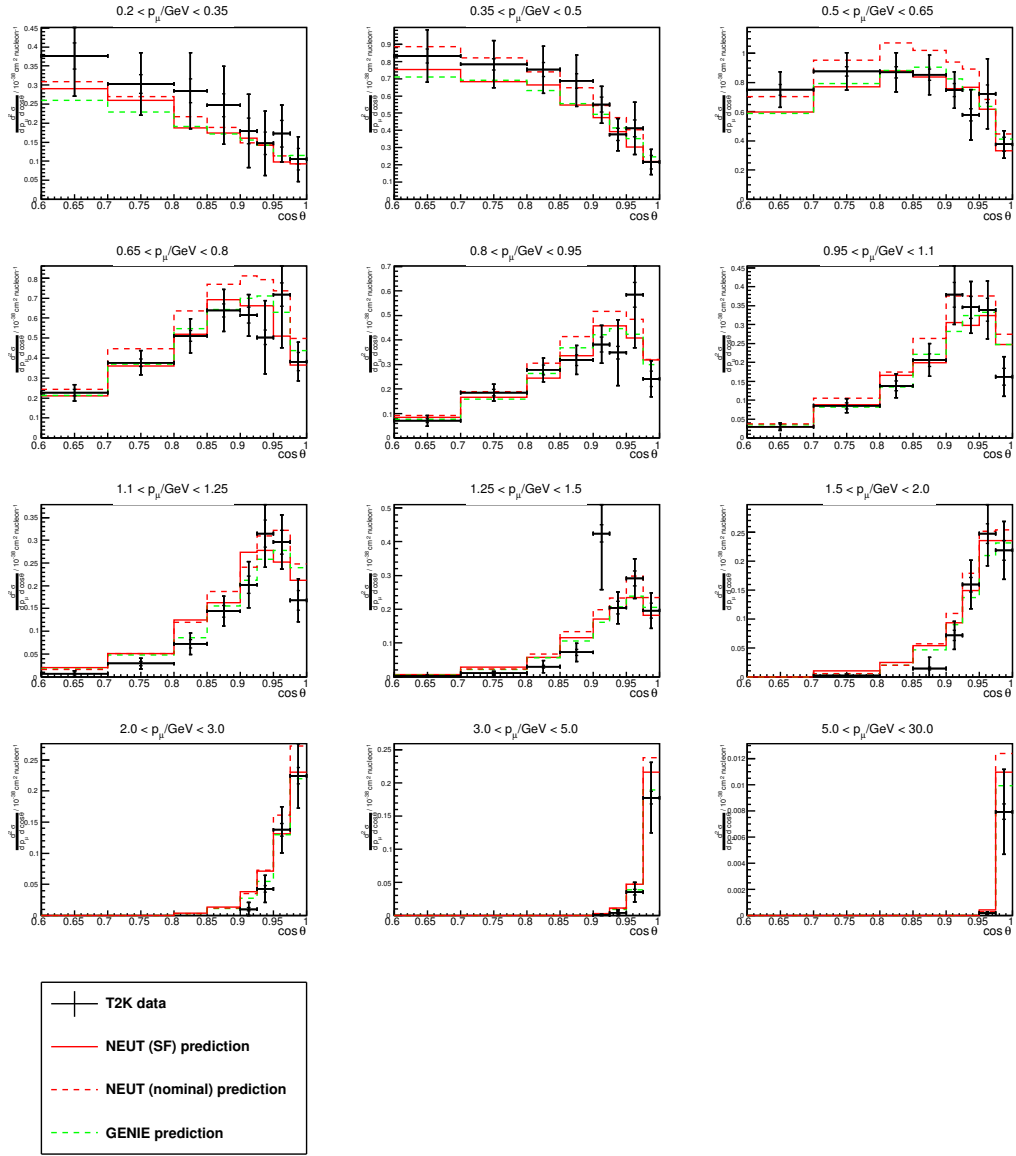


Figure B.2: Restricted phase-space results, compared to the NEUT nominal prediction. Inner error bars are statistical only.

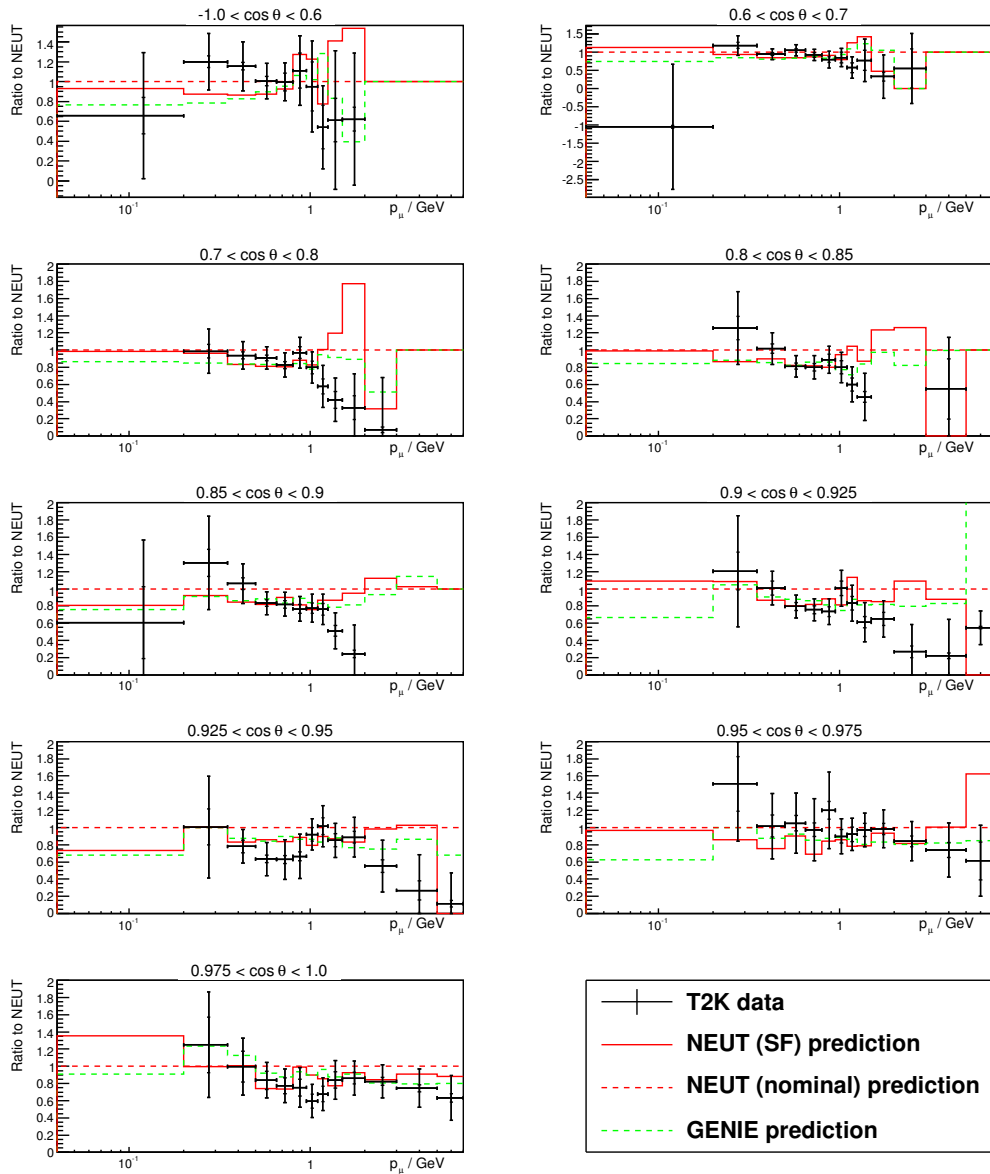


Figure B.3: Full phase-space results, presented as ratios to NEUT MC to inform comparisons with generators. Inner error bars are statistical only.

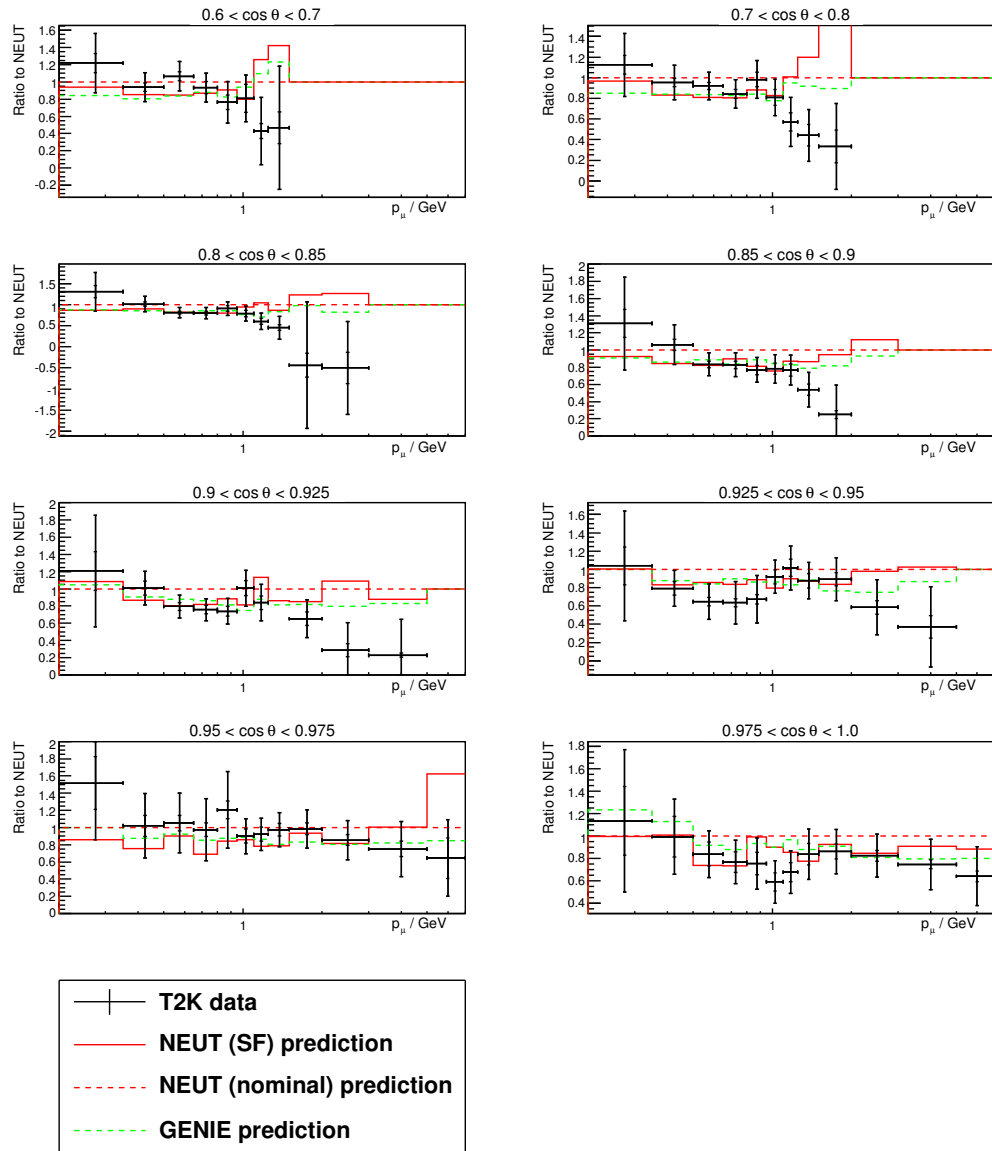


Figure B.4: Restricted phase-space results, presented as ratios to NEUT MC to inform comparisons with generators. Inner error bars are statistical only.

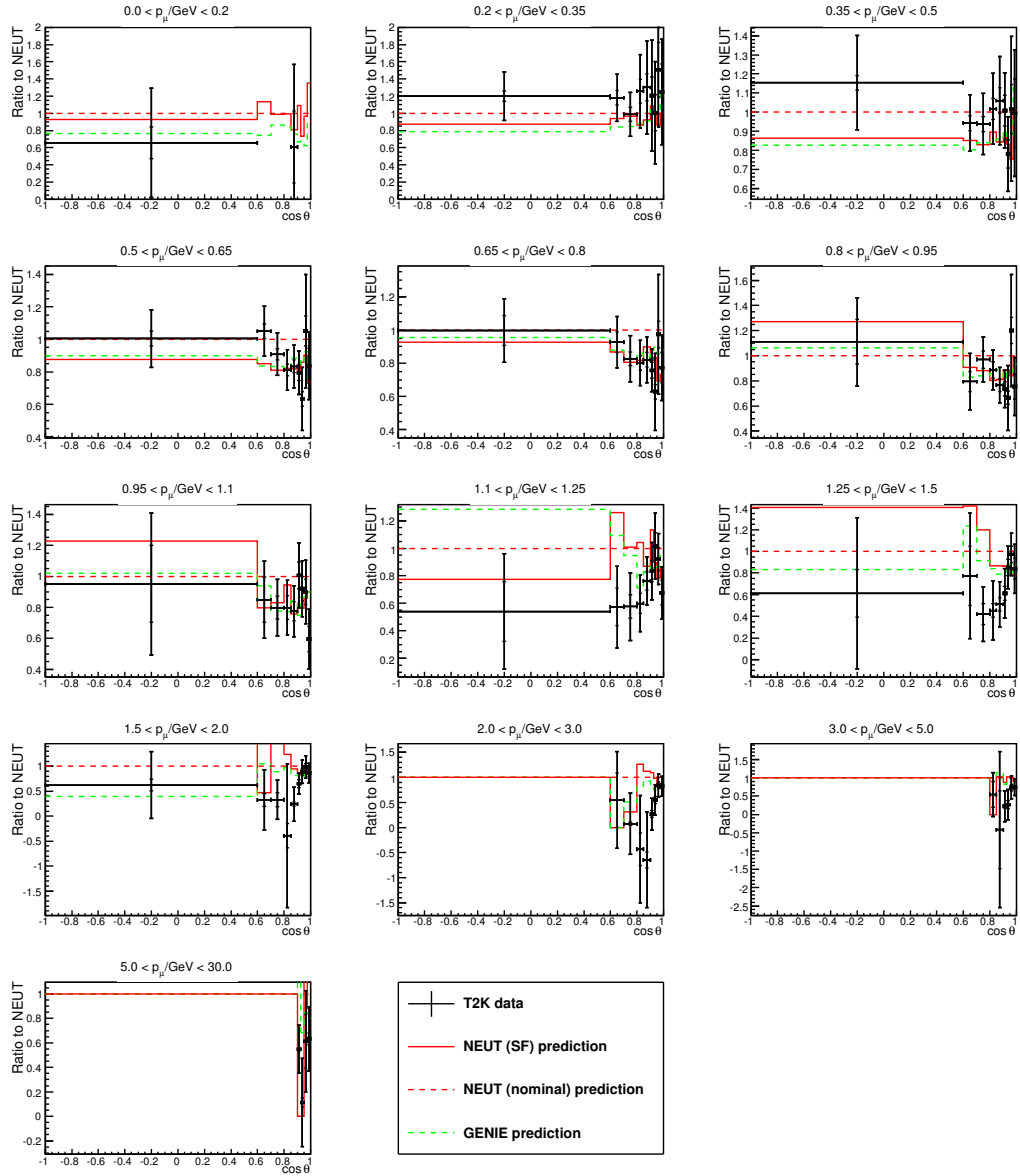


Figure B.5: Full phase-space results, presented as ratios to NEUT MC to inform comparisons with generators. Inner error bars are statistical only.

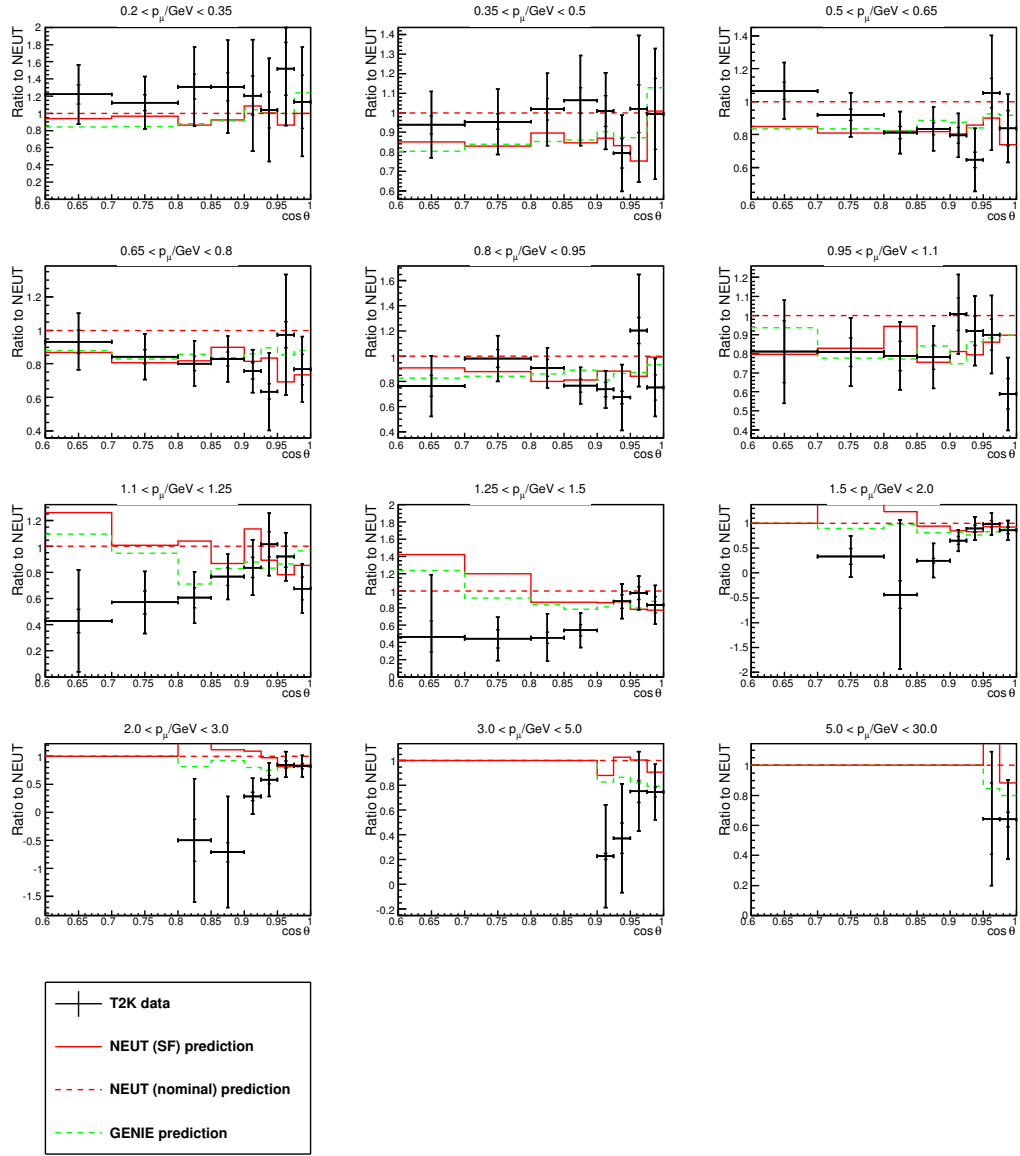


Figure B.6: Restricted phase-space results, presented as ratios to NEUT MC to inform comparisons with generators. Inner error bars are statistical only.

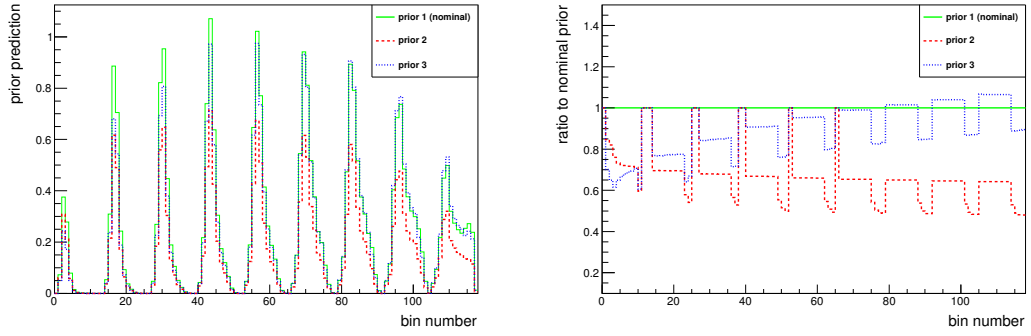


Figure B.7: (left) the nominal and two alternate priors, and (right) the ratios of all to the nominal prior. The full phase space is shown.

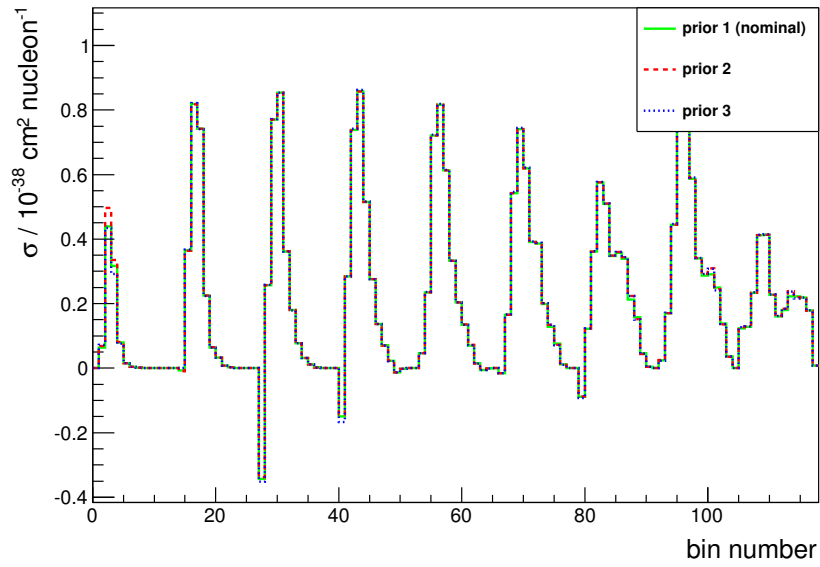


Figure B.8: Results over the full phase space, for the three priors shown in figure B.7.

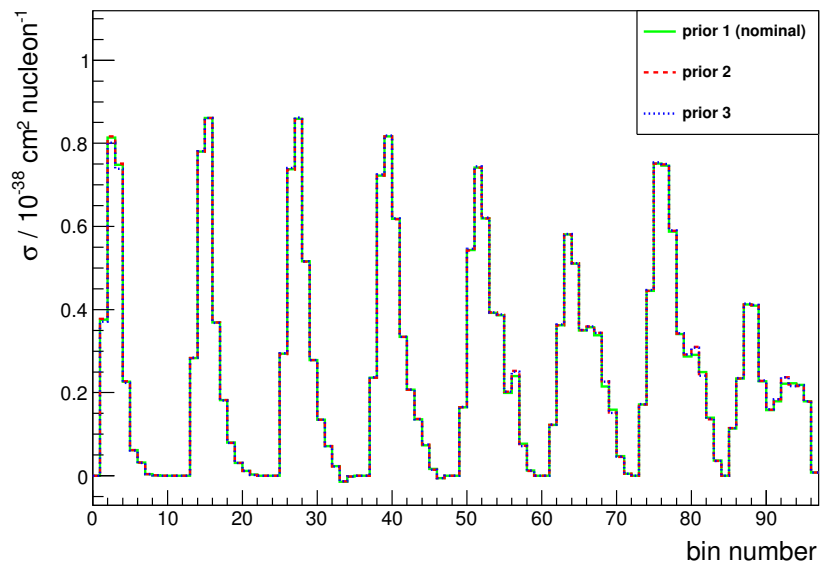


Figure B.9: Results over the restricted phase space, for the three priors shown in figure B.7.

# Bibliography

- [1] Q. R. Ahmad, et al. (The SNO experiment). Direct evidence for neutrino flavor transformation from neutral-current interactions in the sudbury neutrino observatory. *Phys. Rev. Lett.*, 89:011301, Jun 2002. doi: 10.1103/PhysRevLett.89.011301. URL <http://link.aps.org/doi/10.1103/PhysRevLett.89.011301>.
- [2] Y. Fukuda et al. Evidence for oscillation of atmospheric neutrinos. *Phys. Rev. Lett.*, 81:1562–1567, Aug 1998. doi: 10.1103/PhysRevLett.81.1562. URL <http://link.aps.org/doi/10.1103/PhysRevLett.81.1562>.
- [3] L. M. Brown. The idea of the neutrino. *Physics today*, 31(9):23, 1978.
- [4] C. L. Cowan, Jr., F. Reines, F. B. Harrison, H. W. Kruse, and A. D. McGuire. Detection of the Free Neutrino: A Confirmation. *Science*, 124:103–104, July 1956. doi: 10.1126/science.124.3212.103.
- [5] G. Danby, J-M. Gaillard, K. Goulianos, L. M. Lederman, N. Mistry, M. Schwartz, and J. Steinberger. Observation of high-energy neutrino reactions and the existence of two kinds of neutrinos. *Phys. Rev. Lett.*, 9:36–44, Jul 1962. doi: 10.1103/PhysRevLett.9.36. URL <http://journals.aps.org/prl/abstract/10.1103/PhysRevLett.9.36>.
- [6] K. Kodama et al. Observation of tau neutrino interactions. *Phys. Lett. B.*, 504(3):218 – 224, 2001. ISSN 0370-2693. doi: [http://dx.doi.org/10.1016/S0370-2693\(01\)00307-0](http://dx.doi.org/10.1016/S0370-2693(01)00307-0). URL <http://www.sciencedirect.com/science/article/pii/S0370269301003070>.
- [7] J. N. Bahcall and R. Davis, Jr. Solar neutrinos: A scientific puzzle. *Science*, 191(4224):pp. 264–267, 1976. ISSN 00368075. URL <http://www.jstor.org/stable/1741261>.

- [8] B. T. Cleveland, T. Daily, R. Davis, Jr., J. R. Distel, K. Lande, C. K. Lee, P. S. Wildenhain, and J. Ullman. Measurement of the solar electron neutrino flux with the homestake chlorine detector. *The Astrophysical Journal*, 496(1): 505, 1998. URL <http://stacks.iop.org/0004-637X/496/i=1/a=505>.
- [9] V. Berezhinsky, G. Fiorentini, and M. Lissia. LAST HOPE for an astrophysical solution to the solar neutrino problem. *Physics Letters B*, 365(14):185 – 192, 1996. ISSN 0370-2693. doi: [http://dx.doi.org/10.1016/0370-2693\(95\)01241-9](http://dx.doi.org/10.1016/0370-2693(95)01241-9). URL <http://www.sciencedirect.com/science/article/pii/S0370269395012419>.
- [10] B. Pontecorvo. Neutrino experiments and the problem of conservation of leptonic charge. *Sov. Phys. JETP*, 26, 1968.
- [11] N. Cabibbo. Unitary symmetry and leptonic decays. *Phys. Rev. Lett.*, 10: 531–533, Jun 1963. doi: 10.1103/PhysRevLett.10.531. URL <http://link.aps.org/doi/10.1103/PhysRevLett.10.531>.
- [12] The LEP Electroweak Working Group. Precision electroweak measurements on the Z resonance. *Physics Reports*, 427(56):257 – 454, 2006. ISSN 0370-1573. doi: <http://dx.doi.org/10.1016/j.physrep.2005.12.006>. URL <http://www.sciencedirect.com/science/article/pii/S0370157305005119>.
- [13] B. Richter. Conventional beams or neutrino factories: The next generation of accelerator-based neutrino experiments. *arXiv::hep-ph/0008222*, 2000. URL [arxiv.org/abs/hep-ph/0008222](http://arxiv.org/abs/hep-ph/0008222).
- [14] L. Wolfenstein. Neutrino oscillations in matter. *Phys. Rev. D*, 17:2369–2374, May 1978. doi: 10.1103/PhysRevD.17.2369. URL <http://link.aps.org/doi/10.1103/PhysRevD.17.2369>.
- [15] S. P. Mikheyev and A. Yu. Smirnov. Resonant amplification of oscillations in matter and solar-neutrino spectroscopy. *Il Nuovo Cimento C*, 9(1):17–26, 1986. ISSN 0390-5551. doi: 10.1007/BF02508049. URL <http://dx.doi.org/10.1007/BF02508049>.
- [16] G. L. Fogli, E. Lisi, A. Marrone, and A. Palazzo. Evidence for Mikheyev-Smirnov-Wolfenstein effects in solar neutrino flavor transitions. *Physics Letters B*, 583(12):149 – 156, 2004. ISSN 0370-2693. doi: <http://dx.doi.org/10.1016/j.physletb.2003.12.045>. URL <http://www.sciencedirect.com/science/article/pii/S0370269304000358>.

- [17] K. A. Olive et al. (Particle Data Group). Review of particle physics. *Chin. Phys. C*, 38:090001, 2014.
- [18] K. Abe et al. (T2K Collaboration). T2K neutrino flux prediction. *Phys. Rev. D*, 87(012001), 2013. doi: 10.1103/PhysRevD.87.012001.
- [19] M. H. Ahn et al. (The K2K Collaboration). Measurement of neutrino oscillation by the K2K experiment. *Phys. Rev. D*, 74:072003, Oct 2006. doi: 10.1103/PhysRevD.74.072003. URL <http://link.aps.org/doi/10.1103/PhysRevD.74.072003>.
- [20] P. Adamson et al. (MINOS collaboration). Measurement of neutrino and antineutrino oscillations using beam and atmospheric data in MINOS. *Phys. Rev. Lett.*, 110:251801, Jun 2013. doi: 10.1103/PhysRevLett.110.251801. URL <http://link.aps.org/doi/10.1103/PhysRevLett.110.251801>.
- [21] K. Abe et al. (The T2K Collaboration). Observation of electron neutrino appearance in a muon neutrino beam. *Phys. Rev. Lett.*, 112:061802, Feb 2014. doi: 10.1103/PhysRevLett.112.061802. URL <http://link.aps.org/doi/10.1103/PhysRevLett.112.061802>.
- [22] K. Abe et al. (The T2K Collaboration). Precise measurement of the neutrino mixing parameter  $\theta_{23}$  from muon neutrino disappearance in an off-axis beam. *Phys. Rev. Lett.*, 112:181801, May 2014. doi: 10.1103/PhysRevLett.112.181801. URL <http://link.aps.org/doi/10.1103/PhysRevLett.112.181801>.
- [23] D. Ayres et al. (NOvA collaboration). Fermilab-design-2007-01, 2007.
- [24] Nova official plots and figures, 2014. URL [http://www-nova.fnal.gov/plots\\_and\\_figures/plot\\_and\\_figures.html](http://www-nova.fnal.gov/plots_and_figures/plot_and_figures.html).
- [25] K. Eguchi et al. First results from KamLAND: Evidence for reactor antineutrino disappearance. *Phys. Rev. Lett.*, 90:021802, Jan 2003. doi: 10.1103/PhysRevLett.90.021802. URL <http://journals.aps.org/prl/abstract/10.1103/PhysRevLett.90.021802>.
- [26] S. Abe et al. Precision measurement of neutrino oscillation parameters with KamLAND. *Phys. Rev. Lett.*, 100:221803, Jun 2008. doi: 10.1103/PhysRevLett.100.221803. URL <http://link.aps.org/doi/10.1103/PhysRevLett.100.221803>.

- [27] M. Apollonio et al. Search for neutrino oscillations on a long base-line at the CHOOZ nuclear power station. *Eur. Phys. J. C*, 27, 2003. doi: 10.1140/epjc/s2002-01127-9. URL [arxiv.org/abs/hep-ex/0301017](http://arxiv.org/abs/hep-ex/0301017).
- [28] Y. Abe et al. Indication of reactor  $\bar{\nu}_e$  disappearance in the double chooz experiment. *Phys. Rev. Lett.*, 108:131801, Mar 2012. doi: 10.1103/PhysRevLett.108.131801. URL <http://link.aps.org/doi/10.1103/PhysRevLett.108.131801>.
- [29] Y. Abe et al. (Double Chooz Collaboration). Background-independent measurement of  $\theta_{13}$  in double chooz. *Physics Letters B*, 735(0):51 – 56, 2014. ISSN 0370-2693. doi: <http://dx.doi.org/10.1016/j.physletb.2014.04.045>. URL <http://www.sciencedirect.com/science/article/pii/S0370269314002858>.
- [30] J. K. Ahn et al. Observation of reactor electron antineutrinos disappearance in the RENO experiment. *Phys. Rev. Lett.*, 108:191802, May 2012. doi: 10.1103/PhysRevLett.108.191802. URL <http://link.aps.org/doi/10.1103/PhysRevLett.108.191802>.
- [31] S-H. Seo. Results from RENO, 2014. Neutrino 2014, XXVI International Conference on Neutrino Physics and Astrophysics, 2-7 June 2014, Boston, Massachusetts, USA.
- [32] F. P. An et al. Observation of electron-antineutrino disappearance at Daya Bay. *Phys. Rev. Lett.*, 108(171803), 2012. doi: 10.1103/PhysRevLett.108.171803.
- [33] F. P. An et al. Spectral measurement of electron antineutrino oscillation amplitude and frequency at Daya Bay. *Phys. Rev. Lett.*, 112:061801, Feb 2014. doi: 10.1103/PhysRevLett.112.061801. URL <http://link.aps.org/doi/10.1103/PhysRevLett.112.061801>.
- [34] C. Athanassopoulos et al. The liquid scintillator neutrino detector and LAMPF neutrino source. *NIM A*, 388(12):149 – 172, 1997. ISSN 0168-9002. doi: [http://dx.doi.org/10.1016/S0168-9002\(96\)01155-2](http://dx.doi.org/10.1016/S0168-9002(96)01155-2). URL <http://www.sciencedirect.com/science/article/pii/S0168900296011552>.
- [35] C. Athanassopoulos et al. Results on  $\nu_\mu \rightarrow \nu_e$  neutrino oscillations from the LSND experiment. *Phys. Rev. Lett.*, 81:1774–1777, Aug 1998. doi: 10.1103/PhysRevLett.81.1774. URL <http://link.aps.org/doi/10.1103/PhysRevLett.81.1774>.

- [36] A. Aguilar et al. Evidence for neutrino oscillations from the observation of  $\bar{\nu}_e$  appearance in a  $\bar{\nu}_\mu$  beam. *Phys. Rev. D*, 64:112007, Nov 2001. doi: 10.1103/PhysRevD.64.112007. URL <http://link.aps.org/doi/10.1103/PhysRevD.64.112007>.
- [37] A. A. Aguilar-Arevalo et al. Improved search for  $\bar{\nu}_\mu \rightarrow \bar{\nu}_e$  oscillations in the MiniBooNE experiment. *Phys. Rev. Lett.*, 110:161801, Apr 2013. doi: 10.1103/PhysRevLett.110.161801. URL <http://link.aps.org/doi/10.1103/PhysRevLett.110.161801>.
- [38] G. Mention, M. Fechner, Th. Lasserre, Th. A. Mueller, D. Lhuillier, M. Cribier, and A. Letourneau. Reactor antineutrino anomaly. *Phys. Rev. D*, 83:073006, Apr 2011. doi: 10.1103/PhysRevD.83.073006. URL <http://link.aps.org/doi/10.1103/PhysRevD.83.073006>.
- [39] K. Abe et al. Letter of intent: The hyper-kamiokande experiment — detector design and physics potential —. *arXiv:1109.3262*, 2011. URL <http://arxiv.org/abs/1109.3262>.
- [40] C. Adams et al. The long-baseline neutrino experiment: Exploring fundamental symmetries of the universe. *arXiv:1307.7335v3*, 2014. URL <http://arxiv.org/abs/1307.7335>.
- [41] C. Anderson, M. Antonello, B. Baller, T. Bolton, C. Bromberg, F. Cavanna, E. Church, D. Edmunds, A. Ereditato, S. Farooq, B. Fleming, H. Greenlee, R. Guenette, S. Haug, G. Horton-Smith, C. James, E. Klein, K. Lang, A. Lathrop, P. Laurens, S. Linden, D. McKee, R. Mehdiev, B. Page, O. Palamara, K. Partyka, S. Pordes, G. Rameika, B. Rebel, B. Rossi, R. Sanders, M. Soderberg, J. Spitz, A. M. Szec, M. Weber, T. Wongjirad, T. Yang, and G. P. Zeller. The argoneut detector in the NuMI low-energy beam line at fermilab. *Journal of Instrumentation*, 7(10):P10019, 2012. URL <http://stacks.iop.org/1748-0221/7/i=10/a=P10019>.
- [42] C. Anderson et al. A proposal for a new experiment using the booster and numi neutrino beamlines: Microboone, October 2007. URL [http://www-microboone.fnal.gov/public/MicroBooNE\\_{ }10152007.pdf](http://www-microboone.fnal.gov/public/MicroBooNE_{ }10152007.pdf).
- [43] Li Y-F, J. Cao, Y. Wang, and L. Zhan. Unambiguous determination of the neutrino mass hierarchy using reactor neutrinos. *Phys. Rev. D*, 88:013008, Jul 2013. doi: 10.1103/PhysRevD.88.013008. URL <http://journals.aps.org/prd/abstract/10.1103/PhysRevD.88.013008>.

- [44] L. Zhan, Y. Wang, J. Cao, and L. Wen. Determination of the neutrino mass hierarchy at an intermediate baseline. *Phys. Rev. D*, 78:111103, Dec 2008. doi: 10.1103/PhysRevD.78.111103. URL <http://link.aps.org/doi/10.1103/PhysRevD.78.111103>.
- [45] C. S. Wu, E. Ambler, R. W. Hayward, D. D. Hoppes, and R. P. Hudson. Experimental test of parity conservation in beta decay. *Phys. Rev.*, 105:1413–1415, Feb 1957. doi: 10.1103/PhysRev.105.1413. URL <http://link.aps.org/doi/10.1103/PhysRev.105.1413>.
- [46] D. Griffiths. *Introduction to Elementary Particles (2nd edition)*. Wiley-VCH, 2008.
- [47] J. A. Formaggio and G. P. Zeller. From eV to EeV: Neutrino cross sections across energy scales. *Rev. Mod. Phys.*, 84:1307–1341, Sep 2012. doi: 10.1103/RevModPhys.84.1307. URL <http://journals.aps.org/rmp/abstract/10.1103/RevModPhys.84.1307>.
- [48] C. H. Llewellyn Smith. Neutrino reactions at accelerator energies. *Physics Reports*, 3(5):261 – 379, 1972. ISSN 0370-1573. doi: [http://dx.doi.org/10.1016/0370-1573\(72\)90010-5](http://dx.doi.org/10.1016/0370-1573(72)90010-5). URL <http://www.sciencedirect.com/science/article/pii/0370157372900105>.
- [49] A. Bodek, S. Avvakumov, R. Bradford, and H. Budd. Vector and axial nucleon form factors: A duality constrained parameterization. *The European Physical Journal C*, 53(3):349–354, 2008. ISSN 1434-6044. doi: 10.1140/epjc/s10052-007-0491-4. URL <http://dx.doi.org/10.1140/epjc/s10052-007-0491-4>.
- [50] M. Day and K. S. McFarland. Differences in quasi-elastic cross-sections of muon and electron neutrinos. *arXiv:1206.6745 [hep-ph]*, 2012. URL [arxiv.org/abs/1206.6745](http://arxiv.org/abs/1206.6745).
- [51] M. L. Goldberger and S. B. Treiman. Decay of the pi meson. *Phys. Rev.*, 110:1178–1184, Jun 1958. doi: 10.1103/PhysRev.110.1178. URL <http://link.aps.org/doi/10.1103/PhysRev.110.1178>.
- [52] D. Rein and L. M. Sehgal. Neutrino-excitation of baryon resonances and single pion production. *Annals of Physics*, 133(1):79 – 153, 1981. ISSN 0003-4916. doi: [http://dx.doi.org/10.1016/0003-4916\(81\)90242-6](http://dx.doi.org/10.1016/0003-4916(81)90242-6). URL <http://www.sciencedirect.com/science/article/pii/0003491681902426>.

- [53] Y. Hayato. Neut. *Nuclear Physics B - Proceedings Supplements*, 112 (13):171 – 176, 2002. ISSN 0920-5632. doi: [http://dx.doi.org/10.1016/S0920-5632\(02\)01759-0](http://dx.doi.org/10.1016/S0920-5632(02)01759-0). URL <http://www.sciencedirect.com/science/article/pii/S0920563202017590>.
- [54] R. A. Smith and E. J. Moniz. Neutrino reactions on nuclear targets. *Nuclear Physics B*, 43(0):605 – 622, 1972. ISSN 0550-3213. doi: [http://dx.doi.org/10.1016/0550-3213\(72\)90040-5](http://dx.doi.org/10.1016/0550-3213(72)90040-5). URL <http://www.sciencedirect.com/science/article/pii/0550321372900405>.
- [55] A. De Rújula, R. Petronzio, and A. Savoy-Navarro. Radiative corrections to high-energy neutrino scattering. *Nuclear Physics B*, 154(3):394 – 426, 1979. ISSN 0550-3213. doi: [http://dx.doi.org/10.1016/0550-3213\(79\)90039-7](http://dx.doi.org/10.1016/0550-3213(79)90039-7). URL <http://www.sciencedirect.com/science/article/pii/0550321379900397>.
- [56] R. Acciarri et al. Detection of back-to-back proton pairs in charged-current neutrino interactions with the argoneut detector in the NuMI low energy beam line. *Phys. Rev. D*, 90:012008, Jul 2014. doi: 10.1103/PhysRevD.90.012008. URL <http://link.aps.org/doi/10.1103/PhysRevD.90.012008>.
- [57] G. A. Fiorentini et al. Measurement of muon neutrino quasielastic scattering on a hydrocarbon target at  $E_\nu \sim 3.5$  GeV. *Phys. Rev. Lett.*, 111:022502, Jul 2013. doi: 10.1103/PhysRevLett.111.022502. URL <http://link.aps.org/doi/10.1103/PhysRevLett.111.022502>.
- [58] J. Nieves, I. Ruiz Simo, and M. J. Vicente Vacas. Inclusive charged-current neutrino-nucleus reactions. *Phys. Rev. C*, 83:045501, Apr 2011. doi: 10.1103/PhysRevC.83.045501. URL <http://link.aps.org/doi/10.1103/PhysRevC.83.045501>.
- [59] M. Martini, M. Ericson, G. Chanfray, and J. Marteau. Unified approach for nucleon knock-out and coherent and incoherent pion production in neutrino interactions with nuclei. *Phys. Rev. C*, 80:065501, Dec 2009. doi: 10.1103/PhysRevC.80.065501. URL <http://link.aps.org/doi/10.1103/PhysRevC.80.065501>.
- [60] M. Martini, M. Ericson, G. Chanfray, and J. Marteau. Neutrino and antineutrino quasielastic interactions with nuclei. *Phys. Rev. C*, 81:045502, Apr 2010. doi: 10.1103/PhysRevC.81.045502. URL <http://link.aps.org/doi/10.1103/PhysRevC.81.045502>.

- [61] A. Bodek, H. S. Budd, and M. E. Christy. Neutrino quasielastic scattering on nuclear targets. *EPJ C*, 71(9):1726, 2011. ISSN 1434-6044. doi: 10.1140/epjc/s10052-011-1726-y. URL <http://dx.doi.org/10.1140/epjc/s10052-011-1726-y>.
- [62] J. Nieves, J. E. Amaro, and M. Valverde. Inclusive quasielastic charged-current neutrino-nucleus reactions. *Phys. Rev. C*, 70:055503, Nov 2004. doi: 10.1103/PhysRevC.70.055503. URL <http://journals.aps.org/prc/abstract/10.1103/PhysRevC.70.055503>.
- [63] V. Bernard, L. Elouadrhiri, and U-G. Meißner. Axial structure of the nucleon. *Journal of Physics G: Nuclear and Particle Physics*, 28(1):R1, 2002. URL <http://stacks.iop.org/0954-3899/28/i=1/a=201>.
- [64] A. A. Aguilar-Arevalo et al. First measurement of the muon neutrino charged current quasielastic double differential cross section. *Phys. Rev. D*, 81:092005, May 2010. doi: 10.1103/PhysRevD.81.092005. URL <http://link.aps.org/doi/10.1103/PhysRevD.81.092005>.
- [65] D. Rein and L. M. Sehgal. Coherent  $\pi^0$  production in neutrino reactions. *Nuclear Physics B*, 223(1):29 – 44, 1983. ISSN 0550-3213. doi: [http://dx.doi.org/10.1016/0550-3213\(83\)90090-1](http://dx.doi.org/10.1016/0550-3213(83)90090-1). URL <http://www.sciencedirect.com/science/article/pii/0550321383900901>.
- [66] D. Scully. *Neutrino induced coherent pion production*. PhD thesis, University of Warwick, 2013.
- [67] A. Kayis-Topaksu et al. Charged-particle multiplicities in charged-current neutrino and anti-neutrino-nucleus interactions. *The European Physical Journal C*, 51(4):775–785, 2007. ISSN 1434-6044. doi: 10.1140/epjc/s10052-007-0366-8. URL <http://dx.doi.org/10.1140/epjc/s10052-007-0366-8>.
- [68] J. J. Aubert et al. The ratio of the nucleon structure functions  $F_{2N}$  for iron and deuterium. *Physics Letters B*, 123(34):275 – 278, 1983. ISSN 0370-2693. doi: [http://dx.doi.org/10.1016/0370-2693\(83\)90437-9](http://dx.doi.org/10.1016/0370-2693(83)90437-9). URL <http://www.sciencedirect.com/science/article/pii/0370269383904379>.
- [69] D. Casper. The nuance neutrino physics simulation, and the future. *Nuclear Physics B - Proceedings Supplements*, 112(13):161 – 170, 2002. ISSN 0920-5632. doi: [http://dx.doi.org/10.1016/S0920-5632\(02\)01756-5](http://dx.doi.org/10.1016/S0920-5632(02)01756-5). URL <http://www.sciencedirect.com/science/article/pii/S0920563202017565>.

- [70] H. Gallagher. The NEUGEN neutrino event generator. *Nuclear Physics B - Proceedings Supplements*, 112(13):188 – 194, 2002. ISSN 0920-5632. doi: [http://dx.doi.org/10.1016/S0920-5632\(02\)01775-9](http://dx.doi.org/10.1016/S0920-5632(02)01775-9). URL <http://www.sciencedirect.com/science/article/pii/S0920563202017759>.
- [71] G. Barr. PhD thesis, Oxford University, 1987.
- [72] C. Andreopoulos et al. The GENIE Neutrino Monte Carlo Generator. *Nucl. Instrum. Meth.*, A614:87–104, 2010. doi: 10.1016/j.nima.2009.12.009.
- [73] C. Juszczak, J. A. Nowak, and J. T. Sobczyk. Simulations from a new neutrino event generator. *Nuclear Physics B - Proceedings Supplements*, 159(0):211 – 216, 2006. ISSN 0920-5632. doi: <http://dx.doi.org/10.1016/j.nuclphysbps.2006.08.069>. URL <http://www.sciencedirect.com/science/article/pii/S0920563206005329>.
- [74] Nuwro, 2014. URL <http://borg.ift.uni.wroc.pl/nuwro/>.
- [75] T. Sjöstrand, P. Edén, C. Friberg, L. Lönnblad, G. Miu, S. Mrenna, and E. Norrbin. High-energy-physics event generation with pythia6.1. *Computer Physics Communications*, 135(2):238 – 259, 2001. ISSN 0010-4655. doi: [http://dx.doi.org/10.1016/S0010-4655\(00\)00236-8](http://dx.doi.org/10.1016/S0010-4655(00)00236-8). URL <http://www.sciencedirect.com/science/article/pii/S0010465500002368>.
- [76] K. Abe et al. (T2K Collaboration). The T2K Experiment. *Nuclear Instruments and Methods A*, 659(1):106, 2011. doi: 10.1016/j.nima.2012.05.028.
- [77] J. K. Ahn et al. (RENO Collaboration). Observation of reactor electron antineutrinos disappearance in the reno experiment. *Phys. Rev. Lett.*, 108 (191802), 2012. doi: 10.1103/PhysRevLett.108.191802.
- [78] K. Abe et al. (The T2K Collaboration). Evidence of electron neutrino appearance in a muon neutrino beam. *Phys. Rev. D*, 88(032002), 2013. doi: 10.1103/PhysRevD.88.032002.
- [79] T2K collaboration photographs, 2014. URL <http://www.t2k.org/docs/photos>.
- [80] K. Abe et al. Measurements of the T2K neutrino beam properties using the INGRID on-axis near detector. *Nuclear Instruments and Methods A*, 694 (0):211 – 223, 2012. ISSN 0168-9002. doi: <http://dx.doi.org/10.1016/j.nima.2012.03.023>. URL <http://www.sciencedirect.com/science/article/pii/S0168900212002987>.

- [81] Y. Uchida et al. ND280 images., 2014. URL <https://www.t2kuk.org/wiki/YoshiUchida/ND280Pictures>.
- [82] S. Assylbekov et al. The T2K ND280 off-axis pizero detector. *NIM A*, 686(0):48 – 63, 2012. ISSN 0168-9002. doi: <http://dx.doi.org/10.1016/j.nima.2012.05.028>. URL <http://www.sciencedirect.com/science/article/pii/S0168900212005153>.
- [83] P. A. Amaudruz et al. The T2K fine-grained detectors. *Nuclear Instruments and Methods A*, 696(0):1, 2012. doi: 10.1016/j.nima.2012.08.020.
- [84] N. Abgrall et al. Time projection chambers for the T2K near detectors. *Nuclear Instruments and Methods A*, 637(1):25, 2011.
- [85] T2K public website gallery, 2014. URL [t2k-experiment.org/gallery/](http://t2k-experiment.org/gallery/).
- [86] D. Allan et al. The electromagnetic calorimeter for the T2K near detector ND280. *Journal of Instrumentation*, 8(10):P10019, 2013. URL <http://stacks.iop.org/1748-0221/8/i=10/a=P10019>.
- [87] S. Aoki et al. The T2K side muon range detector (SMRD). *NIM A*, 698(0):135 – 146, 2013. ISSN 0168-9002. doi: <http://dx.doi.org/10.1016/j.nima.2012.10.001>. URL <http://www.sciencedirect.com/science/article/pii/S0168900212011242>.
- [88] ICRR super-kamiokande photo gallery, 2014. URL [www-sk.icrr.u-tokyo.ac.jp/sk/gallery/index-e.html](http://www-sk.icrr.u-tokyo.ac.jp/sk/gallery/index-e.html).
- [89] N. Abgrall et al. Measurements of cross sections and charged pion spectra in proton-carbon interactions at 31 GeV/c. *Phys. Rev. C*, 84:034604, Sep 2011. doi: 10.1103/PhysRevC.84.034604. URL <http://link.aps.org/doi/10.1103/PhysRevC.84.034604>.
- [90] N. Abgrall et al. Measurement of production properties of positively charged kaons in proton-carbon interactions at 31 GeV/c. *Phys. Rev. C*, 85:035210, Mar 2012. doi: 10.1103/PhysRevC.85.035210. URL <http://link.aps.org/doi/10.1103/PhysRevC.85.035210>.
- [91] M. Bass et al. Future sensitivity task force summary report. *T2K technical note, T2K-TN-173*, 2013.

- [92] M. Friend et al. Future sensitivity task force three flavor log likelihood fitter using a realistic systematic error covariance matrix. *T2K technical note, T2K-TN-151*, 2013.
- [93] M. Glück, E. Reya, and A. Vogt. Dynamical parton distributions of the proton and small-x physics. *Zeitschrift für Physik C Particles and Fields*, 67(3): 433–447, 1995. ISSN 0170-9739. doi: 10.1007/BF01624586. URL <http://dx.doi.org/10.1007/BF01624586>.
- [94] Z. Koba, H. B. Nielsen, and P. Olesen. Scaling of multiplicity distributions in high energy hadron collisions. *Nuclear Physics B*, 40(0):317 – 334, 1972. ISSN 0550-3213. doi: [http://dx.doi.org/10.1016/0550-3213\(72\)90551-2](http://dx.doi.org/10.1016/0550-3213(72)90551-2). URL <http://www.sciencedirect.com/science/article/pii/0550321372905512>.
- [95] A. E. L. Dieperink, T. De Forest Jr., I. Sick, and R. A. Brandenburg. Quasi-elastic electron scattering on  $^3\text{He}$ . *Physics Letters B*, 63(3):261 – 264, 1976. ISSN 0370-2693. doi: [http://dx.doi.org/10.1016/0370-2693\(76\)90258-6](http://dx.doi.org/10.1016/0370-2693(76)90258-6). URL <http://www.sciencedirect.com/science/article/pii/0370269376902586>.
- [96] C. Ciofi degli Atti, E. Pace, and G. Salmè. Realistic nucleon-nucleon interactions and the three-body electrodisintegration of  $^3\text{H}$ . *Phys. Rev. C*, 21: 805–815, Mar 1980. doi: 10.1103/PhysRevC.21.805. URL <http://link.aps.org/doi/10.1103/PhysRevC.21.805>.
- [97] H. Meier-Hajduk, Ch. Hajduk, P. U. Sauer, and W. Theis. Quasi-elastic electron scattering from  $^3\text{He}$ . *Nuclear Physics A*, 395(2):332 – 348, 1983. ISSN 0375-9474. doi: [http://dx.doi.org/10.1016/0375-9474\(83\)90047-7](http://dx.doi.org/10.1016/0375-9474(83)90047-7). URL <http://www.sciencedirect.com/science/article/pii/0375947483900477>.
- [98] C. Ciofi degli Atti, S. Liuti, and S. Simula. Nucleon spectral function in complex nuclei and nuclear matter and inclusive quasielastic electron scattering. *Phys. Rev. C*, 41:R2474–R2478, Jun 1990. doi: 10.1103/PhysRevC.41.R2474. URL <http://link.aps.org/doi/10.1103/PhysRevC.41.R2474>.
- [99] O. Benhar, A. Fabrocini, and S. Fantoni. The nucleon spectral function in nuclear matter. *Nuclear Physics A*, 505(2):267 – 299, 1989. ISSN 0375-9474. doi: [http://dx.doi.org/10.1016/0375-9474\(89\)90374-6](http://dx.doi.org/10.1016/0375-9474(89)90374-6). URL <http://www.sciencedirect.com/science/article/pii/0375947489903746>.
- [100] A. Ramos, A. Polls, and W. H. Dickhoff. Single-particle properties and short-range correlations in nuclear matter. *Nuclear Physics A*, 503(1):1 –

- 52, 1989. ISSN 0375-9474. doi: [http://dx.doi.org/10.1016/0375-9474\(89\)90252-2](http://dx.doi.org/10.1016/0375-9474(89)90252-2). URL <http://www.sciencedirect.com/science/article/pii/0375947489902522>.
- [101] O. Benhar, A. Fabrocini, S. Fantoni, and I. Sick. Spectral function of finite nuclei and scattering of GeV electrons. *Nuclear Physics A*, 579(34):493 – 517, 1994. ISSN 0375-9474. doi: [http://dx.doi.org/10.1016/0375-9474\(94\)90920-2](http://dx.doi.org/10.1016/0375-9474(94)90920-2). URL <http://www.sciencedirect.com/science/article/pii/0375947494909202>.
- [102] H. Nakamura, T. Nasu, M. Sakuda, and O. Benhar. Inclusive electron spectrum in the region of pion production in electron-nucleus scattering and the effect of the quasi-elastic interaction. *Phys. Rev. C*, 76:065208, Dec 2007. doi: [10.1103/PhysRevC.76.065208](https://doi.org/10.1103/PhysRevC.76.065208). URL <http://link.aps.org/doi/10.1103/PhysRevC.76.065208>.
- [103] A. M. Ankowski and J. T. Sobczyk. Argon spectral function and neutrino interactions. *arXiv:nucl-th/0512004*, 2012. URL [arXiv:nucl-th/0512004](https://arxiv.org/abs/nucl-th/0512004).
- [104] O. Benhar, N. Farina, H. Nakamura, M. Sakuda, and R. Seki. Electron- and neutrino-nucleus scattering in the impulse approximation regime. *Phys. Rev. D*, 72:053005, Sep 2005. doi: [10.1103/PhysRevD.72.053005](https://doi.org/10.1103/PhysRevD.72.053005). URL <http://link.aps.org/doi/10.1103/PhysRevD.72.053005>.
- [105] C. Ciofi degli Atti and S. Simula. Realistic model of the nucleon spectral function in few- and many-nucleon systems. *Phys. Rev. C*, 53:1689–1710, Apr 1996. doi: [10.1103/PhysRevC.53.1689](https://doi.org/10.1103/PhysRevC.53.1689). URL <http://link.aps.org/doi/10.1103/PhysRevC.53.1689>.
- [106] P. de Perio et al. Implementation of the NIWG cross section parametrization. *T2K technical note, T2K-TN-113*, 2012.
- [107] E. J. Moniz, I. Sick, R. R. Whitney, J. R. Ficenec, R. D. Kephart, and W. P. Trower. Nuclear Fermi momenta from quasielastic electron scattering. *Phys. Rev. Lett.*, 26:445–448, Feb 1971. doi: [10.1103/PhysRevLett.26.445](https://doi.org/10.1103/PhysRevLett.26.445). URL <http://link.aps.org/doi/10.1103/PhysRevLett.26.445>.
- [108] A. Bercellie, Y. Hayato, K. Ieki, A. Kaboth, K. Mahn, K. McFarland, P. Rodrigues, R. Terri, M. Wascko, and C. Wilkinson. Cross section parameters for 2014 oscillation analysis. *T2K technical note, T2K-TN-192*, 2014.

- [109] M. Hartz, A. Kaboth, and K. Mahn. Constraining the flux and cross section models with data from the ND280 detector for the 2013 oscillation analysis. *T2K technical note, T2K-TN-166*, 2013.
- [110] C. Bocjehko et al. CC-multiple-pion  $\nu_\mu$  event selections in the ND280 tracker using run 1+2+3+4 data. *T2K technical note, T2K-TN-152*, 2013.
- [111] G. D'Agostini. A multidimensional unfolding method based on Bayes' theorem. *NIM A*, 362:487–498, 1995.
- [112] T. Adye et al. RooUnfold, 2014. URL <http://hepunix.rl.ac.uk/~adye/software/unfold/RooUnfold.html>.
- [113] S. Oser. Elemental composition of the FGD XY modules. *T2K technical note, T2K-TN-091*, 2010.
- [114] LBNE collaboration. The long-baseline neutrino experiment: Exploring fundamental symmetries of the universe. *arXiv:1307.7335 [hep-ex]*, 2014.
- [115] C. Juszczak. private communication, 2014.